SAPIENZA
UNIVERSITÀ DI ROMA

Sapienza University of Rome

Faculty of Civil and Industrial Engineering
Department of Mechanical and Aerospace Engineering
Ph.D. Programme in Theoretical and Applied Mechanics

XXXIV CYCLE
Ph.D. Thesis

A Novel High-Fidelity Two-Way Coupling Model for Fluid-Structure Interaction in Wind Energy

Supervisors
Prof. Matteo Bernardini
Prof. Stefano Leonardi

Tutor
Prof. Paolo Gualtieri

Candidate
Giacomo Della Posta
1532252

In collaboration with
The Univerisity of Texas at Dallas

Academic Year 2021 - 2022

Abstract

A Novel High-Fidelity Two-Way Coupling Model
for Fluid-Structure Interaction in Wind Energy

PhD in Theoretical and Applied Mechanics - Cycle XXXIV
Department of Mechanical and Aerospace Engineering, Sapienza University of Rome

Supervisors: prof. M. Bernardini, prof. S. Leonardi (The University of Texas at Dallas)
Tutor: prof. P. Gualtieri

To increase the attractiveness of wind energy, wind turbines are continuously scaling up, with diameters now exceeding 200 m. If on the one hand, this trend guarantees an increased power production, on the other hand, it imposes harsher aerodynamical and structural requirements – on the blades in particular – that are difficult to characterise.

In particular, the significant size of the state-of-the-art wind turbines suggests a more relevant Fluid-Structure Interaction (FSI) that could alter dramatically the operating life of the full machine. Given the difficulties and the costs of measuring the phenomena occurring at significant scales, researchers advocate the development of high-fidelity numerical models exploiting Computational Fluid and Structural Dynamics (CFD-CSD models). For this reason, in this work we present a novel FSI model for wind turbines combining our Large Eddy Simulation (LES) fluid solver with a modal beam-like structural solver. In the first part of the work, we present the details of our FSI methodology, and we analyse the effects of different coupling conditions. A loose algorithm couples the Actuator Line Model (ALM), which represents the blades in the fluid domain by means of body forces, with the structural model, which represents the flexural and torsional deformations. For a reference utility-scale wind turbine, we compare the results of three sets of simulations. Firstly, we consider one-way coupled simulations where only the fluid solver provides the structural solver with the aerodynamic loads; then, we consider two-way coupled simulations where the structural feedback to the fluid solver is made of the out-of-plane and in-plane bending deformation velocities only; finally, we add to the feedback also the torsional deformation.

However, to accurately reproduce the airloads, one should notice that the blades in particular are subjected to many relevant sources of unsteadiness, e.g. tower shadowing, yawed and waked conditions, environmental effects. Therefore, researchers have questioned the use of steady aerodynamics in the numerical fluid and aeroelastic models used in wind energy that do not have the sufficient resolution to solve the flow close to the blade, arguing that the use of tabulated airfoil coefficients could neglect effects that alter the estimation of the turbine behaviour. Different unsteady aerodynamics models have been proposed to account for these effects but have been mainly implemented in low-fidelity engineering models, which lack the complete capability of describing the multiscale and multi-physics phenomena characterising the wind turbine. For this reason, in the second part of the work, a 2D unsteady aerodynamics model is implemented in the sectional estimation of the airloads of the Actuator Line Model. At each section of the blade, a semi-empirical Beddoes-Leishman model includes the effects of additional noncirculatory terms, unsteady trailing edge separation and dynamic stall in the dynamic evaluation of the aerodynamic coefficients of the airfoils, used to determine the ALM body forces. Different inflow conditions and aeroelastic behaviours are examined with the aim of examining the effects of the model, and thus of providing a deeper insight into the unsteady characterisation of large wind turbines by means of a high-fidelity CFD-CSD model.

Keywords: Wind Energy, Fluid-Structure Interaction, Unsteady Aerodynamics, Large Eddy Simulation, Actuator Line Model, Modal Structural Dynamics, CFD-CSD method

Detailed Contents

Figures

Tables

Introduction

1 Introduction

In this chapter, we offer an overview of the background of this doctoral thesis, whose aim is to present a novel high-fidelity aeroelastic tool for wind energy applications.

At first, we introduce wind energy in the context of the larger family of the renewable energy sources, with a particular focus on the technological trends driving the field. After having explained the rationale behind the increase in the wind turbines' size, we present the challenges that this tendency poses. Thus, we concentrate on the importance of the numerical aeroelastic modelling, and we present a broad literature review particularly concerning high-fidelity models. Furthermore, we stress the importance of a proper modelling of the unsteady aerodynamics, and we present its main physical processes and the most widely used models. Finally, we state the aim of the work, and we outline the content of the thesis.

1.1 Wind of Change

With a global population exceeding almost 8 billion people [1] and a corresponding electricity demand going far beyond the limit of about 25.000 TWh [2], energy is, and still will be for many years, a critical field for mankind.

[1]: United Nations (2019), *The 2019 Revision of World Population Prospects*

[2]: Enerdata (2019), *Electricity domestic consumption.*

In particular, given the increasing environmental concerns attempting to shift energy generation from fossil fuels to sustainable sources, clean power production is at the centre of the public debate. Moreover, as attested by many reports [3], the development of the so-called *renewables* improves health outcomes, reduces healthcare costs, and provides more jobs than fossil fuels, besides contributing to the reduction of CO_2 emissions and thus of climate impact.

[3]: Gencsu et al. (2019), *Unlocking the inclusive growth story of the 21st century: accelerating climate action in urgent times*

The credits for the image above the chapter title go to Inga Spence (Alamy Stock Photo) for National Geographic https://www.nationalgeographic.org/encyclopedia/wind-energy/

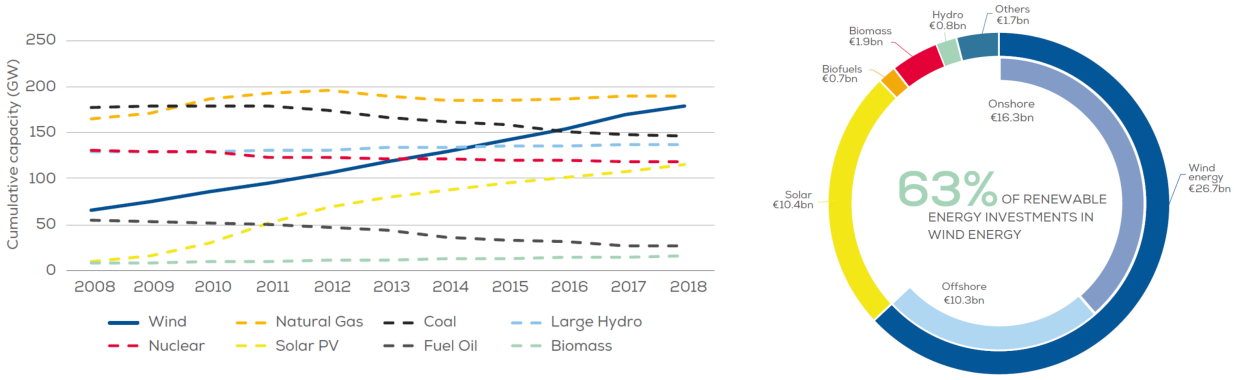

Figure 1.1: On the left, the total power generation capacity in the European Union in the period 2008-2018 according to the 2018 Wind Europe report. On the right, the renewable energy investments in 2018 (€ bn) [5].

According to recent statistics, in 2020, cost reductions allowed renewables to reach almost 30% of the global electricity supply, halving the gap with coal. The majority of this energy share, almost 90 %, is nowaday sustained by hydropower, solar photovoltaic and wind. In particular, wind power increased the most in absolute generation terms among all the renewables and confirmed the trend in the total power generation capacity observed in Europe in the period 2008-2018 (see Figure 1.1) [4, 5].

[4]: International Energy Agency (2020), *Global Energy Review 2020*
[5]: Komusanac et al. (2018), *Wind Energy in Europe in 2018 – Trends and statistics*

Although wind energy has been always leveraged by mankind, by means of sailing vessels and later by means of windmills, it was only after the oil crisis of the 1970s that a renewed interest in wind power generation brought to the born and the commercial adoption of grid-integrated wind energy systems. Research and technological innovations have thus allowed the field to grow in maturity and to make wind energy competitive even without subsidies [6], by reducing the Levelised Costs Of Energy (LCOE), *i.e.* the average revenue per unit of electricity generated that would be required to recover the costs of building and operating a generating plant during an assumed financial life and duty cycle. Figure 1.2 [7] reports the shrinkage of the costs per unit of energy in the last decade for wind and solar energy: in many regions of the world, wind energy is today the most convenient source of electricity.

[6]: Lantz et al. (2012), *IEA Wind Task 26: past and future cost of wind energy*

[7]: Lazard (2016), *Lazard's Levelized Cost of Energy Analysis–Version 9.0*

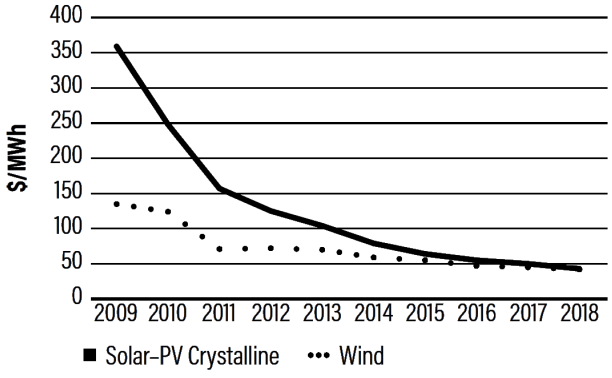

Figure 1.2: Solar and wind energy costs since 2009. Onshore wind power is today the cheapest source of renewable electricity generation in the majority of places in the world [7].

In the attempt of reducing even further the LCOE, to fulfill the L_3 condition, *i.e.* low cost, long-lasting, and low service requirement power stations, wind energy defines continuously new challenges that are strictly related to the productive trends shown in recent years.

Productive trends of wind energy

According to Veers et al., 2019 [8], the cost reduction of wind energy has been and will be driven mainly by three *"increasing"* trends, that are: increasing hub height, increasing power rating, and increasing rotor diameter. The rationale behind these drivers can be clearly understood observing the classical expression of the power production for a wind turbine:

$$P = \frac{1}{2}\rho C_P A U_\infty^3 \tag{1.1}$$

where P is the instantaneous power generated, ρ is the air density, C_P is the power coefficient of the turbine, A is the area swept by the rotor, and U_∞ is the free-stream air velocity.
The benefits brought by the increasing trends are thus clear:

Hub height. The increase of the hub height allows turbines to operate with faster wind speeds, more independent from the surface friction.

Power rating. Technological innovations has led to larger generator capacity coupled with more sophisticated power electronics, enabling variable-speed operations. Turbines are thus now able to operate in a wide range of regimes constantly at peak power coefficient C_P, boosting the power production.

Rotor diameter. Advances in material science and rotor design has made it possible to increase the length of the blades without reaching impractical weights and costs (see Figure 1.3). Modern blades are 90% lighter than the corresponding 1980s blades simply scaled to current sizes [9]. The larger swept area by the longer blades increases the wind turbine capture and exploits fully the wind resource.

To have an idea of such augmentation process, in 2020 the average rated capacity of a newly installed wind turbine in Europe was 8.2 MW for an offshore turbine and 3.3 MW for an onshore turbine, with huge blades tipically longer than 80 m [10]. The latest prototype of General Electric, the Haliade-X offshore wind turbine, has a rated power of 14 MW, a colossal rotor diameter of 220 m and a hub height of 260 m, for a total height slightly smaller than that of the Empire State Building [11].

Obviously, many other important solutions are catching on in order to answer the large number of requirements asked to wind energy. For example, large groups of turbines, the so-called *wind farms*, are built more and more in the *offshore* configuration, with turbines bodies in water. The higher and more stable offshore wind speeds compared to onshore ones allow wind farms to generate more electricity per amount of capacity installed at a now competitive price. Moreover, the placement of the turbines far from inhabited lands guarantees a weaker

[8]: Veers et al. (2019), 'Grand challenges in the science of wind energy'

[9]: Manwell et al. (2010), *Wind energy explained: theory, design and application*

[10]: Komusanac et al. (2020), *Wind Energy in Europe - 2020 Statistics and the outlook for 2021-2025*

[11]: Winters et al. (2018), 'The Largest Wind Turbine Ever'

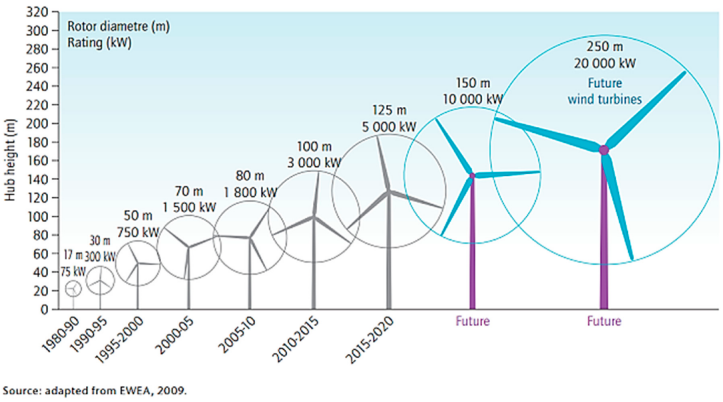

Figure 1.3: Growth in wind turbine size in the last 40 years and beyond. [12]

NIMBY (Not In My Back Yard) opposition, which sometimes hinders the development of large and intrusive projects.

Big wind turbines challenges

The presented trends delineates specific challenges for the wind energy field. Some issues were already there, others are new, and others have been exacerbated by the increase in size. A variety of questions for the future of wind energy spans from the need for improved analysis of the electricity conversion to the request of improved reliability and uncertainty modelling, from the increased attention to societal and economic aspects to the critical elements to characterise soil and floating basements [13].

[13]: van Kuik et al. (2016), 'Long-term research challenges in wind energy – a research agenda by the European Academy of Wind Energy'

However, among all the aspects, Veers et al., 2019 [8] underlined three of them as the principal challenges of *big wind energy*:

- The physics of the atmospheric flow needs an improved effort to better understand, model and estimate the coupling between the micro- and mesoscales defining the heterogeneous wind source. Moreover, the now comparable dimensions of the turbines – and of wind farms – with respect to the typical dimensions of the Atmospheric Boundary Layer (ABL), question the usual assumptions adopted in fluid dynamics studies and introduces the need to consider what Calaf et al., 2010 [14] calls the *fully developed wind turbine array boundary layer*.
- The response of enlarged wind turbines is still an open challenge, despite the separated advancements in the single physical fields like aerodynamics, structural dynamics, and hydrodynamics. Coupling phenomena between unsteady, nonlinear fluid and structural dynamics, and also control systems, are increasingly important and still neglected or misrepresented in the design process, where they can potentially play a central role.
- In order to tackle the electricity demand in the best way, further study is needed on the integrated optimisation and control of fleets of wind plants within the larger electric grid system.

[14]: Calaf et al. (2010), 'Large eddy simulation study of fully developed wind-turbine array boundary layers'

Given the above-mentioned trends, it is thus clear how the larger dimensions take the technological and physical design of a single wind turbine to an extreme. For instance, the design of new, grand wind

turbines must reckon with the increase in weight of their components, with the mutual interaction among the fluid fields of the turbines in wind farms and the ABL, but also with the new crucial role of fluid-structure-control interaction for the more flexible structures.

In fact, nowadays, the blades of the horizontal-axis wind turbines are stiff enough to guarantee sufficient tower clearance and structural properties. Increasing dimensions and keeping stiffness constant would cause massive blades and expensive supports with huge nacelles and towers, which would result in impractical and inconvenient solutions. As a result, blades are going to be not only longer and slenderer, but also more flexible, and hence aeroelasticity will have to be considered during the design process to predict potential performance alterations and possible new instability problems affecting the turbine operating life.

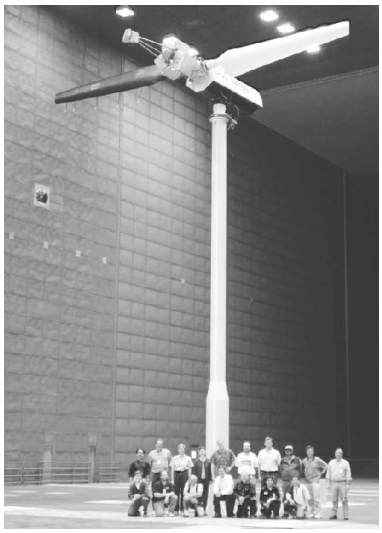

Figure 1.4: The NREL Phase VI wind turbine: a 10-metre diametre, two-blade wind turbine tested in the NASA Ames 24.4 by 36.6 metre wind tunnel [15]. During the NREL NASA Ames experiment the wind turbine was instrumented to chacterise both strutural and aerodynamic response of a full-scale rotor. The wind tunnel is powered by six 18,000 HP fans that produce test section wind velocities up to 50 m/s, and is primarily used to characterise full-scale aircrafts and rotorcrafts.

Ideally, the entire energy conversion process for the overall operating life of the machines should be evaluated a priori by means of appropriate and well-validated experimental, theoretical and numerical modelling to ensure reliability and predictability. However, each of these design strategies presents, in each of the physical fields involved, its own limitations and still needs further study to be able to tackle the complete problem of big wind energy properly.

For example, the fluid dynamics of the wind turbines includes different scales and phenomena, like wind shear, atmospheric turbulence, ground effects, time and space changes in wind direction, wake interaction on scales that range from the order of the metre to the one of the hundreds of kilometres. Trying to study these phenomena by means of controlled experiments (see Figure 1.4) has obviously a limited validity and huge costs, while fields tests, even if possible for example with Lidar technique [16], are limited due to costs and complexity. On the other hand, simplified analytical or semi-empirical models have limiting assumptions that restrict severely their validity and question their applicability to real operating conditions for predicting purposes. At last, numerical models would be ideal candidates to model the complete response of the wind turbines, by means of increased-fidelity simulations able to overcome the reduced-order models adopted in the industrial practice and able to exploit the growing computational power and advances. At the moment, however, a straightforward application of Computational Fluid Dynamics (CFD) for the entire lifetime of the wind turbine, but even for much shorter periods, is beyond the actual capabilities of classic models.

[16]: Iungo et al. (2013), 'Field measurements of wind turbine wakes with lidars'

As a result, a main scientific open challenge is about working out rigorous modelling and methods to better represent this fascinating multi-disciplinary engineering problem, considering also different requirements and levels of fidelity of the various subsystems, whose mutual couplings are intensified by the large scale of the wind turbines.

1.2 Fluid-Structure Interaction in Wind Energy

In order to study the interaction between the fluid and structural dynamics of flexible wind turbines, different studies adopting different approaches are present in the literature.

From a theoretical point of view, classic flutter analysis has usually characterised the aeroelastic stability analysis of the wind turbines [17]. Unsteady aerodynamic models, like the classic model of Theodorsen in the frequency domain or its counterpart in the time domain given by the indicial response theory (see Section 1.4), provided the typical description of the fluid dynamics. However, despite the capabilities of these models to predict the aeroelastic instability boundaries limiting the design of the wind turbines, the inherent linearities and strong simplifying assumptions of the models prevent them from predicting accurately the precise aeroelastic response of the wind turbines.

[17]: Lobitz (2004), 'Flutter speed predictions for MW-sized wind turbine blades'

On the other hand, as already explained in the previous section, gathering data by means of controlled or field experiments is difficult and expensive. Moreover, combining the information provided by fluid and structural measurements to obtain significant information about the aeroelastic behaviour of wind turbines requires additional effort. The interaction between fluid and structure is strongly nonlinear and Fluid-Structure Interaction (FSI) problems usually do not scale. Therefore, to charactertise the response of the new, large blades and rotors, only few facilities in the world can afford controlled experiments with accurate monitoring of interesting quantities. Systematic investigations of the interaction between fluid flow and structure dynamic deformation is rare for utility-scale wind turbines, with measurements available for turbines with ratings up to 2.5 MW and diametres up to approximately 90 m [18]. Moreover, although these experiments provide precious information of real cases, the aeroelastic interaction for such "small" turbines could still be secondary, and extracting the distinct role of the increased blades flexibility from raw measurements remains challenging.

[18]: Gao et al. (2020), 'Effects of inflow turbulence on structural response of wind turbine blades'

Figure 1.5: Structural failure of a wind turbine at Invenergy's Prairie Breeze wind farm.

Numerical modelling of FSI

Having explained the disadvantages and limitations of theoretical and experimental study of the FSI problem of wind turbines, it is clear that the numerical modelling is hopefully the most promising approach to study this phenomenon. The progress of the numerical models for FSI is central for the future development of wind energy, in order to better predict critical and possibly catastrophic conditions for wind turbines (Figure 1.5) and crucial fatigue properties to extend the operating life of the turbines beyond the current limit of twenty years.

Nowadays, the majority of the numerical aeroelastic codes used in wind energy adopt low-fidelity engineering models to describe the aerodynamics, in particular by means of the widespread Blade Element Momentum (BEM) theory.
For example, the standard multi-physics software OpenFAST [19, 20]

[19]: Jonkman et al. (2005), *Fast user's guide-updated august 2005*
[20]: NREL (2020), *OpenFAST*

(formerly known as FAST), developed by the National Renewable Energy Laboratory (NREL), couples BEM theory for the aerodynamics with a finite-element Computational Structural Dynamics (CSD) solver based on the Geometrically-Exact Beam Theory (GEBT) [21]. This last category of beam theories allows for arbitrarily large displacement, and finite rotation of the cross-sectional frame is treated exactly, without small angle approximations.
In a similar way, the aeroelastic tool HAWC2 [22] of the Risø National Laboratory and the Technical University of Denmark, couples a BEM aerodynamic model with a multi-body structural solver.

[21]: Hodges (2006), *Nonlinear composite beam theory*

[22]: Larsen et al. (2007), *How 2 HAWC2, the user's manual*

Despite the effectiveness and efficiency of the model in different conditions, many studies [23–25] have proved that the BEM theory, even if corrected with engineering models [9], is unable to represent correctly the unsteady and multi-scale flow phenomena. As a result, its strong limiting assumptions force designers to adopt conservative safety factors that, in the end, undermine the competitiveness of the wind turbines.

Some groups have tried instead to couple different structural models with more accurate potential methods, like lifting line, panel and vortex methods [26–28]. Elegant three-dimensional inviscid aerodynamic models, like in the works of Okulov [29], allow an improved description of the spatial and temporal evolution of the wake behind the wind turbines and help to better understand the flow dynamics of wind energy with a reasonable computational effort. However, the absence of the viscous effects requires the introduction of models to take into account the viscous-inviscid interaction [30], which are still immature.

As a consequence, the wind energy community encourages and urges the development of high-fidelity aeroelastic models that are able to study properly the effects of the unsteady fluid-structure-control interaction in the new, big wind energy [13]. As reported in the many reviews about the topic [31, 32], recent studies have tried to leverage the superior capabilities of combined CFD-CSD methods, which exploit today's computational resources to describe accurately the fluid motion and the structural dynamics.

[23]: Simms et al. (2001), *NREL unsteady aerodynamics experiment in the NASA-Ames wind tunnel: a comparison of predictions to measurements*
[24]: Gupta (2006), 'Development of a time-accurate viscous Lagrangian vortex wake model for wind turbine applications'
[25]: Kecskemety et al. (2016), 'Influence of wake dynamics on the performance and aeroelasticity of wind turbines'
[26]: Milne-Thomson (1973), *Theoretical aerodynamics*
[27]: Hess (1975), 'Review of integral-equation techniques for solving potential-flow problems with emphasis on the surface-source method'
[28]: Tietjens et al. (1957), *Applied hydro-and aeromechanics: based on lectures of L. Prandtl*
[29]: Alekseenko et al. (2007), *Theory of concentrated vortices: an introduction*
[30]: Sørensen et al. (1986), 'Three-Level, Viscous-Inviscid Interaction Technique for the Prediction of Separated Flow Past Rotating Wing'
[31]: Hansen et al. (2006), 'State of the art in wind turbine aerodynamics and aeroelasticity'
[32]: Zhang et al. (2011), 'Review of aeroelasticity for wind turbine: Current status, research focus and future perspectives'

1.3 High-Fidelity FSI Models: CFD-CSD coupling

For what concerns the fluid modelling, CFD is able to provide a sounder and more accurate representation of the various regimes of wind turbines, and thus makes it possible to gain a deeper physical insight into realistic turbulent conditions [33, 34]. As a consequence of the huge range of the spatial and temporal flow scales of the problem, Direct Numerical Simulation (DNS) of the Navier-Stokes equations is still beyond the reach even of today's supercomputers for typical Reynolds numbers of wind energy and for the fine body-conformal resolution required by the solid boundaries of the turbines.
Reynolds-Averaged Navier-Stokes Equations Simulation (RANS) reduces the computational effort needed, by means of turbulence modelling, but known problems in the treatment of separated regions and

[33]: Cortina et al. (2016), 'Distribution of mean kinetic energy around an isolated wind turbine and a characteristic wind turbine of a very large wind farm'
[34]: Meneveau (2019), 'Big wind power: Seven questions for turbulence research'

of unsteady flows [35] can limit the accuracy of the results.
The Large Eddy Simulation (LES) methodology allows the simulation of unsteady turbulent flows with reduced computational cost compared to DNS but increased accuracy compared to RANS. However, the resolution needed to deal with wall-bounded flows by means of appropriate body-fitted meshes increases the computational requirements of the method, which tend to the ones of the DNS method for high Reynolds numbers [36].

An alternative approach that combines the advantages of CFD solvers and blade-element methods is represented by the use of generalised actuator disc models [37]: supplementary body forces are added to the Navier-Stokes equations with the aim of mimicking the action of the solid boundaries of the blades on the fluid, avoiding the resolution of the exact surface geometry. In practice, a blade-element approach, using the tabulated airfoil characteristics and the local flow kinematics, defines the blades' aerodynamic loading, while the 3D Navier-Stokes equations describe the wake dynamics that results from that blades' forcing. A popular example of this family of methods is the Actuator Line Model (ALM) [38], where the body forces are distributed along radial lines taking the place of the blades and thus rotating with the angular rotor speed. The method has been proved particularly adequate to predict the flow features of wind turbines especially in LES frameworks [39–41], combining model simplicity and accuracy.

For what concerns the structural modelling, the most important and challenging components to consider in FSI are the blades, because of their peculiar shapes and their mechanical properties stemming from composite materials and because of the high stiffness of the other components, like the tower and the shaft. The most widespread structural mechanics numerical models in aeroelasticity are the Finite-Element Method (FEM), the multi-body formulation and the modal approach.

The well-known finite-element method allows the description of complex deformation states and of complex geometries, with a potentially high computational expense.
The modal approach instead offers a very cheap method to determine the structural response with satisfactory results, based on the eigenmodes of the structure.
Finally, the multi-body formulation is a good compromise between the two methods above in terms of computational cost and allows to consider large displacements by connecting rigid and/or flexible subelements.

In general, however, three-dimensional structural models of the complete machine in unsteady FSI simulations would mean adding a relevant computational expense on the structural side that could affect negatively the overall performance of coupling methods using already costly CFD models for the fluid side. Hence, in wind energy aeroelasticity, blades are commonly represented as a combination of one-dimensional equivalent beams, given their high slenderness.

A final comment should be made about the available procedures adopted

[35]: Spalart (2009), 'Detached-eddy simulation'

[36]: Choi et al. (2012), 'Grid-point requirements for large eddy simulation: Chapman's estimates revisited'

[37]: Mikkelsen et al. (2003), 'Actuator disc methods applied to wind turbines'

[38]: Sørensen et al. (2002), 'Numerical modeling of wind turbine wakes'

[39]: Shen et al. (2012), 'Actuator line/ Navier–Stokes computations for the MEXICO rotor: comparison with detailed measurements'
[40]: Sørensen et al. (2015), 'Simulation of wind turbine wakes using the actuator line technique'
[41]: Xie et al. (2015), 'Self-similarity and turbulence characteristics of wind turbine wakes via large-eddy simulation'

to couple the fluid and structural *subsystems*. In general, the dynamic analysis of coupled physical subsystems or fields, can be addressed by means of:

Strong-coupled or monolithic treatment. The problem is considered as a whole, and the different subsystems are advanced simultaneously. These methods are more robust and stable, and they do not need data transfer between the subsystems. However, writing a fully-integrated FSI solver can be complex and can require the same discretisation method for the two fields. Case examples that need strong coupling are biological FSI [42] and the problems in which the structure is light and the fluid is heavy, *e.g.* parachutes [43].

Loosely-coupled or partitioned or staggered treatment. The fields are treated as isolated and are advanced in time separately. This approach enables the use of existing solvers for the single partition, exploiting all the know-how about the single field. Moreover, for several problems, staggered approaches are robust and efficient. However, in some cases, they present convergence difficulties and moreover, stability and accuracy of the coupled staggered system are difficult to characterise. Aeroelasticity of aeronautical structures [44] was among the first FSI problems studied by means of loosely-coupled algorithms.

[42]: Bazilevs et al. (2006), 'Isogeometric fluid–structure interaction analysis with applications to arterial blood flow'
[43]: Stein et al. (2000), 'Parachute fluid–structure interactions: 3-D computation'

[44]: Farhat et al. (1996), 'On the accuracy, stability, and performance of the solution of three-dimensional nonlinear transient aeroelastic problems by partitioned procedures'

For FSI in wind energy, several works proved that a loose coupling approach is sufficient to capture the relevant interaction taking place [45, 46]. For an enlightening review about partitioned analysis of coupled systems and possible algorithmic implementations, see Felippa et al., 2001 [47].

[45]: Hsu et al. (2012), 'Fluid–structure interaction modeling of wind turbines: simulating the full machine'
[46]: Heinz (2013), 'Partitioned fluid-structure interaction for full rotor computations using CFD'
[47]: Felippa et al. (2001), 'Partitioned analysis of coupled mechanical systems'

Moreover, in the literature, it is also present the definition of *weak* or *one-way* coupling. This open-loop technique reduces the two-way coupling between the physical fields to the one-way application of the solution of one of the subsystems to the other, in a sort of "post-processing" procedure. This technique, which does not represent strictly a real coupling, is used effectively, anyway, in the case of extremely high solid stiffness and reduced fluid forces, or in the case of mass ratio between air moved and structure far different than 1, or in the case that the characteristic time scales of the subsystem dynamics are extremely different. In the improper cases, this approach can cause non-physical positive feedback, which leads to a divergent response, or even worse, to an oscillatory response that is not representative of the real phenomenon, with wrong amplitudes and frequencies.

During the last years, several groups have developed various high-fidelity CFD-CSD models, implementing different aerodynamics and structural formulations and coupling them by means of different algorithmic procedures and rationales. In what follows, we present a review of the CFD-CSD models in the literature, classified on the basis of the CFD approach used, *i.e.* body-conformal or generalised actuator disc models.

Body-conformal CFD models

Classic Arbitrary Lagrangian-Eulerian (ALE) formulation requires a relevant computational overhead given by the need for repeated grid updates, by means of moving body-conformal mesh algorithms like the Solid-Extension Mesh Moving Technique (SEMMT) [48], and of a projection procedure to represent the solution on the updated grid [49]. Moreover, preserving the necessary quality of the grid for high-Reynolds number simulations can be particularly cumbersome and demanding, which makes the body-conformal approach complex and computationally expensive, despite the remarkable advancements in the field of FSI [50]. Moreover, most of the staggered approaches reported below adopt RANS modelling for the fluid dynamics, whose disadvantages have been already presented. On the other hand, however, these methods allow considering the exact geometry of the blades and evaluating explicitly and locally the forces and displacements that take place at the boundaries between the fluid and solid domains.

[48]: Stein et al. (2004), 'Automatic mesh update with the solid-extension mesh moving technique'
[49]: Bazilevs et al. (2013), *Computational fluid-structure interaction: methods and applications*

[50]: Tezduyar (2001), 'Finite element methods for flow problems with moving boundaries and interfaces'

Probably the first model of this category was developed by Hsu and Bazilevs in 2012 [45]. In this work, the NREL 5 MW reference onshore wind turbine [51], including the nacelle and the tower, was simulated by means of a 3D FSI model. Their methodology coupled tightly a low-order finite-element based ALE-VMS technique for the aerodynamics with a NURBS-based isogeometric analysis for the structural dynamics of the blades, represented by means of thin composite shells. Boundary conditions at the fluid-solid and sliding interfaces were imposed weakly. The results showed that the tower has a great impact on the instantaneous torque and on the blades' structural dynamics, though coupled simulations did not point out particular differences on the time-averaged power production compared to the cases without FSI coupling.

[51]: Jonkman et al. (2009), *Definition of a 5-MW reference wind turbine for offshore system development*

Other groups have tried instead to couple CSD models mostly with blade-resolved RANS finite-volume fluid solvers, to avoid the heavy state structure and complex assembly procedure of finite-element formulation for the aerodynamics, but also to exploit pre-existent fluid solvers in a staggered rationale.

A partitioned coupling method joined the structural multi-body model of HAWC2 [22] with the 3D RANS solver EllipSys3D [52] in the work of Heinz, 2013 [46]. Preliminary studies comparing strong and loose FSI implementations showed that the loose approach is sufficiently accurate for wind energy applications.

[52]: Michelsen (1994), *Block structured Multigrid solution of 2D and 3D elliptic PDE's*

Yu and Kwon, 2014 [53] analysed again the NREL 5 MW turbine but by means of a staggered coupling between an incompressible RANS solver employing mesh deformation techniques and a FEM beam solver. First of all, they confirmed the tower interference on the structural dynamics, then they found that gravity is the main actor in the lead-lag or in-plane bending, and finally that the induced nose-down torsion of the blades present in the coupled simulations reduces the blades' airloads, and consequently the power and the thrust of the turbine. The results agree qualitatively with the ones reported in other works adopting low-fidelity fluid models [54, 55].

[53]: Yu et al. (2014), 'Predicting wind turbine blade loads and aeroelastic response using a coupled CFD–CSD method'
[54]: Jeong et al. (2014), 'Effects of torsional degree of freedom, geometric nonlinearity, and gravity on aeroelastic behavior of large-scale horizontal axis wind turbine blades under varying wind speed conditions'
[55]: Li et al. (2020), 'Aerodynamic and aeroelastic characteristics of flexible wind turbine blades under periodic unsteady inflows'

Li et al., 2015 [56] carried out coupled simulations of the NREL 5 MW wind turbine with a synthetic turbulent inflow generated according to the widely adopted turbulence model proposed by Mann for sheared flows [57]. The authors coupled a delayed Detached Eddy Simulation (DES) fluid solver with a multi-body structural solver. Dynamic overset grids accounted for the grid deformations and the relative motion of the wind turbine components. Their analysis showed that the fluid field quantities are relatively insensitive to the flexibility of the machine, and hence they concluded that the wake of multi-MW wind turbines can be studied, from a fluid dynamics point of view, assuming rigid structure and neglecting FSI.

[56]: Li et al. (2015), 'Coupled multi-body dynamics and CFD for wind turbine simulation including explicit wind turbulence'
[57]: Mann (1998), 'Wind field simulation'

The same reference turbine was simulated by Dose et al., 2018 [58], but neglecting the tower and the nacelle. A staggered approach coupled the OpenFOAM 3D RANS solver [59], with dynamic mesh motion and deformation, and an in-house FEM solver based on a GEBT [60]. The results showed a reduced torsion compared to the simulations of Yu and Kwon, and moreover, rigid and deformables cases differed only in yawed and tilted cases.

[58]: Dose et al. (2018), 'Fluid-structure coupled computations of the NREL 5 MW wind turbine by means of CFD'
[59]: Jasak et al. (2007), 'OpenFOAM: A C++ library for complex physics simulations'
[60]: Reissner (1972), 'On one-dimensional finite-strain beam theory: the plane problem'

Finally, the NREL presented recently the open-source simulation environment ExaWind [61], which couples their own CFD solver Nalu-Wind [62], able to use RANS, LES and DES methods with or without different actuator disc models, together with the turbine-simulation code OpenFAST. A loose conventional serial-staggered algorithm [44] is adopted. Their preliminary body-conformal RANS simulations on the NREL 5 MW wind turbine showed that minimal effects of the aeroelasticity on the time-averaged performance of the wind turbine, given the stiff nature of the turbine under consideration in the authors' opinion.

[61]: Sprague et al. (2020), 'ExaWind: A multi-fidelity modeling and simulation environment for wind energy'
[62]: Domino (2015), *Sierra low mach module: Nalu theory manual 1.0*

Generalised disc actuator CFD models

Some groups have tried instead to take advantage of the generalised actuator disc models in order to avoid generating heavy moving meshes and to simplify the physical and computational interface between the fluid and the structural problems. To the authors' knowledge, the few following works are the only ones adopting this approach. Although the validity of the generalised actuator disc models and of computational structural models has been widely proved separately, care must be taken on the accuracy of the full coupled partitioned integration, and further research is needed to evaluate the credibility of such CFD-CSD models.

A first attempt to exploit the capabilities of the generalised actuator disc models is present in Storey et al., 2013 [63], where a one-way approach coupled the servo-elastic tool FAST with a LES-based Actuator Sector Model [64]. Local aerodynamic forces were evaluated by means of the FAST's Aerodyn package. However, the one-way procedure still considered the turbine as a rigid structure, and hence flexibility and structural dynamics did not play any role in the determination of the local incidence of the blades.

[63]: Storey et al. (2013), 'Large eddy simulation of dynamically controlled wind turbines in an offshore environment'
[64]: Storey et al. (2015), 'An actuator sector method for efficient transient wind turbine simulation'

The NREL coupled the actuator line model in the LES fluid solver SOWFA to the structural module of FAST, in which a modal method considered only flexural structural dynamics of the blades. Various works [65, 66] validated the aeroelastic tool and used it to study the effects of roughness and atmospheric stability on wind turbines, without, however, assessing extensively the distinct influence of the blades flexibility.

[65]: Churchfield et al. (2012), 'A numerical study of the effects of atmospheric and wake turbulence on wind turbine dynamics'
[66]: Lee et al. (2013), 'A numerical study of atmospheric and wake turbulence impacts on wind turbine fatigue loadings'

Recently, Meng et al. [67, 68] coupled the actuator line model, first in RANS and then in LES finite-volume fluid solvers, with a finite-difference structural solver for rotating Euler-Bernoulli beams. The structural solver modelled only in- and out-of-the-plane bending, and the two-way coupling procedure included in the definition of the local effective incidence only the additional effect of the structural vibration velocities, which modify the local relative flow velocity. Tower and nacelle were neglected, and the analysis was mainly concerned on structural issues.

[67]: Meng et al. (2018), 'Elastic actuator line modelling for wake-induced fatigue analysis of horizontal axis wind turbine blade'
[68]: Meng et al. (2019), 'Study on wake-induced fatigue on wind turbine blade based on elastic actuator line model and two-dimensional finite element model'

1.4 Unsteady Aerodynamics

To accurately reproduce the complex aerodynamic loads, it is important to notice that wind turbines are subjected to many sources of unsteadiness such as the ones induced by the tower shadowing, by yawed conditions, by the mutual interaction between turbines in wind farms, and by environmental effects. Moreover, the unsteady environment (see Figure 1.6) also forces the blades' vibration, affecting the aeroelastic response of the wind turbine and in particular of the blades.

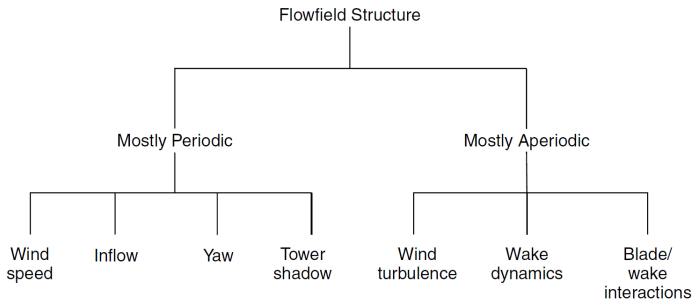

Figure 1.6: The fluid dynamics sources of unsteadiness for the airloads can be divided mainly in periodic and aperiodic disturbances [69]. Structural vibrations then provides the turbine with additional unsteadiness due to flap, lead-lag and pitch motions.

As a result, it is evident that Unsteady Aerodynamics (UA) phenomena can potentially affect wind turbines, and thus that they should be considered in the numerical modelling. Many studies have highlighted the critical importance of UA phenomena for Vertical Axis Wind Turbines (VAWTs) [70, 71]. However, several works confirmed that one must include UA also for Horizontal Axis Wind Turbines (HAWTs) to accurately predict the response of the wind turbine, especially if stall-regulated [72, 73]. For example, phenomena like dynamic stall can critically affect the aerodynamic damping that limits the structural vibrations in well-designed rotor blades [74]. Moreover, researchers showed that neglecting UA can generate non-existing flapwise vibrations [75], and that, in general, instantaneous aerodynamics i in aeroelastic codes

[70]: Mendoza et al. (2016), 'Validation of an Actuator Line Model Coupled to a Dynamic Stall Model for Pitching Motions Characteristic to Vertical Axis Turbines'
[71]: Mendoza et al. (2019), 'Near-wake flow simulation of a vertical axis turbine using an actuator line model'
[72]: Quarton (1998), 'The evolution of wind turbine design analysis—a twenty year progress review'
[73]: Haans et al. (2012), 'Airfoil models in the actuator line code assessed with near-wake measurements on a yawed rotor'
[74]: Rasmussen et al. (2003), 'Present status of aeroelasticity of wind turbines'
[75]: Øye (1991), 'Dynamic stall simulated as time lag of separation'

can be defective when calculating stalled rotor dynamic performance [76]. Although pitching control mechanisms reduce the importance of the severe load fluctuations due to flow separation, Leishman, 2002 [69] underlined that load hysteresis with respect to quasi-steady values is observable also if the flow remains attached.

[76]: Rasmussen et al. (1993), *Response of stall regulated wind turbines. Stall induced vibrations*

To quantify the *degree of unsteadiness* of the aerodynamic force F on an airfoil of semi-chord $b = c/2$, oscillating at an angular frequency ω in a flow with velocity U, the so-called *reduced frequency* k is usually introduced. From dimensional analysis, the functional form of the force is:

$$\frac{F}{\rho U^2 c^2} = f\left(Re, M, k\right), \tag{1.2}$$

where Re is the Reynolds number, $M = U/a$ is the Mach number, with a being the speed of sound, and k is the reduced frequency, which is typically defined in terms of the airfoil semi-chord $b = c/2$ as:

$$k := \frac{\omega b}{U} = \frac{\omega c}{2U}. \tag{1.3}$$

According to Leishman, 2006 [77], flow unsteadiness can not be neglected if $k > 0.05$, with highly unsteady effects for $k > 0.2$.

[77]: Leishman (2006), *Principles of helicopter aerodynamics*

Although the angular speed of the rotor is far smaller than the helicopters's ones, where unsteady effects are critical for the design of the blades, the values of the typical reduced frequencies for wind turbines can still suggest the presence of unsteady phenomena. Vijayakumar et al, 2019 [78] reported the reduced frequency along the blades of three wind turbines for two typical forcing conditions (Figure 1.7). For long blades, flow unsteadiness is dominant, and severe phenomena occur close to the hub. Moreover, induced structural vibrations could cause further unsteadiness, resulting in a critical FSI.

[78]: Vijayakumar et al. (2020), 'Enhancement of Unsteady and 3D Aerodynamics Models using Machine Learning'

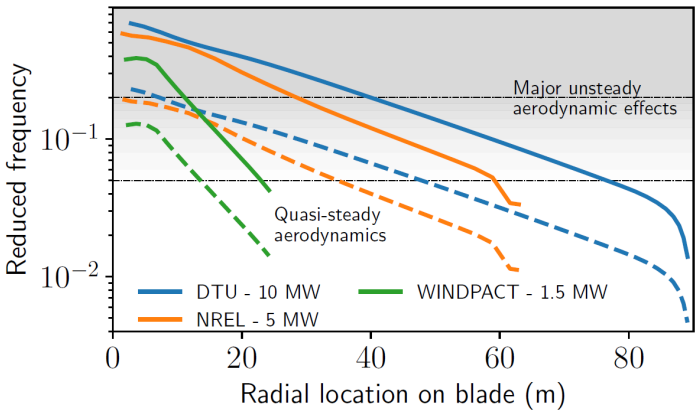

Figure 1.7: Reduced frequency along the span of the blades of three wind turbines of increasing dimensions and capacities [78]. Revolution frequency (dashed lines) and three times the revolution frequency (solid lines) are considered. The local velocity is used to define the reduced frequency.

Finally, although the Mach number $M = U/a$ is small and the characteristic unsteadiness frequencies are much smaller than the sonic velocity ($M\,k << 1$), the possibility of high-k phenomena and the increase in the tip Mach number, due to rotor upscaling, [79] also signal the potential role of compressibility in UA.

[79]: Farsadi et al. (2020), 'Classical flutter analysis of composite wind turbine blades including compressibility'

Despite its potential role especially for increasingly long blades, UA is usually neglected in those state-of-the-art CFD solvers for HAWTs that do not use the necessary resolution to solve explicitly the blades' boundary layer, *e.g.* CFD-ALM solvers, leading to an incomplete description of the local aerodynamic response. Furthermore, the majority of the studies of UA in wind energy is mainly focused on VAWTs [80], while few works studied explicitly the effect of UA for HAWTs and only by means of low-order fidelity fluid methodologies [81].

[80]: Bachant et al. (2016), 'Actuator line modeling of vertical-axis turbines'

[81]: Pereira et al. (2013), 'Validation of the Beddoes–Leishman dynamic stall model for horizontal axis wind turbines using MEXICO data'

Physical mechanisms

The numerical solution of the Navier-Stokes equations allows a proper description of the non-uniform effects induced by the vorticity shed in the wake of the turbine. However, the widely adopted approach of using static tabulated airfoil data prevents a correct and complete representation of the unsteady aerodynamic response of the blade section, which should be associated with circulatory and noncirculatory flow effects heavily depending on the complete history of the local incidence. Here in the following, we present the main physical mechanisms of UA, and we highlight how these are usually modelled in the literature.

2D Unsteady Aerodynamics

The physical unsteady phenomena occurring on a 2D airfoil can be grouped and classified depending on whether the flow is attached, mildly separated, or largely separated. We introduce below the main features of 2D UA, and then the most widespread family of 2D UA models.

Attached Flow Notorious works [82–87] provided the basis for UA models of 2D airfoils under fully attached flow conditions, mostly in the frequency domain, and showed that high-frequency fluctuations of the incidence can produce significant differences in the airloads relative to their corresponding quasi-steady values.

[82]: Theodorsen et al. (1935), 'General theory of aerodynamic instability and the mechanism of flutter'
[83]: Wagner (1924), 'Über die Entstehung des dynamischen Auftriebes von Tragflügeln'
[84]: Küssner (1935), *The Present Stage of Development of the Problem of Wing Flutter*
[85]: Karman et al. (1938), 'Airfoil theory for non-uniform motion'
[86]: Lomax et al. (1952), *Two-and three-dimensional unsteady lift problems in high-speed flight*
[87]: Loewy (1957), 'A two-dimensional approximation to the unsteady aerodynamics of rotary wings'

However, time domain formulations are more useful for a generic forcing. According to the *indicial response method*, the loading response to a generic history of the angle of attack is expressed as the superposition of fundamental indicial aerodynamic responses. Once determined the indicial response ϕ on a thin airfoil undergoing a transient step change in the incidence, the resulting lift, containing all the information about the history of the forcing, is calculated by means of the so-called *Duhamel integral*.
For example, if a system with indicial response ϕ is forced by a generic function $f(t)$ for $t \geq 0$, the output of the system can be written as:

$$y(t) = f(0)\phi(t) + \int_0^t \frac{\mathrm{d}f}{\mathrm{d}t}\phi(t-\sigma)\mathrm{d}\sigma. \tag{1.4}$$

In the case of the lift response, forced by the incidence $\alpha(t)$, the function $\phi(t)$ is called Wagner function [83], whose complex analytical expression

is usually described by the simpler Jones' exponential approximation [88] (see Figure 1.8):

$$\phi(s) = 1 - A_1 \exp\left(-b_1 \beta_M^2 s\right) - A_2 \exp\left(-b_2 \beta_M^2 s\right), \tag{1.5}$$

where A_1, A_2, b_1, b_2 are empirical constants depending on the specific airfoil, and $\beta_m = \sqrt{1 - M_\infty^2}$ is the Prandtl-Glauert compressibility factor. Finally, the so-called *reduced time* s is used to quantify more transient problems where a single reduced frequency is not significant, and is equal to:

$$s = \frac{1}{b} \int_0^t U \mathrm{d}t\,. \tag{1.6}$$

[88]: Jones (1940), *The unsteady lift of a wing of finite aspect ratio*

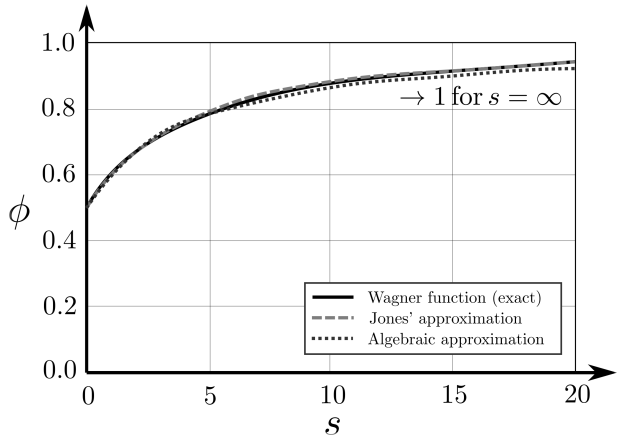

Figure 1.8: Exact Wagner function and different analytical and algebraic approximations as a function of the reduced time variable [77].

As a result, the *circulatory* part of the lift coefficient, taking into account the history effects of the shed wake on the unsteady airloads, can be expressed as

$$C_l^c(t) = 2\pi \left(\alpha(0)\phi(s) + \int_0^t \frac{\mathrm{d}\alpha(\sigma)}{\mathrm{d}t} \phi(s-\sigma)\mathrm{d}\sigma \right) = 2\pi \alpha_e(t) \tag{1.7}$$

with $\alpha_e(t)$ being an effective angle of attack including the possible effects of pitching, plunging and velocity variations in time.

To complete the estimation of the lift coefficient, a distinct *apparent mass* or *noncirculatory* part must be considered, taking into account the pressure forces required to accelerate the fluid in the proximity of the airfoil. This term, strictly related to the time derivatives of the incidence and of the pitching rate, is usually derived by means of other exponential indicial response functions [89] and can lead also to strong impulsive contributions to the lift response for fast variations of the incidence [90].

[89]: Leishman (1988), 'Validation of approximate indicial aerodynamic functions for two-dimensional subsonic flow'
[90]: Brunton et al. (2013), 'Reduced-order unsteady aerodynamic models at low Reynolds numbers'

The study of the unsteady attached flow is usually carried out in the context of the incompressible thin-airfoil theory for an inviscid fluid [91]. However, as already pointed out, the potential role of compressibility questions the validity of such models for higher frequencies and velocities. However, several studies demonstrated that correcting incompressible data by means of β_M is sufficient for subcritical Mach numbers.

[91]: McCroskey (1982), 'Unsteady airfoils'

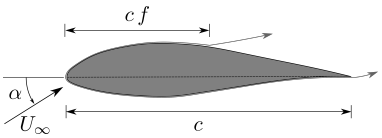

Figure 1.9: The nondimensional distance f locates the separation point along the chord.

Separated flow: trailing edge separation As the angle of attack increases however, flow tends to separate unavoidably. Mainly two kinds of separation are possible, depending on whether this takes place at the leading or at the trailing edge. The formation, dynamics and consequences of the leading edge vortex originating in the front region of the airfoil are analysed in the following section.

As usually done in the literature, the degree of separation can be quantified by the nondimentional distance f, which is such that cf indicates the approximate position from the leading edge where the separation starts (see Figure 1.9 at the side). Thus, if $f = 1$ the flow is attached, while if $f = 0$ the flow is completely separated. Usually, f is a specific function of the angle that is approximated analytically or is inferred from the static airfoil data (see Section 2.5 for the practical implementation).

On the one hand, if the flow is attached, the theory presented in the section above describes the delayed development of the lift. On the other hand, if the flow is separated, also the degree of separation f needs some time to reach its steady value, affecting in turn the force history.

In order to model the trailing edge separation, the Kirchhoff 2D plate theory [92, 93] is widely adopted. According to this model, for a generic airfoil, the normal and chordwise force coefficients, C_n and C_c respectively (see Figure 1.10), are expressed as

$$C_n = C_{n\alpha}(\alpha - \alpha_0)\left(\frac{1+\sqrt{f}}{2}\right)^2 \tag{1.8a}$$

$$C_c = \eta_e C_{n\alpha}(\alpha - \alpha_0)\sqrt{f}\tan\alpha \tag{1.8b}$$

where $C_{n\alpha} = \partial C_n/\partial\alpha|_{\alpha=\alpha_0}$ is the slope of the linear portion of the $C_n - \alpha$ curve, α_0 is the incidence of zero normal force, and η_e is a recovery factor in the range $[0.85, 0.95]$ used to consider viscous effects.

In order to take into account temporal effects, caused by the boundary layer response, f is delayed relative to its instantaneous value corresponding to the instantaneous effective incidence, and a first-order model is adopted to define a new lagged value of f that can be finally used in Equation 1.8a and Equation 1.8b.

[92]: Thwaites (1960), *Incompressible aerodynamics*
[93]: Gurevich (1966), *The theory of jets in an ideal fluid*

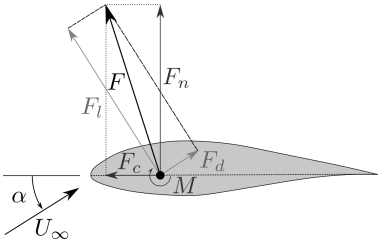

Figure 1.10: Different components of the aerodynamic force F for a generic airfoil. F_n and F_c are the normal and tangent components, while F_l and F_d are the lift and drag components. M is the pitching moment.

Separated flow: leading edge separation Highly dynamic separation can also start from the leading edge under certain conditions, as can be seen in Figure 1.11. This phenomenon, which goes under the name of *dynamic stall*, can influence dramatically the lifting properties of the airfoil, prolonging, for example, the linear region of the lift curve beyond the static stall angle and causing large hysteresis cycle characterised by a more abrupt, new stall.

Even though a complete understanding of dynamic stall is still missing, and contrasting results come out also from CFD simulations, it is widely accepted that dynamic stall occurs when the effective angle of attack varies above and around the normal static stall angle, causing a

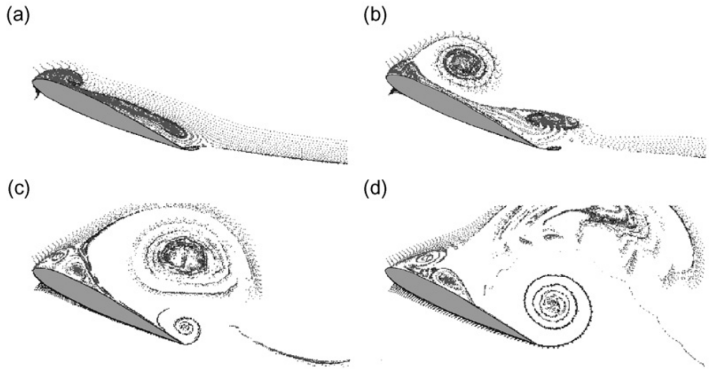

Figure 1.11: Different phases of dynamic stall from CFD-based flow visualisation [94]. Onset (a), build-up (b), and detachment (c) of the leading-edge vortex. A counter-rotating trailing-edge vortex build up at (c) and leaves the airfoil at (d).

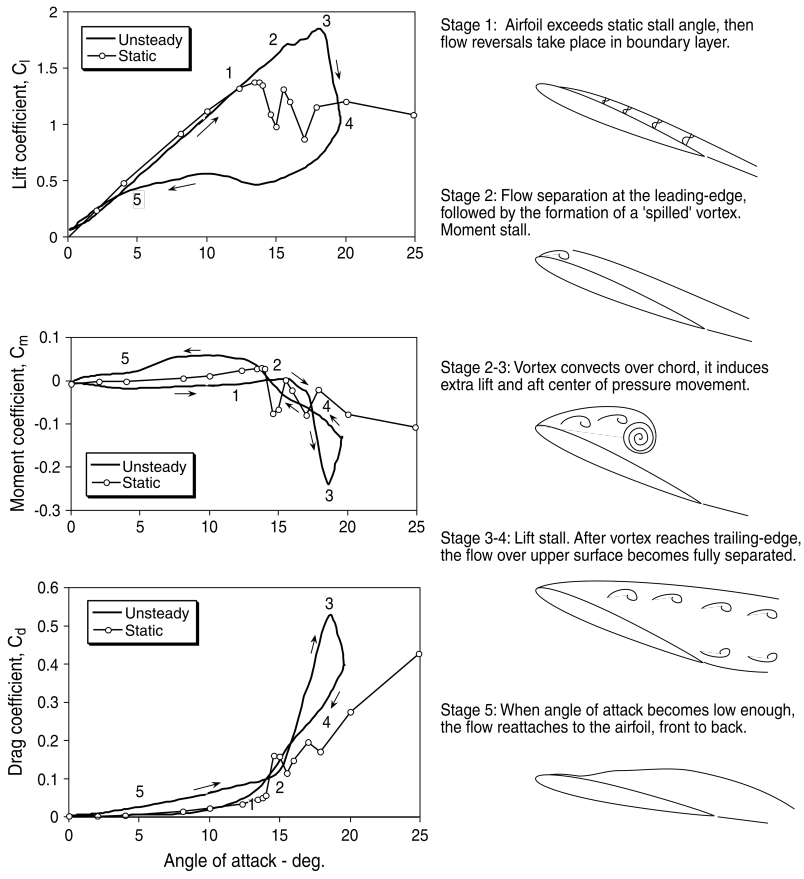

Figure 1.12: Dynamic aerodynamic polars, on the left, and vortical structures on the airfoil, on the right, during dynamic stall for a 2D airfoil [69].

completely different dynamics of the airloads compared to the instantaneous and quasi-steady ones, and potentially exceeding the structural fatigue limits too.

The main feature determining the different stages of the dynamic stall, observable in Figure 1.12, is certainly the development of a Leading-Edge Vortex (LEV). At high angles of attack, if a critical onset leading-edge pressure is reached, the high adverse pressure gradient in the region induces the formation of a concentrated vortex that travels progressively along the suction side, prolonging the attached region, until it leaves the trailing edge. The additional lift can produce even 100% overshoots in the maximum lift with an abrupt stall, and a large hysteresis in flow reattachment.

Semi-empirical models

The modelling of the complex phenomena taking place in the more general context of UA is still challenging, and researchers agree that at present a universal dynamic stall model does not exist.

Even if modern data-driven methods are catching on [90], the most popular approach still consists in using *semi-empirical models* representing 2D UA by means of simple relations, based mainly on the thin-airfoil theory and involving several – more or less physical – empirical coefficients. Despite being mainly developed for helicopters, several studies proved the ability of these models to describe also wind energy airfoils.

Among the different models [75, 94–98], the most famous ones are: the ONERA model, the Øye model, the Risø/Hansen model, the Boeing-Vertol model, the Larsen model, the Beddoes-Leishman model. Among them, the latter is undoubtedly the most complete and widespread, and for this reasing it is the model used in this work.

[75]: Øye (1991), 'Dynamic stall simulated as time lag of separation'
[94]: Larsen et al. (2007), 'Develop-stall model for wind turbine airfoils'
[95]: Tran et al. (1980), 'Semi-empirical model for the dynamic stall of airfoils in view of the application to the calculation of responses of a helicopter blade in forward flight'
[96]: Hansen et al. (2004), *A Beddoes-Leishman type dynamic stall model in state-space and indicial formulations*
[97]: Tarzanin (1972), 'Prediction of control loads due to blade stall'
[98]: Leishman et al. (1989), 'A Semi-Empirical model for dynamic stall'

Three-Dimensional Effects

Additionally, three-dimensional effects can alter the airloads, even if UA is mainly driven by 2D flow aspects [99]. Among the most important effects, there are:

Finite span effects Even if oscillations of 2D airfoils with the aforementioned models generally predict well the airloads along the blades, some nonlinear quasi-steady effects have been observed towards the tip of the blades [100]. Although the effect of the finiteness of the span is not particularly relevant on current turbines, the substantial increase in size of the blades could lead to more relevant consequences, that could not be easily managed only by means of tip loss correction functions.

Rotational effects The interaction of Coriolis and centrifugal forces on the boundary layer can affect the airloads coefficients. For example, Snel, 1991 [101] showed that Coriolis forces can retard the stall. In order to consider three-dimensional rotational augmentation effects, the models of Du and Selig and of Eggers [102, 103] have been adopted to modify the static tabulated data available for the wind turbine considered in this study.

Local sweep effects The radial component of the velocity, which can be significant for yawed cases, can influence the three-dimensional boundary layer on the blade and could, for example, compromise the use of the independence principle at the basis of all the blade element theories. However, St Hilaire and Carta [104] showed that, at least in the attached regime, the effect of the sweep is negligible, and the independence principle still holds. For larger incidence, sweep models could be considered but still have a reduced impact on the final airloads estimations if the angle of attack is not too large.

[99]: Damiani et al. (2016), 'Dynamic ment and Validation of a New Unsteady Airfoil Aerodynamics Model Within AeroDyn'

[100]: Lorber et al. (1991), 'Dynamic stall experiments on a swept 3D wing in compressible flow'

[101]: Snel (1991), 'Scaling laws for the boundary layer flow on rotating wind turbine blades'
[102]: Du et al. (1998), 'A 3-D stall-delay model for horizontal axis wind turbine performance prediction'
[103]: Eggers et al. (2000), 'Modeling of yawing and furling behavior of small wind turbines'

[104]: St Hilaire et al. (1983), *Analysis of Unswept and Swept Wing Chordwise Pressure Data from an Oscillating NACA 0012 Airfoil Experiment.*

1.5 Aim of the Work

The aim of this work is to present a novel two-way coupling high-fidelity CFD-CDS model for the study of the aeroelasticity for wind turbines including a dynamic modelling of the unsteady aerodynamics.
The staggered FSI method couples the in-house LES solver named UTD-WF [105], developed by the University of Texas at Dallas, with a modal beam-like solver developed for this work. As a result, our simulations are able to describe the fluid dynamics with high accuracy, and to represent at the same time, in an efficient way, the structural dynamics of the cantilever blades clamped at the hub. The model exploits the Actuator Line Model formulation and uses it as a natural and efficient fluid-solid interface to mutually exchange information about the blades loading and motion. In its general formulation, the blade dynamics can include also the instantaneous torsional Degree of Freedom (DOF) and even the complete elastic state, which is a novelty among the aeroelastic solvers based on the generalised actuator disc models in a CFD framework, to the authors' knowledge. Moreover, because of their demonstrated role in standalone fluid dynamics and in FSI [106, 107], the fluid model includes also the tower and the nacelle, assumed to be rigid and modelled by an Immersed Boundary Method (IBM) [108].
Finally, a modified Beddoes and Leishman (BL) model is implemented in the FSI solver to evaluate dynamically the aerodynamic coefficients of the airfoils in the blade-element approach of the Actuator Line Model. The popular semi-empirical model aims at completing the description of the non-instantaneous response of the 2D aerodynamics in the ALM framework, and thus at enhancing the estimation of the airloads along the blades, which is critical for the evaluation of the fatigue properties of the entire machine.

[105]: Santoni et al. (2020), 'One-way mesoscale-microscale coupling for simulating a wind farm in North Texas: Assessment against SCADA and LiDAR data'

[106]: Santoni et al. (2017), 'Effect of tower and nacelle on the flow past a wind turbine'
[107]: De Cillis et al. (2021), 'POD-based analysis of a wind turbine wake under the influence of tower and nacelle'
[108]: Orlandi et al. (2006), 'DNS of turbulent channel flows with two-and three-dimensional roughness'

In order to prove the capabilities of our model, we carried out different sets of simulations to examine the distinct and coupled effects of various possible levels of FSI coupling and of the UA modelling on the complete aeroelastic response of a reference utility-scale Horizontal Axis Wind Turbine (HAWT).

This project is in collaboration with the research group of prof. Stefano Leonardi of the Mechanical Engineering Department of the University of Texas at Dallas, where the candidate spent three months as a visiting researcher during the first year of his PhD.

1.6 Outline of the Thesis

The thesis is organised into four parts, as follows:

Introduction This part contains the ending Chapter 1, which introduced the general background and motivation delineating the research question addressed by this work, reported the state of the art of the methodologies adopted to answer to this question, and finally defined the aim of this work, our own proposal and the work done.

Methodology This part is divided into three chapters, presenting the methodology adopted in the fluid solver (Chapter 2), in the structural solver (Chapter 3), and in the coupling procedure defined to join the two subsystems (Chapter 4).

Results This part is divided into three chapters. Chapter 5 describes in detail the case under study, the computational setup adopted for the final simulations and its validation. Chapter 6 describes the results of a first campaign of simulations assessing the distinct effects of flexibility for a utility-scale wind turbine. Chapter 7 describes instead a second set of simulations assessing the effects of the unsteady aerodynamic modelling, in both rigid and coupled simulations.

Conclusions This part contains Chapter 8, which includes a final summary of the main findings of the work, highlighting advantages and disadvantages of the proposed model, and outlining the possible future developments.

Finally, Appendix A clarifies some additional details about the validation and the implementation of the unsteady aerodynamic model.

Method

2 The Fluid Model

This chapter presents the details of the fluid model in our FSI method.

At first, we present the physical model and its governing equations, then we introduce the LES approach to solve the fluid equations. Next, we report the numerical methodology used to discretise the governing equations. Subsequently, we describe the modelling of the solid bodies in the fluid domain and the turbine modelling adopted. Finally, we present the modelling of the unsteady aerodynamics.

2.1 Physical Model and Governing Equations

It is common practice in the literature to assume the flow around wind turbines as incompressible.
Recent studies have started to take into account the effect of compressibility, especially towards the tip of the blades of the big modern turbines [79] [110]. However, under normal operating conditions, the typical Mach number of the flow is low enough to reasonably justify the neglection of compressibility effects in the fluid domain. Thus, we decided to model the flow as incompressible.

[110]: Chaviaropoulos et al. (2003), 'Viscous and aeroelastic effects on wind turbine blades. The VISCEL project. Part I: 3D Navier–Stokes rotor simulations'

The governing equations in differential form of the fluid model are thus the *incompressible Navier-Stokes equations* together with the *incompressible continuity equation*:

$$\frac{\partial \boldsymbol{u}}{\partial t} + \boldsymbol{u} \cdot \nabla \boldsymbol{u} = -\frac{1}{\rho}\nabla p + \nu \nabla^2 \boldsymbol{u} + \boldsymbol{f}, \tag{2.1}$$

$$\nabla \cdot \boldsymbol{u} = 0, \tag{2.2}$$

Smoke visualization of tip vortices in the New Mexico experiment.
The credits for the image above the chapter title go to Schepers and Schreck [109].

where $\boldsymbol{u}$ is the velocity vector, p is the pressure, $\boldsymbol{f}$ is a generic body force acting on the fluid, ρ is the constant fluid density and ν is the constant fluid kinematic viscosity.

It is possible to obtain a non-dimensional form of the governing equations by dividing all the dimensional quantities by appropriate reference dimensions, typical of the problem under consideration:

$$\boldsymbol{u}^* = \frac{\boldsymbol{u}}{U_0} \quad x^* = \frac{x}{L_0} \quad t^* = \frac{tL_0}{U_0} \quad p^* = \frac{p}{\rho_0 U_0^2}, \tag{2.3}$$

where the asterisk indicates the corresponding non-dimensional quantities and the subscript 0 indicates the reference quantities.
In such a way, we can express Equation 2.1 and Equation 2.2 as:

$$\frac{\partial \boldsymbol{u}^*}{\partial t^*} + \boldsymbol{u}^* \cdot \nabla_* \boldsymbol{u}^* = -\nabla_* p^* + \frac{1}{Re} \nabla_*{}^2 \boldsymbol{u}^* + \boldsymbol{f}^*, \tag{2.4}$$

$$\nabla_* \cdot \boldsymbol{u}^* = 0, \tag{2.5}$$

where $[\nabla_*]_i = \frac{\partial}{\partial x_i^*}$ and $Re = U_0\, L_0/\nu_0$ is the so-called Reynolds number.

The Reynolds number is a non-dimensional group indicating the importance of the inertial forces compared to the viscous forces and is the only similarity parameter in the incompressible form of the Navier-Stokes equations considered in our model. In non-dimensional terms, flows with similar geometries and equal Reynolds numbers obey the same equations and boundary conditions and thus have the same *non-dimensional* solution (*dynamic similarity principle* [111]).

[111]: Anderson Jr (2010), *Fundamentals of aerodynamics*

In the next sections of this chapter, we consider only the non-dimensional governing equations, so we omit the asterisk on the variables for ease of notation.

Figure 2.1: Andrej Nikolaevič Kolmogorov (Tambov 1903 - Moscow 1987)

Large Eddy Simulation approach

A first approach to solve numerically the Navier-Stokes equations consists in directly discretising the equations in a sufficiently large domain on a fine mesh for a sufficiently long time with a fine temporal resolution, to be able to describe all the possible scales relevant to the flow under study. The so-called DNS approach can potentially provide the most accurate results possible, but requires a relevant computational cost. Indeed, it is possible to show that for Reynolds numbers of interest for engineering applications, the computational requirements exceed even the increased capabilities of today's most powerful supercomputers.

From the theory of *homogeneous isotropic turbulence* by Kolmogorov [112], we know that the ratio between the largest and the smallest representative scales of the flow is:

$$\frac{L}{\eta} = \mathcal{O}\left(Re^{3/4}\right), \tag{2.6}$$

where L is the integral scale of the flow and η is the Kolmogorov scale, which is the smallest scale not directly dissipated by viscosity. Moreover, the theory presents a similar estimation also for the characteristic time scales, which is:

$$\frac{T}{t_\eta} = \mathcal{O}\left(Re^{1/2}\right), \tag{2.7}$$

where T is the integral time of the flow and t_η is the Kolmogorov time. In order to simulate a turbulent flow and to take a correct picture of the full energy cascade, a well-resolved DNS should have a grid spacing in each direction at most equal to the Kolmogorov scale η and a domain size at least equal to the integral scale L. It follows that the direct simulation of a 3D unsteady turbulent flow requires at least a number of points $N_S \sim Re^{9/4}$ *for each time step*. Moreover, if the time step is at most equal to the Kolmogorov time scale t_η and the total time of the simulation is at least equal to the integral time T, the minimum number of iterations should be $N_T \sim Re^{1/2}$. As a consequence, the total number of unknowns would be of the order of $N_S \cdot N_T \sim Re^{11/4}$. For a modern wind turbine, characterised by a diameter $D \approx 100\,m$ and a velocity $U_0 = U_\infty \approx 10\,m/s$, the typical Reynolds number $Re = U_0 D/\nu$ is of the order of 10^8, which makes it evident how the requirements for DNS are too demanding even for the modern supercomputing resources.

Another common approach to simulate turbulent flows is conceptually opposite to DNS and involves a statistical description of turbulence by mathematical models instead of the explicit resolution of all the scales. By decomposing the velocity field in a mean and a fluctuating component (the *Reynolds decomposition*) and by ensamble-averaging the Navier-Stokes equations, it is possible to obtain the so-called *Reynolds-Averaged Navier-Stokes equations*. These equations are formally equal to the original governing equations, except for the fact that the new variable is the mean velocity field and that in the right-hand side a new term, the so-called *Reynolds stress tensor*, expresses the action of the fluctuating turbulent scales on the resolved ones. Given the difficulties to explicitly express the Reynolds stress tensor (the *closure problem*), turbulence models are needed to shape the action of the turbulent stresses. The modelling of the smallest scales dramatically reduces the computational burden of the simulations, and allows researchers to study flows with Reynolds numbers of practical interest. Satisfactory results have been obtained also in the field of wind energy [113].
However, despite the many models suggested, sources of uncertainty are still significant and the "ideal model" suggested by Wilcox in 1998 [114] is still far from being achieved especially for separated flows. Moreover, the unsteady simulation of the Reynolds-Averaged Navier-Stokes equations, has proved to be poorly accurate, highly sensitive to the turbulence model and with higher computational cost compared to its steady-state version [35].

[113]: Sørensen (2008), 'The EllipSys 2D/3D code and its application within wind turbine aerodynamics'

[114]: Wilcox et al. (1998), *Turbulence modeling for CFD*

The LES approach offers a method with intermediate requirements but with higher accuracy compared to RANS.
The method consists in solving only the largest scales of motion, the *large eddies*, which contain most of the energy of the flow and which are directly linked to the peculiar features of the fluid under study.

Considered the Kolmogorov hypothesis on local isotropy of small scales, the unresolved scales are assumed to be universal and their effect on the filtered variables is modelled through the resolved scales. At sufficiently high Reynolds number, the small-scale turbulent motion (smaller than the characteristic length ℓ_0 of the flow case under study) is assumed to be statistically isotropic. Moreover, in every turbulent flow at sufficiently high Reynolds number, Kolmogorov's theory assumes that the statistics of the motion at scale $\ell << \ell_0$ have a universal form that is uniquely determined by the rate of dissipation of the energy ϵ and the viscosity ν. The above-defined *universal equilibrium range* is subdivided into two subranges, the *dissipation range*, where ℓ approaches η and viscous effects dominate, and the larger *inertial subrange* where viscous effects are negligible. The scale range of the largest eddies is referred to as the *energy-containing range* (Figure 2.2). As far as the Reynolds number is larger, the scale separation increases and the energy cascade process is "long". Thus, it is reasonable to assume that the vortical structures lose memory of the large anisotropic flow-dependent eddies in the cascade towards small local isotropic eddies.

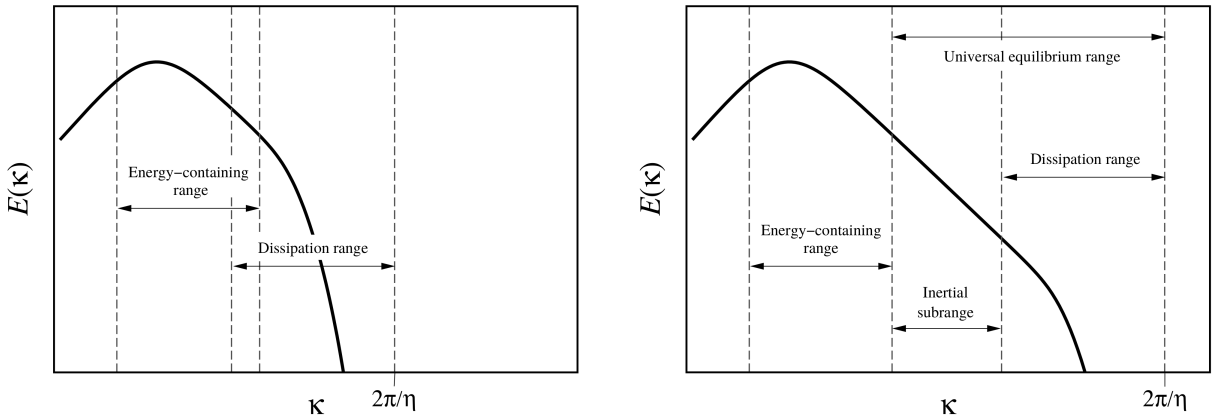

Figure 2.2: Turbulence Energy Spectrum $\widehat{E}(\kappa)$ and regions of the turbulence energy cascade as a function of the wavelength $k = 2\pi/\ell$ for two different Reynolds number. a) $Re_{\ell_0} = 10^3$, b), $Re_{\ell_0} = 10^5$. It is visible as at low Reynolds numbers the inertial subrange shrinks to vanish [115].

Although LES inherits the requirements of three-dimensional spatial resolution and unsteadiness operations from DNS, the empiricism introduced for the modelling of the new terms in the governing equations reduces the computational burden, but still guarantees superior accuracy compared to RANS, especially for unsteady simulations.

[116]: Breton et al. (2017), 'A survey of modelling methods for high-fidelity wind farm simulations using large eddy simulation'

Recent studies [116] have demonstrated the validity of the use of LES for the study of the fluid dynamics of the wind turbines and have shown that this methodology can give unmatched accuracy and physical insight compared to other approaches.

Filtered Navier-Stokes equations

In the following, we provide a brief description of the filtering procedure on the Navier-Stokes equations to separate resolved and unresolved

scales.

The filtering operation on a variable $\phi(\boldsymbol{x}, t)$ is a convolution product in space and time through a kernel function $G_{\widetilde{\Delta},\widetilde{\tau}}$, associated with a length cut-off scale $\widetilde{\Delta}$ and a time cut-off scale $\widetilde{\tau}$:

$$\tilde{\phi}(\boldsymbol{x}, t) \coloneqq \int_{-\infty}^{+\infty} \int_{-\infty}^{+\infty} G_{\widetilde{\Delta},\widetilde{\tau}}(\boldsymbol{x} - \boldsymbol{\xi}, t - t')\phi(\boldsymbol{\xi}, t')\mathrm{d}t'\mathrm{d}\boldsymbol{\xi}, \tag{2.8}$$

where $\tilde{\phi}(\boldsymbol{x}, t)$ is the *filtered* resolved component of the variable $\phi(\boldsymbol{x}, t)$. The remaining unresolved part of the variable $\phi'(\boldsymbol{x}, t)$ is called *residual* or *Subgrid-Scale (SGS)* component, and is such that:

$$\phi(\boldsymbol{x}, t) = \tilde{\phi}(\boldsymbol{x}, t) + \phi'(\boldsymbol{x}, t). \tag{2.9}$$

The filtering operation must verify the following properties [117]:

[117]: Sagaut (2006), *Large eddy simulation for incompressible flows: an introduction*

- conservation of constants: $\tilde{a} = a$;
- linearity: $\widetilde{\phi + \psi} = \tilde{\phi} + \tilde{\psi}$;
- commutation with derivation (*spatially and temporally uniform filter*):

$$\widetilde{\nabla\phi} = \nabla\tilde{\phi}, \quad \widetilde{\frac{\partial\phi}{\partial t}} = \frac{\partial\tilde{\phi}}{\partial t}.$$

By applying the filtering operation to Equation 2.4-Equation 2.5 it is possible to obtain the filtered governing equations, which are:

$$\frac{\partial\tilde{\boldsymbol{u}}}{\partial t} + \tilde{\boldsymbol{u}} \cdot \nabla\tilde{\boldsymbol{u}} = -\nabla\tilde{p} - \nabla \cdot \boldsymbol{\tau}^R + \frac{1}{Re}\nabla^2\tilde{\boldsymbol{u}} + \tilde{\boldsymbol{f}}, \tag{2.10}$$

$$\nabla \cdot \tilde{\boldsymbol{u}} = 0. \tag{2.11}$$

While the continuity equation maintains its form, the filtered Navier-Stokes equations differ from their non-filtered form only by the presence of the term $\nabla \cdot \boldsymbol{\tau}^R$, where $\boldsymbol{\tau}^R$ is the so-called *SGS* or *residual stress tensor* and is defined as:

$$\boldsymbol{\tau}^R \coloneqq \widetilde{\boldsymbol{u} \otimes \boldsymbol{u}} - \tilde{\boldsymbol{u}} \otimes \tilde{\boldsymbol{u}}. \tag{2.12}$$

Similarly to the Reynolds-averaged equations, the filtered Navier-Stokes equations need a closure model for the residual stress tensor, although there are two main differences:

- the filtered fields in the equations are in general random, three-dimensional and unsteady, even under conditions of statistical stationarity or homogeneity;
- the stress tensor depends on the choice of the type and width of the filter.

Subgrid-scale stress tensor

The subgrid-scale stress tensor $\boldsymbol{\tau}^R$ arises from the non-linearity of the convective term in Equation 2.4, and represents the interaction between the unresolved scales and the resolved ones.

In order to better understand the meaning of the residual stress tensor, Leonard introduced the triple decomposition of $\boldsymbol{\tau}^R$ that now brings his name [118]. By filtering the tensor product $\boldsymbol{u} \otimes \boldsymbol{u}$ and by using the decomposition in Equation 2.9, it can be easily proved that:

[118]: Leonard (1975), 'Energy Cascade in Large-Eddy Simulations of Turbulent Fluid Flows'

$$\boldsymbol{\tau}^R = \mathscr{L} + \mathscr{C} + \mathscr{R}, \tag{2.13}$$

where the *Leonard stresses* $\mathscr{L}$ are:

$$\mathscr{L} \coloneqq \widetilde{\tilde{\boldsymbol{u}} \otimes \tilde{\boldsymbol{u}}} - \tilde{\boldsymbol{u}} \otimes \tilde{\boldsymbol{u}}, \tag{2.14}$$

the *cross stresses* $\mathscr{C}$ are:

$$\mathscr{C} \coloneqq \widetilde{\tilde{\boldsymbol{u}} \otimes \boldsymbol{u}'} + \widetilde{\boldsymbol{u}' \otimes \tilde{\boldsymbol{u}}}, \tag{2.15}$$

and the *SGS Reynolds stresses* $\mathscr{R}$ are:

$$\mathscr{R} \coloneqq \widetilde{\boldsymbol{u}' \otimes \boldsymbol{u}'}, \tag{2.16}$$

By considering the decomposition in wavenumber space of the filtered governing equations and by examining the triad interactions in the nonlinear term [119], it is possible to interpret the physical meaning of each component of the residual stress tensor:

[119]: Pope (2001), *Turbulent flows*

- the Leonard stresses represent the contribution to the unresolved scales from the interaction of the resolved scales;
- the cross stresses represent the contribution to the resolved scales from the interaction between resolved and unresolved scales;
- the SGS Reynolds stresses represent the contribution to the resolved scales from the interaction of the residual scales.

The Leonard decomposition is not the only possible one, and due to the fact that two of its component stresses are not Galilean-invariant [120], other researchers have proposed different solutions, like for example the Galilean-invariant triple decomposition presented by Germano, 1986 [121].

[120]: Speziale (1985), 'Galilean invariance of subgrid-scale stress models in the large-eddy simulation of turbulence'

[121]: Germano (1986), 'A proposal for a redefinition of the turbulent stresses in the filtered Navier–Stokes equations'

In order to solve the closure problem of the filtered Navier-Stokes equations, a model has to express the residual stress tensor as a function of the resolved filtered velocity. Typically, only the anisotropic part of the tensor is modelled, while the isotropic residual stress is included in the definition of a modified filtered pressure:

$$\tilde{p}^* \coloneqq \tilde{p} + \frac{1}{3}\mathrm{tr}(\boldsymbol{\tau}^R) \tag{2.17}$$

where $\mathrm{tr}(\boldsymbol{\tau}^R)$ is the trace of the residual stress tensor. In some cases, the difference $p^* - p$ could be relevant and a model to estimate the residual kinetic energy $k_r = \frac{1}{2}\mathrm{tr}(\boldsymbol{\tau}^R)$ would be necessary.

The *eddy viscosity models* are the most widespread family of SGS models. These consider the action of the unresolved scales analogous to the viscous mechanisms taking place at a molecular level in the fluid, such as momentum or thermal exchanges. Hence, if on one hand a molecular viscosity ν is associated to the microscopic dissipation and is a material property of the fluid, on the other hand, an *eddy viscosity*

ν_r is associated with the turbulent macroscopic motion and is a local property of the resolved flow features.

According to this assumption, following the Boussinesq hypothesis [122], the deviatoric part of the SGS stress tensor $\boldsymbol{\tau}_d^R$ in dimensional form is determined as:

[122]: Lesieur (2012), *Turbulence in fluids*

$$\begin{aligned}\boldsymbol{\tau}_d^R &= \boldsymbol{\tau}^R - \frac{1}{3}\mathrm{tr}(\boldsymbol{\tau}^R)\mathbf{I} = \\ &= -2\nu_r\widetilde{\mathbf{S}} = \\ &= -\nu_r\left(\nabla\tilde{\boldsymbol{u}} + \nabla^T\tilde{\boldsymbol{u}}\right)\end{aligned} \tag{2.18}$$

where $\widetilde{\mathbf{S}}$ is the filtered strain-rate tensor, which is the symmetric part of the filtered velocity gradient, and the superscript T indicates the transpose operation. In such a way, the additional term in Equation 2.10 can be expressed as:

$$-\nabla\cdot\boldsymbol{\tau}_d^R = \nabla\cdot\left[\nu_r\left(\nabla\tilde{\boldsymbol{u}} + \nabla^T\tilde{\boldsymbol{u}}\right)\right] = \nu_r\nabla^2\tilde{\boldsymbol{u}} \tag{2.19}$$

where we consider only the deviatoric part of the residual stress tensor. The linear proportionality between $\boldsymbol{\tau}_d^R$ and $\widetilde{\mathbf{S}}$ makes the principal axes of these tensors locally parallel. However, even if for many important cases the assumption is reasonable, for some flows it is not valid.

Our fluid model adopts the widely-used Smagorinsky model [123], which assumes the eddy viscosity in Equation 2.18 to be:

[123]: Smagorinsky (1963), 'General circulation experiments with the primitive equations: I. The basic experiment'

$$\nu_r = (C_s\widetilde{\Delta})^2\,\widetilde{S} = (C_s\widetilde{\Delta})^2\,\sqrt{2\widetilde{\mathbf{S}}:\widetilde{\mathbf{S}}} \tag{2.20}$$

where $\widetilde{S}$ is the characteristic filtered strain-rate, $\widetilde{\Delta}$ is the filter width, and the symbol : indicates the Frobenius inner product ($\boldsymbol{A}:\boldsymbol{B} = \sum_{i,j}A_{ij}B_{ij}$). The Smagorinsky constant C_s is in general flow-dependent and usually ranges between $C_s \approx 0.1 - 0.2$. According to previous works of our group on LES of wind turbines, we tuned the Smagorinsky constant to the value of $C_s = 0.09$ [124][106].

[124]: Santoni et al. (2015), 'Development of a high fidelity CFD code for wind farm control'

According to Equation 2.18, it is possible to demonstrate that the rate of transfer of energy to the residual motion, $\epsilon = -\boldsymbol{\tau}_d^R:\widetilde{\mathbf{S}}$, is equal to $\nu_r\widetilde{S}^2$ [119]. Given the fact that $\nu_r > 0$, and thus the energy transfer can take place only from the resolved scales to the residual ones (*forward energy cascade*), the Smagorinsky model is not able to capture the *inverse energy cascade* or *backscatter*, which can be important in some particular processes.

The behaviour of the model in the near-wall region is the main problem of the Smagorisky model. In fact, in the viscous wall region very close to the wall, the eddy viscosity defined in Equation 2.20 does not vanish at the wall, and thus leads to a non-zero residual viscosity and shear stress at the wall. To solve this problem, the model uses a van Driest damping function as proposed in Moin and Kim, 1982 [125], to artificially impose a null value to C_s at the wall:

[125]: Moin et al. (1982), 'Numerical investigation of turbulent channel flow'

$$(C_s\widetilde{\Delta})_{damped} = C_s\widetilde{\Delta}\left[1 - \exp\left(\frac{y^+}{A}\right)\right] \tag{2.21}$$

where $A = 25$ is the Van Driest's constant, and $y^+ = u_\tau y/\nu$. In the definition of the friction velocity $u_\tau = \sqrt{\tau_w/\rho}$, τ_w is the shear at the wall and y is the distance from the wall.

The importance of the choice of the filter is well-known and several filters can be applied explicitly. However, the *explicit filtering* procedure is rarely performed, mostly because of its computational expense. More commonly, an *implicit filtering* is operated by the mesh grid itself, without any computational overhead. In fact, according to the Nyquist theorem, the grid is equivalent to the application of a top-hat filter, with cut-off wavenumber $k_c = \pi/\Delta x$, that filters all the eddies smaller that the grid spacing.

Because of this, the mesh size has to guarantee a cut-off wavenumber including all the active scales of the flow, *i.e.* k_c has to belong to the dissipative range of the energy spectrum. To correctly define the mesh and to avoid potential errors resulting from an improper cut-off wavenumber, grid sensitivity studies have to be performed to assess the independency of the results from the grid.

2.2 Numerical Method

In this section, we describe the discretisation procedure adopted to numerically solve the physical and mathematical model presented in Section 2.1.

The code, named *UTD-WF* code [105], uses a second-order central finite-difference approximation to evaluate spatial derivatives on a Cartesian orthogonal grid. Time advances by means of a fractional step method based on a low-storage third-order Runge-Kutta scheme for the explicit treatment of the non-linear terms and on a Crank-Nicolson scheme for the implicit treatment of the linear terms. To invert the large sparse matrix obtained by the implicit treatment of the linear terms in the filtered governing equations, the code uses an approximate factorisation technique that reduces dramatically the computational expense of the operation. A projection method corrects the velocity field to guarantee the solenoidal constraint imposed by Equation 2.11, and according to it, a new pressure field is estimated. For more details on the discretisation procedure, the interested reader can look at Orlandi, 2012 [126].

[105]: Santoni et al. (2020), 'One-way mesoscale-microscale coupling for simulating a wind farm in North Texas: Assessment against SCADA and LiDAR data'

[126]: Orlandi (2012), *Fluid flow phenomena: a numerical toolkit*

The grid is *staggered*, which means that the different flow variables are referred to different positions in the computational grid. This arrangement avoids the presence in the numerical solution of spurious pressure modes that give rise to so-called checkboard patterns [127, 128]. Moreover, it makes the stencil used in the discretisation of the derivatives compact, and thus increases the numerical accuracy of the scheme. As shown in Figure 2.3, while the pressure field is located at the centre of the cell, each velocity component in a certain direction is defined at the centre of the first face of the cell whose normal is parallel to the considered direction.

[127]: Fletcher (2012), *Computational techniques for fluid dynamics 2: Specific techniques for different flow categories*
[128]: Ferziger et al. (2002), *Computational methods for fluid dynamics*

The code is written in FORTRAN 77 and FORTRAN 90, and is parallelised by means of the Message Passing Interface (MPI) paradigm.

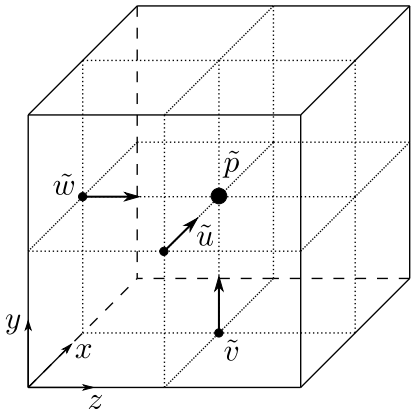

Figure 2.3: Computational cell with the position of the flow variables. The pressure is evaluated at the centre of the cell, while the velocity components are referred to the centre of the corresponding faces.

Discretisation schemes

In order to better focus on the different schemes adopted for the discretisation of the filtered Navier-Stokes equations, Equation 2.10 can be recast in the following form:

$$\frac{\partial \widetilde{\boldsymbol{u}}}{\partial t} = \boldsymbol{N}\left(\widetilde{\boldsymbol{u}}\right) + \boldsymbol{L}\left(\widetilde{\boldsymbol{u}}\right) + \widetilde{\boldsymbol{f}}(\widetilde{\boldsymbol{u}}) \tag{2.22}$$

where $\boldsymbol{N}\left(\widetilde{\boldsymbol{u}}\right)$ includes all the non-linear terms:

$$\boldsymbol{N}\left(\widetilde{\boldsymbol{u}}\right) = \widetilde{\boldsymbol{u}} \cdot \nabla \widetilde{\boldsymbol{u}} \tag{2.23}$$

and $\boldsymbol{L}\left(\widetilde{\boldsymbol{u}}\right)$ includes all the linear terms:

$$\boldsymbol{L}\left(\widetilde{\boldsymbol{u}}\right) = \left(\frac{1}{Re} + \frac{1}{Re_r}\right) \nabla^2 \widetilde{\boldsymbol{u}} - \nabla \widetilde{p} \tag{2.24}$$

where Re_r is the Reynolds number based on the eddy viscosity.
In the remaining part of this section, we will neglect the term $\widetilde{\boldsymbol{f}}(\widetilde{\boldsymbol{u}})$ and we will deal with its definition and discretisation in Section 2.4.

Non-linear terms

Because of the demanding computational cost of an implicit treatment of the convective terms at each time step, the non-linear terms are discretised in time by means of a low-storage third-order Runge-Kutta explicit method, originally developed by Wray, 1986 [129]. The solution advances of a time step Δt from time t^n to time t^{n+1} in three intermediate substeps which require only two memory spaces. In such a way, the method is third-order accurate, but with the same memory storage of a second-order accurate scheme.
According to the method, the updated solution of the intermediate step l at point i, for a generic component $\tilde{u}$, is:

[129]: Wray (1986), 'Very low storage time-advancement schemes'

$$\tilde{u}_i^{l+1} = \tilde{u}_i^l + \rho_l \Delta t N_i(\tilde{\boldsymbol{u}}^l) + \gamma_l \Delta t N_i(\tilde{\boldsymbol{u}}^{l-1}) \qquad l = 0, \ldots, 2 \tag{2.25}$$

where $\tilde{u}_i^0 = \tilde{u}_i^n$ is the solution at the current time step t^n, $\tilde{u}_i^2 = \tilde{u}_i^{n+1}$ is the solution at the following time step t^{n+1}, and $N_i(\tilde{\boldsymbol{u}}^l)$ is the spatially-discretised non-linear term defined by the velocity field at time l.
The coefficients ρ_l and γ_l are defined by the requirements of the method [126], that are:

- no more than two memory locations must be used;
- the new approximation produced must be evaluated by a Taylor's series expansion;
- the operations must be cyclic, *i.e.* all the quantities necessary for the following step are known at the end of the current time step.

Moreover, to have a self-starting method, *i.e.* it does not need any information from time instants preceding the starting time t^n, the coefficient ρ_0 must be zero.
The summation of Equation 2.25 for each substep l and the comparison of the obtained expression with the Taylor's expansion, bring to a system of five unknown coefficients. The possible solution chosen for this work is:

$$\rho_0 = 0 \qquad \rho_1 = -\frac{17}{60} \qquad \rho_2 = -\frac{5}{12} \tag{2.26a}$$

$$\gamma_0 = +\frac{8}{15} \qquad \gamma_1 = +\frac{5}{12} \qquad \gamma_2 = +\frac{3}{4}. \tag{2.26b}$$

Linear terms

The linear terms are discretised in time by means of a Crank-Nicolson implicit scheme centered at time $t^{l+1/2}$ for each Runge-Kutta step l.

In order to synchronise the linear and the non-linear terms advancement, the constants α_l defining the time substeps ($\alpha_l \Delta t = t^{l+1} - t^l$) must satisfy the condition:

$$\alpha_l = \rho_l + \gamma_l \tag{2.27}$$

The discretised filtered Navier-Stokes equations of the model are:

$$\begin{aligned} &\frac{\tilde{u}_i^{l+1} - \tilde{u}_i^l}{\Delta t} + \rho_l N_i(\tilde{\boldsymbol{u}}^l) + \gamma_l N_i(\tilde{\boldsymbol{u}}^{l-1}) = \\ &\qquad = -\alpha_l \left.\frac{\delta p}{\delta x_i}\right|_{l+1/2} + \alpha_l \left(\frac{1}{Re} + \frac{1}{Re_r}\right) L_{jj}\left(\frac{\tilde{u}_i^{l+1} + \tilde{u}_i^l}{2}\right) \end{aligned} \tag{2.28}$$

where $\frac{\delta}{\delta x_i}$ is the discrete gradient operator and L_{jj} is the discrete Laplace operator, both using second-order finite difference approximation.

Complete scheme: approximate factorisation and pressure correction

Direct integration of Equation 2.28 is not possible, because of the estimation of the pressure gradient at time $l + 1/2$. Indeed, pressure is only known at the first time instant t^l, and if the solution was evaluated by using p^l a non-solenoidal velocity field $\hat{\boldsymbol{u}}$ would result.

Moin and Kim, 1982 [125] have proposed the so-called *fractional step method* to solve this problem: the intermediate non-solenoidal velocity field is estimated by using the known pressure field at the current time instant, a pseudo-pressure field enforces the continuity equation and projects the velocity field onto a solenoidal space; finally the pressure field is updated.

[125]: Moin et al. (1982), 'Numerical investigation of turbulent channel flow'

If we substitute $\tilde{\boldsymbol{u}}^{l+1}$ with $\hat{\boldsymbol{u}}$, and we introduce in Equation 2.28 the new variable $\Delta\tilde{u}_i \coloneqq \hat{u}_i - \tilde{u}_i^l$, we obtain:

$$\begin{aligned}&\Delta\tilde{u}_i + \alpha_l \Delta t \left(\frac{1}{Re} + \frac{1}{Re_r}\right) L_{jj}\left(\frac{\Delta\tilde{u}_i}{2}\right) = \\ &= -\alpha_l \Delta t \left.\frac{\delta p}{\delta x_i}\right|_l - \rho_l N_i(\tilde{\boldsymbol{u}}^l) - \gamma_l N_i(\tilde{\boldsymbol{u}}^{l-1}) + \alpha_l \Delta t \left(\frac{1}{Re} + \frac{1}{Re_r}\right) L_{jj}\left(\tilde{u}_i^l\right)\end{aligned} \tag{2.29}$$

that can be summarised in the form:

$$\left[\delta_{jj} + \frac{\alpha_l \Delta t}{2}\left(\frac{1}{Re} + \frac{1}{Re_r}\right) L_{jj}\right] \Delta\tilde{u}_i = RHS_i \tag{2.30}$$

where RHS_i includes all the terms in the right-hand side of Equation 2.29 and δ_{jj} is the Kronecker's delta.

Because of the second-order stencil used to discretise the spatial derivatives in the Laplace operator, the matrix of the linear system in Equation 2.30 is a seven-diagonal sparse matrix. The matrix inversion of such a matrix for a problem with N points would involve N^3 floating point operations, which is a considerable number even for a coarse computational grid. In order to efficiently solve this linear system, the code adopts an approximate factorisation technique in three steps, such that:

$$\left[\delta_{jj} + \frac{\alpha_l \Delta t}{2}\left(\frac{1}{Re} + \frac{1}{Re_r}\right) L_{11}\right] \underline{\underline{\Delta\tilde{u}}}_i = RHS_i \tag{2.31a}$$

$$\left[\delta_{jj} + \frac{\alpha_l \Delta t}{2}\left(\frac{1}{Re} + \frac{1}{Re_r}\right) L_{22}\right] \underline{\Delta\tilde{u}}_i = \underline{\underline{\Delta\tilde{u}}}_i \tag{2.31b}$$

$$\left[\delta_{jj} + \frac{\alpha_l \Delta t}{2}\left(\frac{1}{Re} + \frac{1}{Re_r}\right) L_{33}\right] \Delta\tilde{u}_i = \underline{\Delta\tilde{u}}_i \tag{2.31c}$$

where L_{ii} indicates the Laplace operator in the i-th coordinate direction, while $\underline{\Delta\tilde{u}}_i$ and $\underline{\underline{\Delta\tilde{u}}}_i$ are intermediate solutions. Now, the problem involves the inversion of three three-diagonal matrices (one for each direction), which can be efficiently inverted by means of the Thomas' algorithm. The total cost thus becomes only $3\,N$ floating point operations, but the splitting operation reduces the time accuracy to the second order.

At this point of the solving procedure, the non-solenoidal velocity field ($\hat{u}_i = \Delta\tilde{u}_i - \tilde{u}_i^l$) is estimated. In order to enforce the continuity equation, a scalar *pseudo-pressure* ϕ projects $\hat{u}_i$ onto the solenoidal space:

$$\tilde{\boldsymbol{u}}^{l+1} = \hat{\boldsymbol{u}} - \Delta t \nabla\phi \tag{2.32}$$

It is possible to obtain the Poisson equation for the pseudo-pressure by

taking the divergence of Equation 2.32 and by imposing the solenoidal constraint on the velocity at the new time step ($\nabla \tilde{\boldsymbol{u}}^{l+1} = 0$):

$$\nabla^2 \phi = \frac{1}{\Delta t} \nabla \cdot \hat{\boldsymbol{u}} \tag{2.33}$$

If we assume periodicity in the spanwise direction and an inflow-outflow condition in the streamwise direction, Equation 2.33 is efficiently solved by means of Fourier decomposition in direction x and z.

The continuity equation at the boundaries imposes homogeneous Neumann boundary conditions for the Poisson equation, thus the solution is determined up to constants. As in the case of the pressure field, only differences are relevant to the behaviour of the fluid rather than the absolute values. To resolve the mathematical indefiniteness of the pseudo-pressure, the value of the mean pressure is subtracted at each time step and point.

Once obtained the pseudo-pressure at the cell centers, for consistency, it is possible to update the pressure field at time $l + 1$. By substituting Equation 2.32 in Equation 2.28, the pressure at the new time step is:

$$p^{l+1} = p^l + \phi - \frac{\alpha_l \Delta t}{2} \left(\frac{1}{Re} + \frac{1}{Re_r} \right) L_{jj} \phi \tag{2.34}$$

The pressure-correction procedure highlights that the pressure in the incompressible flows enforces the mass conservation, in order for the *discrete* system to accurately represent the physical *continuous* model.

Accuracy and stability

The numerical scheme described in Section 2.2 is sometimes called hybrid third-order Runge-Kutta/Crank-Nicolson scheme. While the adopted Runge-Kutta method is third-order accurate in time, the complete scheme is second-order accurate in time and space. Despite the overall decrease in accuracy, the scheme is low-storage, thus requiring a reduced additional amount of memory compared to a typical second-order scheme.

However, the stability properties of this Runge-Kutta scheme are the actual advantage of the method.
As a result of the explicit treatment of the convective terms, the Courant-Friedrichs-Lewy (CFL) condition [130] imposes that a particle can travel in a time step at most a maximum distance proportional to the mesh size:

[130]: Courant et al. (1967), 'On the Partial Difference Equations of Mathematical Physics'

$$CFL = \max_{i=1,\dots,3} \left| \frac{\tilde{u}_i \Delta t}{\Delta x_i} \right| \leq CFL_{max}. \tag{2.35}$$

The limit Courant number CFL_{max} depends on the scheme and limits the amplitude of the time step. As a consequence, the lower is CFL_{max}, the lower must be the time step Δt and the longer has to run a simulation to reach a desired flow time. As a result, if the grid is refined, the condition can be particularly critical.

The multi-stage nature of the Runge-Kutta method allows an increased stability margin. While for most of the explicit methods $CFL_{max} \leq 1$, in the case of the three-stage Runge-Kutta method, the limit CFL_{max} estimated for a linear advection problem is:

$$CFL_{max} = \sqrt{3} \tag{2.36}$$

In practice, the presence of viscous terms helps the stability properties of the Navier-Stokes solutions, and thus CFL values larger than $\sqrt{3}$ are normally used.

In our work, however, the main limitation for the CFL comes from the turbine modelling described in Section 2.4.
As reported in different studies [131, 132], it is suggested to limit the CFL in a way that the blade tip does not move for more than a grid cell in a single time step. This condition, related to the rotor revolution velocity, could be particularly severe and would strictly impose:

[131]: Martínez-Tossas et al. (2015), 'Large eddy simulations of the flow past wind turbines: actuator line and disk modeling'
[132]: Troldborg et al. (2009), 'Actuator line modeling of wind turbine wakes'

$$CFL \leq \frac{U\Delta t}{\Delta x} = \frac{U\ (\Delta x/\Omega R)}{\Delta x} = \frac{1}{TSR} \tag{2.37}$$

where $TSR = \Omega R/U$ is the so-called *tip speed ratio*, Ω is the angular velocity of the blades, R is the radius of the wind turbine and U is the typical inflow velocity. However, the stability properties of the complete scheme allows the use of larger values, even if the Courant number rarely exceeds $2/TSR$.

The implicit treatment of the viscous-like terms allows overcoming other stability limitations, which can be particularly demanding especially at low Reynolds numbers. For example, according to the viscous stability restriction [133]:

[133]: Peyret et al. (2012), *Computational methods for fluid flow*

$$\frac{\Delta t}{\Delta x^2 Re} \leq \frac{1}{2n} \tag{2.38}$$

where n is the dimensionality of the problem, the information diffused by viscous terms would not have been able to travel for more than Δx in one time step Δt.

2.3 Solid Bodies Model: Immersed Boundary Method

Our model uses the IBM [134] to represent the solid interfaces in the fluid domain, such as the tower and the nacelle, without generating computationally expensive body-fitted grids.

[134]: Peskin (2002), 'The immersed boundary method'

Previous works have extensively validated the methodology for many applications and have proved its validity to derive a more physically sound model also for the study of wind turbines [106].

The technique implementation consists in imposing a null velocity field for the points inside the solid boundaries and in correcting the discretisation of the space derivatives for the points closest to the body (Figure 2.4). Instead of using the distance between the outside and inside points, the discretisation of the derivatives uses the actual

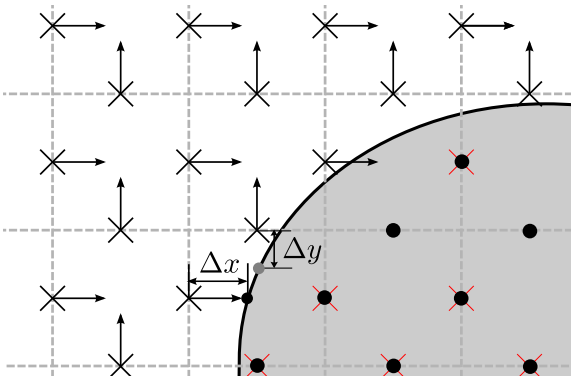

Figure 2.4: 2D sketch of the grid in the region close to the body. Horizontal and vertical velocity components are indicated with arrows at the points indicated with × according to the staggered definition of the grid. Inside the body (•), the velocity is set at zero, while the derivatives of the points just outside the body are corrected by using the actual distances Δx and Δy from the solid boundaries (•). Modification of Santoni et al. [106]

distance between the surface of the "immersed body" and the points immediately outside of it. This method prevents the representation of the body by means of a fictitious stepwise geometry.

We have not used the IBM method to represent also the rotating blades because this would have involved an extremely fine mesh to resolve the complex geometry of the blade. Morevover, we would have needed a moving IBM strategy to consider the unsteady revolution of the rotor [135]. Therefore, we decided to use the Immersed Boundary Method only to model the bluff bodies in the domain and to adopt a more efficient generalised actuator disc model to consider the rotor.

[135]: Kim et al. (2006), 'Immersed boundary method for flow around an arbitrarily moving body'

2.4 Turbine Model

To model the blades of the rotor inside the fluid domain, the code adopts the widely used generalised actuator disc model proposed by Sørensen and Shen, 2002 [38]: the Actuator Line Model. The aerodynamic forces that the blades impose on the flow are determined with a blade element approach and are then distributed as body forces along rotating lines in correspondence of the position of the blades.

[38]: Sørensen et al. (2002), 'Numerical modeling of wind turbine wakes'

According to a blade element analysis, for a 2D airfoil located at distance r from the hub center, the lift force F_l and the drag force F_d per unit length are

$$F_l = \frac{1}{2}\rho U_{rel}^2\, c\, C_l(\alpha)\, F \qquad \text{and} \qquad F_d = \frac{1}{2}\rho U_{rel}^2\, c\, C_d(\alpha)\, F\,, \tag{2.39}$$

where ρ is the air density, U_{rel} is the local relative velocity in the plane of the profile, c is the local chord length of the airfoil, $C_l(\alpha)$ and $C_d(\alpha)$ are the lift and drag coefficients for a certain local angle of attack α, and F is a modified Prandtl correction factor.
For example, if the structure of the wind turbine is rigid, at the generic section r of the blade (Figure 2.5), the local relative velocity and incidence are:

$$U_{rel} = \sqrt{\tilde{u}_1^2 + (\tilde{u}_\theta - \Omega r)^2} \tag{2.40}$$

$$\alpha = \arctan\left(\frac{\tilde{u}_1}{\tilde{u}_\theta - \Omega r}\right) - \phi \tag{2.41}$$

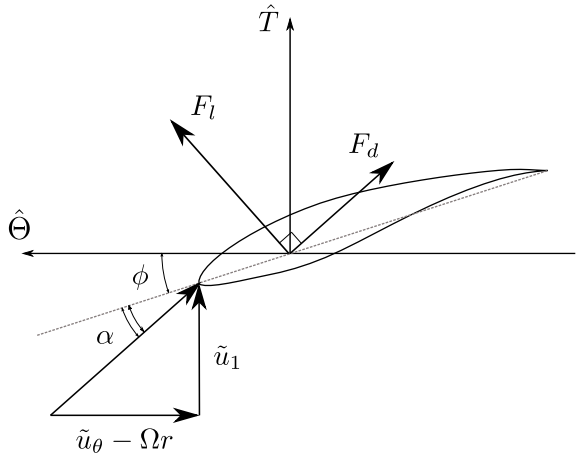

Figure 2.5: Sketch of the flow at a cross-section of a wind turbine blade. $\hat{T}$ is the direction of the thrust force and $\hat{\Theta}$ is the azimuthal direction, positive in the direction of the rotor revolution.

where $\tilde{u}_\theta$ is the azimuthal velocity component in the plane of the rotor and ϕ is the local twist angle.
For a more general definition of the local relative velocity and incidence in the case of deformable blades, see Chapter 4.

The look-up tables of the aerodynamic coefficients of the 2D airfoils are not able to replicate the three-dimensional effects of the circulation distribution, and therefore, to correct the typical overprediction of the loads at the blade tip and root, the model considers in Equation 2.39 a modified Prandtl tip correction factor [136] given by:

[136]: Shen et al. (2005), 'Tip loss corrections for wind turbine computations'

$$F = \frac{4}{\pi^2}\cos^{-1}\left[\exp\left(\frac{g\,B\,(r-R)}{2\,r\sin(\alpha+\phi)}\right)\right]\cos^{-1}\left[\exp\left(\frac{g\,B\,(R_h-r)}{2\,r\sin(\alpha+\phi)}\right)\right], \tag{2.42}$$

with

$$g = \exp\left[-0.125\,(B\cdot TSR - 21.0)\right] + 0.1\,, \tag{2.43}$$

where B is the number of the blades, R is the radius of the rotor, and R_h is the hub radius.

The total *local* aerodynamic force vector $\boldsymbol{f}^{aero}$ is then projected onto the flow. A 2D Gaussian kernel η spreads the aerodynamic forces in cylinders surrounding each actuator line, to avoid numerical instabilities arising when a concentrated force is applied to the flow field (see Figure 2.6). Thus, in Equation 2.10, the body force vector $\widetilde{\boldsymbol{f}}$ acting on the fluid in the cylindrical regions of the actuator lines is equal to:

$$\tilde{\boldsymbol{f}} = -\boldsymbol{f}^{aero}\eta = -\boldsymbol{f}^{aero}\frac{1}{\epsilon^2\pi}\exp\left[-\left(\frac{r_\eta}{\epsilon}\right)^2\right], \tag{2.44}$$

where r_η is the radial distance of a generic point of the cylinder from the relative actuator line and ϵ is the spreading parameter.

Several studies have shown that the spreading parameter ϵ strongly influences the evolution of the flow field and its most appropriate value is still debated. Troldborg, 2009 [132] suggested a dependence of the spreading parameter on the grid spacing, and specifically that it should be such that $\epsilon/\Delta \geq 2$ to avoid numerical instabilities. On the other hand, recent studies [137–139] have proposed to link ϵ to the distribution of the chord length. In particular, Martínez-Tossas [139] concluded that for simulations with grid spacing larger than the chord,

[137]: Jha et al. (2014), 'Guidelines for volume force distributions within actuator line modeling of wind turbines on large-eddy simulation-type grids'
[138]: Churchfield et al. (2017), 'An advanced actuator line method for wind energy applications and beyond'
[139]: Martínez-Tossas et al. (2017), 'Optimal smoothing length scale for actuator line models of wind turbine blades based on Gaussian body force distribution'

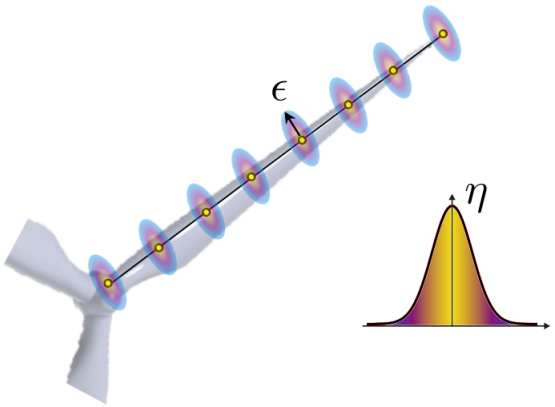

Figure 2.6: Schematic representation of the Actuator Line Model. The Gaussian kernel η spreads the aerodynamic forces around the actuator lines.

ϵ should be a function of Δ, whereas for grid spacing smaller than the chord, ϵ should be a function of c. In our simulations, even if for the finest cases Δ/c was smaller than 1, we preferred to use a spreading value depending on the grid spacing, according to the classic condition $\epsilon/\Delta = 2$, since we observed numerical instabilities when decreasing further the spreading radius.

Finally, to estimate the aerodynamic pitching moment acting on the blades necessary for the structural dynamics, a blade element approach is followed similarly. Thus, the pitching moment per unit length referred to the airfoil quarter of chord is equal to:

$$M^{aero} = -\frac{1}{2}\rho U_{rel}^2 c^2 C_m(\alpha) F\,, \tag{2.45}$$

where $C_m(\alpha)$ is the local pitching moment coefficient. The minus sign takes into account that, by convention, the pitching moment coefficient is positive when it pitches the airfoil in the nose-up direction, and thus induces a negative rotation around the radial axis pointing towards the tip of the blade (see Section 4.1).

Time discretisation

For what concerns the discretisation in time of the nonlinear body force vector field $\widetilde{\boldsymbol{f}}$, the vector explicit approximation at time t^n is used.
In order to treat this term implicitly, the code would have needed to estimate the non-linear aerodynamic forces from the unknown local velocity field at the time t^{n+1}, which would have complicated the matrix at the left-hand side of Equation 2.30.
Alternatively, the code could have solved the velocity field at each time step iteratively, by introducing at every iteration a new approximation of the forces determined with the new local velocity. However, this would have increased relevantly the computational cost of the full scheme.

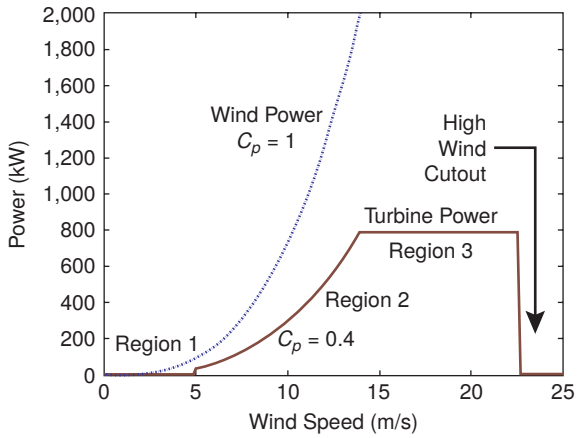

Figure 2.7: Typical behaviour of the steady-state power curve of a small turbine. In region I, the turbine is stopped or is starting up. In region II, a variable-speed turbine tries to maximise the energy capture. In region III, mechanical and electrical safety imposes a limited power up to the high wind cut-out [140].

Rotor dynamics

The low-shaft angular speed Ω advances in time according to the single-DOF model equation:

$$I_d\dot{\Omega} = T_{aero} - T_{gen}\,, \tag{2.46}$$

where I_d is the drivetrain rotational inertia, which includes the combined inertia of the rotor and the generator, T_{aero} is the torque due to the aerodynamic forces acting on the blades, and T_{gen} is the generator torque.

In this study, we considered a variable-speed turbine operating in region II (see Figure 2.7), for which the standard quadratic control law [140] holds and is such that:

$$T_{gen} = k_{gen}\Omega^2\,, \tag{2.47}$$

where the torque gain k_{gen} is a function of the optimal conditions of the wind turbine.

[140]: Johnson et al. (2006), 'Control of variable-speed wind turbines: standard and adaptive techniques for maximizing energy capture'

2.5 Unsteady Aerodynamics Model

Given its wide use, its demonstrated capabilities and the research and industry community support, we decided to implement in our code the semi-empirical model of Beddoes and Leishman [98] to describe the unsteady aerodynamics. The model is *postdictive*, since it is not derived from a precise theoretical model for unsteady flows and as such has some limitations in its predictive capabilities. Moreover, predetermined constants in the first-order differential equations of each subsystem should be tuned to match experimental data, when available. Despite this and other limitations that are presented below, the model is able to limit the complexity of the description and to hold a physical meaning of each submodule, with a complete and sufficiently accurate representation of the thorough unsteady aerodynamics.

The method includes compressibility effects, and it is made by three subsystems (see Figure 2.8):

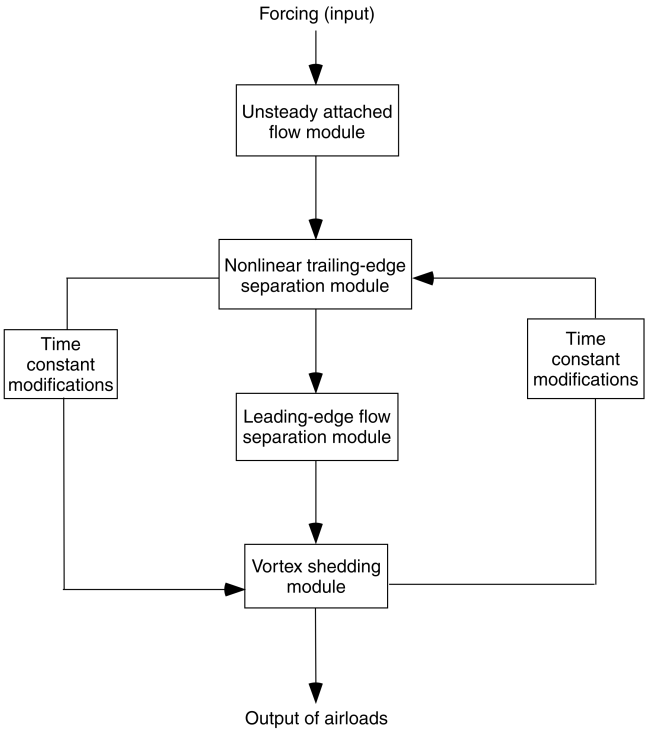

Figure 2.8: Schematic flowchart of the Beddoes and Leishman model [69].

1. a model for the unsteady aerodynamics for attached flow, based on Duhamel superposition;
2. a model for the unsteady aerodynamics with dynamic trailing edge separation, based on the Kirchhoff model;
3. a criterion to determine the dynamic stall onset and a dynamic stall model for the airloads induced by LEV.

In the literature, several works showed that the model has some deficiencies, like the ones reported in Sheng, 2008 [141], such as: an early stall onset strongly depending on the empirical constants; a missing stalled flow convection on the upper surface in the reattachment process; an underpredicted normal force hysteresis at low Mach numbers. To solve these problems, various models have been proposed [94, 96, 141]. However, also these models depend on additional empirical constants that should be tuned on experimental measurements on the different kinds of motion, such as pitching, plunge or mixed ones, for the different kinds of airfoil. Unfortunately, there is not such a complete experimental database for the specific airfoils of the turbine that will be studied, and thus it is difficult to consider these models in our methodology. On the other hand, the empirical constants of the specific airfoils used in this work for the original BL model have been tuned for the NREL AeroDyn15 module [142], and have been already used in the literature with satisfactory results [99].

[141]: Sheng et al. (2008), 'A modified dynamic stall model for low Mach numbers'

[142]: Damiani et al. (2019), *The Unsteady Aerodynamics Module For FAST8*

Although the mentioned inconsistencies limit the accuracy of the airloads estimation, we believe that our simulations are still able to assess the effects of some form of unsteadiness in the aerodynamics on the performance of the turbine and most of all on the aeroelastic response of the blades, thus providing in any case an improved physical insight on the phenomena taking place.

Before presenting the equations that define the particular implementation of the BL model chosen for this work and based on the reference paper of Damiani and Hayman [142], we present some useful definitions for the remaining sections. In particular, according to the definition of the force components in different frames of reference (see Figure 1.10), we have that:

$$C_l = C_n \cos\alpha + C_c \sin\alpha \tag{2.48}$$
$$C_d = C_n \sin\alpha - C_c \cos\alpha + C_{d0} \tag{2.49}$$

and

$$C_n = C_l \cos\alpha + (C_d - C_{d0}) \sin\alpha \tag{2.50}$$
$$C_c = C_l \sin\alpha - (C_d - C_{d0}) \cos\alpha \tag{2.51}$$

where C_{d0} is the 2D drag coefficient at zero lift.

Finally, we define the angle of attack and the pitch rate. The nondimensional pitch rate q is defined as:

$$q = \frac{\dot{\alpha} c}{U} \approx \frac{K_{\alpha_n} c}{U} \qquad \text{with} \qquad K_{\alpha_n} = \frac{\alpha_n - \alpha_{n-1}}{\Delta t} \tag{2.52}$$

where the time derivative of the angle of attack is approximated by a backward finite difference approximation and the index n denotes the n-th time step. As suggested in the reference paper, the angle of attack and the pitch rate are low-pass filtered, given the fact that for small time steps, the backward finite differences of the incidence and of the pitch rate could be subjected to significant numerical noise. The simple infinite impulse response filtering procedure that we adopt is defined as follows:

$$\alpha_{LP_n} = C_{LP} \alpha_{LP_{n-1}} + (1 - C_{LP}) \alpha_n \,, \tag{2.53a}$$
$$q_n = \frac{\left(\alpha_{LP_n} - \alpha_{LP_{n-1}}\right) c}{U_n \Delta t} \,, \tag{2.53b}$$
$$q_{LP_n} = C_{LP} q_{LP_{n-1}} + (1 - C_{LP}) q_n \,, \tag{2.53c}$$
$$K_{\alpha, LP_n} = \frac{q_{LP_n} U_n}{c} \,, \tag{2.53d}$$
$$K_{q_n} = \frac{q_n - q_{n-1}}{\Delta t} \,, \tag{2.53e}$$
$$K_{q, LP_n} = C_{LP} K_{q, LP_{n-1}} + (1 - C_{LP}) K_{q_n} \,, \tag{2.53f}$$

where the subscript LP indicates the corresponding low-pass filtered quantities and $C_{LP} = \exp\left(-2\pi \Delta t \zeta_{LP}\right)$ is the low-pass filter constant defined by a low-pass-filter frequency cutoff ζ_{LP}. Hereinafter, the LP subscript is dropped, implicitly assuming that the quantities indicated have been filtered.

Unsteady attached flow

As anticipated, the unsteady response of the attached flow to a generic forcing is considered in the BL model as a superposition of indicial response functions to steps variation in the forcing. In general, the

indicial responses of this model are composed of two distinct parts: the noncirculatory part, derived from piston theory and acoustic wave theory, and the circulatory part, originating from the evolution of the circulation around the airfoil. Both parts are expressed as exponential functions that approximate the exact and complex analytical formulations.

In the following, we present in detail the formulation for the normal force, the chordwise force and the pitching moment coefficients according to the indicial response method. For additional information please refer to Leishman, 2006 [77].

Normal force component

The variation of the normal force coefficient ΔC_n following a step change in the angle of attack $\Delta\alpha$ and in the pitch rate Δq is expressed by Leishman, 1989 [98] as:

$$\Delta C_n(s) = \left[\frac{C_{n\alpha}}{\beta_M}\phi_\alpha^c + \frac{4}{M}\phi_\alpha^{nc}\right]\Delta\alpha + \frac{1}{M}\phi_q^{nc}\Delta q \tag{2.54}$$

where the function ϕ_α^c is the circulatory part of the indicial response function related to a step change in the angle of attack (and pitch rate, in the lumped approach described below), ϕ_α^{nc} is the noncirculatory part of the indicial response function related to a step change in the angle of attack, and ϕ_q^{nc} is the noncirculatory part of the indicial response function related to a step change in the pitch rate.

According to Leishman and Beddoes, 1989 [98] and Johansen, 1999 [143], the response functions for the normal force component are:

[143]: Johansen (1999), *Unsteady airfoil flows with application to aeroelastic stability*

$$\phi_\alpha^c = 1 - A_1\exp\left(-b_1\beta_M^2 s\right) - A_2\exp\left(-b_2\beta_M^2 s\right), \tag{2.55}$$

$$\phi_\alpha^{nc} = \exp\left(-s/T'_\alpha\right), \tag{2.56}$$

$$\phi_q^{nc} = \exp\left(-s/T'_q\right), \tag{2.57}$$

where the first expression is the Jones' approximation of the circulatory response function in Equation 1.5, whereas T'_α and T'_q are the time constants regulating the separate decays of the noncirculatory impulsive responses to a step increase in incidence or in pitch rate. According to the exact results of Lomax, 1952 [86] for $0 \le s \le 2M/(M+1)$, the constants are defined according to the following equations:

$$T_\alpha(M) = 0.75\frac{c}{2Ma_s}T'_\alpha = 0.75k_\alpha(M)T_I \tag{2.58}$$

$$T_q(M) = 0.75\frac{c}{2Ma_s}T'_q = 0.75k_q(M)T_I \tag{2.59}$$

where a_s is the speed of sound, $T_I = c/a_s$, the factor 0.75 takes into account 3D effects, and

$$k_\alpha(M) = \left[(1-M) + 0.5C_{n_\alpha}M^2\beta_M^2(A_1b_1 + A_2b_2)\right]^{-1}, \tag{2.60}$$

$$k_q(M) = \left[(1-M) + \quad C_{n_\alpha}M^2\beta_M^2(A_1b_1 + A_2b_2)\right]^{-1}. \tag{2.61}$$

Given its indicial response function, the circulatory part of the normal force component from the Duhamel integral $C^c_{n_{\alpha,q}}$, *could* be defined analogously to Equation 1.7 as:

$$C^c_{n_{\alpha,q}} = C^c_{n\alpha}(M)\left[\alpha(s_0)\phi^c_\alpha(s) + \int_{s_0}^{s} \frac{\mathrm{d}\alpha(\sigma_s)}{\mathrm{d}\sigma_s}\phi^c_\alpha(s-\sigma_s, M)\mathrm{d}\sigma_s\right] = \\ = \frac{C^c_{n\alpha}}{\beta_M}\alpha_e\,, \quad (2.62)$$

where a lumped approach is adopted, defining an effective incidence α_e at 3/4-chord, summarising all the time history information of the shed vorticity and taking into account step variations in both α and q, *i.e.* no separate $C^c_{n_\alpha}$ and $C^c_{n_q}$ contributions. As can be seen, the numerical solution of the integral above would require storing the entire history of the incidence, which is unfeasible from a practical point of view. However, by further manipulating the Duhamel integral, it is possible to obtain the following recursive solution for the effective angle of attack at time n:

$$\alpha_{e_n} = (\alpha_n - \alpha_0) - X_{1_n}(\Delta s) - X_{2_n}(\Delta s) \quad (2.63)$$

where α_0 is the zero-lift angle of attack, $\Delta s = 2U\Delta t/c$ is the reduced time step, and X_{1_n}, X_{2_n} are the so-called *deficiency functions* defined as:

$$X_{1_n} = X_{1_{n-1}}\exp\left(-b_1\beta^2_M\Delta s\right) + A_1\exp\left(-b_1\beta^2_M\frac{\Delta s}{2}\right)\Delta\alpha_n\,, \quad (2.64)$$

$$X_{2_n} = X_{2_{n-1}}\exp\left(-b_2\beta^2_M\Delta s\right) + A_2\exp\left(-b_2\beta^2_M\frac{\Delta s}{2}\right)\Delta\alpha_n\,. \quad (2.65)$$

where $\Delta\alpha_n$ is the variation of the angle of attack.
These functions represent the *"deficiency"* in the angle of attack due to the UA effects and contain all the information about the time history of the shed wake effects on the airloads [98].

The idea of considering deficiency functions that adjust the instantaneous quantities according to history effects is crucial for the BL model and will be used again for several quantities in the model. However, our method couples the UA module to an LES solver, which already explicitly solves the shedding of the vorticity and thus already includes its effects in the local kinematics of the flow used to determine the instantaneous angle of attack. For this reason, even if the theoretical explanation above is essential to understand the rationale of the entire model, the effective incidence used at this stage of our model is the geometric one, evaluated from the local kinematics of the flow from the CFD solver like in the *steady* case, *i.e.* $X_{1_n} = X_{2_n} = 0$.

After having defined the circulatory component, the noncirculatory part is considered. In this case, a lumped approach is not possible, and so the two contributions resulting from step changes in α and q, $C^{nc}_{n_\alpha}$ and $C^{nc}_{n_q}$ respectively, have to be defined separately. According to the reference model, carrying out the Duhamel integration and considering

Equation 2.54, one obtains that:

$$C_{n_\alpha}^{nc} = \frac{4T_\alpha}{M}\left(K_\alpha - K'_\alpha\right), \tag{2.66}$$

$$K'_{\alpha_n} = K'_{\alpha_{n-1}} \exp\left(-\frac{\Delta t}{T_\alpha}\right) + \left(K_{\alpha_n} - K_{\alpha_{n-1}}\right) \exp\left(-\frac{\Delta t}{2T_\alpha}\right), \tag{2.67}$$

$$C_{n_q}^{nc} = -\frac{T_q}{M}\left(K_q - K'_q\right), \tag{2.68}$$

$$K'_{q_n} = K'_{q_{n-1}} \exp\left(-\frac{\Delta t}{T_q}\right) + \left(K_{q_n} - K_{q_{n-1}}\right) \exp\left(-\frac{\Delta t}{2T_q}\right), \tag{2.69}$$

The final expression of the normal force coefficient is given by the sum of the terms from Equation 2.62, Equation 2.66 and Equation 2.68:

$$C_n^{pot} = C_n^{pot,c} + C_n^{pot,nc} = C_{n_{\alpha,q}}^{c} + C_{n_\alpha}^{nc} + C_{n_q}^{nc}. \tag{2.70}$$

where the superscript *pot* indicates that these are contributions related to the attached module.
As one can notice, however, the noncirculatory terms in Equation 2.66 and Equation 2.68 tend to infinite when the Mach number goes to zero. To avoid too large concentrated forces possibly causing numerical instabilities and given the small velocities in particular close to the hub, we substituted the aforementioned terms with the corresponding expressions from the incompressible Theodorsen theory [144]. In the latter case, the absence of compressibility effects makes the added mass terms instantaneous and related only to the time derivatives of the incidence and the pitch rate, without the need to take into account exponential response functions.

[144]: Bisplinghoff et al. (2013), *Principles of aeroelasticity*

The theory states that the added mass terms in the normal force coefficient – the lift coefficient for small angles of attacks – for arbitrary free-stream velocity fluctuations [145] can be expressed as:

$$C_n^{nc} = \frac{\pi b}{U^2}\left(\ddot{h} + \frac{\mathrm{d}(U\alpha)}{\mathrm{dt}} + \frac{b}{2}\ddot{\alpha}\right). \tag{2.71}$$

[145]: Wall et al. (1994), 'On the influence of time-varying flow velocity on unsteady aerodynamics'

Assuming that for our case the plunge acceleration $\ddot{h}$ is null, and adopting a backward finite-difference approximation, it is possible to evaluate the above noncirculatory contributions from a variation in the angle of attack and in the pitch rate at time n as follows:

$$C_{n_{\alpha,q}}^{nc} = \frac{\pi b}{U_n}\left(K_{\alpha_n} + \frac{K_{q_n}}{4}\right) + \frac{\pi}{\Delta s_n}\left(1 - \frac{U_{n-1}}{U_n}\right)\left(\alpha_{n-1} + \frac{q_{n-1}}{4}\right), \tag{2.72}$$

where the terms include also the effect of the time variation in the free-stream velocity.

Chordwise force component

Given the fact that the noncirculatory part is not relevant for drag [77], and that in potential flow the D'Alambert paradox imposes a null drag, and so one has that $C_c = C_n \tan\alpha$, the chordwise force resulting from

the attached flow module is defined as:

$$C_c^{pot} = C_n^{pot,c} \tan(\alpha_e + \alpha_0)\,. \tag{2.73}$$

Pitching moment

The situation is more complex for the pitching moment coefficient, which needs a treatment similar to the one of the normal force. As in the case of the normal force response to a step change in angle of attack and pitch rate (Equation 2.54), the pitching moment coefficient variation can be expressed as:

$$\Delta C_m(s) = \left[-\frac{C_{n\alpha}}{\beta_M}\phi_\alpha^c(\hat{x}_{ac} - 0.25) - \frac{1}{M}\phi_{m,\alpha}^{nc}\right]\Delta\alpha + \\ + \left[-\frac{C_{n\alpha}}{16\beta_M}\phi_{m,q}^c - \frac{7}{12M}\phi_{m,q}^{nc}\right]\Delta q + C_{m0} \tag{2.74}$$

where $\phi_{m,\alpha}^{nc}$ and $\phi_{m,q}^{nc}$ are the noncirculatory indicial response functions to step changes in α and q, while $\phi_{m,q}^c$ is the circulatory indicial response function to a step change in Δq. Finally, $\hat{x}_{ac}$ is the aerodynamic center position from the leading edge, regulating the circulatory response to a step change in α, and C_{m0} is the pitching moment coefficient at zero lift. The pitching moment is positive when pitches up the airfoil.

The procedure for the noncirculatory step response to q is similar to the normal force. The indicial response function is defined as:

$$\phi_{m,q}^{nc} = \exp\left(-\frac{s}{T'_{m,q}}\right), \tag{2.75}$$

in which the Mach-dependent time constant is defined as:

$$T_{m,q}(M) = 0.75\frac{c}{2Ma_s}T'_{m,q} = 0.75k_{m,q}(M)T_I\,, \tag{2.76}$$

where

$$k_{m,q}(M) = \frac{7}{15(1-M) + 1.5C_{n\alpha}A_5b_5\beta_M^2M^2}\,. \tag{2.77}$$

By further developing the terms in the Duhamel's integral, one obtains, similarly to the corresponding contribution to the normal force coefficient in Equation 2.66 and in Equation 2.68:

$$C_{m_q}^{nc} = -\frac{7k_{m,q}^2T_I}{12M}(q - K''_q)\,, \tag{2.78}$$

$$K''_{q_n} = K''_{q_{n-1}}\exp\left(-\frac{\Delta t}{k_{m,q}^2T_I}\right) + (K_{q_n} - K_{q_{n-1}})\exp\left(-\frac{\Delta t}{2k_{m,q}^2T_I}\right)\Delta q_n\,. \tag{2.79}$$

For the other noncirculatory component from a step change in α, Leishman and Baddoes, 1986 [146] found that $\phi_{m,\alpha}^{nc} = \phi_\alpha^{nc}$, and so that:

$$C_{m_\alpha}^{nc} = -\frac{C_{n_\alpha}^{nc}}{4}\,. \tag{2.80}$$

Finally, for what concerns the circulatory component $C_{m,q}^c$, according

[146]: Leishman et al. (1986), 'A general model for airload unsteady behavior and dynamic stall using the indicial method'

to Johansen, 1999 [143], one has that:

$$C^c_{m_q} = -\frac{C_{n\alpha}}{16\beta_M}(q - K'''_q)\,, \tag{2.81}$$

$$K'''_{q_n} = K'''_{q_{n-1}} \exp\left(-b_5\beta_M^2\Delta s\right) + A_5 \exp\left(-b_5\beta_M^2\frac{\Delta s}{2}\right)\Delta q_n\,. \tag{2.82}$$

with A_5 and b_5 being two constants set at 1 and 5 respectively from an experimental tuning in Leishman, 2006 [77]. As a result, the total unsteady pitching moment for attached flow at 1/4-chord is given by:

$$\begin{aligned} C^{pot}_m &= C^{pot,c}_m + C^{pot,nc}_m = \\ &= C_{m0} - \frac{C_{n\alpha}}{\beta_M}\phi^c_\alpha(\hat{x}_{ac} - 0.25) + C^{nc}_{m_\alpha} + C^c_{m_q} + C^{nc}_{m_q}\,. \end{aligned} \tag{2.83}$$

Consistently with the formulation of the lift, and after having verified that the original formulation produced a too large contribution caused by the small Mach number, we decided to express also the noncirculatory contributions of the pitching moment according to the incompressible Theodorsen theory.

In general, the added-mass terms of the pitching moment, referred to the quarter of the chord, are:

$$C^{nc}_m = \frac{\pi}{2}\left[-\frac{b\ddot{h}}{2U^2} - \frac{3}{8}\frac{b^2\ddot{\alpha}}{U^2} + \frac{\dot{h}}{U} + \alpha\right]\,. \tag{2.84}$$

In our case $\ddot{h} = \dot{h} = 0$, since we are only interested in the contributions related to variations in the angle of attack and in pitching rate. For what concerns the term $\pi\alpha/2$, being it present for the steady case ($\ddot{\alpha} = \dot{\alpha} = 0$), it is already included in the static measurements of the airfoils, and so it is not included as a separate distinct term but rather is considered to be inherently contained in the separation functions f introduced in the following section. As a result, the only term surviving is the one related to $\ddot{\alpha}$ ($C^{nc}_{m_\alpha} = 0$), that can be recast as:

$$C^{nc}_m = C^{nc}_{m_q} = -\frac{3}{8}C^{nc}_{n_q}\,. \tag{2.85}$$

Unsteady trailing edge separation

The BL model describes the dynamic flow separation at the trailing edge by means of the widely adopted Kirchhoff's theory framework, described by Equation 1.8a and Equation 1.8b.

A critical parameter for this model is the separation point distance f as a function of α. The original model of Beddoes and Leishman proposed an analytical curve depending on four coefficients derived from a best-fit on the static measurements. Even if this approach provides quite satisfactory results, it still lacks the ability to reproduce in the limit the exact static data. Moreover, the use of a single $f(\alpha)$ curve, derived from the normal coefficient data only, has proved to provide unsatisfactory results for the estimation of the chordwise force coefficient. To attempt to solve this problem, Moriarty and Hansen,

2005 and later Liu et al., 2020 [147, 148] proposed to invert both Equation 1.8a and Equation 1.8b, using C_n and C_c experimental data, to define two different separation functions f_n and f_c. Figure 2.9 shows the difference of the two curves obtained for a DU25 A17 profile, where it is possible to notice the differences between the two functions.

[147]: Moriarty et al. (2005), *AeroDyn theory manual*
[148]: Liu et al. (2020), 'An improved dynamic stall model and its effect on wind turbine fatigue load prediction'

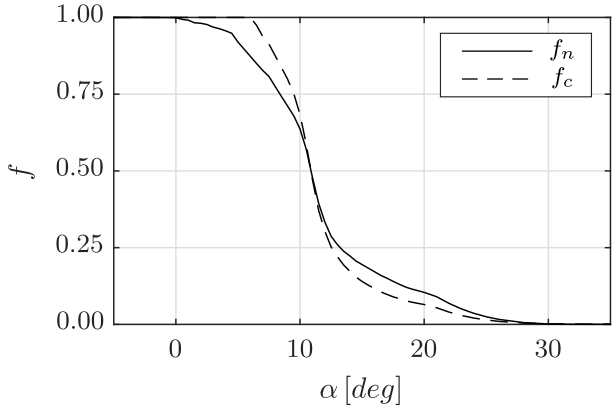

Figure 2.9: Separation point curves for a DU25 A17 airfoil: f_n curve obtained inverting the normal coefficient Kirchhoff formula (solid line), f_c curve obtained inverting the chordwise coefficient Kirchhoff formula (dashed line).

Moriarty and Hansen pointed out also that for large angles of attack, an always-positive square root of f is not able to reproduce all the static aerodynamic polars. For this reason, to reproduce the entire aerodynamic polars, the sign of the effective separation point is preserved and introduced in the equations of the Kirchhoff theory, which are modified as follows:

$$C_n = C_{n\alpha}(\alpha - \alpha_0)\left(\frac{1 + \text{sign}(f_n)\sqrt{\text{abs}(f_n)}}{2}\right)^2 , \tag{2.86}$$

$$C_c = \eta_e C_{n\alpha}(\alpha - \alpha_0)\,\text{sign}(f_c)\sqrt{\text{abs}(f_c)}\,\tan\alpha\,. \tag{2.87}$$

Normal force component

According to the original BL model, the circulatory force needs some modifications to include the effect of the lagged boundary layer response, whose details and dynamics cannot be solved accurately by the grid resolutions generally used by the generalised actuator disc models in CFD simulations.

As a first step, an effective location of the separation under unsteady conditions is interpolated on the $\alpha - f_n$ curve in correspondence of an effective incidence α_f incorporating the unsteady pressure response. For this purpose, an effective C_n' is evaluated by means of a first-order lag on C_n^{pot}:

$$C_n' = C_n^{pot} - D_p\,, \tag{2.88}$$

$$D_{p_n} = D_{p_{n-1}} \exp\left(-\frac{\Delta s}{T_p}\right) + \left(C_n^{pot}{}_{,n} - C_n^{pot}{}_{,n-1}\right)\exp\left(-\frac{\Delta s}{2T_p}\right), \tag{2.89}$$

where D_p is the deficiency function of the normal force coefficient, and T_P is the time constant that regulates the leading-pressure gradient

response, *i.e.* the boundary layer time constant, and its value should be extracted from a tuning on experimental data, if available.

After having evaluated C'_n, the effective incidence α_f can be expressed as:

$$\alpha_f = \frac{C'_n}{C^c_{n\alpha}/\beta_M} + \alpha_0 \,. \tag{2.90}$$

Given the effective value of the separation point $f' = f_n(\alpha_f)$, a definitive separation point location f'' is then used in Equation 2.86. Its expression is found by considering the additional delays in the boundary layer response given by the deficiency function D_f and regulated by the time constant T_f, which is associated with the separation point motion along the airfoil. Analogously to previous steps, one has:

$$f'' = f' - D_f \,, \tag{2.91}$$

$$D_{f_n} = D_{f_{n-1}} \exp\left(-\frac{\Delta s}{T_f}\right) + \left(f'_n - f'_{n-1}\right) \exp\left(-\frac{\Delta s}{2T_f}\right). \tag{2.92}$$

Even if only a starting value T_{f0} is provided to the model, the time constant T_f is modified, depending if the flow is separating or reattaching, by means of the variable σ_1, as follows:

$$T_f = \frac{T_{f0}}{\sigma_1} \,. \tag{2.93}$$

The modifications of σ_1 are the ones indicated in the reference paper [142] and are illustrated in the Appendix A.

Finally, the total normal force coefficient including the effect of the trailing edge separation is given by:

$$\begin{aligned} C_n^{fs} &= C_n^{fs,c} + C_n^{pot,nc} = \\ &= C_n^{pot,c} \left(\frac{1 + \text{sign}(f'')\sqrt{\text{abs}(f'')}}{2} \right)^2 + C_n^{pot,nc} \,. \end{aligned} \tag{2.94}$$

Chordwise force component

As stated above, to correctly estimate the chordwise force coefficient, a different separation curve f_c is used. Once the final delayed effective value of the separation point f'' is estimated, one should invert the f_n curve in correspondence of the f'' value, to finally evaluate the value of the f_c curve in correspondence of the angle $\alpha(f'') = f_n^{-1}(f'')$.

However, given the fact that the full $f_n(\alpha)$ function is not injective (it is approximately symmetric around the zero-lift angle), a local inversion in the region close to the central maximum is problematic. We tried to implement different iterative procedures to extract the effective delayed angle of attack in correspondence of f'' , on the actual side of the curve, but all proved to be rather unstable and unreliable. To overcome this critical issue, inspired by the work of Sheng et al., 2008 [141], we defined a first-order lag acting directly on the effective angle α_f, in the same fashion of the rationale behind all the model. We thus defined an

angle α'' such that:

$$\alpha'' = \alpha_f - D_\alpha \,, \tag{2.95}$$

$$D_{\alpha_n} = D_{\alpha_{n-1}} \exp\left(-\frac{\Delta s}{T_f}\right) + \left(\alpha_{f_n} - \alpha_{f_{n-1}}\right) \exp\left(-\frac{\Delta s}{2T_f}\right). \tag{2.96}$$

where T_f is the same time constant regulating the boundary layer delay in Equation 2.91. We thus assumed that, locally, the approximation $\alpha(f'') \approx \alpha''$ holds and that also the dynamics of the delayed effective angle of attack is controlled by T_f.
The method provides a stable estimate of the real delayed effective angle of attack and has proved to provide accurate results, when tested in the regions in which the α-oscillations take place entirely in injective regions of the $f(\alpha)$ function.

Alternative procedures define distinct effective separation points for the normal and chordwise components and for the pitching moment by means of formulations similar to Equation 2.91. However, in these cases, new time constants need to be defined to control the delay dynamics of the auxiliary separation variables, and additional uncertainty is introduced by additional tuning of the new semi-empirical constants.

Once obtained the value of the *chordwise-defined* separation point location $f_c'' = f_c(\alpha'')$, the total chordwise force coefficient is:

$$C_c^{fs} = \eta_e C_c^{pot} \eta_e \,\mathrm{sign}(f_c'') \sqrt{\mathrm{abs}(f_c'')} \,. \tag{2.97}$$

Pitching moment

To determine the total value of the pitching moment, including the effects of the unsteady separation at the trailing edge, we decided to adopt the method proposed by Leishman, 2011 [149], according to which, the expression in Equation 2.83 remains unaltered except for the value of the aerodynamic centre x_{ac}, that is substituted by the position from the leading edge of the centre of pressure $\hat{x}_{cp}$. However, instead of using a best-fit curve from experimental data, we decided to use a look-up table defined by the static aerodynamic data, according to the relation:

[149]: Leishman (2011), *Final report: assessment of 'Aerodyn' theory basis including unsteady aerodynamics modules*

$$\hat{x}_{cp} = 0.25 - \frac{C_m^{st} - C_{m0}}{C_n^{st}} \,, \tag{2.98}$$

where the subscript *st* denotes the tabulated airfoil data. The use of such a defined parameter allows the model to recover also the data of the pitching moment coefficient in steady cases, without noncirculatory effects.

Also in this case, given the non-injectivity of the $\hat{x}_{cp}(\alpha)$ function, the model uses the angle α'' to interpolate the delayed effective centre of pressure position. As a result, the expression of the total pitching moment becomes:

$$\begin{aligned} C_m^{fs} &= C_m^{fs,c} + C_m^{pot,nc} = \\ &= C_{m0} - \frac{C_{n\alpha}}{\beta_M} \phi_\alpha^c (\hat{x}_{cp} - 0.25) + C_{m_\alpha}^{nc} + C_{m_q}^{c} + C_{m_q}^{nc} \,. \end{aligned} \tag{2.99}$$

Dynamic stall

The final module includes the effects induced by the formation of a leading-edge vortex that originates, convects along the airfoil, and then detaches.

First of all, a criterion to establish when the vortex starts to build up is needed. Although different conditions have been proposed in the literature [141], we decided to maintain the criterion defined in the original work of Beddoes and Leishman. According to it, the vorticity starts to accumulate and its contribution to the aerodynamic response starts to be present, when the following conditions are satisfied:

$$C_n' > C_{n1} \quad \text{for} \quad \alpha \geq \alpha_0 \,, \tag{2.100}$$

$$C_n' < C_{n2} \quad \text{for} \quad \alpha \leq \alpha_0 \,, \tag{2.101}$$

where C_{n1} and C_{n2} are airfoil-dependent parameters, that are taken in this work equal to the value of the static normal force data in correspondence of the break of the chordwise force at the onset of stall. Usually, these values are close to the normal force at the positive and negative stalls.

Once determined that the leading-edge separation is taking place, a nondimensional time variable τ_V is introduced to track the position of the vortex along the upper surface of the airfoil from a certain time t_0 to time t:

$$\tau_V = \frac{1}{c/2} \int_{t_0}^{t} U dt \,. \tag{2.102}$$

This variable is such that if $\tau_V = 0$, the vortex is at the leading edge; if $\tau_V = T_{VL}$, the vortex is at the trailing edge; if $\tau_V > T_{VL}$, the vortex has been shed in the wake, and so vorticity is no longer accumulated. The time constant T_{VL} regulates the vortex advection and represents the nondimensional time that it takes for the vortex to travel from the leading edge to the trailing edge of the airfoil. Although its value should be tuned, as the other parameters, on the basis of experimental measurements, it has been demonstrated that the vortex convection speed is quite general and approximately equal to one-half/one-third of the free-stream velocity [94, 146], which makes the time constant belonging to the range $T_{VL} \in [6, 13]$.

Finally, it is important to underline that multiple shedding can take place at a certain shedding frequency, that is defined in the original BL model by the Strouhal number whose Mach-independent value is $St_{sh} \approx 0.19$. According to the model, the nondimensional time constant τ_V should be reset to null value, each time it reaches the value $T_{VL}+T_{sh}$, where the period T_{sh} is defined as:

$$T_{sh} = 2\frac{1 - f''}{St_{sh}} \tag{2.103}$$

[150]: Rocchio et al. (2020), 'A simple model for deep dynamic stall conditions'

Despite being questioned in the recent literature [150], the model provides a simple, effective, and widely used approach to determine the conditions for multiple shedding. For these reasons, we decided to maintain these indications also in our methodology.

Once defined the physical conditions identifying the different stages of the dynamic stall, we define in the following the values assumed by the force and moment coefficients according to the parameters introduced.

Normal force component

When dynamic stall is taking place and the vortex is on the profile, *i.e.* C_n' condition satisfied and $\tau_V \in [0, T_{VL}]$, the normal force component receives an additional contribution regulated by another first-order time lag and depending on the accumulated vorticity at the leading-edge vortex. This contribution, always of the same sign of C_n^{fs}, is expressed as:

$$C_{n,n}^{v} = C_{n,n-1}^{v} \exp\left(-\frac{\Delta s}{T_V}\right) + (C_{V_n} - C_{V_{n-1}}) \exp\left(-\frac{\Delta s}{2T_V}\right), \quad (2.104)$$

where the term C_V represents the additional normal force contribution, proportional to the difference between the circulatory components of the normal force in the attached and the separated conditions:

$$C_V = C_n^{pot,c} - C_n^{fs,c} = C_n^{pot,c} \left[1 - \left(\frac{1 + \text{sign}(f'')\sqrt{\text{abs}(f'')}}{2}\right)^2\right], \quad (2.105)$$

and with T_V being the time constant related to the decay of the vortex lift. As in the case of T_f, the initial value of this time constant T_{V0} is modified, depending on the different phases of the vortex evolution, by means of a variable σ_3, as follows:

$$T_V = \frac{T_{V0}}{\sigma_3}. \quad (2.106)$$

The modifications of σ_3 are the ones indicated in the reference paper [142] and are illustrated in the Appendix A.

On the other hand, when dynamic stall is not taking place or when the vortex has left the airfoil, $\tau_V > T_{VL}$, no additional contribution to the normal force should be considered, and an accelerated decay should be imposed on C_n^v, taking into account the missing vorticity from the eventual previous leading-edge vortices. Under these conditions, the dynamic stall contribution must be written as:

$$C_{n,n}^{v} = C_{n,n-1}^{v} \exp\left(-\frac{\Delta s}{T_{V0}/\sigma_3}\right) \quad \text{with} \quad \sigma_3 = 2, \quad (2.107)$$

where the halved time constant considers the accelerated vorticity decay, at twice the original pace, when there is no vorticity accretion.

In the end, the final total normal force coefficient is given by the sum:

$$C_n = C_n^{fs} + C_n^{v}. \quad (2.108)$$

Chordwise force component

The original work of Beddoes and Leishman does not provide a formulation for the C_c^v component. Different models have been proposed during the years, even by Beddoes and Leishman themselves, but, in order to avoid the definition of additional best-fit curves for C_c, as done in some works, we preferred to adopt the method presented by Pierce, 1996 [151] and also adopted in the reference paper [142], in which:

[151]: Pierce (1996), 'Wind turbine load prediction using the Beddoes-Leishman model for unsteady aerodynamics and dynamic stall'

$$C_c^v = C_n^v \tan(\alpha_e) \left(1 - \frac{\tau_V}{T_{VL}}\right) . \tag{2.109}$$

In the end, the final total chordwise force coefficient is given by the sum:

$$C_c = C_c^{fs} + C_c^v . \tag{2.110}$$

Pitching moment

Finally, to express the additional contribution from the dynamic stall process to the pitching moment with respect to the quarter of chord, Leishman, 2011 [149] proposed a simple and efficient model expressing the pitching moment during the vortex advection as:

$$C_m^v = -\hat{x}_{cp}^v C_n^v , \tag{2.111}$$

where the distance $\hat{x}_{cp}^v$ of the centre of pressure from the quarter of chord is given by:

$$\hat{x}_{cp}^v = \bar{\bar{x}}_{cp} \left[1 - \cos\left(\frac{\pi \tau_V}{T_{VL}}\right)\right] , \tag{2.112}$$

with $\bar{\bar{x}}_{cp}$ being an airfoil-dependent constant, usually set at 0.2.

In the end, the final total pitching moment coefficient is given by the sum:

$$C_m = C_m^{fs} + C_m^v . \tag{2.113}$$

3 The Structural Model

This chapter presents the details of the structural model we adopt in our FSI method.

Our interest was to implement a model of FSI more concerned with fluid mechanics rather than with a detailed structural dynamics. Hence, we have decided to describe the structural behaviour by observing the dynamics of the blades only. We modelled them as independent cantilevered beams, whose roots are fixed in time at the hub, under the effects of gravity, inertia and aerodynamics. The model does not take into account the motion of the other parts of the structure, because blades are the most relevant components in the wind turbine structural response for what concerns the interaction with the fluid, as suggested in other studies [74] [152], and also the most flexible ones.

In the following, as a start, we derive the governing equations of the structural dynamics from the Cauchy's equation, without inertial effects. We then take into account the effects of the inertia forces, as prescribed by the principle of D'Alembert. Later, we consider beam elemental shape functions for a linear description of the structural dynamics, in accordance with the procedure of the Finite Element Method (FEM), and we deduce the expressions for the generalised loads. Then, we present the modal method and we derive the inertial coupling terms according to it, including also the effect of the centre of mass offset. Next, we make a brief comment on the linearity assumptions that limit the structural configuration and the definition of the loads. Finally, we present some of the most widespread numerical methods that we considered for the time advancement of the structural dynamics, explaining why we have chosen the generalised-α method.

[152]: Hansen (2007), 'Aeroelastic instability problems for wind turbines'

The LM 107.0 P is one of the biggest single-components ever built. It will be installed on GE's Haliade-X 12-MW offshore wind turbine. The credits for the image above the chapter title go to LM Wind Power.

3.1 Structural Dynamics Model

We derive here the general equations for a body undergoing deformation under dynamic loading by means of the weak formulation of the *Cauchy's equation* [153], also known as *virtual work principle*.
An alternative procedure that starts from first principles, and uses the Lagrange's equations for an elastic body, can be carried out and it brings to the same final equations [154].

[153]: Morino et al. (1977), 'FCAP—A new tool for the performance and structural analysis for complex flexible aircraft with active control'
[154]: Przemieniecki et al. (1968), *Theory of matrix structural analysis*

By multiplying the Cauchy's equation by a virtual displacement $\delta\boldsymbol{x}$, we obtain the fully-coupled equations of rigid-body and structural dynamics for a flexible body:

$$\iiint_{\mathscr{V}_s} \rho_s \boldsymbol{a}_s \cdot \delta\boldsymbol{x}\,\mathrm{d}\mathscr{V} = \iiint_{\mathscr{V}_s} \rho_s \boldsymbol{f}_s \cdot \delta\boldsymbol{x}\,\mathrm{d}\mathscr{V} + \iint_{\mathscr{S}_s} \boldsymbol{t}_s \cdot \delta\boldsymbol{x}\,\mathrm{d}\mathscr{S} + - \iiint_{\mathscr{V}_s} \boldsymbol{T}_s : \delta\boldsymbol{E}\,\mathrm{d}\mathscr{V}, \quad (3.1)$$

where ρ_s is the body density, $\boldsymbol{a}_s$ is the body acceleration, $\boldsymbol{f}_s$ and $\boldsymbol{t}_s$ are the external forces per unit volume and surface, $\boldsymbol{T}_s$ is the stress tensor in the body, and $\delta\boldsymbol{E}$ is the virtual strain increment tensor.
From now on in this chapter, we neglect for ease of notation the pedix s, which states that the quantities are referred to the structure.

We then express the virtual displacement $\delta\boldsymbol{x}$ for an unconstrained flexible body as:

$$\delta\boldsymbol{x} = \delta\boldsymbol{x}_G + \delta\boldsymbol{\theta} \times \boldsymbol{r} + \sum_{n=1}^{\infty} \delta q_n \boldsymbol{\psi}^n, \quad (3.2)$$

where $\delta\boldsymbol{x}_G + \delta\boldsymbol{\theta} \times \boldsymbol{r}$ is the virtual rigid-body motion of a general point at distance $\boldsymbol{r}$ from the centre of mass $\boldsymbol{x}_G$, made up of a translational part and a (rigid) rotational part. The last contribution is given by the virtual elastic deformation $\delta\boldsymbol{d}$, described as a linear combination of shape functions $\boldsymbol{\psi}^n(\boldsymbol{x})$, regulated by the generalised coordinates $\delta q_n(t)$.

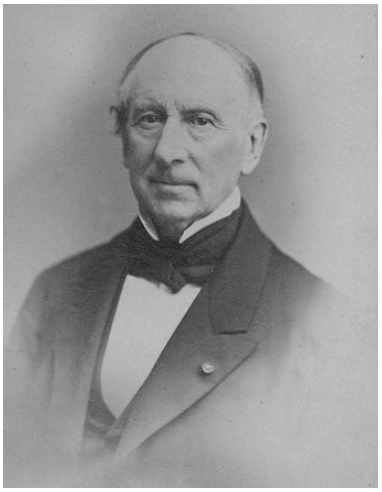

Figure 3.1: Augustin-Louis Cauchy (Parigi 1789 - Sceaux 1857)

By introducing Equation 3.2 in Equation 3.1, the arbitrary virtual rigid-body displacement gives the *translational* and *rotational rigid-body motion dynamics equations*, which include in general the coupling with the elastic motion and are:

$$m\frac{\mathrm{d}\boldsymbol{v}_G}{\mathrm{d}t} = \boldsymbol{f}_T, \quad (3.3)$$

$$\frac{\mathrm{d}\boldsymbol{h}_G}{\mathrm{d}t} = \boldsymbol{m}_G, \quad (3.4)$$

with m being the total mass of the body, $\boldsymbol{v}_G$ being the velocity of the centre of mass, $\boldsymbol{f}_T$ and $\boldsymbol{m}_G$ being the total external forces and moments and $\boldsymbol{h}_G$ being the angular momentum of the flexible body.

In the definition of our wind turbine structural model, we did not consider the first equation and we considered only a simplified version of the rotational equilibrium for the entire rotor.

In fact, we neglected the full two-way coupling between rigid-body motion and structural dynamics, by assuming a fixed polar mass moment of inertia in the time derivative of the angular momentum (see Equation 2.46). As a result, we decided to ignore the influence of the flexibility on the angular momentum in the rotational equation, to obtain a simpler one-way coupling model, which is meaningful for typical values of angular speed and angular acceleration of the wind turbines' rotor, and still capable of sensing the inertial forces in the elastic dynamics.

The assumptions of linearity in the constitutive and the kinematic relationships allow us to reduce the elastic part of the Cauchy's equation to the classic equation of the linear structural dynamics:

$$\mathbf{M}\ddot{\boldsymbol{q}} + \mathbf{C}\dot{\boldsymbol{q}} + \mathbf{K}\boldsymbol{q} = \boldsymbol{e}, \tag{3.5}$$

where $\mathbf{M}$ is the mass matrix, $\mathbf{C}$ is the damping matrix, $\mathbf{K}$ is the stiffness matrix, $\boldsymbol{e}$ are the generalised loads and $\boldsymbol{q}$ are the generalised coordinates that describe the structure according to the relation:

$$\boldsymbol{d}(\boldsymbol{x}, t) = \sum_{n=1}^{\infty} q_n(t)\boldsymbol{\psi}^n(\boldsymbol{x}), \tag{3.6}$$

with $\boldsymbol{d}(\boldsymbol{x}, t)$ being the three-dimensional displacement vector of the continuous structure.

3.2 Uncoupled Structural Dynamics

As a start, we derive the formulation of the structural dynamics for an elastic body without the coupling with the rigid-body motion. In these conditions, the structure does not feel any inertial effect, and the only acceleration of the body is due to the time variation of the deformation. In the following, we present the formulation of each of the terms in Equation 3.5.

Mass matrix

In this case, by ignoring the rigid contribution to the virtual displacement, we can express the body acceleration as only due to the deformation $\mathrm{D}\boldsymbol{v}/\mathrm{Dt} = \sum_{m=1}^{\infty} \ddot{q}_m \boldsymbol{\psi}^m$, and so we have that:

$$\begin{aligned}
\iiint_{\mathscr{V}} \rho \boldsymbol{a} \cdot \delta\boldsymbol{d} \,\mathrm{d}\mathscr{V} &= \sum_{n=1}^{\infty} \delta q_n \iiint_{\mathscr{V}} \rho \frac{\mathrm{D}\boldsymbol{v}}{\mathrm{Dt}} \cdot \boldsymbol{\psi}^n \,\mathrm{d}\mathscr{V} = \\
&= \sum_{n=1}^{\infty} \delta q_n \sum_{m=1}^{\infty} \left(\iiint_{\mathscr{V}} \rho \boldsymbol{\psi}^m \cdot \boldsymbol{\psi}^n \,\mathrm{d}\mathscr{V} \right) \ddot{q}_m = \\
&= \sum_{n=1}^{\infty} \delta q_n \sum_{m=1}^{\infty} \mathrm{M}_{mn} \ddot{q}_m,
\end{aligned} \tag{3.7}$$

where M_{mn} is the (m, n)-th element of the *mass matrix* $\mathbf{M}$ and we neglected all the time and space dependencies for ease of reading.

It is evident, because of the properties of the scalar product, that the mass matrix satisfies the condition of symmetry $\mathrm{M}_{mn} = \mathrm{M}_{nm}$. Moreover, the matrix must satisfy certain properties such as:

Conservation. At least the total element mass should be conserved, in order for the linear momentum to be conserved by applying a uniform translational velocity.

Positive definiteness. The mass matrix is definite positive, or at least it must be non-negative, given the fact that we can express the kinetic energy as one half of the quadratic form $\boldsymbol{q}^T\mathbf{M}\boldsymbol{q}$, that is zero only for $\boldsymbol{q} = 0$.

Physical symmetry. The existence of some kind of symmetry must be evident also in the mass matrix elements.

Stiffness matrix

Similarly to the procedure carried out for the mass matrix, we have that:

$$\iiint_{\mathscr{V}} \boldsymbol{T} : \delta\boldsymbol{E}\,\mathrm{d}\mathscr{V} = \sum_{n=1}^{\infty} \delta q_n \iiint_{\mathscr{V}} \boldsymbol{T} : \boldsymbol{\nabla}\boldsymbol{\psi}^n\,\mathrm{d}\mathscr{V}. \tag{3.8}$$

Because of the symmetry of $\boldsymbol{T}$, only the symmetric part of $\boldsymbol{\nabla}\boldsymbol{\psi}^n$ is filtered by the Frobenius inner product.

If the body is made of an elastic material, the internal energy is given by the *elastic energy* $e(\boldsymbol{E})$ only, and it is possible to show that Equation 3.8 can be expressed as:

$$\sum_{n=1}^{\infty} \delta q_n \iiint_{\mathscr{V}} \boldsymbol{T} : \boldsymbol{\nabla}\boldsymbol{\psi}^n\,\mathrm{d}\mathscr{V} = \sum_{n=1}^{\infty} \delta q_n \frac{\partial}{\partial q_n}\mathscr{E}, \tag{3.9}$$

where $\mathscr{E} = \frac{1}{2}\iiint_{\mathscr{V}} \tau_{ij}\epsilon_{ij}\,\mathrm{d}\mathscr{V}$ is the *total elastic energy*.

If we consider a linear elastic material, the stress tensor τ_{ij} is proportional to the deformation tensor $\tau_{ij} = C_{ijkm}\epsilon_{km}$ by means of the fourth-order *stiffness tensor* C_{ijkm} and so Equation 3.9 becomes:

$$\begin{aligned}\iiint_{\mathscr{V}} \boldsymbol{T} : \delta\boldsymbol{E}\,\mathrm{d}\mathscr{V} &= \sum_{n=1}^{\infty} \delta q_n \frac{\partial}{\partial q_n}\mathscr{E} = \\ &= \sum_{n=1}^{\infty} \delta q_n \sum_{m=1}^{\infty} \iiint_{\mathscr{V}} \frac{1}{4}\left(\psi^n_{i,j} + \psi^n_{j,i}\right) C_{ijkl}\left(\psi^m_{k,l} + \psi^m_{l,k}\right)\mathrm{d}\mathscr{V} = \\ &= \sum_{n=1}^{\infty} \delta q_n \sum_{m=1}^{\infty} \mathrm{K}_{nm} q_m,\end{aligned} \tag{3.10}$$

where $\psi^n_{i,j}$ is the j-th derivative of the i-th component of the n-th shape function and K_{nm} is the (n, m)-th component of the *stiffness matrix* $\mathbf{K}$.

Also the stiffness matrix must satisfy some properties:

Matrix Symmetry. Given the symmetry of the fourth-order tensor C_{ijkl} for the elastic bodies, the expression in Equation 3.10 is

completely symmetric with respect to the indices n and m. Thus, the matrix $\mathbf{K}$ is symmetric.

Positive Semi-Definiteness. Given the definition of the stiffness matrix, it is easy to show that, in the case of linear elastic material, the total elastic energy is one half of the quadratic form $\boldsymbol{q}^T\mathbf{K}\boldsymbol{q}$. This is always positive, except in the case of rigid body motion, which does not produce strain energy. Thus, the stiffness matrix is only semi-definite positive.

Physical symmetry. As in the case of the mass matrix, any sort of physical symmetry of the system must be observable also in the structure of the stiffness matrix.

Generalised loads

For what concerns the first and the second term of the right-hand side of Equation 3.1, we can group them in a single term. Hence, we have a contribution from the *surface loads*, *e.g.* the aerodynamic loads, and another one from the volume forces, *e.g.* the gravity load. Thus, we have that:

$$\begin{aligned}\iiint_{\mathscr{V}} \rho\boldsymbol{f}\cdot\delta\boldsymbol{x}\,\mathrm{d}\mathscr{V} + \iint_{\mathscr{S}} \boldsymbol{t}\cdot\delta\boldsymbol{x}\,\mathrm{d}\mathscr{V} &= \\ = \sum_{n=1}^{\infty}\delta q_n\left(\iiint_{\mathscr{V}}\rho\boldsymbol{f}\cdot\boldsymbol{\psi}^n\,\mathrm{d}\mathscr{V} + \iint_{\mathscr{S}}\boldsymbol{t}\cdot\boldsymbol{\psi}^n\,\mathrm{d}\mathscr{S}\right) &= \\ = \sum_{n=1}^{\infty}\delta q_n e_n.\end{aligned} \tag{3.11}$$

The projection e_n of the surface and volume forces on the n-th shape function is called *generalised load*.

Damping matrix

In general, for a viscoelastic material, the stress tensor can be divided into two parts: a part that is responsible for the reversible deformation described by the stiffness matrix, and another part that is related to the structural damping.

Several models exist to describe the behaviour of the inner viscous forces, and they can be taken into account generally by adding to the equation of the structural dynamics a damping matrix $\mathbf{D}$ acting on the time derivative of the generalised DOFs. As a result, the principle of virtual displacement finally becomes:

$$\sum_{n=1}^{\infty}\delta q_n\left[\mathrm{M}_{nm}\ddot{q}_m + \mathrm{D}_{nm}\dot{q}_m + \mathrm{K}_{nm}q_m - \mathrm{e}_n\right] = 0. \tag{3.12}$$

By virtue of the universality of the virtual displacement δq_n, the general equation of the uncoupled structural dynamics in matrix form are:

$$\mathbf{M}\ddot{\boldsymbol{q}} + \mathbf{D}\dot{\boldsymbol{q}} + \mathbf{K}\boldsymbol{q} = \boldsymbol{e}. \tag{3.13}$$

Uncoupled structural eigenproblem

Neglecting at first the structural damping, it is possible to associate to Equation 3.13 the *generalised eigenproblem*:

$$\mathbf{K}\boldsymbol{Z}^n = \lambda_n \mathbf{M}\boldsymbol{Z}^n, \tag{3.14}$$

where λ_n and $\boldsymbol{Z}^n$ are respectively the n-th eigenvalue and eigenfunction.

Given the properties of positivity and symmetry of the mass and stiffness matrices, it is possible to demonstrate that the eigenvalues are all real and positive (zero only for rigid-body motion) and the eigenfunctions are all real. Finally, it is possible to show that the eigenfunctions are M- and K-orthonormal, *i.e.*

$$\boldsymbol{Z}^{mT}\mathbf{M}\boldsymbol{Z}^n = \delta_{mn} m_n, \qquad \boldsymbol{Z}^{mT}\mathbf{K}\boldsymbol{Z}^n = \delta_{mn} k_n. \tag{3.15}$$

It is possible to normalise the eigenfunctions in several ways. Among them, the *mass normalisation* approach transforms the mass matrix in an identity matrix and the stiffness matrix in a diagonal matrix in which the terms on the diagonal are the eigenvalues:

$$\frac{\boldsymbol{Z}^{mT}}{\sqrt{m_n}}\mathbf{M}\frac{\boldsymbol{Z}^n}{\sqrt{m_n}} = \delta_{mn}, \qquad \frac{\boldsymbol{Z}^{mT}}{\sqrt{m_n}}\mathbf{K}\frac{\boldsymbol{Z}^n}{\sqrt{m_n}} = \delta_{mn}\lambda_n. \tag{3.16}$$

The symbols $\overline{\mathbf{M}}$ and $\overline{\mathbf{K}}$ denote the mass and stiffness matrices transformed by the eigenfunctions.

3.3 Inertially-Coupled Structural Dynamics

In the case of a moving flexible body, it is convenient to define an inertial Frame of Reference (FOR) ($\mathscr{R}_e$) and a relative FOR ($\mathscr{R}_E$), moving with respect to the inertial frame with certain angular speed $\boldsymbol{\Omega}$, angular acceleration $\dot{\boldsymbol{\Omega}}$ and translational velocity $\boldsymbol{v}_{O'}$. For example, in the case of the rotating blade of a wind turbine, it is convenient to define a relative FOR rotating about the center of the hub, and whose origin is the root of the blade. In this last FOR, the relative velocity and acceleration are only related to the deformation of the body and are described by the time derivatives of the displacement in Equation 3.6.

Following the approach described in Saltari et al., 2017 and Reschke, 2005 [155, 156], we derive in the following the modified equations for the structural dynamics in the case of a body undergoing deformation under a dynamic loading in a relative FOR, by means of the weak formulation of the Cauchy's equation.

[155]: Saltari et al. (2017), 'Finite-Element-Based Modeling for Flight Dynamics and Aeroelasticity of Flexible Aircraft'
[156]: Reschke (2005), 'Flight loads analysis with inertially coupled equations of motion'

In accordance with the assumption of neglecting the full two-way coupling of structural dynamics with rigid-body motion, we considered the projection of the Cauchy's equation on the elastic virtual – *relative* – displacement only. However, we take into account the effect of the

inertial forces by fully expressing the absolute acceleration of a generic point of the structure in Equation 3.1, as:

$$\boldsymbol{a} = \underbrace{\boldsymbol{a_{rel}}}_{\text{Relative acc.}} + \underbrace{\boldsymbol{a_{O'}}}_{\text{O' acc.}} + \underbrace{\boldsymbol{\Omega} \times (\boldsymbol{\Omega} \times \boldsymbol{r_{rel}})}_{\text{Centrifugal acc.}} + \underbrace{\dot{\boldsymbol{\Omega}} \times \boldsymbol{r_{rel}}}_{\text{Euler acc.}} + \underbrace{2\boldsymbol{\Omega} \times \boldsymbol{v_{rel}}}_{\text{Coriolis acc.}}, \tag{3.17}$$

where $\boldsymbol{r_{rel}}$, $\boldsymbol{v_{rel}}$ and $\boldsymbol{a_{rel}}$ are respectively the position, the velocity and the acceleration of a generic point in $\mathscr{R}_E$, $\boldsymbol{a_{O'}}$ is the acceleration of the origin O' of $\mathscr{R}_E$ with respect to the origin of $\mathscr{R}_e$, $\boldsymbol{\Omega} \times (\boldsymbol{\Omega} \times \boldsymbol{r_{rel}})$ is the centrifugal acceleration, $\frac{\mathrm{d}\boldsymbol{\Omega}}{\mathrm{d}t} \times \boldsymbol{r_{rel}}$ is the Euler acceleration, and $2\boldsymbol{\Omega} \times \boldsymbol{v_{rel}}$ is the Coriolis acceleration.
So, we finally have:

$$\begin{aligned} &\iiint_{\mathscr{V}} \rho \Big[\boldsymbol{a_{rel}} + \boldsymbol{a_{O'}} + \boldsymbol{\Omega} \times (\boldsymbol{\Omega} \times \boldsymbol{r_{rel}}) + \dot{\boldsymbol{\Omega}} \times \boldsymbol{r_{rel}} + 2\boldsymbol{\Omega} \times \boldsymbol{v_{rel}} \Big] \cdot \delta \boldsymbol{d} \, \mathrm{d}\mathscr{V} = \\ &\quad = \iiint_{\mathscr{V}} \rho \boldsymbol{f} \cdot \delta \boldsymbol{d} \, \mathrm{d}\mathscr{V} + \iint_{\mathscr{S}} \boldsymbol{t} \cdot \delta \boldsymbol{d} \, \mathrm{d}\mathscr{S} - \iiint_{\mathscr{V}} \boldsymbol{T} : \delta \boldsymbol{E} \, \mathrm{d}\mathscr{V}. \end{aligned} \tag{3.18}$$

In the case of a wind turbine blade, $\boldsymbol{r_{rel}} = \boldsymbol{R_{O'P}} + \boldsymbol{d}$, $\boldsymbol{v_{rel}} = \dot{\boldsymbol{d}}$, and $\boldsymbol{a_{rel}} = \ddot{\boldsymbol{d}}$, where $\boldsymbol{R_{O'P}}$ is the relative position of a point in the reference configuration and $\boldsymbol{d}$ is the instantaneous displacement with respect to the rotating reference configuration.

Furthermore, our angular momentum model allowed us only to observe angular accelerations parallel to the original angular speed vector $\dot{\boldsymbol{\Omega}} = \dot{\Omega}\hat{\boldsymbol{\Omega}}$, where $\hat{\boldsymbol{\Omega}}$ is the fixed angular speed versor, orthogonal to the rotor plane.

For what concerns the right-hand side of the equation, it is exactly the same of Equation 3.1, except for the fact that here $\delta \boldsymbol{d} = \delta \boldsymbol{r_{rel}}$, and forces and deformations are in this case relative to the moving FOR and so have to be described in $\mathscr{R}_E$.

In the following section, we focus on each single term in the left-hand side of Equation 3.18 to obtain the final elastic equations. A fictitious force corresponds to each of them, according to the D'Alambert's principle, which states that:

Principle 3.3.1 (D'Alambert's principle) *The sum of the differences between the forces acting on a system of mass particles and the time derivatives of the momenta of the system itself projected onto any virtual displacement consistent with the constraints of the system is zero.*

The definition of the inertial generalised forces here follows.

Corollary 3.3.2 (D'Alambert's prin. (Inertial Generalised Forces)) *One can transform an accelerating body into an equivalent static system by adding the so-called* inertial force *and* inertial moment*. The inertial force must act through the center of mass and the inertial moment can act anywhere. The system can then be analysed exactly as a static system subjected to this inertial force and moment and the external forces and moments.*

For the sake of brevity, hereinafter we adopt the following notation:

$$\langle a \rangle = \iiint_{\mathscr{V}} \rho\, a \, \mathrm{d}\mathscr{V}. \tag{3.19}$$

Relative acceleration

Given the fact that Equation 3.6 decomposes the virtual elastic displacement by means of the shape functions, and that the relative acceleration in $\mathscr{R}_E$ is ascribable to the second derivative of the displacement only, the contribution of the relative acceleration can be expressed in the same form of the uncoupled structural dynamics case:

$$\langle \boldsymbol{a_{rel}} \cdot \delta \boldsymbol{d} \rangle = \sum_{n=1}^{\infty} \delta q_n \sum_{m=1}^{\infty} \mathrm{M}_{nm} \ddot{q}_m. \tag{3.20}$$

M_{nm} is the (n, m)-th element of the mass matrix in Equation 3.7.

Origin O' acceleration

The generic acceleration of the origin O' of $\mathscr{R}_E$ in $\mathscr{R}_e$ is:

$$\boldsymbol{a_{O'}} = \frac{\mathrm{d}\boldsymbol{r_{O'}}}{\mathrm{d}t} = \dot{\boldsymbol{\Omega}} \times \boldsymbol{r_{O'}} + \boldsymbol{\Omega} \times (\boldsymbol{\Omega} \times \boldsymbol{r_{O'}}) \tag{3.21}$$

where $\boldsymbol{r_{O'}}$ is the vector $\boldsymbol{OO'}$ that points the point O' from O.
Given the distributive property of the vector product over addition, we grouped the two terms of the origin acceleration with the centrifugal and the Euler accelerations, and so we consider $\boldsymbol{r} = \boldsymbol{r_{O'}} + \boldsymbol{r_{rel}}$ instead of $\boldsymbol{r_{rel}}$ in the next sections.

Centrifugal acceleration

The contributions from the centrifugal acceleration is:

$$\begin{aligned}
&\langle \boldsymbol{\Omega} \times (\boldsymbol{\Omega} \times \boldsymbol{r}) \cdot \delta \boldsymbol{d} \rangle = \\
&\quad = -\sum_{n=1}^{\infty} \delta q_n \left\{ \boldsymbol{\Omega} \cdot \mathrm{sym} \langle (\boldsymbol{r} \cdot \boldsymbol{\psi}^n) \mathbf{I} - \boldsymbol{r} \otimes \boldsymbol{\psi}^n \rangle \, \boldsymbol{\Omega} \right\} = \\
&\quad = -\sum_{n=1}^{\infty} \delta q_n \left\{ \boldsymbol{\Omega} \cdot \mathrm{sym} \langle (\boldsymbol{R_{OP}} \cdot \boldsymbol{\psi}^n) \mathbf{I} - \boldsymbol{R_{OP}} \otimes \boldsymbol{\psi}^n \rangle \, \boldsymbol{\Omega} + \right. \\
&\quad \left. + \sum_{m=1}^{\infty} \left[\boldsymbol{\Omega} \cdot \mathrm{sym} \langle (\boldsymbol{\psi}^m \cdot \boldsymbol{\psi}^n) \mathbf{I} - \boldsymbol{\psi}^m \otimes \boldsymbol{\psi}^n \rangle \, \boldsymbol{\Omega} \right] q_m \right\} = \\
&\quad = \sum_{n=1}^{\infty} \delta q_n \left(-\mathrm{e}^c_n + \sum_{m=1}^{\infty} \mathrm{K}^c_{nm} q_m \right),
\end{aligned} \tag{3.22}$$

where $\boldsymbol{R_{OP}}$ is the undeformed position of the generic point P, e^c_n is the *centrifugal generalised load* and K^c_{nm} is the (n, m)-th element of the *centrifugal stiffening matrix*.

Proof. We start by decomposing the virtual elastic displacement as:

$$\begin{aligned}&\langle \boldsymbol{\Omega}\times(\boldsymbol{\Omega}\times\boldsymbol{r})\cdot\delta\boldsymbol{d}\rangle = \\ &\quad = \sum_{n=1}^{\infty}\delta q_n\langle\boldsymbol{\Omega}\times(\boldsymbol{\Omega}\times\boldsymbol{r})\cdot\boldsymbol{\psi}^n\rangle.\end{aligned}$$

At this point, we leverage the vector triple product formula stating that

$$\boldsymbol{a}\times(\boldsymbol{b}\times\boldsymbol{c}) = (\boldsymbol{a}\cdot\boldsymbol{c})\boldsymbol{b} - (\boldsymbol{a}\cdot\boldsymbol{b})\boldsymbol{c},$$

and, adopting the Einstein notation, we obtain:

$$\begin{aligned}&\langle\boldsymbol{\Omega}\times(\boldsymbol{\Omega}\times\boldsymbol{r})\cdot\boldsymbol{\psi}^n\rangle = \\ &= \langle\Omega_i r_i\Omega_j\left(\psi^n\right)_j - \Omega_i\Omega_i r_j\left(\psi^n\right)_j\rangle = \\ &= \langle\Omega_i\Omega_j r_i\left(\psi^n\right)_j - \Omega_i\Omega_j\delta_{ij}r_j\left(\psi^n\right)_j\rangle.\end{aligned}$$

Considering that $\Omega_i\Omega_j A_{ij} = (\boldsymbol{\Omega}\otimes\boldsymbol{\Omega}) : \mathbf{A} = (\boldsymbol{\Omega}\otimes\boldsymbol{\Omega}) : \mathrm{sym}(\mathbf{A})$ because $\boldsymbol{\Omega}\otimes\boldsymbol{\Omega}$ is symmetric, we have that:

$$\langle\boldsymbol{\Omega}\times(\boldsymbol{\Omega}\times\boldsymbol{r})\cdot\delta\boldsymbol{d}\rangle = \sum_{n=1}^{\infty}\delta q_n\,\boldsymbol{\Omega}\cdot\mathrm{sym}\langle\boldsymbol{r}\otimes\boldsymbol{\psi}^n - (\boldsymbol{r}\cdot\boldsymbol{\psi}^n)\mathbf{I}\rangle\,\boldsymbol{\Omega}.$$

To finally obtain Equation 3.22, the integral above is divided into two parts, given the fact that $\boldsymbol{r}$ is the sum of $\boldsymbol{R_{OP}}$ and $\sum_{m=1}^{\infty} q_m\boldsymbol{\psi}^m$. □

From the expression of the matrix elements, it is evident that $\mathbf{K}^c$ is symmetric. Therefore, if we consider a structural eigenproblem with a modified stiffness matrix $\mathbf{K}+\mathbf{K}^c$, this will still be symmetric and so the eigenvalues and eigenfunctions will still be real and orthonormal.

Moreover, as we expected, the contribution of the centrifugal inertia forces is made of a centrifugal load related to the reference configuration and a stiffening effect related to the angular speed, represented by the symmetric matrix $\mathbf{K}^c$.

Finally, it is possible to demonstrate, similarly to what is done in Saltari et al., 2017 [155], that the contribution of the centrifugal acceleration to the structural dynamics equations can be written as:

$$\langle\boldsymbol{\Omega}\times(\boldsymbol{\Omega}\times\boldsymbol{r})\cdot\delta\boldsymbol{d}\rangle = -\sum_{n=1}^{\infty}\delta q_n\,\boldsymbol{\Omega}\cdot\mathbf{Y}_n\boldsymbol{\Omega}, \tag{3.23}$$

where $\mathbf{Y}_n = \frac{1}{2}\frac{\partial\mathbf{J}}{\partial q_n}$ is the sensitivity tensor, with respect to the n-th generalised coordinate, of the inertia tensor of the body in the deformed configuration $\mathbf{J_O}$, referred to the absolute origin O:

$$\mathbf{J_O} \coloneqq \langle(\boldsymbol{r}\cdot\boldsymbol{r})\mathbf{I} - \boldsymbol{r}\otimes\boldsymbol{r}\rangle. \tag{3.24}$$

Euler acceleration

We can expand the Euler acceleration contribution by means of the triple product expression:

$$\boldsymbol{a} \cdot (\boldsymbol{b} \times \boldsymbol{c}) = \boldsymbol{b} \cdot (\boldsymbol{c} \times \boldsymbol{a}) = \boldsymbol{c} \cdot (\boldsymbol{a} \times \boldsymbol{b}) \,. \tag{3.25}$$

Considering the equation above and the displacement decomposition, we have that:

$$\begin{aligned}
&\langle \left(\dot{\boldsymbol{\Omega}} \times \boldsymbol{r}\right) \cdot \delta \boldsymbol{d} \rangle = \\
&\quad = \sum_{n=1}^{\infty} \delta q_n \left[\dot{\boldsymbol{\Omega}} \cdot \langle (\boldsymbol{R_{OP}} + \boldsymbol{d}) \times \boldsymbol{\psi}^n \rangle \right] = \\
&\quad = \sum_{n=1}^{\infty} \delta q_n \left[\dot{\boldsymbol{\Omega}} \cdot \langle \boldsymbol{R_{OP}} \times \boldsymbol{\psi}^n \rangle + \dot{\boldsymbol{\Omega}} \cdot \sum_{m=1}^{\infty} \langle \boldsymbol{\psi}^m \times \boldsymbol{\psi}^n \rangle q_m \right] = \\
&\quad = \sum_{n=1}^{\infty} \delta q_n \left[\dot{\boldsymbol{\Omega}} \cdot \langle \boldsymbol{R_{OP}} \times \boldsymbol{\psi}^n \rangle - \dot{\boldsymbol{\Omega}} \cdot \sum_{m=1}^{\infty} \boldsymbol{b}_{nm} q_m \right] = \\
&\quad = \sum_{n=1}^{\infty} \delta q_n \left[-\mathrm{e}_n^{Eu} + \sum_{m=1}^{\infty} \mathrm{K}_{nm}^{Eu} \, q_m \right],
\end{aligned} \tag{3.26}$$

where $\boldsymbol{b}_{nm} \coloneqq \langle \boldsymbol{\psi}^n \times \boldsymbol{\psi}^m \rangle$, e_n^{Eu} is the n-th component of the load from the Euler acceleration, and K_{nm}^{Eu} is the (n,m)-th element of the stiffening matrix that stems from the Euler acceleration.

Coriolis acceleration

For the contribution of the Coriolis acceleration, given Equation 3.25 and the displacement and velocity decomposition, we have that:

$$\begin{aligned}
&\langle 2 \, (\boldsymbol{\Omega} \times \boldsymbol{v_{rel}}) \cdot \delta \boldsymbol{d} \rangle = \\
&\quad = \sum_{n=1}^{\infty} \delta q_n \sum_{m=1}^{\infty} \langle 2 \, (\boldsymbol{\Omega} \times \boldsymbol{\psi}^m \dot{q}_m) \cdot \boldsymbol{\psi}^n \rangle = \\
&\quad = \sum_{n=1}^{\infty} \delta q_n \sum_{m=1}^{\infty} 2 \, \boldsymbol{\Omega} \cdot \langle \boldsymbol{\psi}^m \times \boldsymbol{\psi}^n \rangle \dot{q}_m = \\
&\quad = \sum_{n=1}^{\infty} \delta q_n \sum_{m=1}^{\infty} \left[-2 \, \boldsymbol{\Omega} \cdot \boldsymbol{b}_{nm} \right] \dot{q}_m = \\
&\quad = \sum_{n=1}^{\infty} \delta q_n \sum_{m=1}^{\infty} \mathrm{D}_{nm}^{Co} \dot{q}_m,
\end{aligned} \tag{3.27}$$

where $\mathbf{D}_{nm}^{Co}$ is the (n,m)-th element of the damping matrix from the Coriolis acceleration.

Given the properties of the cross product, the Coriolis damping matrix is a skew-symmetric matrix related to the gyroscopic forces. According to [157], for a general linear vibration mechanical system characterised by symmetric and positive mass and stiffness matrices, the skew-symmetry property of the damping matrix guarantees that all the roots of the associated eigenproblem are still real.

[157]: Zhuravlev (2009), 'Spectral properties of linear gyroscopic systems'

General equations of the structural dynamics

By considering Equation 3.20, Equation 3.22, Equation 3.26 and Equation 3.27, we obtain the general equations of the structural dynamics for a flexible body, under linear elasticity assumptions, in the case of coupling with rigid-body motion of the body itself.
Given the universality of the virtual displacement δq_n, one obtains:

$$\mathbf{M}\,\ddot{\boldsymbol{q}} + \left[\mathbf{D} + \mathbf{D}^{Co}\left(\boldsymbol{\Omega}\right)\right]\dot{\boldsymbol{q}} + \left[\mathbf{K} + \mathbf{K}^{c}\left(\boldsymbol{\Omega}\right) + \mathbf{K}^{Eu}(\dot{\boldsymbol{\Omega}})\right]\boldsymbol{q} = \\ = \boldsymbol{e} + \boldsymbol{e}^{c} + \boldsymbol{e}^{Eu}. \quad (3.28)$$

We indicate with $\mathbf{D}^{I} \coloneqq \mathbf{D} + \mathbf{D}^{Co}\left(\boldsymbol{\Omega}\right)$ the *total damping matrix*, with $\mathbf{K}^{I} \coloneqq \mathbf{K} + \mathbf{K}^{c}\left(\boldsymbol{\Omega}\right) + \mathbf{K}^{Eu}(\dot{\boldsymbol{\Omega}})$ the *total stiffness matrix*, and with $\boldsymbol{e}^{I} \coloneqq \boldsymbol{e}^{c} + \boldsymbol{e}^{Eu}$ the *inertial additional loads*.

In the end, the resulting system is similar in the form to the one related to the uncoupled dynamics in Equation 3.13. However, the inertial effects are included in new terms that do not affect the mass properties, but only the damping and stiffening behaviour of the body. Moreover, additional inertial loads act on the structure, due to the fact that $\mathscr{R}_E$ is a non-inertial FOR, moving with certain velocity and acceleration.
By using the introduced notation, we finally have:

$$\mathbf{M}\,\ddot{\boldsymbol{q}} + \mathbf{D}^{I}\,\dot{\boldsymbol{q}} + \mathbf{K}^{I}\,\boldsymbol{q} = \boldsymbol{e} + \boldsymbol{e}^{I}. \quad (3.29)$$

3.4 Discretisation Procedure

In the previous section, we derived the equations of the structural dynamics by means of the weak form of the Cauchy's equation and by expressing the virtual elastic displacement as a linear combination of shape functions. As yet, we did not consider any simplifying assumption in the finite representation of the problem, except for general assumptions regarding the physics of the problem, such as linearity and elasticity of the material.

However, for the practical study of a structural problem, only a finite number of DOFs can be considered according to the method chosen. In this way, an infinite-dimensional linear problem for a continuous structure is transformed into a system of second-order differential equations, which in turn can be solved as an algebraic linear system by means of numerical methods.

In the general *Gal'erkin method*, at first the structure is divided into finite subvolumes, the *finite elements* in which the weak equations are valid; then, the analytical shape of the basis functions, the *shape functions* $\boldsymbol{\psi}^{n}$, is defined according to modelling assumptions that reflect the problem under study. This implicitly defines the generalised coordinates, that thus become the real unknowns of the differential problem. Once solved the equations for a discrete dimension approximation of the global problem, the knowledge of both the generalised coordinates and the shape functions is sufficient to reconstruct the displacement field on the structural mesh and in between the nodal grid points.

The Finite Element Method (FEM) is probably the most widespread procedure in the study of complex structures. According to this method, the generalised coordinates are the nodal displacements of the descrete structure's nodes. In a general 3D space, each node of a *discretised* structure has 3 translational DOFs, but also 3 rotational DOFs. Hence, a structure with N nodes has $6\,N$ DOFs.

Following the definition of the generalised coordinates, the shape functions have to describe the generic deformation in a finite element once given the nodal displacements only. This is done by using *tent functions* that are equal to 1 in the position of the node and 0 otherwise, so that they extract the nodal displacement or rotation of a single node when its position is considered.

In some occasions, it is more convenient to define the structural matrices in a certain local FOR, *e.g* a frame of principal axes, that is not coincident with the global FOR used for the description of the full structure. In these cases, an intermediate step is necessary to convert the local matrices and forces into global ones, by means of rotation matrices.

Once defined the elemental quantities, given the structural data and the topology, an assembling procedure is necessary. In fact, a single edge node is shared by at least two elements, and so some form of compatibility must be enforced to finally obtain a single and unique displacement. After this procedure, given a structure with N nodes, one obtains $6\,N \times 6\,N$-matrices and $6\,N$-arrays that describe the structural dynamics.

In the final step before the numerical solution of the discrete second-order differential system, essentials or Dirichlet boundary conditions on the displacements are considered by removing the equations relative to the known displacements. In these last equations, the real unknowns are the generalised constraint reactions enforcing the constraints on the displacement.

The FEM procedure is thus summarised below (see also Figure 3.2):

1. Definition of the element type.
2. Definition of the local element structural matrices and of the local nodal forces.
3. Definition of the global element structural matrices and of the global nodal forces.
4. Definition of the assembled structural matrices and nodal forces.
5. Application of the boundary conditions.
6. Solution of the structural dynamics equations.

It is important to describe the Finite Element Method and its assumptions, regardless of the approach that will be carried out for the structural dynamics, because, even if we used a modal approach, the definition of the modes comes out from a finite-element model of the structure (steps 1 to 5).

In the following sections, we outline the finite-element model we defined for the description of each wind blade, by taking into consideration mass and stiffness matrix only.

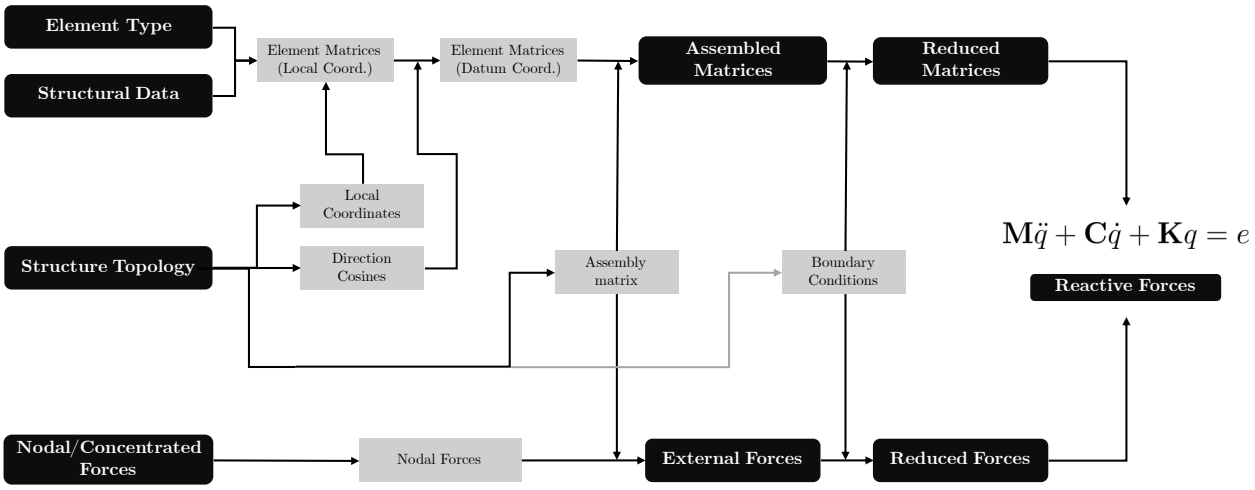

Figure 3.2: Outline of the steps of the Finite Element Method.

Definition of the element type

Different types of element are available in the literature to best fit the structure and its modelling. In the case of the highly slender wind turbine blade, it is common practice to describe its flexural behaviour as the one of an *Euler-Bernoulli beam*.

The *Euler-Bernoulli beam theory* is a simplification of the linear theory of elasticity which provides a means of calculating the load-carrying and deflection characteristics of beams for a one-dimensional problem equivalent to the three-dimensional one. The theory describes the case of beamlike structures subject to lateral loads only under the assumption of small deflections, and it is thus a special case of the *Timoshenko beam theory*, valid for low values of the slenderness ratio.[1]
The main differences between the two most widespread beam theories are that in the Euler-Bernoulli beam theory:

- shear effects are neglected, whereas in the Timoshenko beam theory they are considered;
- beam sections remain perpendicular to the so-called *elastic line*, which is the line that connects the elastic centers of each section along the span of the beam, see Figure 3.3. On the other hand, in the Timoshenko beam theory, the shear deflection is not known a priori;
- only the flexural displacements are needed, because the rotations of the sections are defined by the derivatives along the span of the displacements, in accordance with the hypothesis of plain sections remaining plain. In the Timoshenko beam theory, the shear deflection, approximated by the slope of the deflection, is an additional variable.

1: The *slenderness ratio* is the quotient between the beam thickness of the radius of gyration and the span. The radius of gyration is equal to $r_{gyr} = \sqrt{J/A}$, where J is the second area moment of the cross section and A is the beam section area.

Other than the flexural behaviour in both flapwise and edgewise directions, the complete beam element includes also axial and torsional DOFs that are taken into account in the classical engineering beam theory with simplified models [154].

In the following, we define separately the torsional, flexural and axial

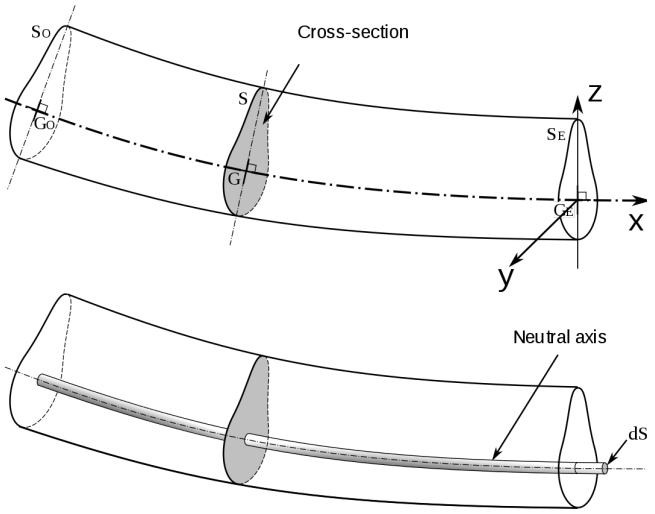

Figure 3.3: Schematic of a cross-section of an Euler-Bernoulli beam, with the neutral axis in evidence.

shape functions for the fundamental 1D beam element of length ℓ and cross-section area A. The element is characterised by two edge nodes, whose DOFs are defined as in Figure 3.4. The local coordinate that locates the generic section on the beam axis is called x.

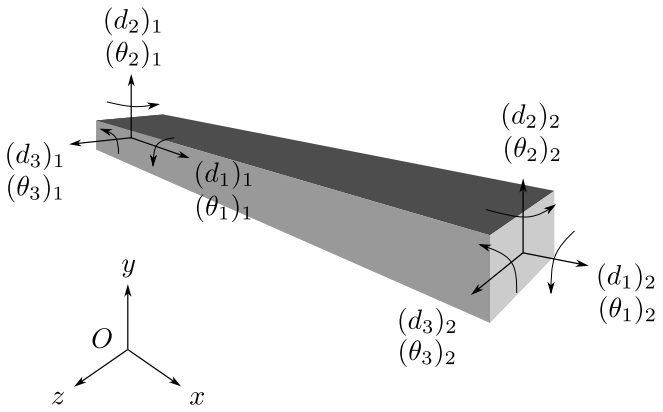

Figure 3.4: Degrees of freedom of a beam element.

1D axial beam element

The axial displacements in correspondence of the two nodes are the only two parameters available to describe the axial displacement for the generic section at position x of an axial beam element. This means that:

$$\boldsymbol{\psi}^e_{ax} = \begin{bmatrix} 1 - \dfrac{x}{\ell} & \dfrac{x}{\ell} \end{bmatrix}. \tag{3.30}$$

It follows that $d_1(0)$ is the axial displacement of the first node and $d_1(\ell)$ is the axial displacement of the second node. Moreover, given Equation 3.7, one obtains that:

$$\mathbf{M}^e_{ax} = \rho A \ell \begin{bmatrix} 1/3 & 1/6 \\ 1/6 & 1/3 \end{bmatrix}. \tag{3.31}$$

To obtain the axial stiffness matrix, one has to consider the generalised constitutive relationship $\boldsymbol{\sigma}^e = E\boldsymbol{\epsilon}^e$ to express the total elastic energy, where $\boldsymbol{\sigma}^e$ is the axial element force N, $\boldsymbol{\epsilon}^e$ is the generalised deformation

$\epsilon_x = \partial d_1/\partial x$, and E is the Young modulus. Given Equation 3.10, one has:

$$\mathbf{K}^e_{ax} = \frac{EA}{\ell}\begin{bmatrix} 1 & -1 \\ -1 & 1 \end{bmatrix}. \tag{3.32}$$

1D torsional beam element

If one observes the axial and torsional vibrations equations of the engineering beam theory, it is possible to notice a similarity in shape that can be leveraged to obtain the mass and stiffness matrix of the torsional beam element.

For the axial equilibrium equation, we have

$$\rho A\frac{\partial^2 d_1}{\partial t^2} - \frac{\partial}{\partial x}\left[EA\frac{\partial d_1}{\partial x}\right] = f_1, \tag{3.33}$$

where f_1 is the external tensile force.
For the torsional equilibrium equation, we have

$$\rho J_x\frac{\partial^2 \theta_1}{\partial t^2} - \frac{\partial}{\partial x}\left[GJ\frac{\partial \theta_1}{\partial x}\right] = c_1, \tag{3.34}$$

where J_x is the polar moment of inertia, G is the shear modulus, J is the torsional constant and c_1 is the external torsional moment.

It is thus evident that the problems are exactly the same, if one substitutes

$$d_1 \leftrightarrow \theta_1, \quad A \leftrightarrow J_x, \quad EA \leftrightarrow GJ, \quad f_1 \leftrightarrow c_1. \tag{3.35}$$

Thus, one obtains the following matrices

$$\mathbf{M}^e_{tor} = \rho J_x \ell \begin{bmatrix} 1/3 & 1/6 \\ 1/6 & 1/3 \end{bmatrix}, \quad \mathbf{K}^e_{tor} = \frac{GJ}{\ell}\begin{bmatrix} 1 & -1 \\ -1 & 1 \end{bmatrix} \tag{3.36}$$

1D bending beam element

For what concerns the flexural behaviour of an Euler-Bernoulli beam, given the cross-section orthogonality assumption, one knows in advance that the rotational field is described by the derivative of the corresponding displacement. This means that

$$\theta_2 = \frac{\partial d_2}{\partial x}, \qquad \theta_3 = -\frac{\partial d_3}{\partial x} \tag{3.37}$$

where the opposite sign in θ_3 definition is evident in Figure 3.4.

For a beam element bending in the plane $x - y$ or $x - z$, the displacements and the rotations in correspondence of the edge nodes 1 and 2 (d_1, θ_1, d_2, θ_2) are the only data available to define the displacement field inside the element. By enforcing the data at the edges by means of polynomial functions of the proper degree,[2] the flexural shape functions

2: Cubic and quadratic polynomials for the displacement and the rotation DOF respectively. The coefficients of the two polynomials are highly connected because of Equation 3.37.

are:

$$\left(\boldsymbol{\psi}_{fl}^{e}\right)^{T} = \begin{bmatrix} 1-3\left(\frac{x}{\ell}\right)^{2}+2\left(\frac{x}{\ell}\right)^{3} & \frac{1}{\ell}\left[-6\left(\frac{x}{\ell}\right)+6\left(\frac{x}{e}\right)^{2}\right] \\ x-2\ell\left(\frac{x}{\ell}\right)^{2}+\ell\left(\frac{x}{\ell}\right)^{3} & 1-4\left(\frac{x}{\ell}\right)-3\left(\frac{x}{\ell}\right)^{2} \\ -3\left(\frac{x}{\ell}\right)^{2}-2\left(\frac{x}{\ell}\right)^{3} & \frac{1}{\ell}\left[6\left(\frac{x}{\ell}\right)-6\left(\frac{x}{e}\right)^{2}\right] \\ -\ell\left(\frac{x}{\ell}\right)^{2}+\ell\left(\frac{x}{\ell}\right)^{3} & -2\left(\frac{x}{\ell}\right)+3\left(\frac{x}{\ell}\right)^{2} \end{bmatrix}. \tag{3.38}$$

The flexural mass matrix is thus:

$$\mathbf{M}_{fl}^{e} = \frac{\rho A\ell}{420}\begin{bmatrix} 156 & 22\ell & 54 & -13\ell \\ 22\ell & 4\ell^{2} & 13\ell & -3\ell^{2} \\ 54 & 13\ell & 156 & -22\ell^{2} \\ -13\ell & -3\ell^{2} & -22\ell^{2} & 4\ell^{2} \end{bmatrix}. \tag{3.39}$$

To obtain the flexural stiffness matrix, one has to consider the generalised constitutive relationship $\boldsymbol{\sigma}^{e} = EI\boldsymbol{\epsilon}^{e}$ to express the total elastic energy, where $\boldsymbol{\sigma}^{e}$ is the bending moment M in the considered plane, EI is the bending stiffness, and $\boldsymbol{\epsilon}^{e}$ is the generalised deformation, the curvature χ in the plane under study.
Given Equation 3.10, and given the fact that the curvature is the second derivative of the displacement in the plane of the bending, one has for the plane $x-y$:

$$\mathbf{K}_{fl}^{e} = \frac{EI}{\ell}\begin{bmatrix} 12 & 6\ell & -12 & 6\ell \\ 6\ell & 4\ell^{2} & -6\ell & 2\ell^{2} \\ -12 & -6\ell & 12 & -6\ell \\ 6\ell & 2\ell^{2} & -6\ell^{2} & 4\ell^{2} \end{bmatrix} \tag{3.40}$$

For the plane $x-z$ the signs of the elements $(2,1)$, $(3,2)$, $(4,1)$, $(4,3)$ and the symmetric ones, are opposite because of the opposite sign in Equation 3.37.

Local elemental matrices: the complete beam element

Once derived the elemental matrices for each single problem of the beam, we can define a complete element state vector as:

$$\begin{aligned}\left(q^{e}\right)^{T} = [&(d_1)_1\,,\,(d_2)_1\,,\,(d_3)_1\,,\,(\theta_1)_1\,,\,(\theta_2)_1\,,\,(\theta_3)_1\,,\\ &(d_1)_2\,,\,(d_2)_2\,,\,(d_3)_2\,,\,(\theta_1)_2\,,\,(\theta_2)_2\,,\,(\theta_3)_2\,]\end{aligned} \tag{3.41}$$

where the external subscript 1 indicates all the DOFs related to the first edge node of the element, and the external subscript 2 indicates those related to the second edge node.

The *complete elemental stiffness matrix* thus becomes Equation 3.42. On the other hand, the *complete consistent elemental mass matrix* becomes Equation 3.43.

$$\mathbf{K}^e = \begin{bmatrix} K_x & 0 & 0 & 0 & 0 & 0 & -K_x & 0 & 0 & 0 & 0 & 0 \\ 0 & 12K_z & 0 & 0 & 0 & 6\ell K_z & 0 & -12K_z & 0 & 0 & 0 & 6\ell K_z \\ 0 & 0 & 12K_y & 0 & -6\ell K_y & 0 & 0 & 0 & -12K_y & 0 & -6K_y & 0 \\ 0 & 0 & 0 & K_\theta & 0 & 0 & 0 & 0 & 0 & -K_\theta & 0 & 0 \\ 0 & 0 & -6\ell K_y & 0 & 4\ell^2 K_y & 0 & 0 & 0 & 6\ell & 0 & 2\ell^2 & 0 \\ 0 & 6\ell K_z & 0 & 0 & 0 & 4\ell^2 K_z & 0 & -6\ell K_z & 0 & 0 & 0 & 2\ell^2 K_z \\ -K_x & 0 & 0 & 0 & 0 & 0 & K_x & 0 & 0 & 0 & 0 & 0 \\ 0 & -12K_z & 0 & 0 & 0 & -6\ell K_z & 0 & 12K_z & 0 & 0 & 0 & -6\ell K_z \\ 0 & 0 & -12K_y & 0 & 6\ell K_z & 0 & 0 & 0 & 12K_y & 0 & 6\ell K_y & 0 \\ 0 & 0 & 0 & -K_\theta & 0 & 0 & 0 & 0 & 0 & K_\theta & 0 & 0 \\ 0 & 0 & -6K_y & 0 & 2\ell^2 K_y & 0 & 0 & 0 & 6\ell K_y & 0 & 4\ell^2 K_y & 0 \\ 0 & 6\ell K_z & 0 & 0 & 0 & 2\ell^2 K_z & 0 & -6\ell K_z & 0 & 0 & 0 & 4\ell^2 K_z \end{bmatrix} \tag{3.42}$$

where $K_x = EA/\ell$, $K_z = EI_z/\ell^3$, $K_y = EI_y/\ell^3$ and $K_\theta = GJ/\ell$.

$$\mathbf{M}_c^e = \rho A\ell \begin{bmatrix} \frac{1}{3} & 0 & 0 & 0 & 0 & 0 & 1/6 & 0 & 0 & 0 & 0 & 0 \\ 0 & \frac{13}{35}+\frac{6M_z}{5\ell} & 0 & 0 & 0 & \frac{11\ell}{210}+\frac{M_z}{10} & 0 & \frac{9}{70}-\frac{6M_z}{5\ell} & 0 & 0 & 0 & -\frac{13\ell}{420}+\frac{M_z}{10} \\ 0 & 0 & \frac{13}{35}+\frac{6M_y}{5\ell} & 0 & -\frac{11\ell}{210}-\frac{M_y}{10} & 0 & 0 & 0 & \frac{9}{70}-\frac{6M_y}{5\ell} & 0 & \frac{13\ell}{420}-\frac{M_y}{10} & 0 \\ 0 & 0 & 0 & \frac{M_\theta}{3} & 0 & 0 & 0 & 0 & 0 & \frac{M_\theta}{6} & 0 & 0 \\ 0 & 0 & -\frac{11\ell}{210}+\frac{M_z}{10} & 0 & \frac{\ell^2}{105}+\frac{2M_y\ell}{15} & 0 & 0 & 0 & -\frac{13\ell}{420}+\frac{M_y}{10} & 0 & -\frac{\ell^2}{140}-\frac{M_y\ell}{30} & 0 \\ 0 & \frac{11\ell}{210}+\frac{M_z}{10} & 0 & 0 & 0 & \frac{\ell^2}{105}+\frac{2M_z\ell}{15} & 0 & \frac{13\ell}{420}-\frac{M_z}{10} & 0 & 0 & 0 & -\frac{\ell^2}{140}-\frac{M_z\ell}{30} \\ \frac{1}{6} & 0 & 0 & 0 & 0 & 0 & \frac{1}{3} & 0 & 0 & 0 & 0 & 0 \\ 0 & \frac{9}{70}-\frac{6M_z}{5\ell} & 0 & 0 & 0 & \frac{13\ell}{420}-\frac{M_z}{10} & 0 & \frac{13}{35}+\frac{6M_z}{5\ell} & 0 & 0 & 0 & -\frac{11\ell}{210}-\frac{M_z}{10} \\ 0 & 0 & \frac{9}{70}-\frac{6M_y}{5\ell} & 0 & -\frac{13\ell}{420}+\frac{M_y}{10} & 0 & 0 & 0 & \frac{13}{35}+\frac{6M_y}{5\ell} & 0 & \frac{11\ell}{210}+\frac{M_y}{10} & 0 \\ 0 & 0 & 0 & \frac{M_\theta}{6} & 0 & 0 & 0 & 0 & 0 & \frac{M_\theta}{3} & 0 & 0 \\ 0 & 0 & \frac{13\ell}{420}-\frac{M_y}{10} & 0 & -\frac{\ell^2}{140}-\frac{M_y\ell}{30} & 0 & 0 & 0 & \frac{11\ell}{210}+\frac{M_y}{10} & 0 & \frac{\ell^2}{105}+\frac{2M_y\ell}{15} & 0 \\ 0 & -\frac{13\ell}{420}+\frac{M_z}{10} & 0 & 0 & 0 & -\frac{\ell^2}{140}-\frac{M_z\ell}{30} & 0 & -\frac{11\ell}{210}-\frac{M_z}{10} & 0 & 0 & 0 & \frac{\ell^2}{105}+\frac{2M_z\ell}{15} \end{bmatrix} \tag{3.43}$$

where $M_z = I_z/(A\ell)$, $M_y = I_y/(A\ell)$ and $M_\theta = J_x/A$.

To simplify the mass matrix expression, the use of the so-called *lumped-mass representation* is widespread in the structural research and industrial community. According to this idealisation, the mass is not distributed uniformly in the element, but instead concentrated masses are located in correspondence of the nodes, where the considered DOFs are located.

The material of the element is redistributed at the edge nodes of the element, and it is assumed that dynamic cross-coupling between the element displacement components and in the resulting mass matrix is neglected. This results in a diagonal elemental mass matrix, that must still satisfy the properties stated in Section 3.2.

Even if, for a limited number of nodes, the use of a lumped-mass matrix produces less accurate results than the case with the full consistent mass matrix, the diagonality of the matrix allows a fast and efficient inversion of the mass matrix.

The lumping process of the mass matrix allows the definition of the following elemental mass matrix for the complete beam element:

$$\mathbf{M}^e = \rho A \ell \begin{bmatrix} \frac{1}{2} & 0 & 0 & 0 & 0 & 0 & 0 & 0 & 0 & 0 & 0 & 0 \\ 0 & \frac{1}{2} & 0 & 0 & 0 & 0 & 0 & 0 & 0 & 0 & 0 & 0 \\ 0 & 0 & \frac{1}{2} & 0 & 0 & 0 & 0 & 0 & 0 & 0 & 0 & 0 \\ 0 & 0 & 0 & \frac{M_\theta}{2} & 0 & 0 & 0 & 0 & 0 & 0 & 0 & 0 \\ 0 & 0 & 0 & 0 & \frac{\ell}{24} & 0 & 0 & 0 & 0 & 0 & 0 & 0 \\ 0 & 0 & 0 & 0 & 0 & \frac{\ell}{24} & 0 & 0 & 0 & 0 & 0 & 0 \\ 0 & 0 & 0 & 0 & 0 & 0 & \frac{1}{2} & 0 & 0 & 0 & 0 & 0 \\ 0 & 0 & 0 & 0 & 0 & 0 & 0 & \frac{1}{2} & 0 & 0 & 0 & 0 \\ 0 & 0 & 0 & 0 & 0 & 0 & 0 & 0 & \frac{1}{2} & 0 & 0 & 0 \\ 0 & 0 & 0 & 0 & 0 & 0 & 0 & 0 & 0 & \frac{M_\theta}{2} & 0 & 0 \\ 0 & 0 & 0 & 0 & 0 & 0 & 0 & 0 & 0 & 0 & \frac{\ell}{24} & 0 \\ 0 & 0 & 0 & 0 & 0 & 0 & 0 & 0 & 0 & 0 & 0 & \frac{\ell}{24} \end{bmatrix}. \tag{3.44}$$

Global elemental matrices

The expressions we obtained for the elemental matrices are relative to a convenient FOR, which is the one formed by the principal axes passing through the centre of mass of the cross section. Moreover, we implicitly assumed that the centre of mass and the elastic centre of the sections are coincident.

In general, however, the convenient frame for the element description is not the global *datum* one that is used for the description of the complete structure. For example, we divide the wind turbine blade into a certain number of chunks, each constituting a beam element. A typical blade has a structural twist angle that varies along the span. So, we assume that the datum rotating frame has its axis coincident with the principal axes of the tip section. In doing so, however, all the other elements have a different orientation that must be considered to take into account the coupling between the flapping in the plane and out of the plane of the rotor.

To take into account a general orientation between the local elemental FOR $\mathcal{R}_{E^e}$ and the datum (*rotating*) FOR $\mathcal{R}_E$, we introduce the coordinate transformation matrix $\boldsymbol{\Xi}^e$ such that $(\boldsymbol{q}^e)_{E^e} = \boldsymbol{\Xi}^e (\boldsymbol{q}^e)_E$. The subscript of a certain array indicates the FOR in which the coordinates of that array are expressed (for further information about coordinate transformation and FORs see Chapter 4). From linear algebra, the matrix transforming the coordinates of a physical 3D vector between two FORs is equal to a 3×3 matrix defined by $(\Xi)_{i,j} = \boldsymbol{E^e}_i \cdot \boldsymbol{E}_j$, where $i, j = 1, 2, 3$ are the versor indices of the respective FORs. Thus, for the complete elemental state vector including all the translation and rotation components of the two nodes, we have that:

$$\boldsymbol{\Xi}^e = \begin{bmatrix} \boldsymbol{\Xi} & \mathbf{0} & \mathbf{0} & \mathbf{0} \\ \mathbf{0} & \boldsymbol{\Xi} & \mathbf{0} & \mathbf{0} \\ \mathbf{0} & \mathbf{0} & \boldsymbol{\Xi} & \mathbf{0} \\ \mathbf{0} & \mathbf{0} & \mathbf{0} & \boldsymbol{\Xi} \end{bmatrix}. \tag{3.45}$$

Given this change of coordinate, the structural dynamics equation for an element described in a datum FOR are:

$$\left[\boldsymbol{\Xi}^{eT} (\mathbf{M}^e)_{E^e} \boldsymbol{\Xi}^e\right] (\ddot{\boldsymbol{q}}^e)_E + \left[\boldsymbol{\Xi}^{eT} (\mathbf{K}^e)_{E^e} \boldsymbol{\Xi}^e\right] (\boldsymbol{q}^e)_E = \boldsymbol{\Xi}^{eT} (\boldsymbol{e}^e)_{E^e}, \tag{3.46}$$

where the matrices $(\mathbf{M}^e)_{E^e}$ and $(\mathbf{K}^e)_{E^e}$, and the array $(\boldsymbol{e}^e)_{E^e}$ are expressed in the local elemental FOR.
From now on, we implicitly assume the local-to-datum coordinate transformation for each element, and we redefine the above equations as:

$$\mathbf{M}^e \ddot{\boldsymbol{q}}^e + \mathbf{K}^e \boldsymbol{q}^e = \boldsymbol{e}^e, \tag{3.47}$$

In the case of our wind blades, given the structural twist angle $\phi(x)$ for each element, the fundamental coordinate transformation matrix is:

$$\boldsymbol{\Xi} = \begin{bmatrix} 1 & 0 & 0 \\ 0 & \cos\phi^e & \sin\phi^e \\ 0 & -\sin\phi^e & \cos\phi^e \end{bmatrix}, \tag{3.48}$$

where ϕ^e is the structural twist angle, which is assumed to be constant in the element and equal to the average value of $\phi(x)$ along the same element.

It is important to underline that, up to now, we have still assumed the lumped masses to be located at the position of the nodes, and the centre of mass to be coincident with the elastic centre for each cross-section.

Assembly of the global matrices

According to FEM, we can approximate the continuous structure as a discrete union of subelements characterised by a specific behaviour. Once the constituting elements are defined, we have to assemble them in a coherent way, such that the boundary displacements and stresses are compatible at least at the common nodes among the elements.

To combine the elemental problems into a single problem, the elemental arrays and matrices are assembled into global ones, where the generalised coordinate vector is now composed of all the DOFs of all the nodes of the assembled structure:

$$\boldsymbol{q}^T = [(d_1)_1\,,\,(d_2)_1\,,\,(d_3)_1\,,\,(\theta_1)_1\,,\,(\theta_2)_1\,,\,(\theta_3)_1\,,\;\ldots \\ (d_1)_N\,,\,(d_2)_N\,,\,(d_3)_N\,,\,(\theta_1)_N\,,\,(\theta_2)_N\,,\,(\theta_3)_N\,]\,, \quad (3.49)$$

where N is the number of nodes, and the coordinates are referred to the global datum coordinate system.

Therefore, for each element, a rectangular matrix $\mathbf{T}^e$ is defined, made of all zeros, except for the unit terms whose positions identify the DOFs of the considered element in the complete state vector in Equation 3.49, such that:

$$\boldsymbol{q}^e = \mathbf{T}^e \boldsymbol{q}. \quad (3.50)$$

Considering the principle of virtual work for the complete structure subdivided into elements, it follows that:

$$\begin{aligned} &\sum_{e=1}^{N_e} \left\{ (\delta \boldsymbol{q}^e)^T \left[\mathbf{M}^e \ddot{\boldsymbol{q}}^e + \mathbf{K}^e \boldsymbol{q}^e - \boldsymbol{e}^e \right] \right\} = 0 \\ &\quad \Longrightarrow \sum_{e=1}^{N_e} \left\{ (\delta \boldsymbol{q})^T \mathbf{T}^{eT} \left[\mathbf{M}^e \mathbf{T}^e \ddot{\boldsymbol{q}} + \mathbf{K}^e \mathbf{T}^e \boldsymbol{q} - \boldsymbol{e}^e \right] \right\} = 0 \\ &\quad \Longrightarrow (\delta \boldsymbol{q})^T \left[\underbrace{\sum_{e=1}^{N_e} \mathbf{T}^{eT} \mathbf{M}^e \mathbf{T}^e}_{\mathbf{M}} \ddot{\boldsymbol{q}} + \underbrace{\sum_{e=1}^{N_e} \mathbf{T}^{eT} \mathbf{K}^e \mathbf{T}^e}_{\mathbf{K}} \boldsymbol{q} - \underbrace{\sum_{e=1}^{N_e} \mathbf{T}^{eT} \boldsymbol{e}^e}_{\mathbf{e}} \right] = 0. \end{aligned} \quad (3.51)$$

where $\mathbf{M}$, $\mathbf{K}$ and $\boldsymbol{e}$ are respectively the *global mass matrix*, the *global stiffness matrix* and the *global nodal loads array* for the entire structure. The number of the elements is indicated as N_e.

Given the universality of the virtual displacement, one has that:

$$\mathbf{M}\ddot{\boldsymbol{q}} + \mathbf{K}\boldsymbol{q} = \boldsymbol{e}. \quad (3.52)$$

The operation to evaluate the global features in Equation 3.51 is equivalent to placing the elemental matrices or arrays in their correct position in the larger framework of the global item, and then summing all the overlapping terms. A similar procedure for the definition of the global structural damping matrix can be carried out.

Loads projection and boundary conditions

For the forces acting on each single element, we define the generalised loads acting on an element as:

$$\boldsymbol{e}^e = \underbrace{\boldsymbol{P}^e}_{\text{Concentrated Loads}} + \underbrace{\iiint_{\mathscr{V}} \rho \boldsymbol{f} \cdot \boldsymbol{\psi}^e \, \mathrm{d}\mathscr{V}}_{\text{Equivalent Volume Loads}} + \underbrace{\iint_{\mathscr{S}} \boldsymbol{t} \cdot \boldsymbol{\psi}^e \, \mathrm{d}\mathscr{S}}_{\text{Equivalent Surface Loads}} . \tag{3.53}$$

We assumed to work with one-dimensional elements and with forces that are only dependent on the span direction. Hence, we can define the surface forces per unit length $\boldsymbol{t}^{2D}$ and the volume forces per unit length $\boldsymbol{f}^{2D}$, such that:

$$\boldsymbol{e}^e = \boldsymbol{P}^e + \int_0^\ell \rho \boldsymbol{f}^{2D} \cdot \boldsymbol{\psi}^e \, \mathrm{d}x + \int_0^\ell \boldsymbol{t}^{2D} \cdot \boldsymbol{\psi}^e \, \mathrm{d}x. \tag{3.54}$$

Furthermore, we assume the forces per unit length to have constant values inside the element, named as $\overline{\boldsymbol{f}^{2D}}$ and $\overline{\boldsymbol{t}^{2D}}$.
The final expression for the elemental loads array in the local FOR is:

$$\boldsymbol{e}^e = \boldsymbol{P}^e + \mathbf{I}_\psi^e \left(\overline{\boldsymbol{f}^{2D}} + \overline{\boldsymbol{t}^{2D}} \right), \tag{3.55}$$

where $\mathbf{I}_\psi^e \coloneqq \int_0^\ell (\boldsymbol{\psi}^e)^T \, \mathrm{d}x$.

For the beam element, using Equation 3.30, Equation 3.38 and considering the order of the DOFs provided by Equation 3.41, the integration gives:

$$\mathbf{I}_\psi^e = \begin{bmatrix} \frac{\ell}{2} & 0 & 0 & 0 & 0 & 0 \\ 0 & \frac{\ell}{2} & 0 & 0 & 0 & -1 \\ 0 & 0 & \frac{\ell}{2} & 0 & 1 & 0 \\ 0 & 0 & 0 & \frac{\ell}{2} & 0 & 0 \\ 0 & 0 & -\frac{\ell^2}{12} & 0 & 0 & 0 \\ 0 & \frac{\ell^2}{12} & 0 & 0 & 0 & 0 \\ \frac{\ell}{2} & 0 & 0 & 0 & 0 & 0 \\ 0 & \frac{\ell}{2} & 0 & 0 & 0 & 1 \\ 0 & 0 & \frac{\ell}{2} & 0 & -1 & 0 \\ 0 & 0 & 0 & \frac{\ell}{2} & 0 & 0 \\ 0 & 0 & \frac{\ell^2}{12} & 0 & 0 & 0 \\ 0 & -\frac{\ell^2}{12} & 0 & 0 & 0 & 0 \end{bmatrix}. \tag{3.56}$$

Once defined the local forces acting on the elements, it is possible to assemble them in the datum FOR by means of the coordinate

transformation matrix $\boldsymbol{\Xi}$:

$$\begin{aligned}\boldsymbol{e} &= \sum_{e=1}^{N_e} \mathbf{T}^{eT} \left(\boldsymbol{e}^e\right)_E = \\ &= \sum_{e=1}^{N_e} \mathbf{T}^{eT} \boldsymbol{\Xi}^T \left(\boldsymbol{e}^e\right)_{E^e} = \\ &= \sum_{e=1}^{N_e} \mathbf{T}^{eT} \boldsymbol{\Xi}^T \left[\left(\boldsymbol{P}^e\right)_{E^e} + \mathbf{I}_\psi^e \left(\overline{\boldsymbol{f}^{2D}} + \overline{\boldsymbol{t}^{2D}}\right)_{E^e}\right] = \\ &= \sum_{e=1}^{N_e} \mathbf{T}^{eT} \left[\left(\boldsymbol{P}^e\right)_E + \boldsymbol{\Xi}^{bT} \mathbf{I}_\psi^e \boldsymbol{\Xi}^b \left(\overline{\boldsymbol{f}^{2D}} + \overline{\boldsymbol{t}^{2D}}\right)_E\right],\end{aligned} \tag{3.57}$$

where $\boldsymbol{\Xi}^b$ is the top-left 6×6 block of the coordinate transformation matrix.

The forces acting on the structure, however, include also the reaction forces and are thus not independent. From the overall equilibrium of the complete blade, it is evident that there are six dependent equations related to the six rigid-body DOFs. Therefore, in order to eliminate the following singularity in the stiffness matrix, the essential boundary conditions must be considered in a way that rigid-body motion is assigned or restrained. In the case of our cantilever blades, we eliminated the equations corresponding to the fixed displacements at the hub by eliminating the rows and columns of the corresponding DOFs, thus removing the equations of the differential system including the reaction forces.

3.5 Modal Approach

In Equation 3.6, we saw that it is possible to express the displacement vector as a linear combination of shape functions regulated by generalised coordinates.

In many occasions, it is general practice to leverage the knowledge of the eigenfunctions of the structural problem, coincident its physical *modes*, to create reduced-order models. In fact, given the initial orthogonal shape functions $\boldsymbol{\psi}^n$, and the modes $\boldsymbol{Z}^m$, it is possible to define the new modal shape functions $\overline{\boldsymbol{\psi}}^m$, by representing the mode shape by means of the old shape functions (see Figure 3.5):

$$\overline{\boldsymbol{\psi}}^m = \sum_{n=1}^{\infty} Z_n^m \boldsymbol{\psi}^n. \tag{3.58}$$

Correspondingly, the new modal coordinates $\bar{q}_m$ are defined so that:

$$\boldsymbol{d}(\boldsymbol{x}, t) = \sum_{n=1}^{\infty} q_n(t) \boldsymbol{\psi}^n(\boldsymbol{x}) = \sum_{m=1}^{\infty} \bar{q}_m(t) \overline{\boldsymbol{\psi}}^m(\boldsymbol{x}). \tag{3.59}$$

The modal coordinates are thus related to the old coordinates by means of the relation:

$$\boldsymbol{q} = \mathbf{Z}\overline{\boldsymbol{q}}, \tag{3.60}$$

where the matrix $\mathbf{Z}$ is the *eigenfunctions matrix*, whose generic n-th column $\boldsymbol{Z}^n$ is a vector containing the nodal representations of the n-th mode.

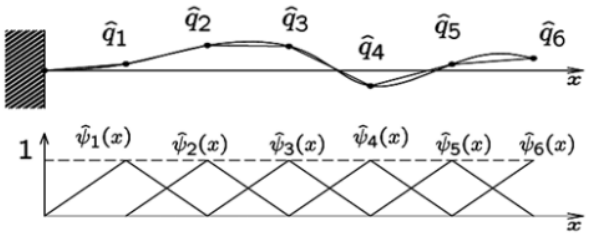

Figure 3.5: Finite element description of a modal shape, by means of the tent functions here indicated as $\hat{\boldsymbol{\psi}}^n$ and the FEM coordinates $\hat{q}^n$.

If we use the modal basis to describe the undamped and uncoupled structural problem, it is possible to demonstrate that Equation 3.52 becomes:

$$\underbrace{\mathbf{Z}^T\mathbf{M}\mathbf{Z}}_{\overline{\mathbf{M}}}\ddot{\overline{\boldsymbol{q}}} + \underbrace{\mathbf{Z}^T\mathbf{K}\mathbf{Z}}_{\overline{\mathbf{K}}}\overline{\boldsymbol{q}} = \underbrace{\mathbf{Z}^T\boldsymbol{e}}_{\overline{\boldsymbol{e}}}, \tag{3.61}$$

where the new mass and stiffness matrices, $\overline{\mathbf{M}}$ and $\overline{\mathbf{K}}$, are diagonal, according to the properties of the eigenvectors, and the loads projections on the modes are called $\overline{\boldsymbol{e}}$.

If the eigenvectors are mass-normalised, the new mass matrix is the $N_m \times N_m$ identity matrix and the stiffness matrix is a $N_m \times N_m$ diagonal matrix whose elements are the eigenvalues λ_n, where N_m is the number of modes used to describe the problem.

In the modal approach, a reduced number of modes can be used, which means that the number of *modal* DOFs considered in the new problem is reduced too. However, neglecting some modes means approximating the representation of the structural behaviour, and so the contribution – at the corresponding eigenfrequencies – of the neglected modes to the structural response is inevitably lost. The possible computational advantage of the modal approach is thus evident, given the lower dimension of the problem and its diagonalisation, despite the loss in accuracy due to the approximation of a finite number of modes.

Moreover, while FEM is highly dependent on the model chosen for the description of the structure (element type and shape functions choice), the modal description is more general. In fact, we can accurately obtain the natural modes of a structure as complicate as desired from any commercial structural software; once obtained the natural modes, the structural equations in the modal basis are formally the same for models of different complexity and also of different structures.

Because of the described advantages, we decided to adopt a modal structural solver for the description of the blades' structural dynamics. Hence, after presenting the model for the structural damping adopted, we express in the following sections also the inertial coupling terms by means of the modal basis, but leveraging also the knowledge of mass and inertia information from the finite element model of the structure.

Structural modal damping

As seen in Section 3.1, the structural damping is of paramount importance to describe the response of a viscoelastic structure. In this work, we adopt the so-called *modal damping* or *Rayleigh-Basile damping model*, according to which the modal damping matrix $\overline{\mathbf{C}}$ is:

$$\overline{\mathbf{C}} = \mathbf{Z}^T \mathbf{C} \mathbf{Z} = \mathrm{diag}\left(2\,\zeta_r \omega_r m_r\right) \tag{3.62}$$

where $\mathrm{diag}(\bullet_r)$ indicates a diagonal matrix with generic element $\bullet_r$, ζ_r is the damping coefficient of the r-th mode, $\omega_r = \sqrt{\lambda_r}$ is the r-th natural angular frequency and m_r is the r-th modal mass.
The model is widely accepted for metallic structures with low modal density or, in general, for low-damped structures. Typical values of ζ_r are in the range $0.01 \div 0.1$ [158].

[158]: Craig et al. (2006), *Fundamentals of structural dynamics*

As a result of the diagonal structure also of the damping matrix, the structural problem in the modal basis becomes a set of uncoupled equations, each describing a mass-spring-damper mechanical system with a single DOF: the r-th modal displacement.

3.6 Modal Inertial Coupling Terms

Up to this moment, we neglected the inertial coupling terms, which in Section 3.3 were expressed in terms of the generic shape functions $\boldsymbol{\psi}$. To consider also the effect of these terms, in modal basis, the inertial coupling coefficients can be discretised as done in Saltari et al., 2017 [155]. However, in our case the origin of the main FOR is not centred in the centre of mass of the entire structure, but in a fixed point, *i.e.* the root of each single blade.

The methodology is completely general and leverages the structural data from a generic finite element model. Moreover, the discretisation is defined for a generic *continuous* structure, and so, the form of all the contributions from the inertial forces does not vary with the finite element model.

The steps of the method are the following:

- The structural domain is divided into a set of complementary subvolumes $\mathscr{V}_i$ with i going from 1 to the number of nodes N. Hence, the total volume integral becomes a sum of subvolumes' integral. The centre of mass of the subvolume $\mathscr{V}_i$ is indicated as $\boldsymbol{r}_{g_i}$ in the relative FOR and $\boldsymbol{R}_{g_i} = \boldsymbol{r}_{O'} + \boldsymbol{r}_{g_i}$ in the absolute one. A generic material point in the element is identified by $\boldsymbol{R} = \boldsymbol{R}_{g_i} + \boldsymbol{\zeta}$ in the absolute FOR.
- We define the mass m_i and the inertia tensor $\mathbf{J}_{\mathbf{g_i}}$ with respect to the centre of mass of the i-th subvolume as:

$$m_i \coloneqq \langle 1 \rangle_i = \iiint_{\mathscr{V}_i} \rho \mathrm{d}\mathscr{V}, \tag{3.63}$$

$$\mathbf{J}_{\mathbf{g_i}} \coloneqq \langle (\boldsymbol{\zeta}\cdot\boldsymbol{\zeta})\,\mathbf{I} - \boldsymbol{\zeta}\otimes\boldsymbol{\zeta}\rangle_i = \iiint_{\mathscr{V}_i} \rho\,(\boldsymbol{\zeta}\cdot\boldsymbol{\zeta})\,\mathbf{I}\mathrm{d}\mathscr{V} + \mathbf{J}^{\boldsymbol{\delta}}_{\boldsymbol{g_i}}, \quad (3.64)$$

where we indicate with $\langle\bullet\rangle_i$ the mass integration in the i-th subvolume, and we define the tensor $\mathbf{J}^{\boldsymbol{\delta}}_{\boldsymbol{g_i}}$ as the inertia tensor $\mathbf{J}_{\mathbf{g_i}}$ minus one half of its trace.
One can derive these quantities from any finite element model. In the case of the lumped mass representation, mass and inertia information of the i-th subvolume is available in the diagonal of the 6×6 mass matrix block corresponding to the i-th node.

- We assume that, *locally*, the displacement field of the n-th modal shape function can be described as a rigid-body motion:

$$\overline{\boldsymbol{\psi}}^n\Big|_{\boldsymbol{x}} = \overline{\boldsymbol{\psi}}^n_t\Big|_{g_i} + \overline{\boldsymbol{\psi}}^n_r\Big|_{g_i} \times \boldsymbol{\zeta}, \quad (3.65)$$

where $\overline{\boldsymbol{\psi}}^n_t\Big|_{g_i} = \overline{\boldsymbol{\psi}}^n_t(\boldsymbol{r}_{g_i})$ and $\overline{\boldsymbol{\psi}}^n_r\Big|_{g_i} = \overline{\boldsymbol{\psi}}^n_r(\boldsymbol{r}_{g_i})$ are respectively the displacement and the rotation associated to the n-th mode at the i-th centre of mass $\boldsymbol{r}_{g_i}$.

The terms reported below results from the application of the described procedure for the discretisation of Equation 3.22, Equation 3.26 and Equation 3.27. For the sake of brevity, in the remaining part of this section we omit the subscript g_i of the modal displacement and rotation; moreover, we indicate the *skew-symmetry operator*[3] with the symbols $\mathscr{A}_m \coloneqq \mathscr{A}_{\overline{\boldsymbol{\psi}}^m_r}$ and $\mathscr{A}_n \coloneqq \mathscr{A}_{\overline{\boldsymbol{\psi}}^n_r}$.

3: The skew-symmetry operator $\mathscr{A}$ applied on a certain vector $\boldsymbol{v}$ is such that:

$$\left[(\mathscr{A}_{\boldsymbol{v}})_e\right]_{ij} = \epsilon_{ijk}\left[(v)_e\right]_k$$

- Centrifugal terms:

$$\begin{aligned}
\mathrm{K}^c_{nm} &= -\boldsymbol{\Omega}\cdot\mathrm{sym}\left\langle\left(\overline{\boldsymbol{\psi}}^n\cdot\overline{\boldsymbol{\psi}}^m\right)\mathbf{I} - \overline{\boldsymbol{\psi}}^n\otimes\overline{\boldsymbol{\psi}}^m\right\rangle\boldsymbol{\Omega} = \\
&\approx -\boldsymbol{\Omega}\cdot\sum_{i=1}^{N}\frac{1}{2}\left\{m_i\left[2\left(\overline{\boldsymbol{\psi}}^n_t\cdot\overline{\boldsymbol{\psi}}^m_t\right)\mathbf{I} - \overline{\boldsymbol{\psi}}^n_t\otimes\overline{\boldsymbol{\psi}}^m_t - \overline{\boldsymbol{\psi}}^m_t\otimes\overline{\boldsymbol{\psi}}^n_t\right] + \right. \\
&\quad \left. -2\left[\mathscr{A}_n : \left(\mathscr{A}_m\,\mathbf{J}^{\boldsymbol{\delta}}_{\boldsymbol{g_i}}\right)\right]\mathbf{I} - \mathscr{A}_n\,\mathbf{J}^{\boldsymbol{\delta}}_{\boldsymbol{g_i}}\,\mathscr{A}_m - \mathscr{A}_m\,\mathbf{J}^{\boldsymbol{\delta}}_{\boldsymbol{g_i}}\,\mathscr{A}_n\right\}\boldsymbol{\Omega}
\end{aligned} \quad (3.66)$$

$$\begin{aligned}
e^c_n &= -\boldsymbol{\Omega}\cdot\mathrm{sym}\left\langle\left(\boldsymbol{R_{OP}}\cdot\overline{\boldsymbol{\psi}}^n\right)\mathbf{I} - \boldsymbol{R_{OP}}\otimes\overline{\boldsymbol{\psi}}^n\mathbf{I}\right\rangle\boldsymbol{\Omega} = \\
&\approx \boldsymbol{\Omega}\cdot\sum_{i=1}^{N}\frac{1}{2}\left\{m_i\left[2\left(\boldsymbol{R}_{g_i}\cdot\overline{\boldsymbol{\psi}}^n_t\right)\mathbf{I} - \boldsymbol{R}_{g_i}\otimes\overline{\boldsymbol{\psi}}^n_t - \overline{\boldsymbol{\psi}}^n_t\otimes\boldsymbol{R}_{g_i}\right] + \right. \\
&\quad \left. + \mathscr{A}_n\,\mathbf{J}^{\boldsymbol{\delta}}_{\boldsymbol{g_i}} - \mathbf{J}^{\boldsymbol{\delta}}_{\boldsymbol{g_i}}\,\mathscr{A}_n\right\}\boldsymbol{\Omega}
\end{aligned} \quad (3.67)$$

- Euler terms:

$$\begin{aligned}
\mathrm{K}^{Eu}_{nm} &= -\dot{\boldsymbol{\Omega}}\cdot\boldsymbol{b}_{nm} = \\
&\approx -\dot{\boldsymbol{\Omega}}\cdot\sum_{i=1}^{N}\left[m_i\,\overline{\boldsymbol{\psi}}^n_t\times\overline{\boldsymbol{\psi}}^m_t - \mathbf{J}^{\boldsymbol{\delta}}_{\boldsymbol{g_i}}\left(\overline{\boldsymbol{\psi}}^n_r\times\overline{\boldsymbol{\psi}}^m_r\right)\right]
\end{aligned} \quad (3.68)$$

$$e_n^{Eu} = -\dot{\boldsymbol{\Omega}} \cdot \langle \boldsymbol{R_{OP}} \times \boldsymbol{\psi}^n \rangle \approx -\dot{\boldsymbol{\Omega}} \cdot \sum_{i=1}^{N} \left[m_i \boldsymbol{R}_{g_i} \times \overline{\boldsymbol{\psi}}_t^n \right] \tag{3.69}$$

- Coriolis terms:

$$\begin{aligned} \mathrm{D}_{nm}^{Co} &= -2\,\boldsymbol{\Omega} \cdot \boldsymbol{b}_{nm} = \\ &\approx -2\,\boldsymbol{\Omega} \cdot \sum_{i=1}^{N} \left[m_i\, \overline{\boldsymbol{\psi}}_t^n \times \overline{\boldsymbol{\psi}}_t^m - \mathbf{J}_{\boldsymbol{g_i}}^{\boldsymbol{\delta}} \left(\overline{\boldsymbol{\psi}}_r^n \times \overline{\boldsymbol{\psi}}_r^m \right) \right] \end{aligned} \tag{3.70}$$

3.7 Effect of the Centre of Mass Offset

Modes are usually described by means of the generalised coordinates in correspondence of the structural nodes. Thus far, we implicitly assumed the centres of mass of the elements to be coincident with their elastic centres and both the centres to be coincident with the nodes' locations. Therefore, in the lumped representation used for the inertial coupling terms, we were allowed to locate the elementary masses in correspondence of the finite element model grid nodes.

However, this is not always the case, and in many occasions, the centre of mass of an element has an offset with respect to the elastic centre. As a result, the lumped mass must have an offset, which changes the inertia of the element with respect to the elastic line.

This offset can be taken into account by expressing the modes at the mass location as:

$$\begin{aligned} \overline{\boldsymbol{\psi}}_t^n \Big|_{g_i} &= \overline{\boldsymbol{\psi}}_t^n \Big|_i + \overline{\boldsymbol{\psi}}_r^n \Big|_{g_i} \times \boldsymbol{s}_i, \\ \overline{\boldsymbol{\psi}}_r^n \Big|_{g_i} &= \overline{\boldsymbol{\psi}}_r^n \Big|_i, \end{aligned} \tag{3.71}$$

where $\boldsymbol{s}_i$ is the offset vector, which goes from the i-th node to the i-th centre of mass; $\overline{\boldsymbol{\psi}}_t^n \Big|_{g_i}$ and $\overline{\boldsymbol{\psi}}_r^n \Big|_{g_i}$ are the translation and rotation corresponding to the n-th mode at the i-th centre of mass; $\overline{\boldsymbol{\psi}}_t^n \Big|_i$ and $\overline{\boldsymbol{\psi}}_r^n \Big|_i$ are the translation and rotation corresponding to the n-th mode at the i-th node.

By using Equation 3.71 to express the modal shape functions in the mass matrix in Equation 3.20, and by following the same procedure carried out for the inertial coupling terms, we obtain a modification of the diagonal mass matrix that considers the mass offsets correctly [156]:

$$\langle \boldsymbol{a_{rel}} \cdot \delta \boldsymbol{d} \rangle = \sum_{n=1}^{\infty} \sum_{m=1}^{\infty} \delta q_n \underbrace{\sum_{i=1}^{N} \begin{bmatrix} \overline{\boldsymbol{\psi}}_t^m \Big|_i \\ \overline{\boldsymbol{\psi}}_r^m \Big|_i \end{bmatrix}^T \begin{bmatrix} m_i \mathbf{I} & -m_i \, \mathcal{A}_{\boldsymbol{s}_i} \\ m_i \, \mathcal{A}_{\boldsymbol{s}_i} & \mathbf{J_i} \end{bmatrix} \begin{bmatrix} \overline{\boldsymbol{\psi}}_t^n \Big|_i \\ \overline{\boldsymbol{\psi}}_r^n \Big|_i \end{bmatrix}}_{\left(\overline{M}_s\right)_{nm}} \ddot{\overline{q}}_m, \tag{3.72}$$

where $\mathcal{A}_{\boldsymbol{s}_i}$ is the skew-symmetric matrix associated with the offset vector, $\mathbf{J_i} = \mathbf{J_{g_i}} + m_i \mathcal{A}_{\boldsymbol{s}_i}^T \mathcal{A}_{\boldsymbol{s}_i}$ is the local inertia tensor with respect to the grid point, and $\left(\overline{M}_s\right)_{nm}$ is the (n,m)-th element of the modified mass matrix.

Proof. The virtual displacement and the relative acceleration in Equation 3.20 are decomposed by means of the modal decomposition:

$$\langle \boldsymbol{a_{rel}} \cdot \delta \boldsymbol{d} \rangle = \sum_{n=1}^{\infty} \sum_{m=1}^{\infty} \delta q_n \left\langle \overline{\boldsymbol{\psi}}^n(\boldsymbol{x}) \cdot \overline{\boldsymbol{\psi}}^m(\boldsymbol{x}) \right\rangle \ddot{\overline{q}}_m.$$

Then, we divide the structure in N elementary volumes and we repeat the discretisation procedure carried out for the inertial coupling terms. So we have:

$$\sum_{n=1}^{\infty} \sum_{m=1}^{\infty} \delta q_n \left\langle \overline{\boldsymbol{\psi}}^n \cdot \overline{\boldsymbol{\psi}}^m \right\rangle \ddot{\overline{q}}_m =$$

$$\sum_{n=1}^{\infty} \sum_{m=1}^{\infty} \delta q_n \sum_{i=1}^{N} \left\langle \left(\overline{\boldsymbol{\psi}}_t^n \Big|_{g_i} + \overline{\boldsymbol{\psi}}_r^n \Big|_{g_i} \times \boldsymbol{\zeta} \right) \cdot \left(\overline{\boldsymbol{\psi}}_t^m \Big|_{g_i} + \overline{\boldsymbol{\psi}}_r^m \Big|_{g_i} \times \boldsymbol{\zeta} \right) \right\rangle \ddot{\overline{q}}_m =$$

$$\sum_{n=1}^{\infty} \sum_{m=1}^{\infty} \delta q_n \sum_{i=1}^{N} \left\langle \left(\overline{\boldsymbol{\psi}}_t^n \Big|_{g_i} \cdot \overline{\boldsymbol{\psi}}_t^m \Big|_{g_i} \right) + \underbrace{\left(\overline{\boldsymbol{\psi}}_r^n \Big|_{g_i} \times \boldsymbol{\zeta} \cdot \overline{\boldsymbol{\psi}}_r^m \Big|_{g_i} \times \boldsymbol{\zeta} \right)}_{\mathbf{J_{g_i}}} \right\rangle \ddot{\overline{q}}_m,$$

where we removed the null quantities related to $\langle \boldsymbol{\zeta} \rangle$, because these are proportional to the position of the centre of gravity of the i-th element with respect to its centre of gravity itself.
Finally, we substitute Equation 3.71 in the equation above, and we recast it in the form expressed in Equation 3.72. □

If one observes the structure of the resultant mass matrix $\overline{\mathbf{M}}_\mathbf{s}$ in the modal basis referred to the grid points, it is evident that we could have obtained it equivalently by properly modifying the finite element lumped mass matrix and then pre- and post-multiplying it by the eigenvector matrix $\mathbf{Z}$, as done in the diagonalisation procedure.

Therefore, it is possible to consider the effects of the centre of mass offset by modifying directly the finite-element mass matrix obtained with the lumped-mass representation. The original diagonal matrix thus becomes a block-diagonal matrix: each 6×6 block becomes equal to the initial correspondent FEM block plus the off-diagonal symmetric terms and the *Huygens-Steiner transport term* for the local inertia tensor:[4]

$$\begin{bmatrix} m_i \mathbf{I}_{3\times3} & \mathbf{0}_{3\times3} \\ \mathbf{0}_{3\times3} & \mathbf{J_{g_i}} \end{bmatrix} + \begin{bmatrix} \mathbf{0}_{3\times3} & -m_i \mathcal{A}_{\boldsymbol{s}_i} \\ m_i \mathcal{A}_{\boldsymbol{s}_i} & m_i \mathcal{A}_{\boldsymbol{s}_i}^T \mathcal{A}_{\boldsymbol{s}_i} \end{bmatrix}, \qquad i = 1, \dots N. \tag{3.73}$$

In this way, the *modified* structural eigenproblem that includes the centre of mass offset is associated to eigenvectors that diagonalise the new block-diagonal mass matrix, and still describe the modes by means of generalised coordinates that are referred to the nodal positions. Moreover, the modifications in the mass matrix correct also the inertial behaviour for the estimation of the inertial coupling terms.

4: We paid attention to the expression of the coordinates of the offset vector. The modifications to the mass matrix take place after the assembling procedure and so the right coordinates are the global ones, $(\boldsymbol{s}_i)_E$, which include, for example, the effect of the structural pre-twist of the blade.

3.8 On the Model Linearity

To evaluate the loads acting on the structure, especially for the aerodynamic loads, the precise statement of the structural configuration considered is fundamental.

In the reality, the forces are determined and applied on the basis of the deformed configuration, and thus the actual deformation is the composition of progressive and cumulative structural updates. For the case of the aerodynamic loads, which are *follower* in nature, the configuration is particularly important, given the fact that it determines the orientation of the profiles, and thus affects importantly the aerodynamic actions in turn.

If the deformations are large enough to modify considerably the body geometry, a more rigorous approach would be necessary for which the equations of the dynamics are written with respect to the deformed configuration. In the case of small deformations and large displacement or in the case of large deformations, *geometrical nonlinearities* modify the equations introducing new terms and modifying radically the theoretical and numerical framework of the structural dynamics (see Holzapfel, 2000 [159]). In particular, for a general finite motion state, the actual body configuration is unknown and furthermore, the actual configuration determines the internal stress state by means of a dependency that is not linear in the general case and depends also on the history of the finite deformation.

[159]: Holzapfel (2000), *Nonlinear Solid Mechanics: A Continuum Approach for Engineering*

Moreover, also the response of the material can be nonlinear, with complex constitutive relations for nonlinearly elastic and plastic or viscoelastic materials.
The design of the wind turbine blade is complex and includes an exterior part, mainly determined on the basis of aerodynamic arguments, and an interior part, mainly determined on the basis of structural arguments. These parts are made of composite materials since the 1970s. Fiberglass in polyester resin and other laminates are the most common choises, but the increase in size of the wind turbines and the concerns about the blade recyclability are pushing the research for new, light and resistant materials whose response is hardly linear.

Additionally, the blades are here considered as straight, without pre-cone and without pre-sweep angles, and geometrical taper is only considered indirectly by means of the sectional aggregated data of the blade. Recent studies [160, 161] showed that the classic beam theory is inadequate to describe non-prismatic and curved beams, due to the non-uniform geometry of the cross sections or the initial curvature of the centerline, and that for large displacements more complex nonlinear models are more appropriate, like the Geometrically-Exact Beam Theory (GEBT) proposed by Hodges, 2006 [21].

[160]: Migliaccio et al. (2020), 'Beam-like models for the analyses of curved, twisted and tapered horizontal-axis wind turbine (HAWT) blades undergoing large displacements'
[161]: Migliaccio et al. (2021), 'The influence of an initial twisting on tapered beams undergoing large displacements'

The model we described and implemented in our FSI is linear and cannot fully capture the high-order effects described above. The configuration adopted to determine the loads and on which the loads are applied is the reference, undeformed one, and there are not terms in the structural dynamics equations explicitely considering the actual and instantaneous

deformed configuration, except for the linear aeroelastic effects in the aerodynamic forces that are presented in Chapter 4.

However, the same studies highlighting the importance of enhanced structural models showed also that the geometrical nonlinearities start to be particularly noteworthy for very long blades with significant initial curvatures. Moreover, various studies [61] [162] showed that for characteristic blades around 70 m of length (which is typical for the average installed wind turbines), the high stiffness of the structure is still able to keep the displacement relatively small, which justifies for state-of-the-art, utility-scale wind turbines the linearity assumptions in the structural model, both in the material response and in the geometrical configuration.

[162]: Riziotis et al. (2008), 'Identification of structural non-linearities due to large deflections on a 5MW wind turbine blade'

Of course, when considering larger wind turbines like the 14 MW Haliade-X or the 16 MW MySE 16.0-242, with their diameters respectively of 220 m and 242 m, the complex structural nonlinearities will probably prevent a correct estimation of the vibratory dynamics of the blades.

3.9 Time Integration

In the previous sections, we described the initial-value problem defined by the semidiscrete equations for the structural dynamics, which is:

$$\mathbf{M}\ddot{\boldsymbol{q}} + \mathbf{C}\dot{\boldsymbol{q}} + \mathbf{K}\boldsymbol{q} = \boldsymbol{e}, \tag{3.74a}$$

$$\boldsymbol{q}(0) = \boldsymbol{q}^{\mathbf{0}}, \tag{3.74b}$$

$$\dot{\boldsymbol{q}}(0) = \boldsymbol{v}^{\mathbf{0}}, \tag{3.74c}$$

where $\boldsymbol{q}$ is the generalised coordinate vector. $\mathbf{M}$, $\mathbf{C}$, and $\mathbf{K}$ are, respectively, the corresponding mass, damping and stiffness matrices, while $\boldsymbol{e}$ is the corresponding generalised load vector. The initial conditions are specified by the initial generalised displacement $\boldsymbol{q}^{\mathbf{0}}$ and by the initial generalised velocity $\boldsymbol{v}^{\mathbf{0}}$.

Modal or finite element bases can be used to describe the displacement and, correspondingly, the structural matrices assume different forms. In particular, as already stated, the modal representation has the advantage of providing more compact matrices and of making reduced-order models possible. Additionally, in the definition of the stiffness and damping matrices, as well as of the generalised load vector, inertial coupling terms can be included, without changing the general form of the equations.

Especially for a time-varying loading, as the one acting on a wind turbine blade in a turbulent wind field, solving analytically the initial-value hyperbolic problem of Equation 3.74a-Equation 3.74c is practically impossible. Therefore, a numerical integration in time of the structural dynamics equations is necessary.

Several algorithms have been presented during the years (see [163] for a description of the most widespread numerical methods in the structural dynamics community), and although there is not a unanimous

[163]: Hughes (2012), *The finite element method: linear static and dynamic finite element analysis*

consensus, it is agreed that a structural algorithm must have the following properties:

- unconditional stability for linear problems;
- second-order accuracy;
- self-starting capabilities;
- controllable algorithmic dissipation in the higher modes, to damp out their spurious participation to the structural response;
- no more than one set of implicit equations to be solved at each time step (*one-step methods* are preferred).

We present briefly the methods we considered for this work in the following sections.

Newmark method

One of the classic family of methods used for structural dynamics is the *Newmark method family* [164], according to which equations are discretised as follows:

[164]: Newmark (1959), 'A Method of Computation for Structural Dynamics'

$$\boldsymbol{d}_{n+1} = \boldsymbol{d}_n + \Delta t \boldsymbol{v}_n + \frac{\Delta t^2}{2}\left[(1-2\beta)\,\boldsymbol{a}_n + 2\beta \boldsymbol{a}_{n+1}\right], \tag{3.75a}$$

$$\boldsymbol{v}_{n+1} = \boldsymbol{v}_n + \Delta t\left[(1-\gamma)\,\boldsymbol{a}_n + \gamma \boldsymbol{a}_{n+1}\right], \tag{3.75b}$$

$$\mathbf{M}\boldsymbol{a}_{n+1} + \mathbf{C}\boldsymbol{v}_{n+1} + \mathbf{K}\boldsymbol{d}_{n+1} = \boldsymbol{F}_{n+1}, \tag{3.75c}$$

where $\boldsymbol{a}$, $\boldsymbol{v}$ and $\boldsymbol{d}$ are the numerical approximations for the acceleration, the velocity and the displacement, $\boldsymbol{F}$ is the force vector, Δt is the time interval, β and γ are constant parameters, and the subscripts n and $n+1$ indicate the time to which the quantities are referred. The methods of the family are *one-step methods*, because the solution at the future instant depends only on the solution at the present instant, and *three-stage methods*, because the definition of the solution is characterised only by $\boldsymbol{d}_n$, $\boldsymbol{v}_n$ and $\boldsymbol{a}_n$.

A particular case in the family is the well-known *average acceleration method*.[5] It is possible to obtain it by imposing $\beta = 1/4$ and $\gamma = 1/2$, which means that the acceleration is approximated by the average between its value at time n and $n+1$. This method is implicit, second-order accurate and unconditionally stable. The starting conditions are:

5: The method is also called *trapezoidal rule method*, because we can derive it also by applying the trapezoidal rule to the first-order form of the system in Equation 3.74a, where the state vector is given by $\{\boldsymbol{q}|\dot{\boldsymbol{q}}\}$

$$\boldsymbol{d}_0 = \boldsymbol{q}^0, \tag{3.76a}$$

$$\boldsymbol{v}_0 = \boldsymbol{v}^0, \tag{3.76b}$$

$$\boldsymbol{a}_0 = \mathbf{M}^{-1}\left(\boldsymbol{F}(0) - \mathbf{C}\boldsymbol{v}_0 - \mathbf{K}\boldsymbol{d}_0\right), \tag{3.76c}$$

The Newmark algorithm satisfies all the properties asked to a structural dynamics algorithm, except for the property of controllable numerical dissipation for higher frequency modes. This point is fundamental because, in a finite element model, the poor spatial resolution of these modes can affect the validity of the entire solution.
In fact, the numerical solution of some test cases we performed, imposing a periodic forcing acting on a wind turbine blade, revealed the presence of small, spurious, high-frequency oscillations.

In order to correct this behaviour, researchers have developed dissipative algorithms. Among them, two of the most widely used methods are the *HHT-α method* and the *generalised-α method*.

HHT-α method

The *Hilber-Hughes-Taylor method* or *HHT-α method* [165] is a one-step, three-stage time integration method of the Newmark family in which Equation 3.75c is substituted with:

[165]: Hilber et al. (1977), 'Improved numerical dissipation for time integration algorithms in structural dynamics'

$$\mathbf{M}\boldsymbol{a}_{n+1} + (1-\alpha)\mathbf{C}\boldsymbol{v}_{n+1} + \alpha\mathbf{C}\boldsymbol{v}_n + (1-\alpha)\mathbf{K}\boldsymbol{d}_{n+1} + \alpha\mathbf{K}\boldsymbol{d}_n = \boldsymbol{F}_{n+1-\alpha}, \tag{3.77}$$

where α is a control parameter and $t_{n+1-\alpha} = t_{n+1} - \alpha\Delta t$. The force $\boldsymbol{F}(t_{n+1-\alpha})$ is usually taken equal to $(1-\alpha)\boldsymbol{F}(t_{n+1}) + \alpha\boldsymbol{F}(t_n)$.

It is evident that if $\alpha = 0$, the HHT method reduces to the classic Newmark method. The control parameter α is introduced to add some numerical dissipation in the system. Increasing α increases the dissipation for frequencies above $1/(2\Delta t)$. However, the introduction of the numerical dissipation could affect the accuracy of the solution and, in fact, the method remains second-order accurate and unconditionally stable only if the parameters abide by the relationships:

$$\alpha \in [0, 1/3]\,, \tag{3.78a}$$

$$\beta = \frac{1}{4}(1+\alpha)^2\,, \tag{3.78b}$$

$$\gamma = \frac{1}{2} + \alpha. \tag{3.78c}$$

The numerical solutions for several unsteady test cases we performed, revealed that even by adopting the parameters suggested above, spurious high-frequency oscillations can appear in the solution, albeit with improved results with respect to the Newmark method. For this reason, we implemented and tested another, last, dissipative method.

Generalised-α method

The *generalised-α method* or *gen-α method* [166] is a family of one-step three-stage time integration methods for the structural dynamics, and is the method we chose for the advancement in time of our structural module.

[166]: Chung et al. (1993), 'A Time Integration Algorithm for Structural Dynamics With Improved Numerical Dissipation: The Generalized-α Method'

It is unconditionally stable, second-order accurate and characterised by an optimal combination of high-frequency and low-frequency dissipation: for a user-defined damping of the high-frequency modes, the low-frequency modes dissipation is minimised.

It contains as special cases the HHT-α method and also another member of the Newmark's method, the WBZ-α method [167], where a modified expression for the acceleration is used in Equation 3.75c.
The gen-α method is recommended for long simulations, has shown smaller errors than the other dissipative schemes in many different cases in the literature, and finally has been used in all the structural modules

[167]: Wood et al. (1980), 'An alpha modification of Newmark's method'

for FSI in wind energy presented in Chapter 1. Moreover, the method performed better than the Newmark and the HHT-α methods in all our test cases, and suppressed with success the spurious oscillations observed with the other methods.

The equations for the generalised-α method are:

$$\boldsymbol{d}_{n+1} = \boldsymbol{d}_n + \Delta t \boldsymbol{v}_n + \frac{\Delta t^2}{2}\left[(1-2\beta)\,\boldsymbol{a}_n + 2\beta \boldsymbol{a}_{n+1}\right], \tag{3.79a}$$

$$\boldsymbol{v}_{n+1} = \boldsymbol{v}_n + \Delta t\left[(1-\gamma)\,\boldsymbol{a}_n + \gamma \boldsymbol{a}_{n+1}\right], \tag{3.79b}$$

$$\mathbf{M}\boldsymbol{a}_{n+1-\alpha_m} + \mathbf{C}\boldsymbol{v}_{n+1-\alpha_f} + \mathbf{K}\boldsymbol{d}_{n+1-\alpha_f} = \boldsymbol{F}(t_{n+1-\alpha_f}), \tag{3.79c}$$

$$\boldsymbol{d}_0 = \boldsymbol{q}^0, \tag{3.79d}$$

$$\boldsymbol{v}_0 = \boldsymbol{v}^0, \tag{3.79e}$$

$$\boldsymbol{a}_0 = \mathbf{M}^{-1}\left(\boldsymbol{F}(0) - \mathbf{C}\boldsymbol{v}_0 - \mathbf{K}\boldsymbol{d}_0\right), \tag{3.79f}$$

where:

$$\mathbf{d}_{n+1-\alpha_f} = (1-\alpha_f)\boldsymbol{d}_{n+1} + \alpha_f \boldsymbol{d}_n, \tag{3.80a}$$

$$\mathbf{v}_{n+1-\alpha_f} = (1-\alpha_f)\boldsymbol{v}_{n+1} + \alpha_f \boldsymbol{v}_n, \tag{3.80b}$$

$$\mathbf{a}_{n+1-\alpha_m} = (1-\alpha_m)\boldsymbol{a}_{n+1} + \alpha_m \boldsymbol{a}_n, \tag{3.80c}$$

$$t_{n+1-\alpha_f} = (1-\alpha_f)t_{n+1} + \alpha_f t_n, \tag{3.80d}$$

and the parameters are such that:

$$\alpha_m = \frac{2\rho_\infty - 1}{\rho_\infty + 1}, \qquad \alpha_f = \frac{\rho_\infty}{\rho_\infty + 1}, \tag{3.81a}$$

$$\beta = \frac{1}{4}(1 - \alpha_m + \alpha_f)^2, \tag{3.81b}$$

$$\gamma = \frac{1}{2} - \alpha_m + \alpha_f. \tag{3.81c}$$

The parameter ρ_∞, the so-called *spectral radius*, specifies the numerical dissipation for the high frequencies modes. In all our simulations, we adopted a spectral radius $\rho_\infty = 0$ that guarantees *asintotic annihilation*, *i.e.* spurious high frequencies are eliminated after one time step.

4 The Fluid-Structure Interaction Model

In this chapter, we present the Fluid-Structure Interaction methodology that we propose to join our fluid and structural solvers.

After having presented the different Frames of Reference (FORs) defined to describe the rotor, the blades and the airfoils' position and orientation, we explain the staggered approach that we implemented, and finally we highlight its advantages and disadvantages.

4.1 Frames of Reference

In the description of the structural dynamics of a wind turbine blade, it is possible to define different frames of reference. The different directional quantities in the blade kinematics and dynamics have sometimes easier representations in specific frames and can be seen in other frames by means of coordinates transformations.

Coordinates transformation operator

In the following, we use the same notation introduced in the previous chapter to describe the coordinates of a directional quantity $\boldsymbol{v}$ in a certain FOR $\mathscr{R}_E$, defined by the versors of its basis $\boldsymbol{E}_i$:

$$(\boldsymbol{v})_E = \begin{pmatrix} \boldsymbol{v} \cdot \boldsymbol{E}_1 \\ \boldsymbol{v} \cdot \boldsymbol{E}_2 \\ \boldsymbol{v} \cdot \boldsymbol{E}_3 \end{pmatrix} = \begin{pmatrix} v_1 \\ v_2 \\ v_3 \end{pmatrix}$$

Over the past decade, the wind energy industry has achieved significant improvements in energy production and cost efficiency, driven in part by increased turbine, blade, and tower sizes. The recent study of the so-called "supersized" turbines involves a growing interest in the characterization of the interaction between the fluid and the inherently more flexible structural components. The credits for the image above the chapter title go to DNV-GL. https://www.dnvgl.com/publications/r-d-pathways-supersized-wind-turbine-blades-142666

We introduce a coodinate transformation operator $\boldsymbol{R}$, such that, given two FORs, $\mathscr{R}_e$ and $\mathscr{R}_E$, we have that:

$$(\boldsymbol{v})_E = \mathsf{R}^{e\to E}\,(\boldsymbol{v})_e \tag{4.1}$$

where $\mathsf{R}^{e\to E}$ is the transformation matrix from $\mathscr{R}_e$ to $\mathscr{R}_E$ corresponding to $\boldsymbol{R}$. From linear algebra, the corresponding matrix is given by:

$$\left(\mathrm{R}^{e\to E}\right)_{ij} = \boldsymbol{E}_i \cdot \boldsymbol{e}_j \tag{4.2}$$

and is such that, if the bases $\boldsymbol{E}_i$ and $\boldsymbol{e}_j$ are orthonormal ($\boldsymbol{E}_i \cdot \boldsymbol{E}_j = \delta_{ij}$ and $\boldsymbol{e}_i \cdot \boldsymbol{e}_j = \delta_{ij}$),

$$\mathsf{R}^{E\to e} = \left(\mathsf{R}^{e\to E}\right)^{-1} = \left(\mathsf{R}^{e\to E}\right)^{T}. \tag{4.3}$$

Orientation angles

In general, the orientation of a wind turbine blade without cone angle, is given by:

The *yaw angle* or *yaw error* $\Psi(t)$. It is individued by the normal-to-rotor direction $\boldsymbol{E}_{\Psi_2}$ and the streamwise direction of the wind $\boldsymbol{e}_1$. A non-zero yaw error entails an asymmetry in the load distribution on the turbine and larger fatigue loads in turn. Moreover, the effective area of the rotor disk is reduced and power production drops as well.
If included, the eventual yaw angle is oriented in a way that a positive angle rotates the disk according to the right-hand rule around the vertical inertial axis y, $\boldsymbol{E}_{\Psi_3} = \boldsymbol{e}_2$.

The *azimuthal angles* $\Theta_i(t)$. They are individued by the radial vectors that describe the span axis of each single blade $\boldsymbol{E}_{\Theta_{1i}}(t)$ and a reference coordinate direction in the rotor plane. The azimuthal angles describe the revolution of each blade for given angular speed $\boldsymbol{\Omega}$ and acceleration $\dot{\boldsymbol{\Omega}}$. The dynamics of the azimuthal angle is defined by the angular momentum balance between the aerodynamic and the generator torques in Equation 2.46. The angles $\Theta_i(t)$, for a three-blade wind turbine, are related each other by the trivial relation:

$$\Theta_i = \Theta_1 + (i-1)\,\frac{2}{3}\pi, \quad i = 1, 2, 3. \tag{4.4}$$

The azimuthal angle is defined with an orientation that is opposite to the right-hand rule around the vector $\boldsymbol{E}_{\Theta_2}$, which is normal to the rotor and points in the direction of the flow. As a result, the angular speed vector is $\boldsymbol{\Omega} = -\dot{\Theta}_i \boldsymbol{E}_{\Theta_2}$ and the angular acceleration is $\dot{\boldsymbol{\Omega}} = -\ddot{\Theta}_i \boldsymbol{E}_{\Theta_2}$. Hence, our wind turbine rotates counterclockwise, if seen from an upwind frontal plane (see Figure 4.5).

Locally then, to describe the effect of the deformation on the orientation of a certain profile, the coordinates need a transformation according to the *deformation angles* from the structural dynamics solver. We call $\theta_i(t)$ the rotation angles around the i-th axis of the undeformed

configuration, according to the right-hand rule. These angles define the orientation of the planes composing the blades, in a proper "beam" fashion.

Finally, given the fact that the blades have a fixed structural twist that varies along the span, to describe the orientation of a profile laying on a certain radial section plane, a coordinate transformation matrix has to consider also the *variable pre-twist* ϕ, and depends only on the radial position.
We decided to orient the pre-twist angle according to the right-hand rule around the deformed radial axis, such that a positive pre-twist rotates the leading edge downward.

In defining the coordinates transformation with the angles Ψ, Θ, θ_i, and ϕ, we decided at first to orient the relative FORs at the initial time instant such that the reference blade is parallel to the fixed spanwise axis z, *i.e.* blade 1 with $\theta_1 = 0$ at $t = 0$. In order to make coherent the orientation of the different FORs and the following transformations, an auxiliary coordinate FOR $\mathscr{R}_\beta$ is defined, such that:

$$\begin{cases} \boldsymbol{E}_{\beta_1} \coloneqq \boldsymbol{e}_3 \\ \boldsymbol{E}_{\beta_2} \coloneqq \boldsymbol{e}_1 \\ \boldsymbol{E}_{\beta_3} \coloneqq \boldsymbol{e}_2 \end{cases} \tag{4.5}$$

Coordinates transformation matrices

Once decided the conventions for the angles orientation, we can define the coordinates transformation matrices accordingly.

FOR $\mathscr{R}_e$ to FOR $\mathscr{R}_\beta$ This change of coordinates is characterized by the combination of two perpendicular rotations that bring to the right-handed coordinates FOR in Equation 4.5. Looking at Figure 4.1, we have:

$$\mathsf{R}^\beta \coloneqq \mathsf{R}^{e\to\beta} = \begin{bmatrix} 0 & 0 & 1 \\ 1 & 0 & 0 \\ 0 & 1 & 0 \end{bmatrix}. \tag{4.6}$$

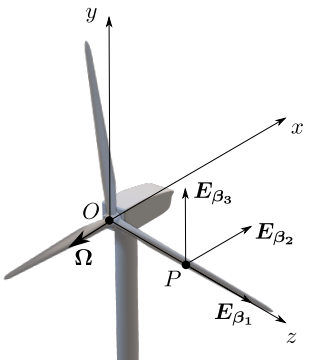

Figure 4.1: FOR $\mathscr{R}_e$ to FOR $\mathscr{R}_\beta$.

FOR $\mathscr{R}_\beta$ to FOR $\mathscr{R}_\Psi$ This change of coordinates is characterized by a rotation around the axis $\boldsymbol{E}_{\Psi_3} = \boldsymbol{E}_{\beta_3}$ of an angle Ψ, as shown

in Figure 4.2. Thus, we have:

$$\mathsf{R}^{\Psi} \coloneqq \mathsf{R}^{\beta\to\Psi} = \begin{bmatrix} \cos\Psi & \sin\Psi & 0 \\ -\sin\Psi & \cos\Psi & 0 \\ 0 & 0 & 1 \end{bmatrix}. \tag{4.7}$$

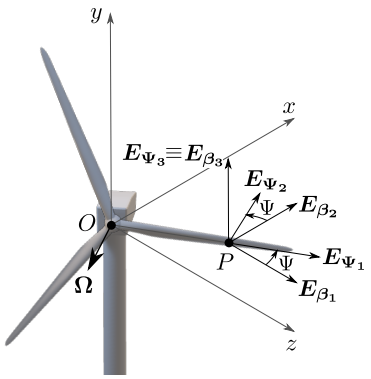

Figure 4.2: FOR $\mathscr{R}_\beta$ to FOR $\mathscr{R}_\Psi$.

FOR $\mathscr{R}_\Psi$ to FOR $\mathscr{R}_\Theta$ This change of coordinates is characterized by a right-hand rotation around the axis $-\boldsymbol{E}_{\Theta_2} = -\boldsymbol{E}_{\Psi_2}$ of an angle Θ, as shown in Figure 4.3. Thus, we have:

$$\mathsf{R}^{\Theta} \coloneqq \mathsf{R}^{\Psi\to\Theta} = \begin{bmatrix} \cos\Theta & 0 & \sin\Theta \\ 0 & 1 & 0 \\ -\sin\Theta & 0 & \cos\phi \end{bmatrix}. \tag{4.8}$$

We call the FOR $\mathscr{R}_\Theta$ also as $\mathscr{R}_E$. This FOR is the one used in the

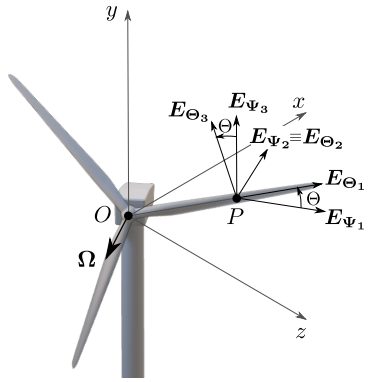

Figure 4.3: FOR $\mathscr{R}_\Psi$ to FOR $\mathscr{R}_\Theta$.

structural dynamics, since the structural twist is already considered in the local-to-datum elemental coordinates transformations. The displacements and their derivatives from the structural solver have hence the directions of the coordinate directions $\boldsymbol{E}_i$ of the FOR $\mathscr{R}_E$, which considers the change of orientation β, the yaw angle Ψ and the azimuthal angle Θ.

We group these first transformations in the rigid coordinates transformation matrix R^E describing the rotation of the radial axis of the blade (*i.e.* the actuator line), at a certain time instant. Thus, we have:

$$\mathsf{R}^{E} \coloneqq \mathsf{R}^{\Theta} \cdot \mathsf{R}^{\Psi} \cdot \mathsf{R}^{\beta} = \begin{bmatrix} s_\Psi\, c_\Theta & s_\Theta & c_\Psi\, c_\Theta \\ c_\Psi & 0 & -s_\Psi \\ -s_\Psi\, s_\Theta & c_\Theta & -c_\Psi\, s_\Theta \end{bmatrix}, \tag{4.9}$$

where we indicate with s_μ and c_μ, respectively, the sine and cosine of the generic subscript angle μ.

FOR $\mathscr{R}_\Theta$ to FOR $\mathscr{R}_\epsilon$ We call $\mathscr{R}_\epsilon$ the configuration that considers the change in orientation of the wind turbine blade sections after the elastic rotational deformation. We can define the coordinates transformation matrix R^{el} using the deformation angles from the structural solver with respect to the undeformed configuration and the undeformed axes defined by $\mathscr{R}_E$.
In general, the elastic transformation can be seen as a combination of the three ordered finite rotations θ_1, θ_2 and θ_3. For the single rotations, the transformation matrices are thus:

$$\mathsf{R}^1 = \begin{bmatrix} 1 & 0 & 0 \\ 0 & c_1 & s_1 \\ 0 & -s_1 & c_1 \end{bmatrix}, \mathsf{R}^2 = \begin{bmatrix} c_2 & 0 & -s_2 \\ 0 & 1 & 0 \\ s_2 & 0 & c_2 \end{bmatrix}, \mathsf{R}^3 = \begin{bmatrix} c_3 & s_3 & 0 \\ -s_3 & c_3 & 0 \\ 0 & 0 & 1 \end{bmatrix}, \tag{4.10}$$

where we indicate with c_i and s_i, respectively, the cosine and sine functions for the angle θ_i. From their ordered combination $(\theta_1 \to \theta_2 \to \theta_3)$, we have that:

$$\begin{aligned} \mathsf{R}^{el} &= \mathsf{R}^{E\to\epsilon} = \mathsf{R}^3 \cdot \mathsf{R}^2 \cdot \mathsf{R}^1 = \\ &= \begin{bmatrix} c_2\, c_3 & c_2\, s_3 & -\, s_2 \\ -c_1\, s_3 + s_1\, s_2\, s_3 & c_1\, c_3 + s_1\, s_2\, s_3 & s_1\, c_2 \\ s_1\, s_3 + c_1\, s_2\, c_3 & -s_1\, c_3 + c_1\, s_2\, s_3 & c_1\, c_2 \end{bmatrix}. \end{aligned} \tag{4.11}$$

More precisely, the final configuration depends on the order in which the three finite rotations are considered. However, under the hypothesis of infinitesimal rotations, where cosine and sine functions are linearised, the commutative property holds, and we have that:

$$\mathsf{R}^{el} = \begin{bmatrix} 1 & \theta_3 & -\theta_2 \\ -\theta_3 & 1 & \theta_1 \\ \theta_2 & -\theta_1 & 1 \end{bmatrix} \tag{4.12}$$

It is important to notice that the assumption of infinitesimal rotations is perfectly in line with the linearity assumptions inherently included in our structural model.
Moreover, at this stage, we have neglected the effect of the displacement in the FSI coupling. Its inclusion would mean changing the position of the velocity sampling points needed for the actuator line and changing the position of application of the forces, with a *fully-deformable* actuator line. Unfortunately, the resolution needed to describe adequately the structural deformation in the fluid domain, would mean having a cell size in the fluid grid much smaller than 1 m. As a result, this would mean either a really computationally expensive simulation or a fine simulation with a reduced extent of the domain size, which could lead to errors in the boundary conditions and a reduced extent of the analysable wake behind the wind turbine.
Furthermore, the linear structural model developed in this study is not able to describe adequately the follower nature of the load on structures with large deformations, and so the inclusion of the

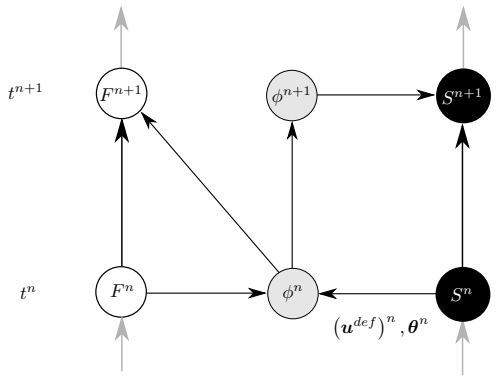

Figure 4.4: Ladder-like scheme of the two-way coupling method for Runge-Kutta (RK)-steps n and $n+1$. The fluid state F is indicated on the left, the structural state S is indicated on the right. The aerodynamic loading Φ and its estimations are indicated in the middle; $\boldsymbol{u}^{def}$ is the local deformation velocity, and $\boldsymbol{\theta}$ is the local vector of the deformation angles.

displacement would question the validity of the adopted structural modelling itself.

FOR $\mathscr{R}_\epsilon$ to FOR $\mathscr{R}_\Sigma$ Once derived the orientation of the planes of the airfoils according to the yaw error, the blade position and the elastic deformation, in order to finally derive the geometrical configuration used to derive the incidence, we must include an additional rotation induced by the structural pre-twist, which defines the effective orientation of the airfoil on the radial planes along the span.

This change of coordinates is characterised by a rotation around the versor $\boldsymbol{E}_{\epsilon_1} = \boldsymbol{E}_{\Sigma_1}$ tangent to the deformed blade's centerline of an angle ϕ. Thus, we have:

$$\mathsf{R}^{\phi} = \mathsf{R}^{\epsilon \to \Sigma} = \begin{bmatrix} 1 & 0 & 0 \\ 0 & \cos\phi & \sin\phi \\ 0 & -\sin\phi & \cos\phi \end{bmatrix}. \tag{4.13}$$

4.2 FSI Coupling Method

In the classic implementation of the ALM, the model assumes that the actuator lines move as rigid bodies and evaluates the local angle of attack only on the basis of the fluid velocity in correspondence of the actuator lines and of the rotational velocity at each section, as reported in Section 2.4.

The schematic rationale of the algorithm adopted in our two-way coupling aeroelastic model is shown in Figure 4.4. The model is based on two independent or partitioned solvers exchanging information once per time substep, in a loose partitioned coupling approach [46].
At the beginning of each RK time substep n, the distribution of the effective angle of attack α^n is estimated along each blade from the fluid state F^n (consisting of the velocity field), the angular speed Ω^n, and the elastic state S^n. In particular, the latter can include the instantaneous information of both the deformation velocity $\boldsymbol{u}^{def}$ and the local vector of the deformation angles $\boldsymbol{\theta}$ (torsion and bendings). Given the aerodynamic look-up tables of the airfoils or the unsteady aerodynamics history, a blade element approach determines the distributions of the aerodynamic forces and moments per unit length Φ^n, then used in the ALM. In order to estimate the structural state at the following instant S^{n+1}, the external loading at time $n+1$, required by the generalised-α method

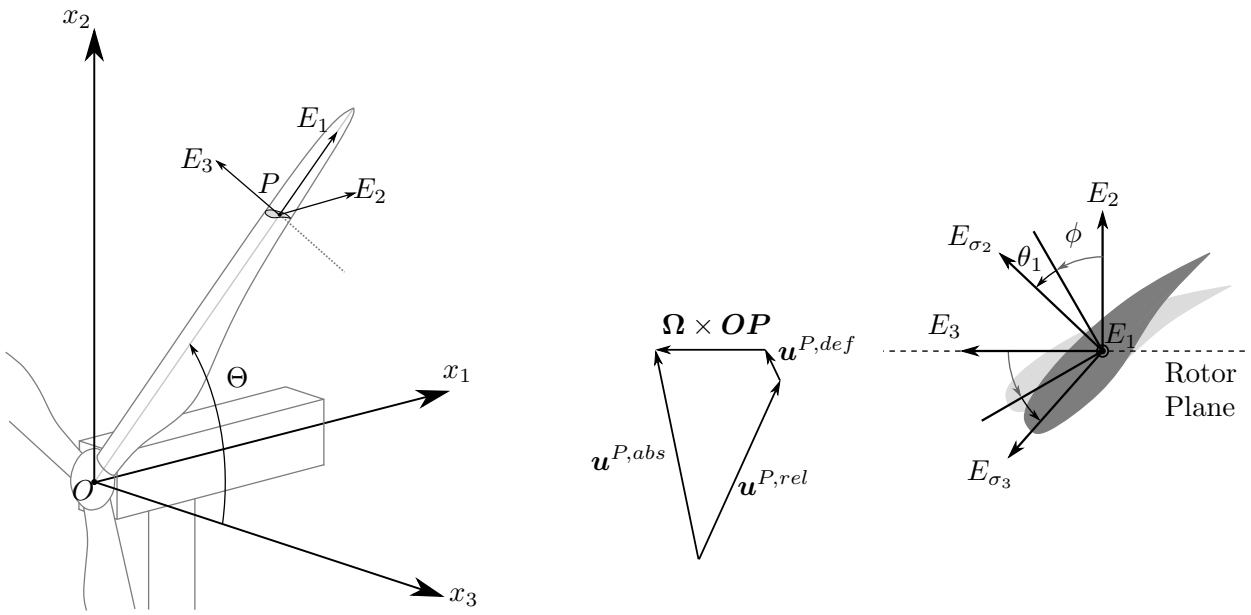

Figure 4.5: Different FORs defined for the description of the FSI problem of wind energy. The frame $\mathcal{R}_E$ rotates rigidly around the hub centre O, with E_2 constantly pointing at the positive streamwise direction (in case of null yaw error, $\Psi = 0$). At a generic section at point P along the blade, the blade pre-twist ϕ and the instantaneous angular deformation (only torsion is shown in figure) define the local FOR $\mathcal{R}_\Sigma$, where the effective angle of attack is defined. The velocity vectors show the combination of the different components in the plane of a generic profile.

for $\rho_\infty = 0$, is approximated by the available aerodynamic loading Φ^n at each RK substep.

We implemented, therefore, a so-called *parallel* staggered algorithm [44], given the fact that we did not correct exactly the prediction of the structural deformation after the final evaluation of the fluid state, but instead we limited inter-field communications only at the beginning of each RK substep, and we used the consecutive approximations of the aerodynamic forces available at those instants. This allows us to leverage the knowledge of the aerodynamic loading from the fine temporal resolution of the fluid RK scheme to increase the accuracy of the structural scheme, without re-evaluating the forces and the structural state in correspondence of the new fluid state, and thus preserving the overall efficiency of the code.

The method is at least first-order accurate, even if the inter-field parallelism is obtained at the expense of possible amplified errors in the mutual interaction and response of the single fields [44]. However, without subcycling the fluid computations, *i.e.* using the same time *(sub)*step for the solid and the fluid dynamics, it has been demonstrated that a non-negligible amplification of the errors appears only in the case of critical conditions like flutter or similar strong instabilities, and that by adopting a reduced time step the error produced is limited and even smaller than with other more sophisticated parallel staggered algorithms. In fact, we adopt a very fine temporal resolution because of the time step limitations in our LES simulations required by the ALM to obtain an accurate description of the wind turbine flow field (see Section 2.2).

Because of the presence of different FORs, the relative velocity and

the effective angle of attack in Equation 2.39 and Equation 2.45 are defined by means of a matricial notation. To better point out the transformations adopted, we use in this section the convention according to which (see Figure 4.5):

- the lower-case subscript indices refer to the components in the inertial FOR $\mathscr{R}_e$;
- the upper-case subscript indices refer to the components in the FOR $\mathscr{R}_E$ rigidly rotating with each blade;
- the lower-case greek subscript indices refer to the components in the local FOR $\mathscr{R}_\Sigma$, defined by the instantaneous orientation of each airfoil.

According to the method presented, the relative velocity $\boldsymbol{u}^{P,rel}$ of a point P belonging to an actuator line is expressed as:

$$\boldsymbol{u}^{P,rel} = \boldsymbol{u}^{P,abs} - \boldsymbol{u}^{P,def} - \boldsymbol{\Omega} \times \boldsymbol{OP}\,, \tag{4.14}$$

where $\boldsymbol{u}^{P,abs}$ is the absolute fluid velocity sampled at point P, $\boldsymbol{u}^{P,def}$ is the deformation velocity of the blades described by the modal composition of $\dot{\boldsymbol{q}}$ (see Chapter 3), and $\boldsymbol{\Omega} \times \boldsymbol{OP}$ is the rotational velocity component at the same point. To determine the local flow at each section, assuming null yaw error, the relative velocity in $\mathscr{R}_\Sigma$ can be expressed in Einstein notation as follows:

$$u_\sigma^{P,rel} = \mathsf{R}_{\sigma j}^{e\to\Sigma}\, u_j^{P,abs} - \mathsf{R}_{\sigma J}^{E\to\Sigma}\, u_J^{P,def} - \mathsf{R}_{\sigma j}^{e\to\Sigma}\, \epsilon_{jkm}\Omega_k OP_m. \tag{4.15}$$

According to the notation introduced in the previous sections, and assuming for simplicity a null yaw error, it follows that:

$$\mathsf{R}^{e\to\Sigma} = \mathsf{R}^{E\to\Sigma}\,\mathsf{R}^{\Theta} = \left(\mathsf{R}^{\phi}\,\mathsf{R}^{el}\right)\,\mathsf{R}^{\Theta} =$$
$$= \begin{bmatrix} 1 & 0 & 0 \\ 0 & \cos\phi & \sin\phi \\ 0 & -\sin\phi & \cos\phi \end{bmatrix} \begin{bmatrix} 1 & \theta_3 & -\theta_2 \\ -\theta_3 & 1 & \theta_1 \\ \theta_2 & -\theta_1 & 1 \end{bmatrix} \begin{bmatrix} 0 & \sin\Theta & \cos\Theta \\ 1 & 0 & 0 \\ 0 & \cos\Theta & -\sin\Theta \end{bmatrix} \tag{4.16}$$

In accordance with the definition of the coordinate directions of $\mathscr{R}_\Sigma$, the effective angle of attack and the relative velocity in Eqs. 2.39 for the generic point P on the actuator line are expressed as:

$$\alpha = \operatorname{atan}\left(-\frac{u_{\sigma_2}^{P,rel}}{u_{\sigma_3}^{P,rel}}\right) \quad \text{and} \quad U_{ref} = \sqrt{\left(u_{\sigma_2}^{P,rel}\right)^2 + \left(u_{\sigma_3}^{P,rel}\right)^2}\,, \tag{4.17}$$

where we consider only the components in the plane of the local profile on directions σ_2 and σ_3, see Figure 4.5.

By means of the described model, we are able to consider the effects of various levels of complexity in the coupling configuration. In the two-way coupled simulations reported in this work, we consider only the effects on the incidence of the flap- and edgewise deformation velocities without any angular deformation ($u_J^{P,def} \neq 0$ in Eq. 4.15 and $\theta_1 = \theta_2 = \theta_3 = 0$ in Eq. 4.16), and also the effect of the torsional angle θ_1 ($u_J^{P,def} \neq 0$ in Eq. 4.15 and $\theta_1 \neq 0$, $\theta_2 = \theta_3 = 0$ in Eq. 4.16), given the fact that the contributions of the other degrees of freedom

are less relevant in the cases under study with respect to the included degrees.

4.3 Advantages and Disadvantages

The main advantage of our simplified aeroelastic method is that it exploits the sectional 1D formulation of the Actuator Line Model to avoid the difficulties in the fluid-solid interface treatment. In the body-conformal approaches, the interface between the solid and the fluid domain involves the imposition of kinematic and traction conditions as mutual boundary conditions on moving surfaces. In our case, the structural motion and the aerodynamic forces on the blades are interpolated by simple 1D polynomial interpolation functions.

Moreover, the reduced computational cost of the modal structural solver, but also the inter-field parallel algorithm implemented, allow the preservation of the computational efficiency of our simulations, which is already dominated by the relevant burden of the Large Eddy Simulation methodology.

On the other hand, as in all the cases of loose coupling, the accuracy and the stability of the method is difficult to characterise. In particular, some studies have pointed out the possible limitations of the parallel staggered algorithm adopted and different implementations could be considered for future works, such as the classic conventional-serial staggered algorithm or other improved parallel algorithms [47].

More complex algorithms would need consecutive re-evaluations to improve the estimation of the aerodynamic forces and of the elastic state. However, we stress once again that the time step required by the fluid methodology is much smaller than the one required by the typical structural unsteadiness of the blades (mainly related to the first structural eigenmodes), and is certainly smaller than the requirements for stability and accuracy of the complete FSI algorithm.
Just to give a practical example of the order of magnitude of the quantities involved, a typical fluid time step of our simulations is $\Delta t_F \approx 0.0021\,s$, which means, for a fluid three-stage RK scheme, that the average time step of the structural dynamics is about $\Delta t_S \approx 0.0007\,s$ with an associated sampling frequency of $1429\,Hz$, far beyond the last natural frequency of the blades considered in this study $f_{20} \approx 20\,Hz$ and even further from the frequencies of the first six modes, which are the most relevant ones for the overall structural response.

Results

5 The Simulations Setup

This chapter presents the setup used in the simulations that we carried out for this work.

At first, we present the features of the wind turbine considered in our study, focusing in particular on the structural and aerodynamic properties of its blades. Then we describe the fluid setup, providing information about the fluid domain of our LES simulations, on the grid used, and on the inflow prescribed. Hence, we describe the structural setup, providing information about the blades discretisation and the modes of the structure. Finally, we present an overview of all the simulations carried out, each with its own specific inflow, coupling and aerodynamic conditions.

5.1 Wind Turbine

In order to use realistic and standard input data for our study, we decided to take into account the 5 MW baseline wind turbine model developed by the National Renewable Energy Laboratory (NREL). The NREL 5 MW wind turbine is a conceptual wind turbine, *i.e.* for which no real model has been built physically, whose essential features are well described by tabulated data representative of a typical utility-scale wind turbine [51].
Because of the availability and representativeness of its aerodynamic, structural and control features, the NREL 5 MW is probably the most widely used wind turbine in the aeroelasticity studies, as can be seen from the literature review in Section 1.3. The main gross properties of the wind turbine are reported in Table 5.1.

Table 5.1: Gross properties of the NREL 5 MW wind turbine [51].

Rating	5 MW
Rotor Orient.	Upwind
Rotor Config.	3 Blades
Control	Var. Speed
Hub Diam. D_{hub}	3 m
Rotor Diam. D	126 m
Hub height h	90 m
Cut-In Wind Speed	3 m/s
Rated Wind Speed	11.4 m/s
Cut-Out Wind Speed	25 m/s
Rated Wind Speed	80 m/s

Four of the turbines on a TransAlta Renewables wind farm in Alberta, Canada. Wind turbines simulation involve challenging computational requirements related to the large separation of the scales of the problem. The computational setup is thus critical and must guarantee a good resolution of both the small flow scales close to the blades and the large flow scales of the wakes.
The credits for the image above the chapter title go to Calgary Drone Photography.
https://news.stanford.edu/2019/07/01/steering-wind-power-new-direction/

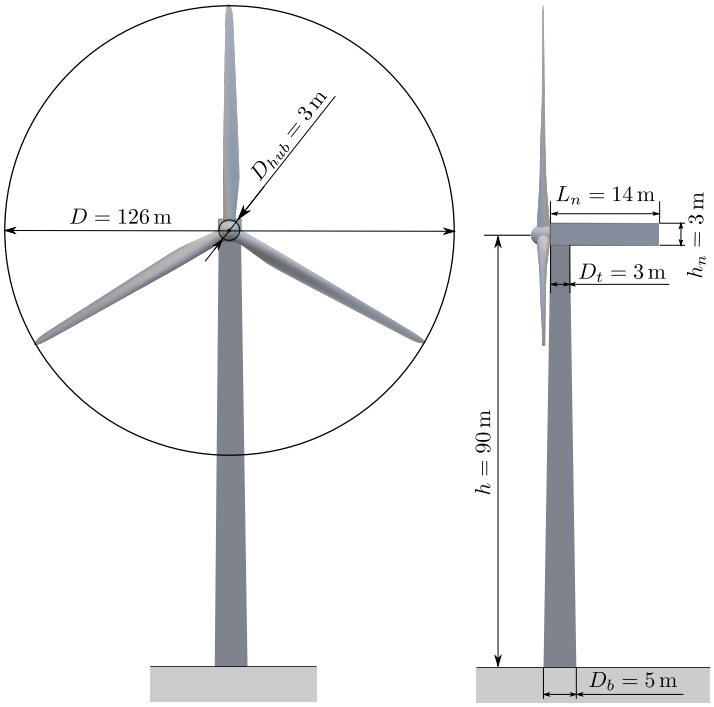

Figure 5.1: Sketch of the NREL 5 MW wind turbine geometry used in this work.

In our study, in order to simplify the representation of the blades, precone is not considered. Moreover, given the absence of precise specifications in this regard, we assumed the nacelle to be a parallelepiped, with dimensions inferred from one of the original references used to define the NREL 5 MW wind turbine [168]. Figure 5.1 shows a detailed sketch of the geometry specifications reported in the reference manual. The wind turbine control system is made of a conventional variable-speed, variable pitch-to-feather mechanisms. In this configuration, a generator-torque controller maximises the power production below the rated conditions, while a blade-pitch controller regulates the generator speed to preserve the machine safety above the rated conditions. As stated in Section 2.4, all the simulations of this work were carried out in conditions of optimal power capture, where the blade-pitch controller is not active and the generator-torque controller guarantees an optimal tip speed ratio. By using a simple BEM algorithm, it is possible to estimate the behaviour of the C_P and C_T coefficients as functions of the operating conditions represented by the tip speed ratio TSR. These curves provide easily the rotor power and thrust coefficients and are inherently dependent on the specific turbine considered and on the airfoils defining the blades. Figure 5.2 shows the $TSR - C_P$ and $TSR - C_T$ curves of the NREL 5 MW wind turbine. The peak power coefficient of $C_P^{max} = 0.486$ is reached at $TSR_{opt} \approx 7.5$, for a thrust coefficient equal to $C_T = 0.786$.
To complete the description of the turbine, we report in the following the structural and aerodynamic properties of the NREL 5 MW blades.

[168]: Lindenburg et al. (2002), *Aeroelastic modelling of the LMH64-5 blade*

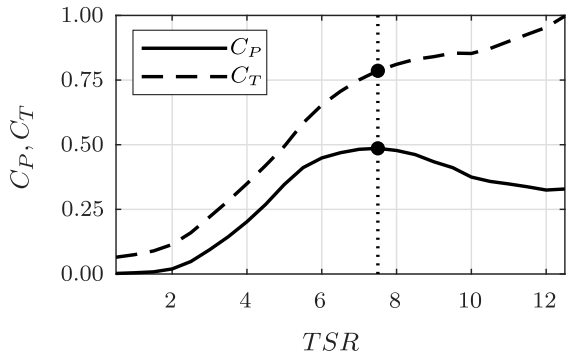

Figure 5.2: Power and thrust coefficients of the NREL 5 MW wind turbine as a function of the tip speed ratio. The dotted vertical line indicates the optimal tip speed ratio.

NREL 5 MW blades

Both the structural and the aerodynamic properties of the NREL 5 MW wind turbine blades are slight modifications of the ones of the DOWEC blades [168], which are longer and larger.

Figure 5.3 reports the plots of the distributed structural properties along the nondimensional radial undeformed structural axis X_1/L, with L being the length of the blade. These are respectively:

1. the structural twist ϕ;
2. the distributed blades section mass per unit length ρA;
3. the principal flapwise section stiffness EI_2;
4. the principal edgewise section stiffness EI_3;
5. the blade torsion stiffness GJ;
6. the blade extensional stiffness EA.

The pitch axis is assumed to pass through each airfoil at the quarter of their own chords. The relative position of the edgewise centre of mass offset and the aerodynamic centre with respect to the quarter of chord is shown in Figure 5.4. The overall integrated blade mass of 17740 kg is distributed along the blade span of 61.5 m.

Finally, the aerodynamic properties of the NREL 5 MW blades are defined by eight unique airfoils distributed as reported in Figure 5.4. After two span sections made of cylindrical regions, six wind energy airfoils of the DU and NACA families define the aerodynamic response of the turbine. In the case of steady aerodynamics, the tabulated data of the airfoil coefficients define at each instant the lift, drag and moment per unit of length (see Figure 5.5); on the other hand, in the case with UA, the dedicated dynamic module determines the sectional forces. The tabulated data, used for the static aerodynamics and in the derivation of the UA parameters, have been originally corrected to account for the three-dimensional behaviour of the airfoils.

We highlight that in the original model described in the reference manual [51], and adopted in this work, the passage from an airfoil kind and an another is abrupt, and so there is no guarantee about the continuity of the aerodynamic forces along the span, especially for the pitching moment coefficient which at the same angle of attack can have different values from airfoil to airfoil, as can be seen from Figure 5.5.

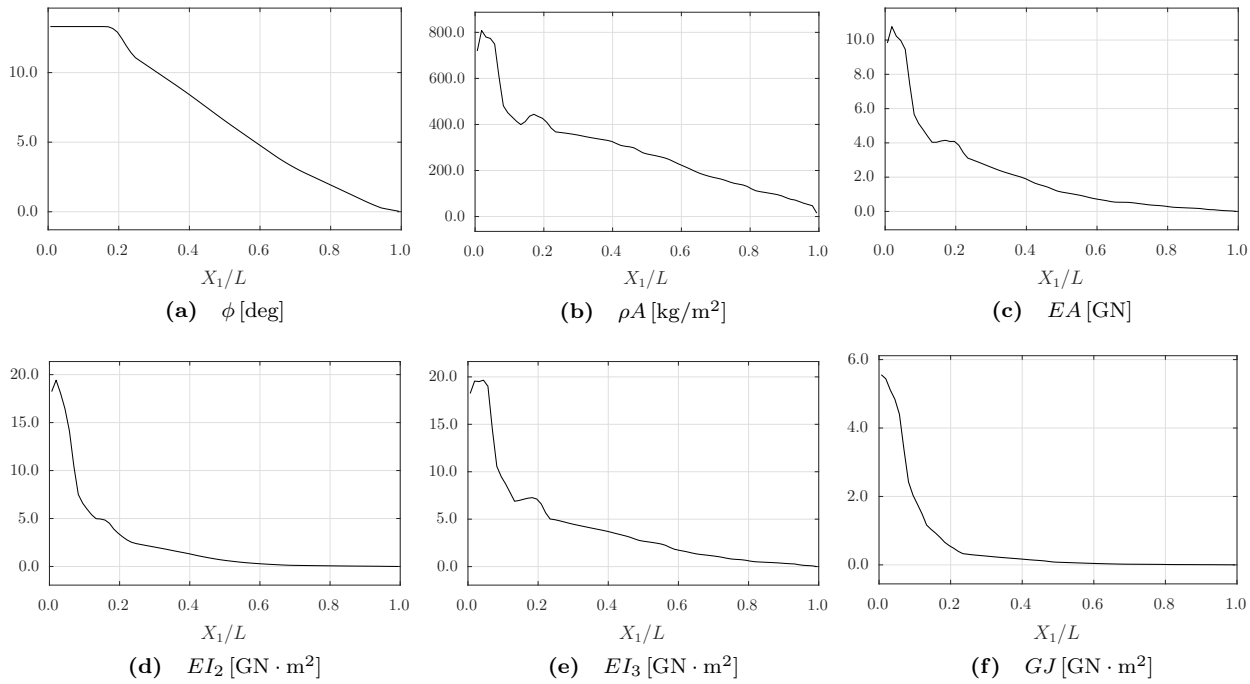

Figure 5.3: Distributed structural properties of the NREL 5 MW wind turbine blade along the radial undeformed axis X_1.

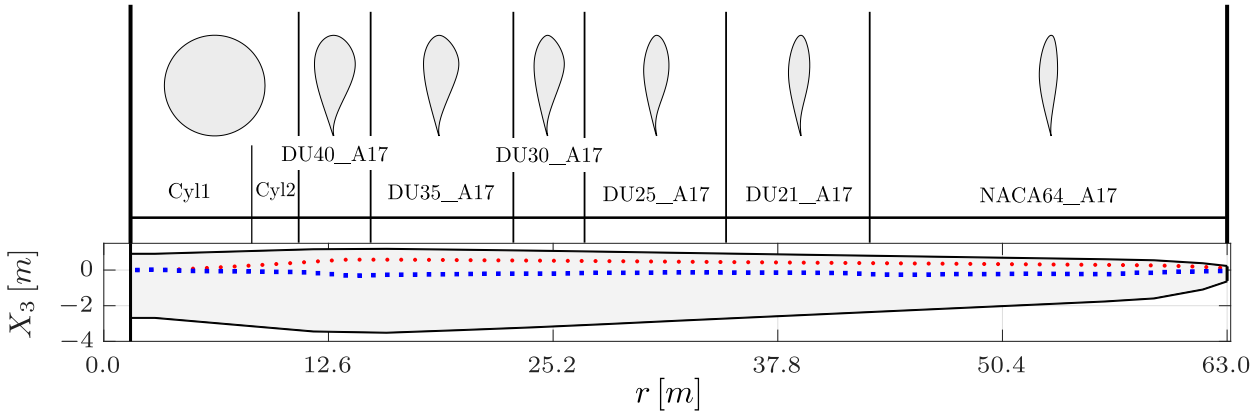

Figure 5.4: Aerodynamic centre (red), centre of mass (blue) and aifoils of the NREL 5 MW wind turbine blade.

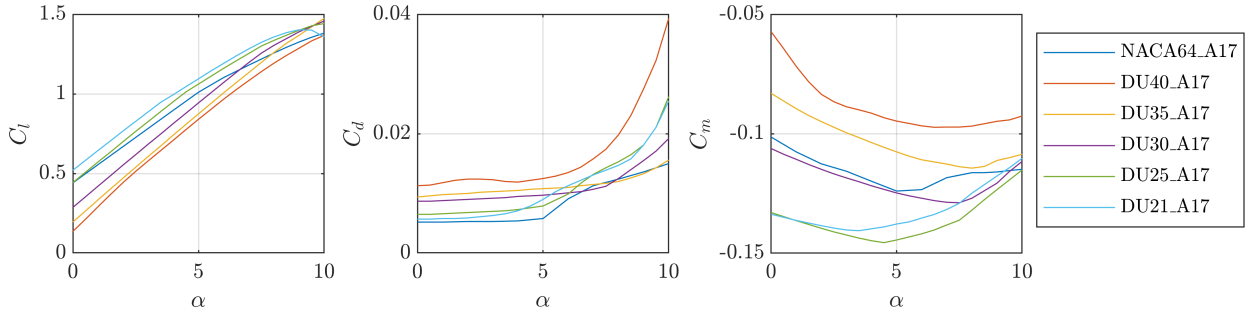

Figure 5.5: Aerodynamic coefficients of the six airfoils of the NREL 5 MW wind turbine.

5.2 Fluid Setup

To define a sound geometrical domain, able to capture the physics of the wake behind the wind turbine, and to adopt a reasonable resolution, balancing accuracy and computational cost, we performed a preliminary study to establish the fluid setup for our simulations.

When Large Eddy Simulations with the Actuator Line Model are adopted to study the flow field produced by the wind turbines, generally large domains are considered to minimise the undesired effects of the boundary conditions. Sarlak et al., 2016 [169] define un upper limit for the blockage ratio BR, *i.e.* the ratio between the area swept by the rotor $\pi D^2/4$ and the frontal section of the computational domain $L_2 L_3$, in correspondence with the optimal TSR equal to approximately 0.05. For larger values of the BR ratio the small computational domain starts to affect also the mean velocity of the wake. Moreover, from previous works in our groups, we noticed that using a reduced extent of the fluid domain in the direction normal to the wall (L_2) can affect the results too, even if the overall blockage ratio is below the Sarlak's threshold.

[169]: Sarlak et al. (2016), 'Assessment of blockage effects on the wake characteristics and power of wind turbines'

For this reason, the starting point of the study of our setup configuration was a mesh with $L_2 = 10D$ and $L_3 = 5.76D$ ($BR = 0.013$). The fluid domain streamwise extension of $L_1 = 9D$ is probably smaller than the usual longitudinal extensions used in similar simulations, but it proved to be sufficient to study the phenomena of interest for this work, and allowed faster simulations with the final fine resolution adopted. After a first set of coarse simulations with 50 points per diameter, we reduced the later extension of the domain to $L_3 = 2.88D$ ($BR = 0.027$) and we increased the number of points to obtain a uniform resolution of 150 points per diameter in the region of the rotor.

Figure 5.6 shows the two-point autocorrelation in the spanwise direction of the three velocity components $R_{u_i u_i}(\zeta)$ at the hub height in a region close to the inlet. The decay of the curves proves that the reduced lateral extension is still sufficient to avoid most of the undesired confinement effects of the large-scale structures from the periodic lateral boundary conditions. As a result, the chosen spanwise extension seems to be a good compromise between computational cost and sufficient domain width.

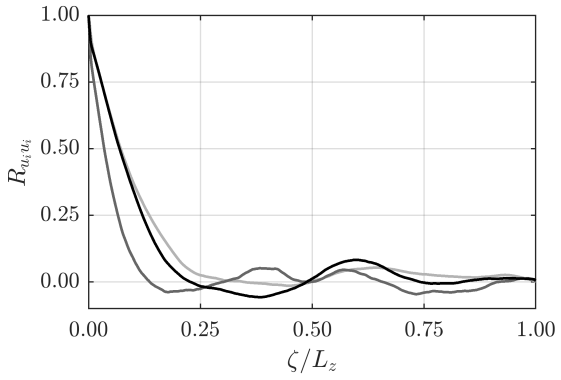

Figure 5.6: Two-point autocorrelation in the spanwise direction of the velocity components at hub height and close to the inlet ($R_{u_1 u_1}$ –, $R_{u_2 u_2}$ –, $R_{u_3 u_3}$ –).

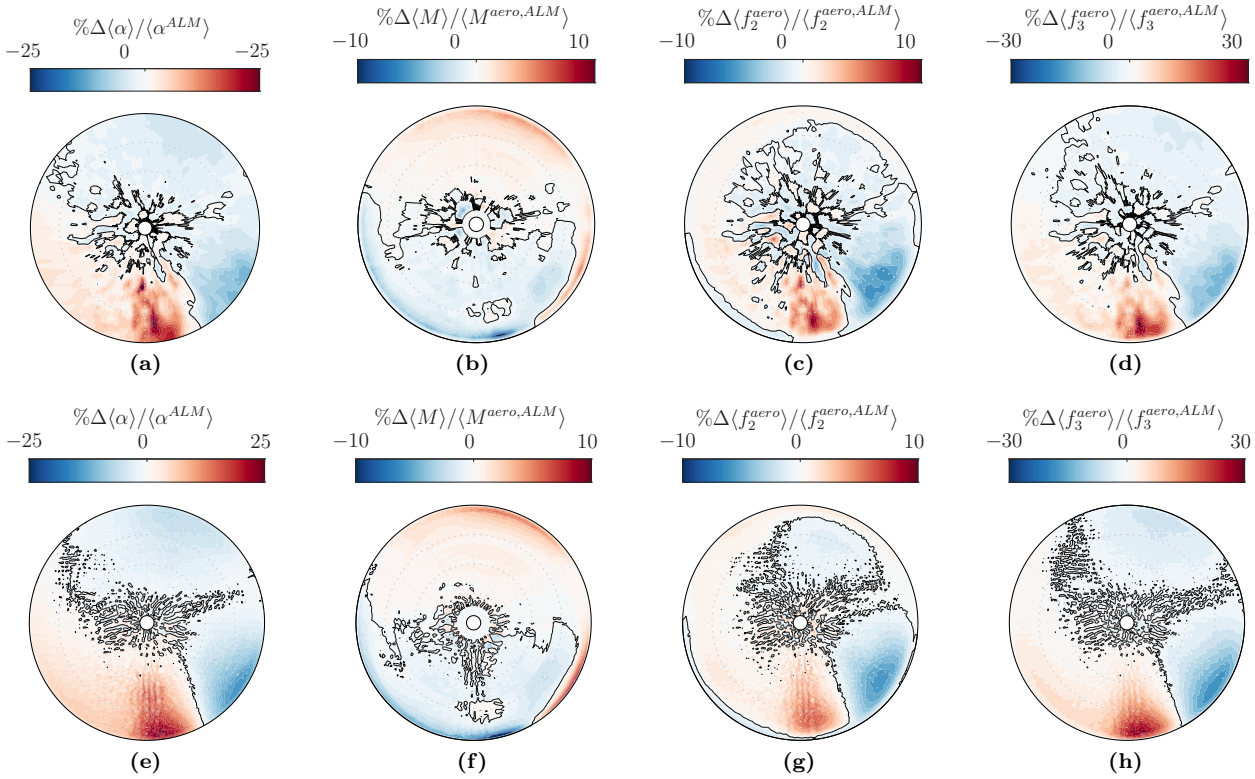

Figure 5.7: Percentage difference of the phase-averaged results of one of the coupled simulations (ALM/IV, see Section 5.4) with respect to the uncoupled simulations (ALM) results (see Chapter 6 for further explaination). The first row reports the difference for the incidence, the aerodynamic moment, the out-of-plane and in-plane aerodynamic force for the case with 50 points per diameter, the second row reports the corresponding plots for the case with 150 points per diameter.

For what concerns the grid sensitivity study, the change in resolution between 50 and 150 points did not produce particular changes except for an obvious increased resolution in the description of the fluid field and the aerodynamic forces. However, the aeroelastic behaviour that will be presented in Chapter 6 did not show relevant changes (see Figure 5.7). We then tried to increase further the resolution to 200 points per diameter, with fixed domain geometry, but even in this case no particular change was observable in the physical description despite a relevant increase in the computational cost of the simulations. For this reason, we opted for the final resolution of 150 points per diameter, which represents a good compromise between accuracy and computational cost. Moreover, such a resolution is far beyond the grid requirements suggested by Troldborg et al., 2009 [132], which indicates in 50 points per diameter the minimum resolution required by the Actuator Line Model.

The final fluid computational domain, shown in Figure 5.8, was thus equal to $9.00D \times 10.00D \times 2.88D$ in the streamwise, wall-normal and spanwise inertial directions respectively. We discretised the domain by means of a structured orthogonal mesh of $1297 \times 433 \times 433$ points. While the streamwise and lateral discretisations are uniform, after 300 equally-spaced points covering the lowest portion of the domain (to obtain an isotropic grid in the rotor region), we stretched the grid in the wall normal direction as shown in Figure 5.9, in order to better optimise the grid in the y direction and to limit the overall grid requirements.

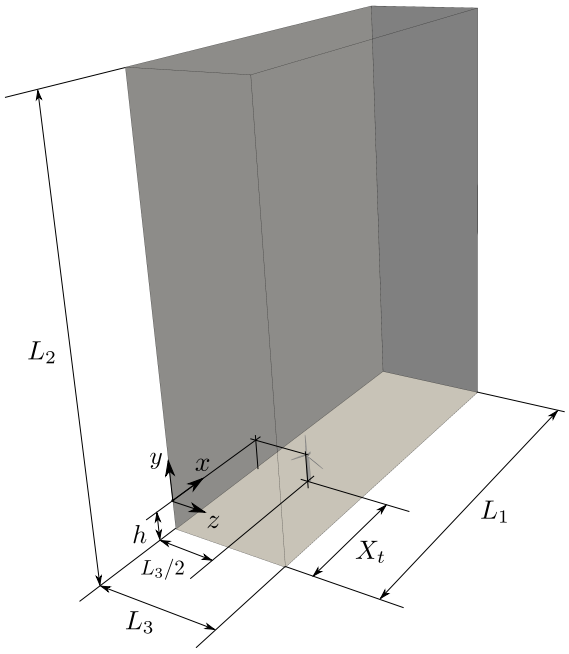

Figure 5.8: Typical fluid domain of our simulations with the adopted nomenclature.

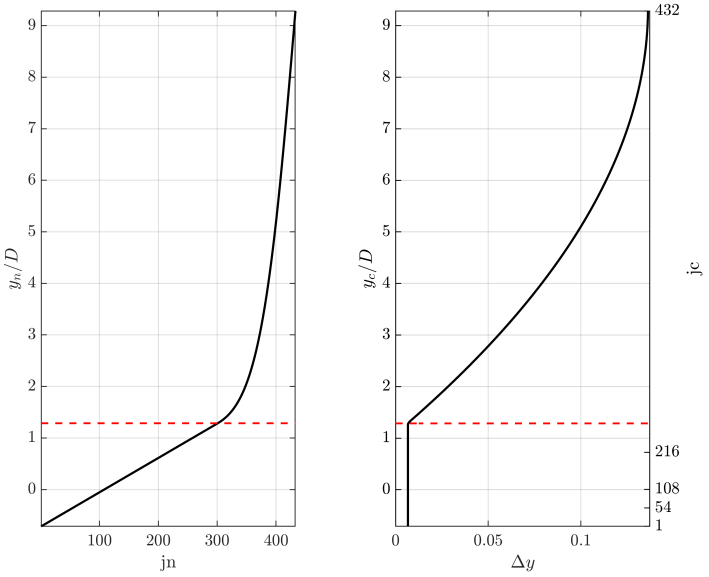

Figure 5.9: Vertical grid distribution. Nondimensional grid point coordinate y_n/D as a function of the node index jn (left). Nondimensional cell centre coordinate y_c/D (left axis) and cell number jc (right axis) as a function of the corresponding cell spacing Δy (right). More than the half of the points is concentrated in the rotor region.

The wind turbine is located at the spanwise centre of the domain and at a streamwise distance of approximately $3D$ from the inlet. Additional tests where the wind turbine was located further downstream from the inlet did not produce relevant differences in the considered computational domain (Figure 5.10).

Finally, we prescribed periodic boundary conditions at the lateral boundaries, free-slip boundary condition at the top surface, and radiative boundary conditions at the outlet. Van Driest damping functions [125] correct the behaviour of the flow close to the no-slip bottom wall.

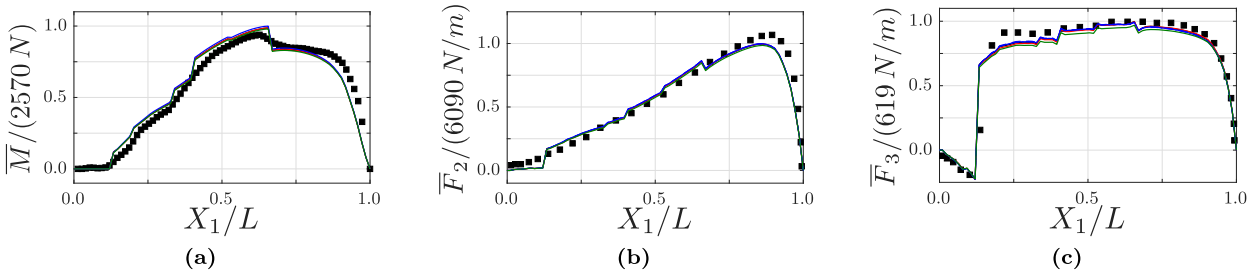

Figure 5.10: Distribution along the blades of the time-averaged aerodynamic moment (a), flapwise force (b), and edgewise force (c) for two different streamwise positions X_t of the wind turbine and two FSI coupling conditions (ALM and ALM/IV). ALM $x_t/D = 3$ –, ALM/IV $x_t/D = 3$ –, ALM $x_t/D = 5$ –, ALM/IV $x_t/D = 5$ –, HAWC2 [46] ■.

Fluid inflow analysis

Given the fact that turbulence and flow asymmetries caused by wind shear can be sources of unsteadiness for the blade dynamics, we assumed for many of the cases in this study to operate in sheared turbulent conditions. We derived the inflow turbulent fluctuations from a precursor simulation in a fully periodic domain with cubic surface roughness, and we imposed a sound mean streamwise velocity profile defined by the power law:

$$\frac{U_\infty(y)}{U_{hub}} = \left(\frac{z}{z_{hub}}\right)^\alpha . \tag{5.1}$$

with shear exponent α and mean hub velocity U_{hub}. Typical values of the shear exponent are $\alpha \in [0.1, 0.3]$ [9].

The inflow velocity fluctuations are sampled at a $y - z$ plane at the end of the precursor domain at a constant frequency rate and are fed in reverse order to the main simulation, assuming the classic Taylor's frozen turbulence hypothesis. Figure 5.11 reports an example of an inflow velocity plane, showing the zero-mean velocity fluctuations for a vertical slice at a generic time instant.

In order to assess the quality of the inflow fields provided by the boundary-layer precursor simulations, we compared the spectra obtained from the LES precursor simulations with the ones obtained from one of the most widely adopted synthetic turbulence models in wind energy, the Mann model [57]. The Mann model represents the fluctuations of the velocity fields by means of a generalised Fourier-Stieltjes integral of spectral components that reproduce by construction the second-order statistics of the atmospheric boundary layer. In fact, a model of the spectral tensor for the atmospheric surface layer turbulence at high speeds is obtained from the linearised Navier-Stokes equations under the assumption of linear shear in the mean velocity [170] and is imposed a priori to build the fluid field. In order to obtain the velocity fluctuations and statistics of the Mann model, we used the IEC turbulence generator distributed by WAsP Engineering [171], a freeware black box tool providing the velocity fields in neutral stability for given parameters of the Mann model, according to the recommendations of the international standard IEC 61400-1 Ed.3 [172].

[57]: Mann (1998), 'Wind field simulation'

[170]: Mann (1994), 'The spatial structure of neutral atmospheric surface-layer turbulence'
[171]: WAsP Engineering (2020), *Wind conditions for fatigue loads, extreme loads and siting*
[172]: IEC (2005), *IEC 61400-1 ed. 3. Wind turbines - part 1: Design requirements*

Figure 5.12 shows the comparison of the premultiplied spectra of the streamwise velocity fluctuations obtained from the precursor simulation results, the Mann model and also the theoretical Von Kármán model for the incompressible isotropic turbulence [173]. The a priori imposition of the spectral quantities makes the Mann model spectrum well defined for the entire wavenumber range. On the other hand, the precursor is able to reproduce the typical $-5/3$ law, although the limited temporal sampling adopted to extract the velocity inflow, then fed to the main simulations, produces an undersampling error observable in the high-wavenumber range. However, the simulation is able to provide a physically sound field without particular limiting assumption on the mean field, as in the theoretical models, and with the accuracy in the fluid dynamics description stemming from a high-fidelity LES simulation of the boundary layer.

[173]: Von Karman (1948), 'Progress in the statistical theory of turbulence'

Finally, Table 5.2 reports a synthetic overview of the main features of the mean fields and of the turbulent fluctuations for the inflow sets adopted in this work. In particular, we report the imposed mean velocity at the hub U_{hub} and the shear exponent α that define the mean shear, the nondimensional integral length scales ℓ_1/D derived from the autocorrelation of the streamwise velocity fluctuations at the hub, and the weighted average of the streamwise turbulence intensity $TI\% = 100\,\sigma_u/U$ on the rotor area. In order to distinguish in the table the different inflows, we indicate with LAM the case of the laminar uniform inflow, with T1 the case of the first turbulent inflow with the lower turbulence intensity, and with T2 the case of the second turbulent inflow with the higher turbulence intensity.

Acronym	U_{hub}	α	ℓ_1/D	$TI\%$
LAM	10 m/s	0.00	–	0
T1	10 m/s	0.14	1.0	2
T2	10 m/s	0.20	2.3	10

Table 5.2: Overview of the main features of the fluid inflows adopted.

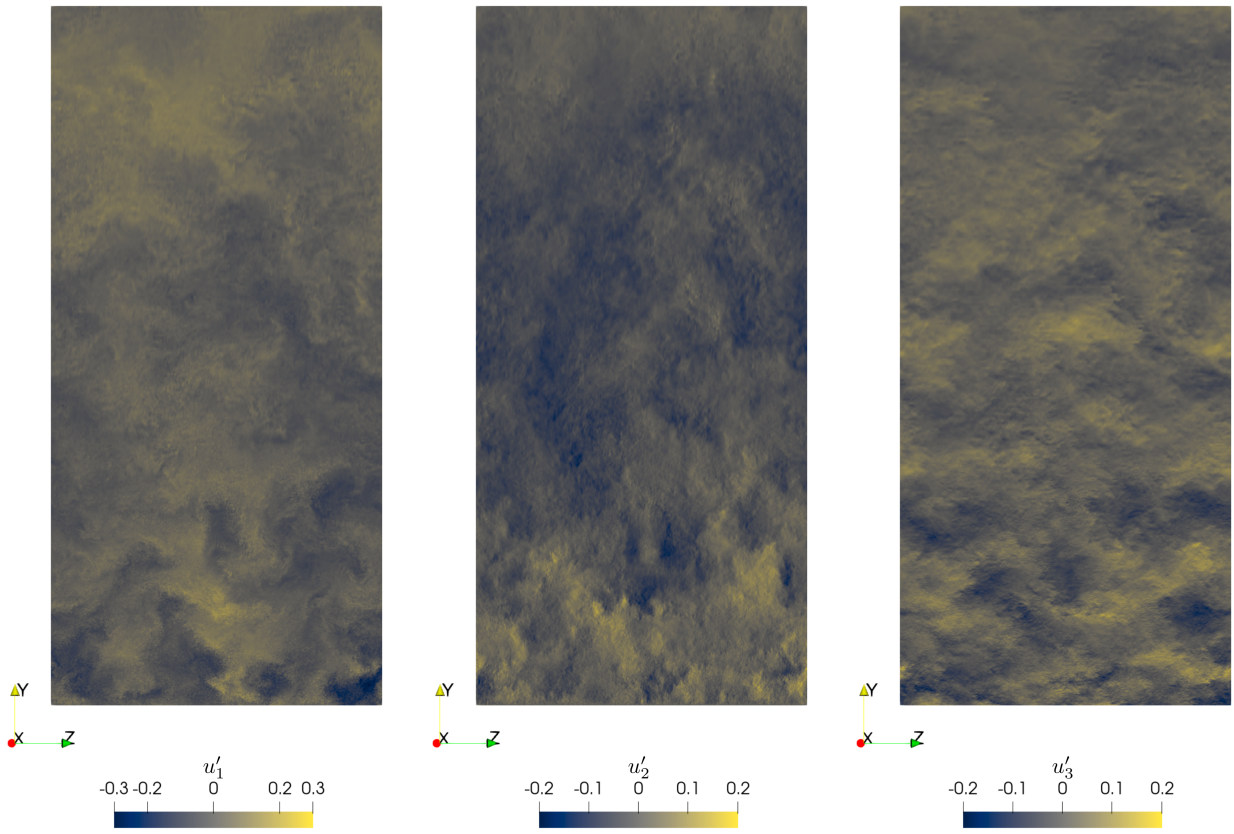

(a) u_1' **(b)** u_2' **(c)** u_3'

Figure 5.11: Instantaneous fluctuations of the velocity components from the precursor simulation on a vertical slice at a generic time instant.

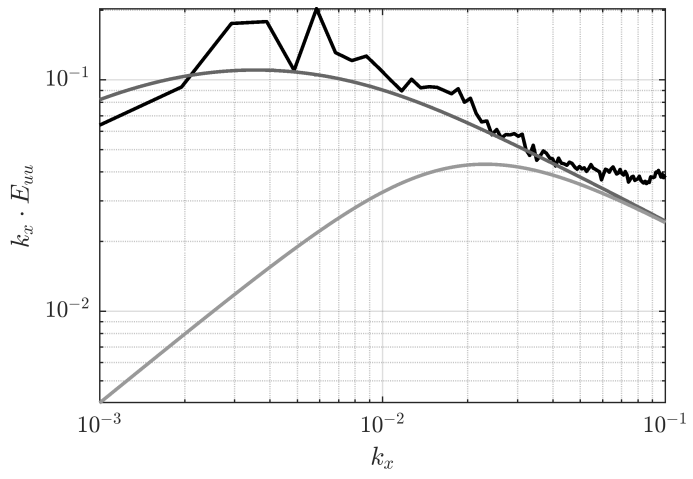

Figure 5.12: Comparison of the pre-multiplied spectra of the streamwise velocity component at hub height. Precursor data –, Mann model –, Von Kármán isotropic turbulence.

5.3 Structural Setup

To define the setup of the structural solver, we also carried out a preliminary study, to decide the proper number of modes and structural nodes for the problem.

As a first thing, we verified that the spatial resolution of the structural model used to carry out the modal analysis was sufficient to obtain converged results in terms of eigenfrequencies. We thus repeated the modal analysis for four different discretisation charaterised by a number of nodes equal to $N = 40, 80, 160, 320$ and we compared the results of the eigenproblem with a fine solution obtained with $N = 500$ nodes. Figure 5.13 shows the percentage relative difference of the first ten eigenfrequencies as a function of the grid uniform spacing with respect to the results of the fine case. It is possible to observe that a discretisation of $N = 80$ points is sufficient to obtain a relative percentage error much smaller than 1 %, although already 40 points guarantee a relative error below 4 %. In order to validate the structural model built for the blade, we compared the results of the eigenproblem also with the ones obtained by a modal analysis in MSC Nastran, and the results are almost identical.

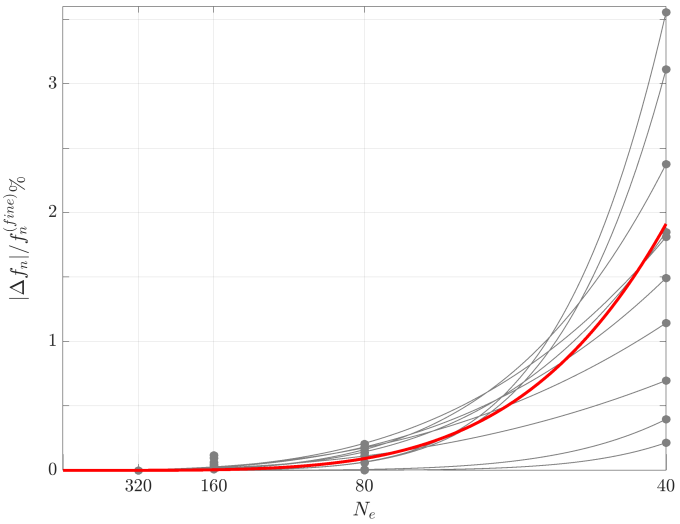

Figure 5.13: Percentage relative difference of the first ten eigenfrequencies as a function of the grid uniform spacing with respect to the reference fine case results. The number of nodes N corresponding to the grid spacings taken into consideration is reported on the x axis instead of the spacing itself. In red the average relative difference.

Figure 5.14 shows a comparison of the final natural frequencies of the blade structural model compared to similar results from the literature (only the first six modes are usually available). Table 5.3, instead, reports the dominant nature of the first fifteen eigenmodes together with the numerical values of the corresponding eigenfrequencies.

As an example, the behaviour of the 6 DOFs for the first 6 natural modes of the blades is reported in Figure 5.15 - Figure 5.20. A three-dimensional representation, with amplified magnitude, of the first flapwise, edgewise and torsional modes is reported instead in Figure 5.21 - Figure 5.23.

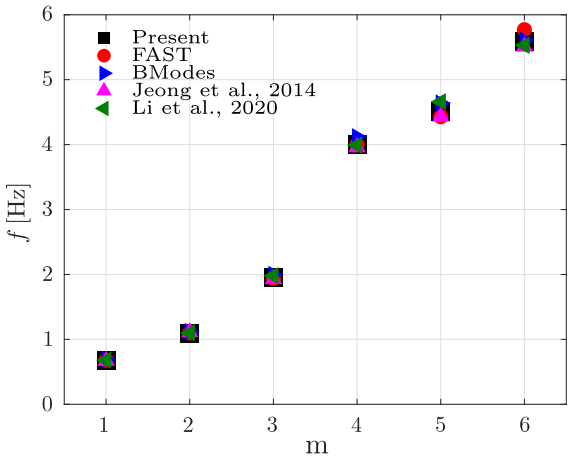

Figure 5.14: Comparison of the first six eigenfrequencies obtained with several results from the literature.

Table 5.3: Eigenfrequencies and main features of the first 15 modes.

#	$f_n\,[Hz]$	Mode
1	0.6763	1st flapwise
2	1.0858	1st edgewise
3	1.9485	2nd flapwise
4	4.0037	2nd edgewise
5	4.5167	3rd flapwise
6	5.5837	1st torsional
7	8.0219	4th flapwise
8	9.3914	3rd edgewise
9	9.7606	2nd torsional
10	12.5399	5th flapwise
11	14.5479	1st axial
12	14.7693	3rd torsional
13	17.1275	4th edgewise
14	18.1003	6th flapwise + 4th torsional
15	20.1605	4th torsional + 6th flapwise

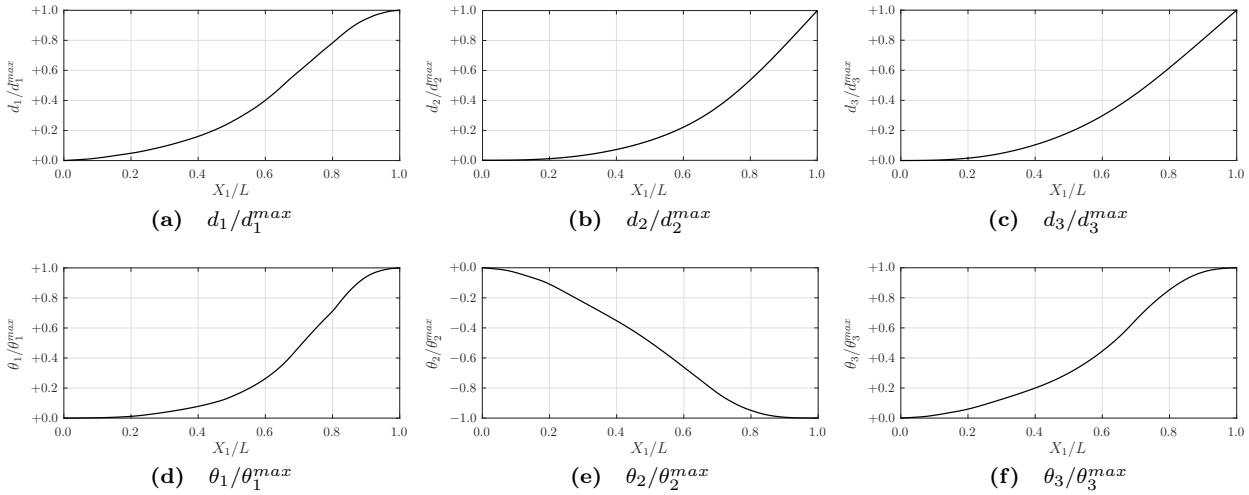

(a) d_1/d_1^{max} **(b)** d_2/d_2^{max} **(c)** d_3/d_3^{max}

(d) θ_1/θ_1^{max} **(e)** θ_2/θ_2^{max} **(f)** θ_3/θ_3^{max}

Figure 5.15: Mode 1 DOFs.
$d_1^{max} = 3.61e-08$, $d_2^{max} = 3.36e-02$, $d_3^{max} = 3.81e-03$, $\theta_1^{max} = 1.66e-04$, $\theta_2^{max} = 1.20e-04$, $\theta_3^{max} = 1.32e-03$.

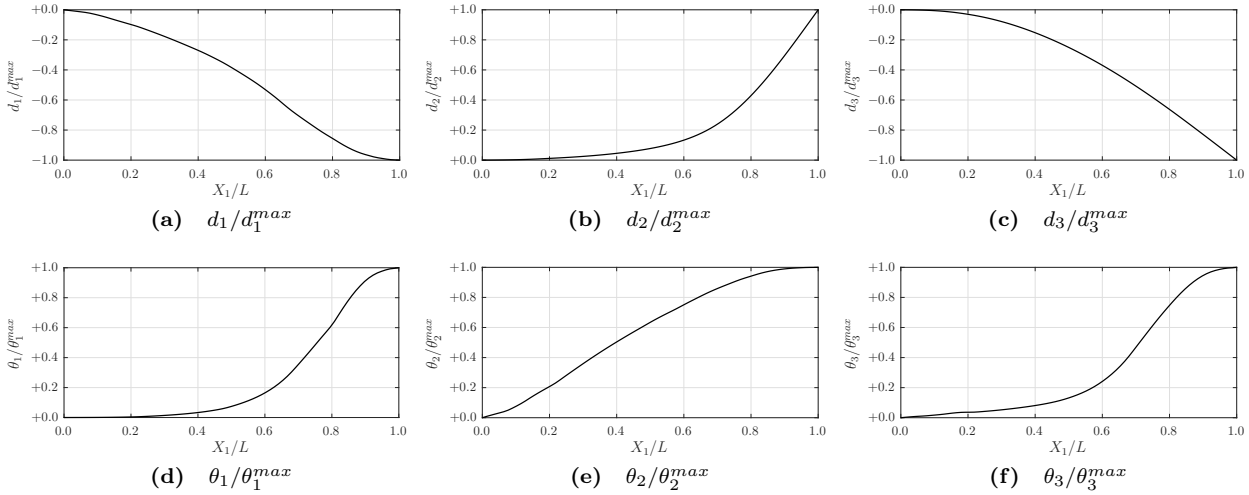

(a) d_1/d_1^{max} **(b)** d_2/d_2^{max} **(c)** d_3/d_3^{max}

(d) θ_1/θ_1^{max} **(e)** θ_2/θ_2^{max} **(f)** θ_3/θ_3^{max}

Figure 5.16: Mode 2 DOFs.
$d_1^{max} = 9.78e-07$, $d_2^{max} = 5.31e-03$, $d_3^{max} = 2.63e-02$, $\theta_1^{max} = 4.41e-05$, $\theta_2^{max} = 7.32e-04$, $\theta_3^{max} = 2.68e-04$.

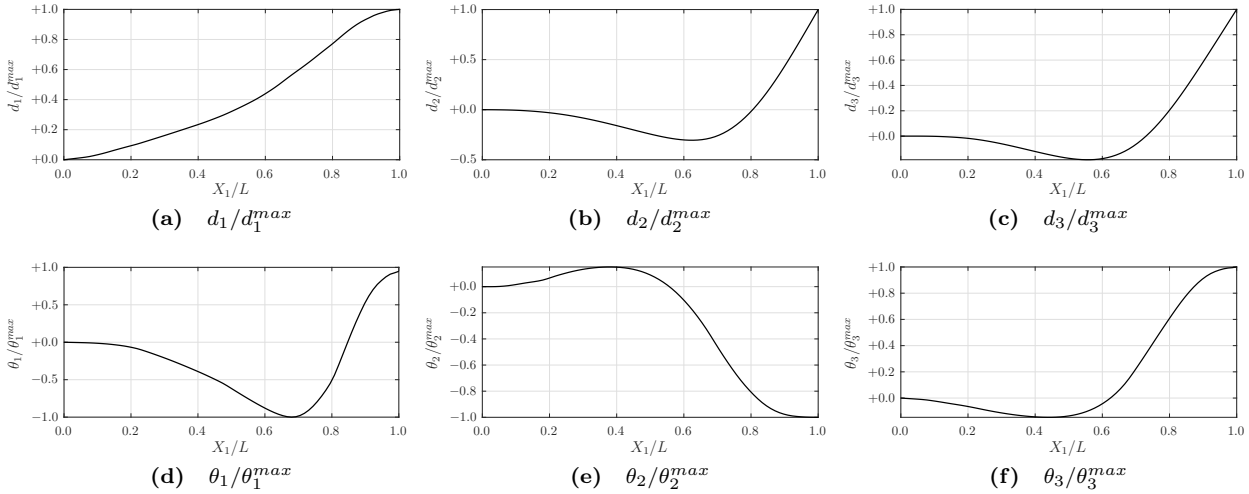

(a) d_1/d_1^{max} **(b)** d_2/d_2^{max} **(c)** d_3/d_3^{max}

(d) θ_1/θ_1^{max} **(e)** θ_2/θ_2^{max} **(f)** θ_3/θ_3^{max}

Figure 5.17: Mode 3 DOFs.
$d_1^{max} = 4.89e-07$, $d_2^{max} = 4.20e-02$, $d_3^{max} = 3.29e-03$, $\theta_1^{max} = 2.09e-04$, $\theta_2^{max} = 2.24e-04$, $\theta_3^{max} = 3.99e-03$.

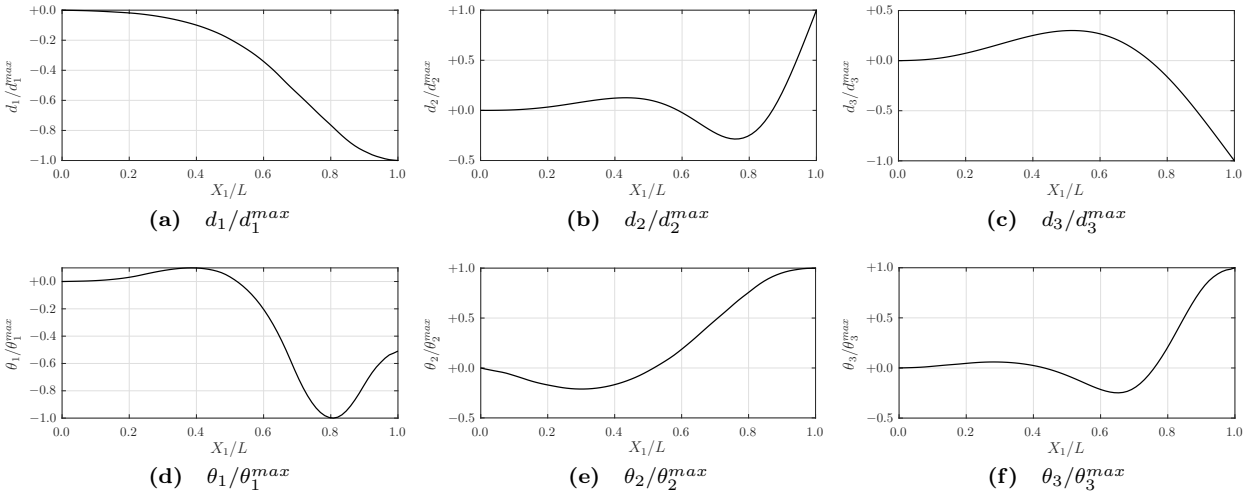

(a) d_1/d_1^{max} **(b)** d_2/d_2^{max} **(c)** d_3/d_3^{max}

(d) θ_1/θ_1^{max} **(e)** θ_2/θ_2^{max} **(f)** θ_3/θ_3^{max}

Figure 5.18: Mode 4 DOFs.
$d_1^{max} = 3.01e-05$, $d_2^{max} = 1.36e-02$, $d_3^{max} = 3.57e-02$, $\theta_1^{max} = 3.70e-04$, $\theta_2^{max} = 2.62e-03$, $\theta_3^{max} = 1.94e-03$.

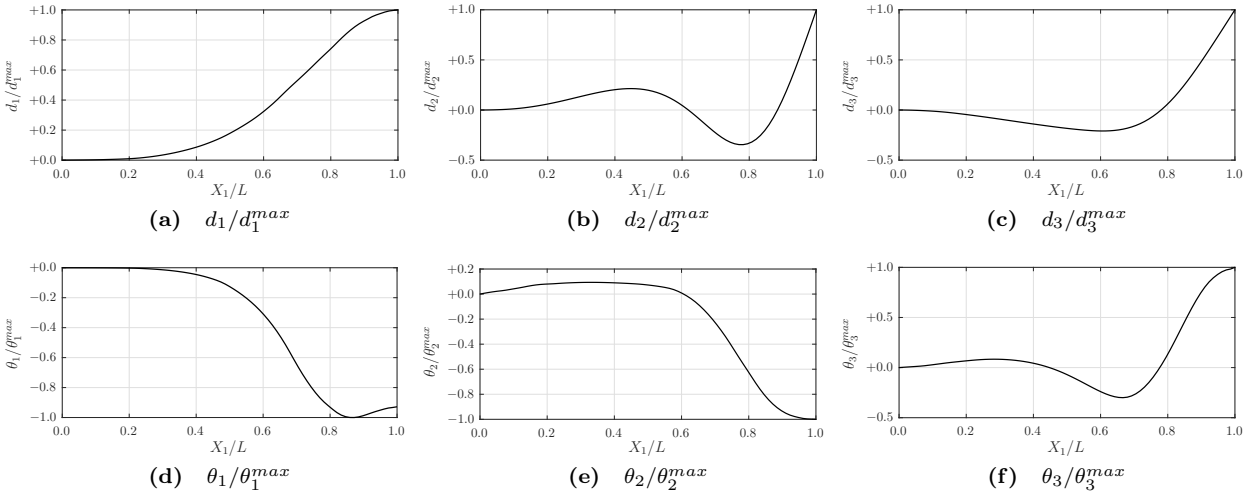

(a) d_1/d_1^{max} **(b)** d_2/d_2^{max} **(c)** d_3/d_3^{max}

(d) θ_1/θ_1^{max} **(e)** θ_2/θ_2^{max} **(f)** θ_3/θ_3^{max}

Figure 5.19: Mode 5 DOFs.
$d_1^{max} = 1.13e-05$, $d_2^{max} = 4.59e-02$, $d_3^{max} = 1.07e-02$, $\theta_1^{max} = 4.51e-03$, $\theta_2^{max} = 9.19e-04$, $\theta_3^{max} = 7.27e-03$.

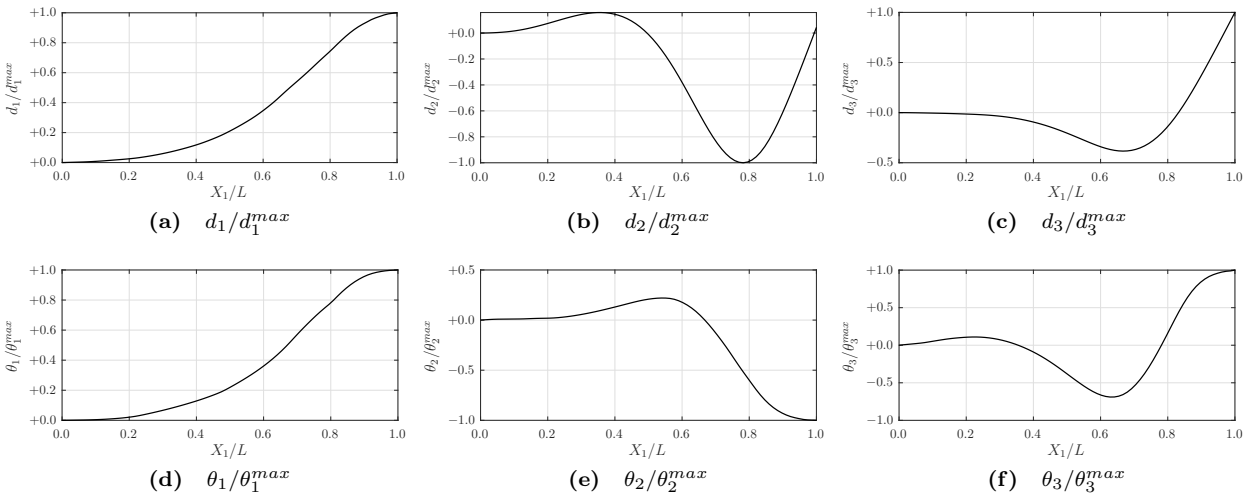

(a) d_1/d_1^{max} **(b)** d_2/d_2^{max} **(c)** d_3/d_3^{max}

(d) θ_1/θ_1^{max} **(e)** θ_2/θ_2^{max} **(f)** θ_3/θ_3^{max}

Figure 5.20: Mode 6 DOFs.
$d_1^{max} = 2.90e-06$, $d_2^{max} = 7.60e-03$, $d_3^{max} = 1.39e-03$, $\theta_1^{max} = 3.44e-02$, $\theta_2^{max} = 1.45e-04$, $\theta_3^{max} = 8.51e-04$.

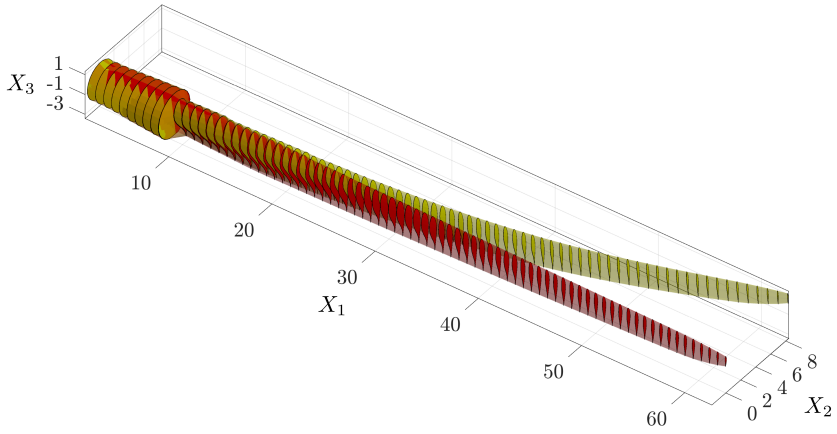

Figure 5.21: First flapwise mode (amplified magnitude).

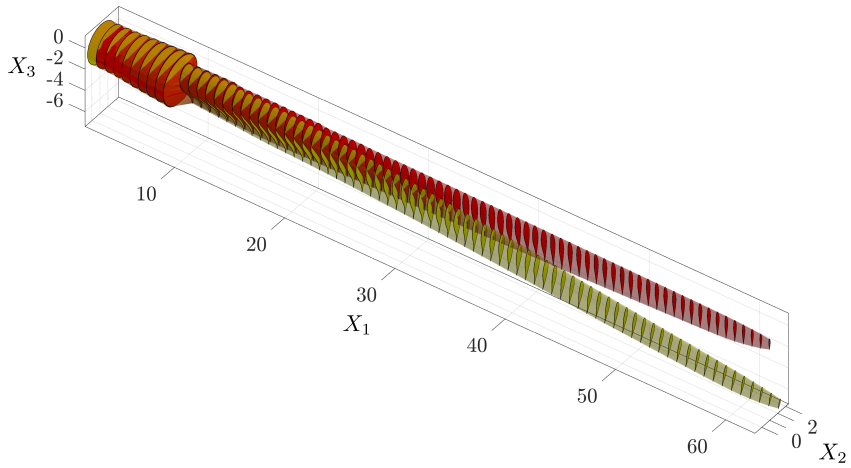

Figure 5.22: First edgewise mode (amplified magnitude).

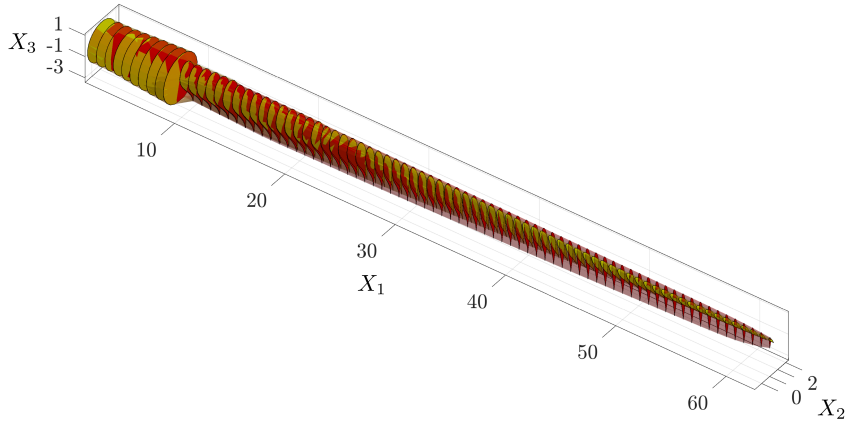

Figure 5.23: First torsional mode (amplified magnitude).

We then tried to carry out a "static" and "dynamic" study of the convergence also of the eigenmodes, in the attempt of establishing the number of nodes and modes to be adopted in the structural model of our simulations. In order to do this, we have considered the following issues:

- the structural resolution defined by the number of nodes along the blade, should not be much different from the fluid one. As already pointed out, several studies in the literature [132, 137] suggest that a discretisation of the actuator line with at least 25 points would be necessary to capture the fluid flow behind the wind turbine. This represents, thus, a lower limit for the structural discretisation too, in order not to lose the spatial accuracy in the airloads distribution provided by the fluid solver. However, this resolution could not be sufficient to obtain convergence and accuracy of the structural dynamics and additional considerations should be taken into account.
- A poor resolution in space of the structure deteriorates the accuracy in space of the eigenmodes from the modal analysis and thus can also compromise the modal projection of the loads, affecting the overall estimation of the structural dynamics.
- The number of structural nodes should be able to actually describe the modal shape and to avoid spatial aliasing for high frequency – and wavenumber – eigenmodes. As a matter of fact, higher frequency modes are characterised by a higher wavenumber content that is fundamental if one wants to attempt to capture the eventual high wavenumber content of the loads acting on the structure. Modal forces are space projections of the nodal loads, given by the convolution of the load distribution along the span and the modal shapes. As a result, an erroneous estimation of the wavenumber spectral content of the modes due to a poor number of nodes, can be highly detrimental for the correct projection of those loads that vary considerably along the blade.
- Finally, the range of eigenfrequency considered defines the structural response in time. Hence, the number of modes should be such that the considered eigenfrequencies are able to describe the typical characteristic frequencies of the loads. Given the typical spectra of the moment reactions (see Figure 5.24), it can be seen that most of the energy content of the forcing is in the low-frequency range, below 4 Hz. Hence, for our structure and its eigenfrequencies (Table 5.3), a minimum number of modes $N_m = 4$ is necessary to describe the essential dynamics of the structure.

Given these considerations, we examined the solution of a reference test case with four different numbers of nodes $N = 40, 50, 80, 100$ and five different numbers of corresponding modes $N_m = 4, 8, 12, 16, 20$. The case consisted in the unsteady response of the blade for a rotor revolution, under the sinusoidal gravity loading and a constant aerodynamic loading in the flapwise, edgewise and torsional directions. The results obtained were then compared with a reference solution derived with a discretisation of $N = 400$ points and a number of modes $N_m = 40$. The norm of the difference between all the degrees of freedom of the

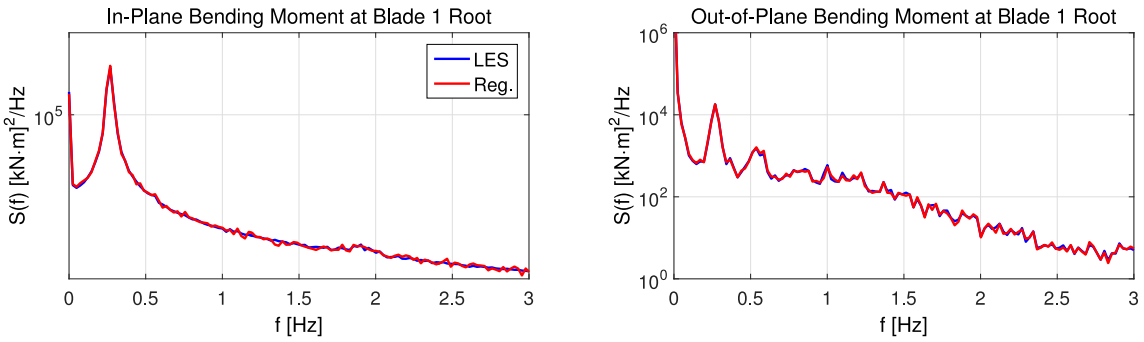

Figure 5.24: Power spectra of the in-plane (left) and out-of-plane (right) bending moments at the blade root. [174]

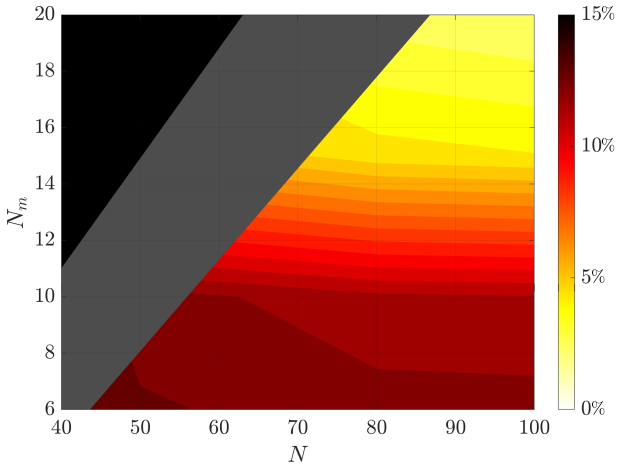

Figure 5.25: Sensitivity map reporting the error of the test case solution obtained with given N and N_m with respect to a reference fine solution. Each of the – percentage – values of the contour is determined as the L2-norm of the difference, for all the degrees of freedom, between the solution obtained with the corresponding N and N_m and the reference solution, divided by the L2-norm of the reference solution itself. Regions of N and N_m producing inadequate description of the modal shapes (black) and of their wavenumber spectra (grey) have been removed.

solutions considered and the ones of the reference solution is reported, with respect to the norm of the reference solution itself, as a function of N and N_m in Figure 5.25. As it can be noticed, we considered an increased minimum number of modes equal to $N_m^{min} = 6$, given also the large error produced by the use of too few modes. Moreover, we have excluded from the maps the regions for which the number of nodes adopted is not able to produce an adequate description of the modal shapes and of their wavenumber spectra, according to errors' thresholds that have been tuned manually.

In the end, in order to obtain a reduced error and to use a reduced number of nodes and modes, we chose a number of modes $N_m = 15$ and a structural discretisation of the blades given by $N = 80$ equally-spaced nodes. As proved also in the next chapter, this setup is sufficient to capture the most important features of the structural dynamics of the blades.

5.4 Summary of the Simulations

At last, we report a brief overview of the simulations that we analyse in the following chapters in Table 5.4. For the sake of brevity, we define some acronyms to identify the set of simulations performed in terms of FSI coupling and aerodynamics model. In particular, we have:

ALM One-way FSI coupled simulations with steady aerodynamics. The fluid solver sees the blades as rigid and the structural solver evaluates at runtime the blades' deformation on the basis of the actuator line aerodynamic forces provided only by the fluid solver using the static tabulated data of the airfoils.

ALM/IV Two-way FSI coupled simulations with steady aerodynamics. In these simulations, the structural feedback to the fluid solver is made only of the instantaneous *bending deformation velocities* of the blades provided by the structural solver at runtime.

ALM/IVT Two-way FSI coupled simulations with steady aerodynamics. In these simulations, the structural feedback to the fluid solver includes also the instantaneous *torsional deformation* of the blades in the definition of the local incidence.

ALM-UA One-way FSI coupled simulations with UA. The fluid solver does not include any structural feedback to determine the local incidence, but adopts a UA model to determine dynamically the airfoil force and moment coefficients.

ALM/IV-UA Two-way FSI coupled simulations with UA. The instantaneous local incidence includes the effect of the blades structural motion and the UA model determines dynamically the aerodynamic coefficients.

We ran each simulation set for a Reynolds number based on the rotor diameter and the hub velocity $Re = 8.5 \times 10^7$, for approximately 60 revolutions, corresponding to almost 300 s, after the initial transient.

Table 5.4: Outline of all the simulations carried out.

#	Name	Inflow	Def.Vel.	Torsion	UA
1	ALM	T1	No	No	No
2	ALM/IV	T1	Yes	No	No
3	ALM/IVT	T1	Yes	Yes	No
4	ALM	LAM	No	No	No
5	ALM/IV	LAM	Yes	No	No
6	ALM-UA	LAM	No	No	Yes
7	ALM/IV-UA	LAM	Yes	No	Yes
8	ALM	T2	No	No	No
9	ALM/IV	T2	Yes	No	No
10	ALM-UA	T2	No	No	Yes
11	ALM/IV-UA	T2	Yes	No	Yes

6 Effects of the Flexibility

This chapter presents the analysis of the results of the first three sets of simulations, ALM, ALM/IV and ALM/IVT, under T1 inflow conditions. The aim of the comparison is to assess the capabilities of our novel model to represent the aeroelastic response of our reference wind turbine and to evaluate the effect of the flexibility on its overall behaviour.

At first, we consider the power and thrust coefficients. Next, we discuss the structural dynamics in terms of displacement and deformation velocity components. Then, we analyse the change of the aerodynamic forces and the dynamics of the root reaction. Finally, we present a fluid flow analysis presenting mean field slices and visualisations of the coherent structures in the domain.

Before proceeding further, we inform the reader that hereinafter, we indicate the time average with an overbar symbol $\overline{\bullet}$ and the phase average with angle brackets $\langle\bullet\rangle$. The phase average of a generic quantity χ defined for each azimuthal position $\Theta(t)$ is defined as:

$$\langle\chi\rangle\left(\overline{\Theta}\right) = \mathrm{E}(\chi|\Theta(t) = \overline{\Theta}) \text{ with } \overline{\Theta} \in [0, 2\pi), \tag{6.1}$$

where we indicate with $\mathrm{E}(\chi|\Theta = \overline{\Theta})$ the conditional average of the variable χ given the sampling variable $\overline{\Theta}$. For ease of notation, we simply indicate the sampling variable of the phase average with Θ.

6.1 Power and Thrust Coefficients

From the time history of the power coefficient C_P and the thrust coefficient C_T, normalised by means of the mean hub velocity U_{hub},

The GE Haliade-X prototype is the world's most powerful wind turbine operating to date. It operates at a 13 MW power output and has a 220-metre rotor diameter. It is reasonable to believe that for similar wind turbines, the structural deformations can affect the normal operating conditions.
The credits for the image above the chapter title go to GE Renewable Energy. https://www.ge.com/renewableenergy/wind-energy/offshore-wind/haliade-x-offshore-turbine

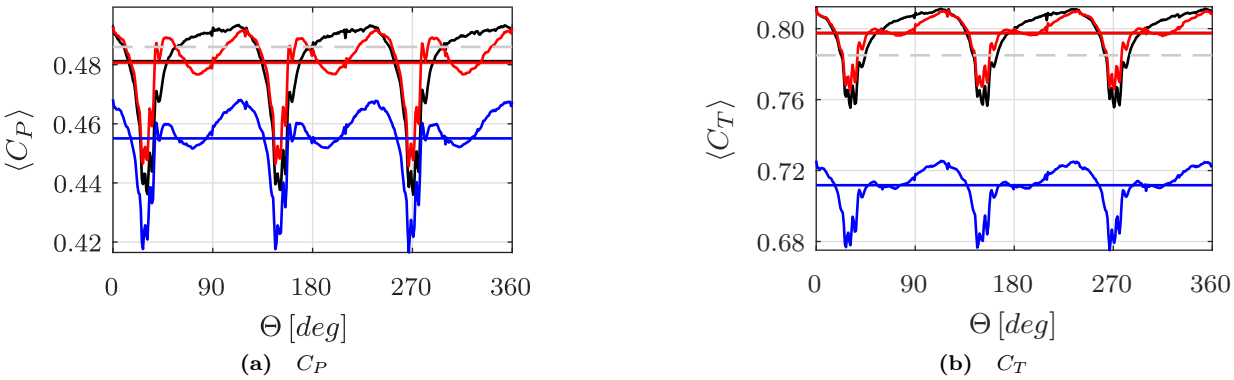

(a) C_P **(b)** C_T

Figure 6.1: Phase average of the power and thrust coefficients. ALM —, ALM/IV —, ALM/IVT —, BEM [51] - -. Horizontal straight lines indicate the corresponding time-averaged values.

Table 6.1: Comparison of the statistics of the power and thrust coefficients between the cases considered. The last two columns report the percentage difference of the statistics for the ALM/IV and ALM/IVT cases with respect to the ALM one.

	BEM	ALM	ALM/IV	ALM/IVT	$\Delta_{ALM/IV}$	$\Delta_{ALM/IVT}$
$\overline{C}_P$	0.4860	0.4812	0.4807	0.4551	- 0.1 %	- 5.4 %
$\overline{C}_T$	0.7860	0.7975	0.7975	0.7117	0.0 %	- 10.8 %
σ_{C_P}	–	0.0167	0.0128	0.0133	- 23.3 %	- 20.4 %
σ_{C_T}	–	0.0165	0.0130	0.0133	- 21.2 %	- 19.4 %

we computed the phase-averaged behaviour reported in Figure 6.1, to filter out the instantaneous fluctuations due to the turbulent inflow.

The periodic passage of the blades in front of the tower induces a tower shadow effect with a drop in the power and thust coefficients by about 10 %. The blade vibration influences the aerodynamic forces especially when the blade passes in front of the tower, consistently with previous observations [56]. In particular, the addition of the aeroelastic coupling reduces the amplitude of the oscillations, and thus the standard deviation of the two coefficients (Table 6.1). The time-averaged power and thrust coefficient obtained with rigid ALM and ALM/IV are almost identical (see Table 6.1 and the horizontal lines in Figure 6.1), despite the differences observed before in the instantaneous value of the forces. However, when we also consider the torsion of the airfoil section, the power is significantly reduced, by approximately 5 % with respect to the other two cases. Similarly, the thrust is about 10 % smaller, which could also affect a possible *a posteriori* estimation of the tower deflection [175]. In general, this seems to imply that simulations perfomed considering the blades as infinitely rigid overestimate the power coefficient and also the momentum deficit behind the turbine.

[175]: Feliciano et al. (2018), 'Generalized analytical displacement model for wind turbine towers under aerodynamic loading'

Figure 6.2 presents the Power Spectral Density (PSD) obtained from the time signals of the coefficients, to assess if the coupling procedure affects the frequency content of the power and thrust signals. The periodic passage of the three blades and the tower shadow effect induces distinct peaks observable at the frequencies multiple of $3\,P$, with P being the rotational frequency. The spectral content of the ALM/IV case is almost the same as the one of the ALM case, whereas in the ALM/IVT case, the direct influence of the torsional deformation on the aerodynamic forces adds a small, but distinct, contribution of the first torsional

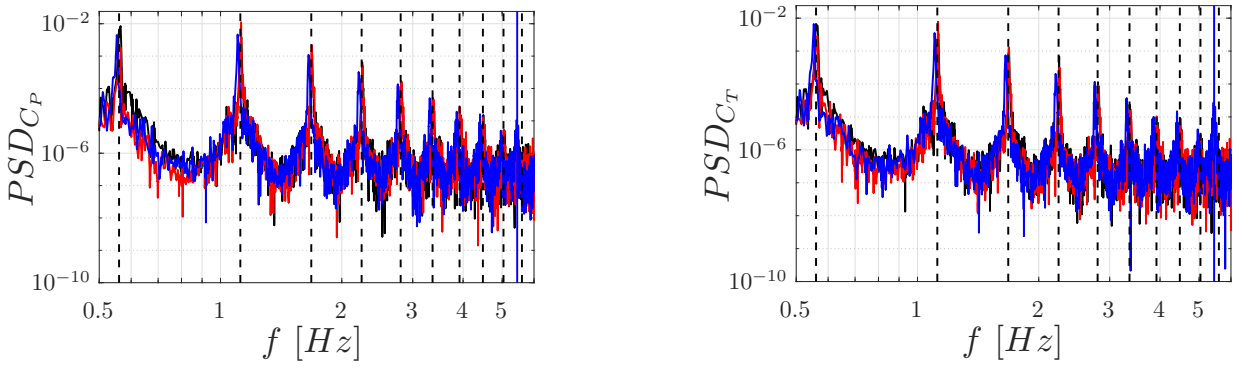

(a) C_P **(b)** C_T

Figure 6.2: PSD of the power and thrust coefficients signals. The peaks at multiples frequencies correspond to the multiples of $3\,P$, highlighted by vertical dashed lines, given the periodicity of the signal and of the passage of the blades. The vertical blue line indicates the first torsional natural frequency of the blade $f = 5.58\,\text{Hz}$ and underlines the peak of the PSD in the ALM/IVT case, especially for the thrust coefficient. ALM —, ALM/IV —, ALM/IVT —.

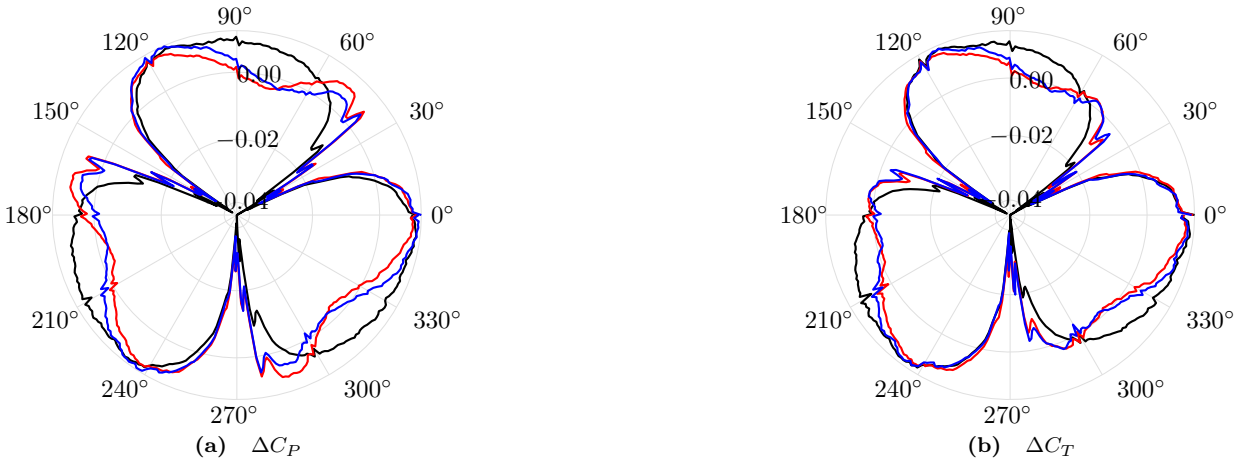

(a) ΔC_P **(b)** ΔC_T

Figure 6.3: Polar plots of the phase-averaged power and thrust coefficients fluctuations. ALM —, ALM/IV —, ALM/IVT —

natural frequency of the blades $f = 5.58\,\text{Hz}$ (see Table 5.3), typical of the torsional vibration, especially to the thrust coefficient.

To investigate the specific effect of the torsional dynamics in addition to the mean value reduction, Figure 6.3 compares the coefficients fluctuations for the three cases in a polar plot. The plots show that the torsional dynamics, and in particular the oscillation of the torsional angle caused by the tower, produces also a modification in the region between the two following minima of the coefficients compared to the ALM/IV case.

In Figure 6.4, we also report the probability density function (pdf) of the two coefficients, showing how the coupling procedures redistribute in different ways the torque and the thrust. Obviously, all the results show the presence of an asymmetrical negatively skewed distribution with a peak close to the time-averaged values of the coefficients, related to the undisturbed aerodynamic forces, and a longer tail below the main peak, related to the drops in the coefficients caused by the tower shadow effect. Except for the different averages, Figure 6.4 shows that the two-way coupled cases have a mean closer to the mode, *i.e.* the value

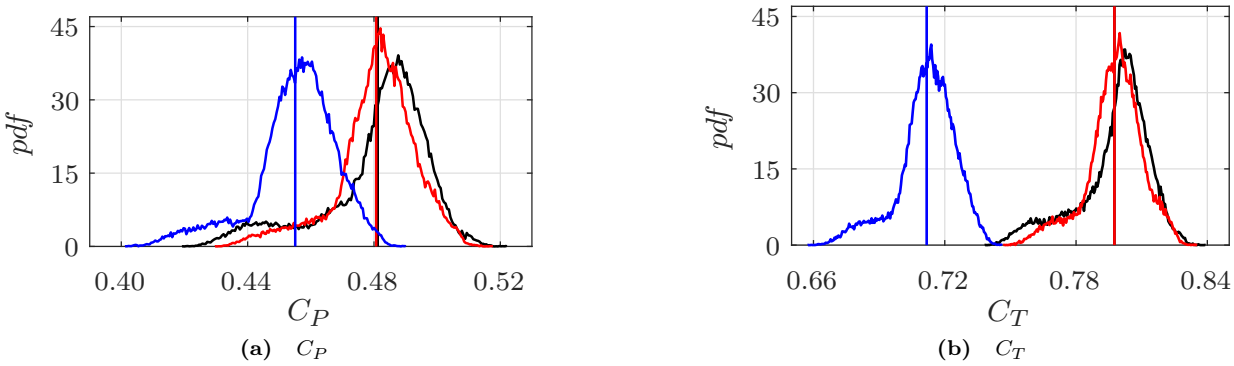

(a) C_P **(b)** C_T

Figure 6.4: Probability density function of the power and thrust coefficients. Vertical lines indicate the respective time-averaged values. ALM —, ALM/IV —, ALM/IVT —.

that appears most often in a set of data values, and a more compact tail below the mean. The absence of the fluctuations in the coefficients that are caused by the aeroelastic coupling makes the tower shadow effect sharper for the ALM case. In fact, the pdf of the one-way coupled case can be considered in the limit as a sort of bimodal distribution with one major peak, related to the condition with no blades in front of the tower, and an other minor peak, related to the condition with one blade in front of it.

6.2 Structural Dynamics: Displacement and Deformation Velocity

In this section, the structural dynamics of the blades is analysed. Figure 6.5 and Figure 6.6 report the phase-averaged displacements and deformation velocities of the six DOFs in correspondence of the free edge of the blades. The figures show that the axial (Figure 6.5a) and edgewise (Figure 6.5c and Figure 6.5e) structural dynamics are mainly dominated by gravity, as also reported in other works [54], and thus that they are only slightly affected by the aeroelastic coupling procedure. On the other hand, the flapwise (Figure 6.5b and Figure 6.5f) and the torsional (Figure 6.5d) dynamics are influenced considerably by the aerodynamic forces, and especially by the presence of the tower, which represents the main source of unsteadiness for the structural response of these two DOFs. The local reduction in the aerodynamic loading, which produces also the observed drops in the power and the thrust coefficients, breaks the low-frequency structural vibrations just after the position of the tower at $\Theta = 270°$, given the fact that the structure does not react instantaneously to the sudden change in the forcing, and that the tower has a certain width.
As a consequence of the larger influence of the aerodynamic forces on the flapwise and torsional structural dynamics, it is evident that these DOFs are considerably influenced both in the unsteady and the mean distributions by the instantaneous aeroelastic interaction.

The contribution of the deformation velocity in the definition of the angle of attack dampens the structural response ascribable to the first

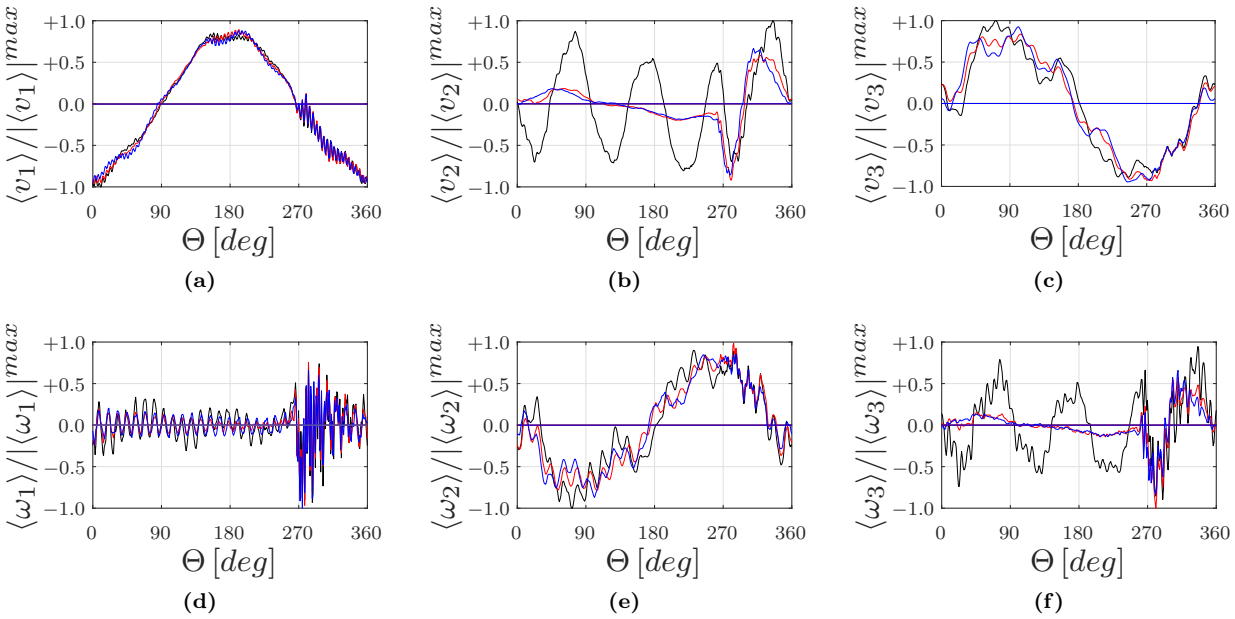

Figure 6.5: Phase-averaged tip deformation velocity. The curves represent the averages on the three blades. ALM —, ALM/IV —, ALM/IVT —.
The maximum absolute values of the phase-averaged fluctuations used for the normalisations are: $|\langle v_1\rangle|^{max} = 0.0031\,m/s$, $|\langle v_2\rangle|^{max} = 2.42\,m/s$, $|\langle v_3\rangle|^{max} = 0.71\,m/s$, $|\langle \omega_1\rangle|^{max} = 5.29\,deg/s$, $|\langle \omega_2\rangle|^{max} = 1.22\,deg/s$, $|\langle \omega_3\rangle|^{max} = 7.72\,deg/s$

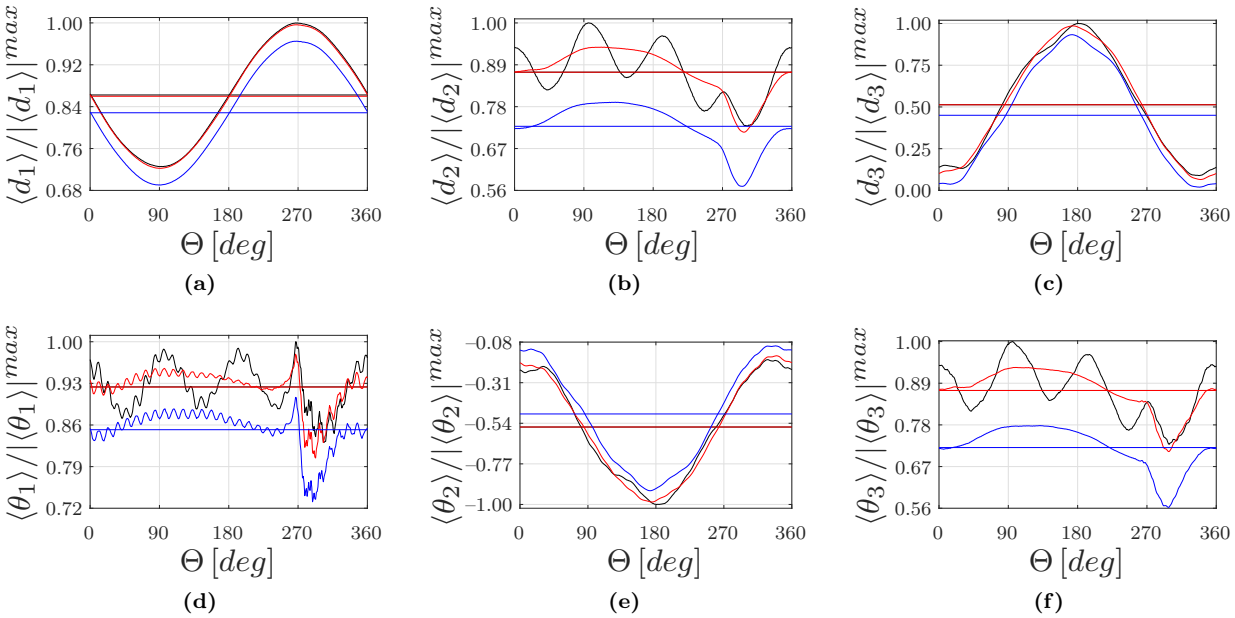

Figure 6.6: Phase-averaged tip displacement. The curves represent the averages on the three blades. ALM —, ALM/IV —, ALM/IVT —. The maximum absolute values of the phase-averaged fluctuations used for the normalisations are: $|\langle d_1\rangle|^{max} = 0.015\,m$, $|\langle d_2\rangle|^{max} = 5.45\,m$, $|\langle d_3\rangle|^{max} = 1.06\,m$, $|\langle \theta_1\rangle|^{max} = 2.55\,deg$, $|\langle \theta_2\rangle|^{max} = 1.75\,deg$, $|\langle \theta_3\rangle|^{max} = 12.00\,deg$

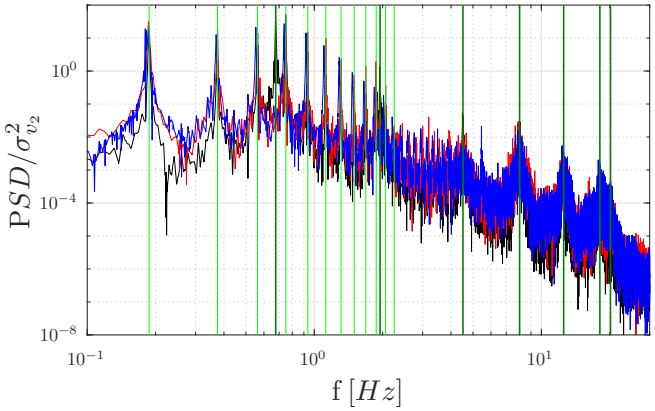

Figure 6.7: Normalised PSD of the flapwise deformation velocity component v_2 in logarithmic scale. Light green vertical lines denote the first twelve multiples of the mean rotor angular frequency, and indicate the influence of the periodic motion of the rotor. Dark green vertical lines denote the first seven natural frequencies of the modes with dominant flapwise bending features. ALM —, ALM/IV —, ALM/IVT —.

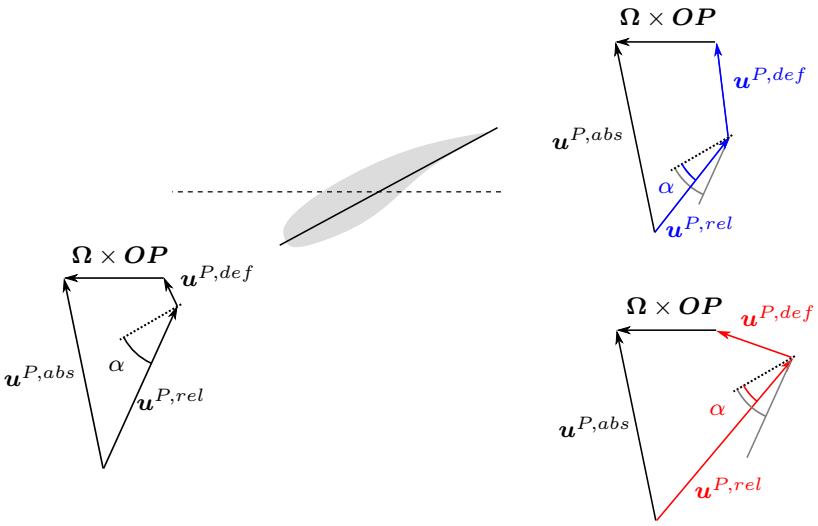

Figure 6.8: Sketch to highlight the different aerodynamic damping mechanisms for flapwise and edgewise motion. On the left, a generic initial condition with positive deformation velocity components is reported. On the right, we increase the flapwise (top) and edgewise (bottom) deformation velocity components, and we indicate in blue and red respectively the new kinematics. While in the first case both incidence and relative velocity magnitude decrease, in the second case only incidence decreases whereas the relative velocity magnitude increases. Moreover, especially towards the tip of the blade, the rotational velocity dominates the edgewise motion, while the flapwise deformation velocity remains comparable to the streamwise flow velocity throughout blade revolution.

structural mode, which is essentially a flapwise bending mode with a mild influence on torsion, as also shown in the spectrum of the flapwise deformation velocity v_2 in Figure 6.7. As a matter of fact, it is known in the literature [152] that the aerodynamic damping in the flapwise direction is relatively high when the flow is attached, in contrast to the small aerodynamic damping that characterises the edgewise motion. As shown in Figure 6.8, a positive flapwise deformation velocity, caused by a positive flapwise airload, induces a negative variation of the angle of attack and of the relative velocity magnitude that finally reduces the aerodynamic forces, and vice versa. Moreover, as shown in Figure 6.5b, peaks of $\langle v_2 \rangle$ reach relevant values, approximately 20 % of the mean hub velocity, exactly in the region where the presence of the tower and also the sheared mean velocity profile reduce the local absolute wind velocity in correspondence of the airfoils. As a result, it is clear that the flapwise motion plays a key role in the definition of the local aerodynamic forces and that the one-way coupling approach is unable to describe the resulting flapwise aerodynamic damping.
Conversely, a positive edgewise motion would reduce the angle of attack, but would increase the relative velocity magnitude (Figure 6.8). However, given the large values of the rotational tangential velocity compared to the small edgewise velocities provided by the structural dynamics, the damping effect of the edgewise motion is much smaller than the flapwise one.

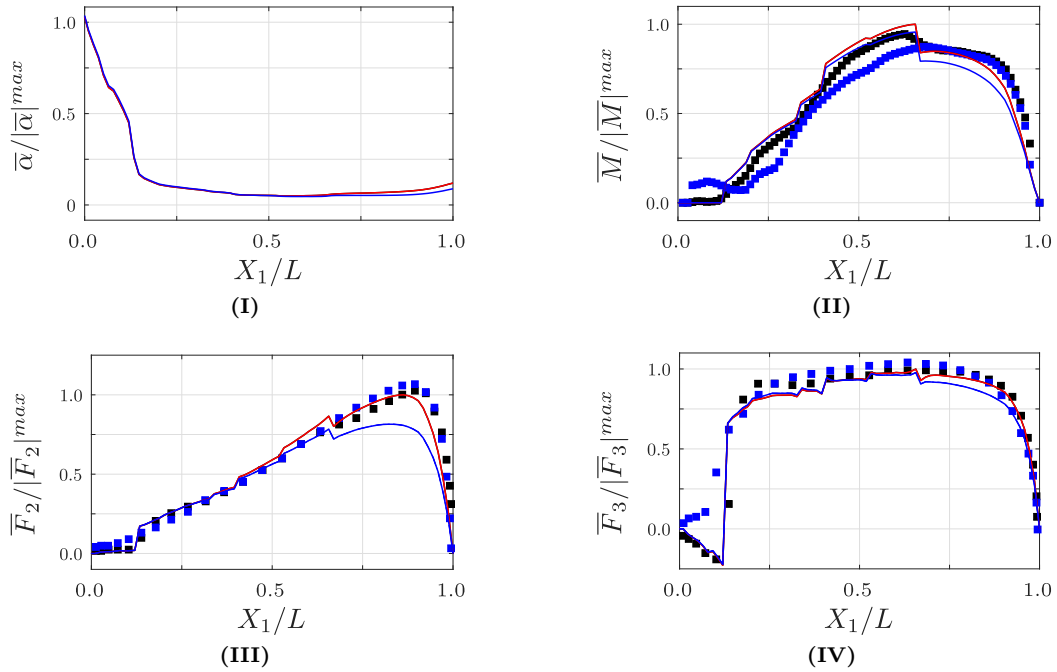

Figure 6.9: Time-averaged aerodynamic quantities along the blades: I) local incidence; II) aerodynamic moment; III) flapwise aerodynamic force; IV) edgewise aerodynamic force. ALM —, ALM/IV —, ALM/IVT —, ■ HAWC2, ■ Heinz, 2013 [46]. The ALM curves are not visible because they are exactly behind the ALM/IV curves.
The maximum absolute values of the time-averaged quantities used for the normalisations are: $|\overline{\alpha}|^{max} = 60\,deg$, $|\overline{M}|^{max} = 2550\,N$, $|\overline{F}_2|^{max} = 6090\,N/m$, $|\overline{F}_3|^{max} = 622\,N/m$.

Finally, the blades show a nose-down torsion (Figure 6.6d) mainly affected by the tower unsteadiness and by the first torsional mode, observable in the high frequency vibrations. The introduction of the torsional deformation in the angle of attack thus reduces in general the aerodynamic forces and, as a consequence, the mean deformations (Figure 6.6). However, except for the mean value of the deformations, the torsional dynamics of the ALM/IV and ALM/IVT cases exhibits only minor differences in the first and last quarters of rotation, when the blades rise after having passed in front of the tower.

6.3 Aerodynamic Forces

Figure 6.9 displays the time-averaged aerodynamic quantities along the span of the blades: the local incidence in Figure 6.9-I, the aerodynamic pitching moment in Figure 6.9-II, the flapwise aerodynamic force component in Figure 6.9-III, and the edgewise aerodynamic force component in Figure 6.9-IV. The results obtained without torsion agree well with the analogous quantities reported in Heinz, 2013 [46] for the same mean hub velocity. In fact, the ALM and ALM/IV curves show that the coupling by means of the deformation velocity reduces only slightly the mean incidence, and thus that the induced vibrations of this case have almost a net zero effect for what concerns the aerodynamic forces. On the other hand, the torsional deformation in ALM/IVT, mainly ascribable to the first torsional mode, imposes a

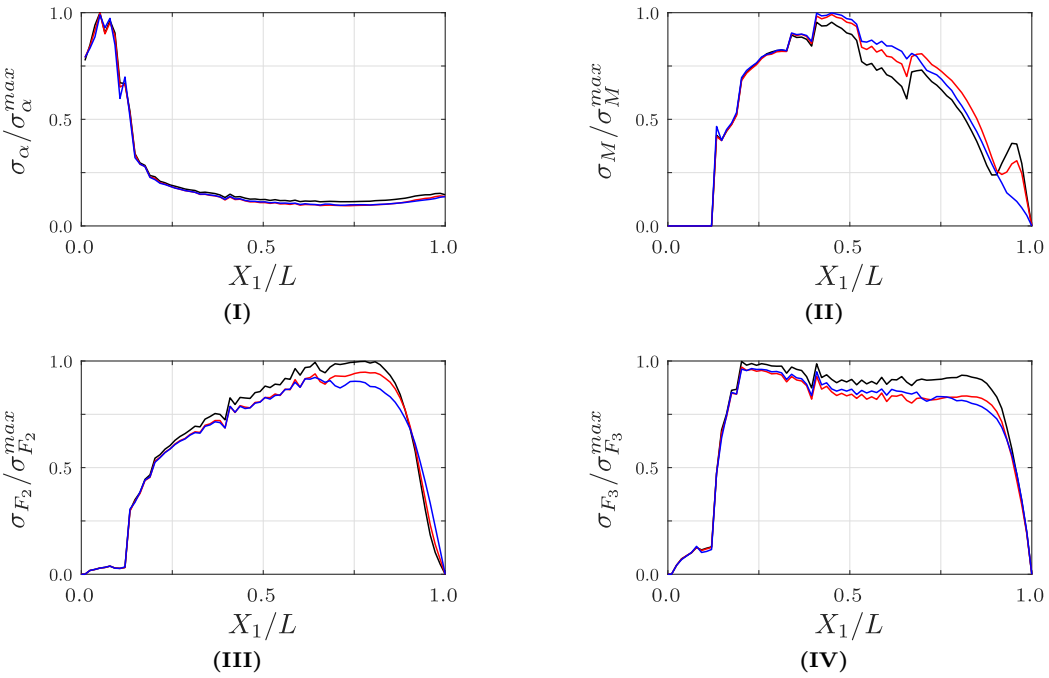

Figure 6.10: Normalised standard deviation of the aerodynamic quantities along the blades: I) local incidence; II) aerodynamic moment; III) flapwise aerodynamic force; IV) edgewise aerodynamic force. ALM —, ALM/IV —, ALM/IVT —.
The maximum values of the standard deviations used for the normalisations are: $\sigma_\alpha^{max} = 4.70\,deg$, $\sigma_M^{max} = 102\,N$, $\sigma_{F_2}^{max} = 435\,N/m$, $\sigma_{F_3}^{max} = 104\,N/m$.

monotonically increasing nose-down torsion, which significantly reduces the aerodynamic forces towards the tip of the blade.

Despite the mild influence of the two-way coupling procedures on the time averages, the standard deviation of the aerodynamic quantities along the blades in Figure 6.10 suggests that the FSI modifies the local statistics of the aerodynamic forces, and that the structural motion reduces the dispersive effect of the turbulent fluctuations, especially in the outward region of the blades where the structural vibrations are more important.

To better understand the local behaviour of the aerodynamic loading, we evaluated the phase-averaged quantities, better suited than the time-averaged ones for describing the effect of the aeroelasticity.
Figure 6.11a reports the percentage difference of the phase-averaged aerodynamic quantities of the ALM/IV case with respect to the ones of the ALM case, normalised by the local values of the ALM case itself.[9] The contours show that, while the net effect of the fluctuations is null, a relevant variation takes place in the fourth, and last, quadrant of revolution. The sudden and abrupt fluctuation of the flapwise deformation velocity, induced by the presence of the tower, causes a relevant change in the local angle of attack, which affects the aerodynamic forces and moment in turn. In fact, by looking at the sign of the flapwise deformation velocity at the tip in Figure 6.5b and at the sign of the relative difference of the incidence in Figure 6.11a-I, it can be seen that the azimuthal regions in which the difference is positive correspond to the regions with negative flapwise deformation velocity, which is in accordance with the physical explanation reported in Figure 6.8.

9: For the generic quantity χ of the generic case ALM/x, we have reported the local quantity, for each r and Θ:

$$100 \cdot \left(\frac{\langle \chi \rangle^{ALM/x}(r,\Theta)}{\langle \chi \rangle^{ALM}(r,\Theta)} - 1 \right) \quad (6.2)$$

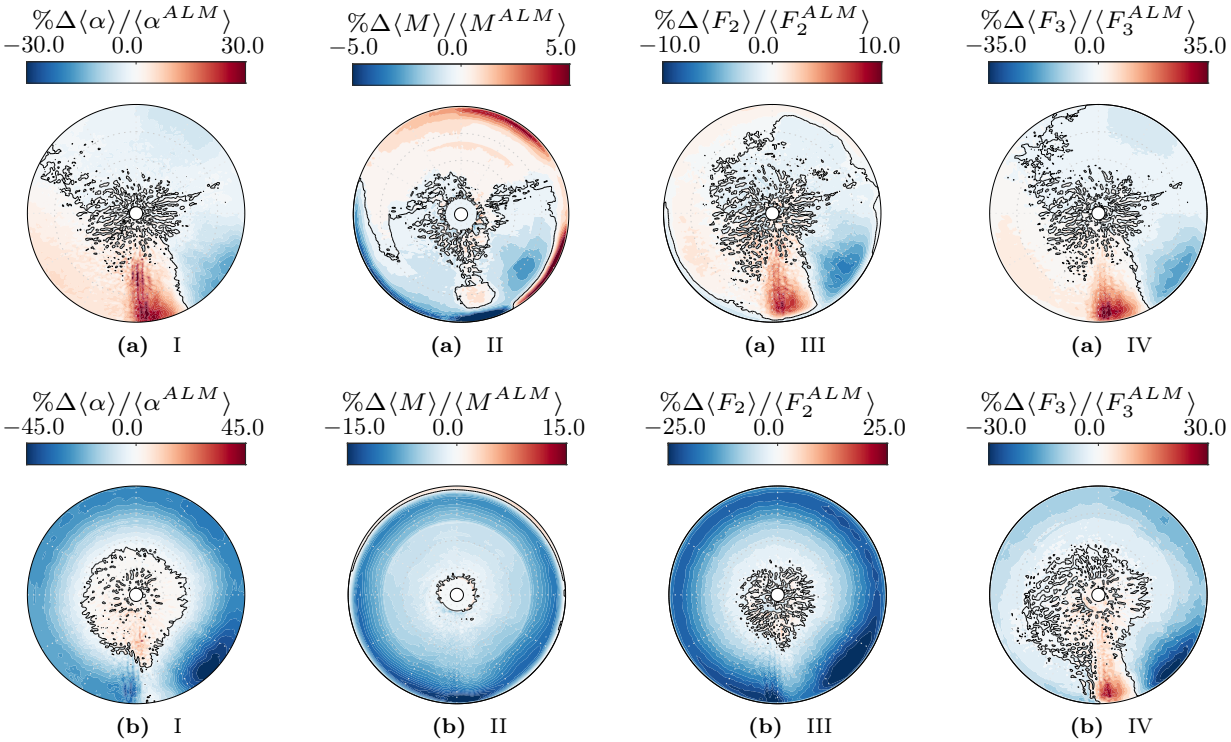

Figure 6.11: Phase-averaged contours of the percentage differences of the aerodynamic quantities between: a) ALM/IV and ALM case; b) ALM/IVT and ALM case. Differences are normalised with respect to the local values of the ALM case. Iso-lines for null differences are indicated in black. I) Local incidence; II) aerodynamic moment; III) flapwise aerodynamic force; IV) edgewise aerodynamic force.

The distribution of the pitching moment (Figure 6.11a-II) follows the behaviour imposed by the angle of attack, especially in the bottom part. However, some differences are present. First of all, radial discontinuities reflect the transition from one type of airfoil to the other along the span, given the discontinuous features in terms of pitching moment of the different airfoils, as shown also in Heinz, 2013 [46]. Second of all, an opposite behaviour is shown in the top part. Here, the lower aerodynamic forces opposing the fluid in the two-way coupled cases allow slightly larger velocities. Given the fact that the variation of incidence in that region is limited and that the corresponding variation of the pitching moment coefficient is small, the effect of the local increase in the velocity prevails according to Equation 2.45 and produces a slight increase in $\langle M \rangle$ in the end.

Figure 6.11b reports the analogous percentage differences for the ALM/IVT case with respect to the ALM case. In general, the behaviour is similar to the one reported in Figure 6.11a, and the most significant variations are in correspondence of the passage of the blades in front of the tower and in the following quadrant, although the nose-down torsion causes a general reduction of all the aerodynamic quantities. Moreover, the reduced angular velocity of the ALM/IVT case, caused by the smaller loading of the blades, increases slightly the local angle of attack (Figure 6.11b-I). This is particularly evident in the root region, where the nose-down torsion is still small and thus there is a net increase in the local incidence compared to the ALM case. However, proceeding towards the tip, the torsional deformation

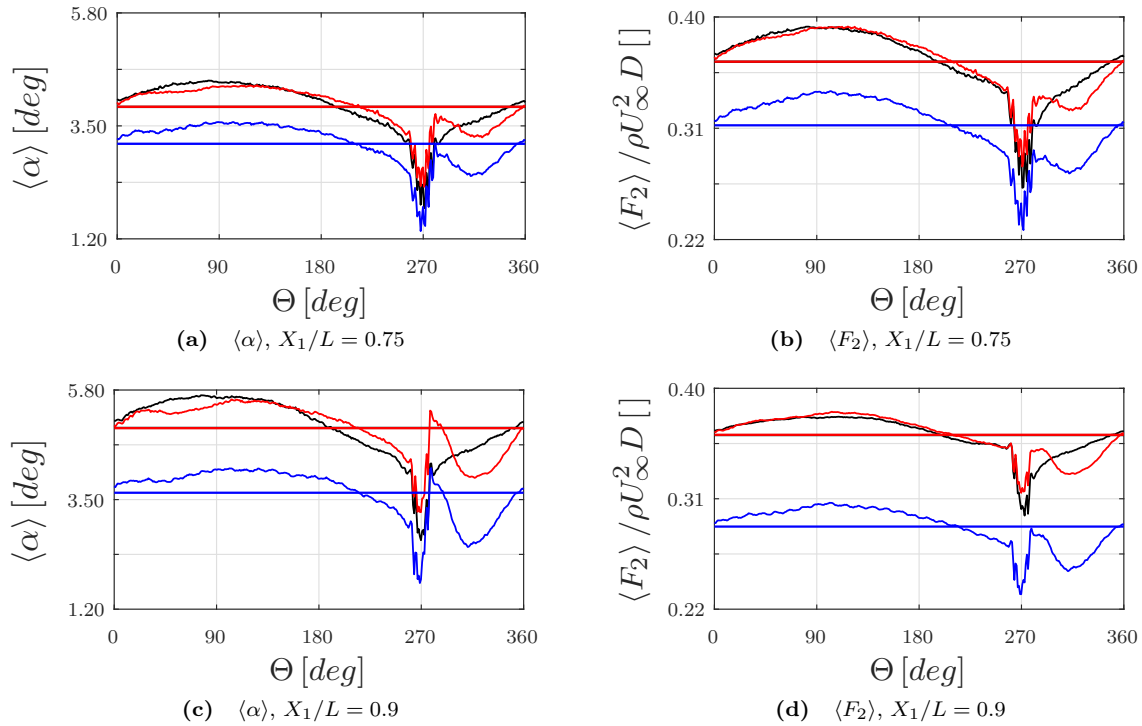

(a) $\langle\alpha\rangle$, $X_1/L = 0.75$ **(b)** $\langle F_2\rangle$, $X_1/L = 0.75$

(c) $\langle\alpha\rangle$, $X_1/L = 0.9$ **(d)** $\langle F_2\rangle$, $X_1/L = 0.9$

Figure 6.12: Phase-averaged incidence and flapwise aerodynamic force at radial positions from the hub $X_1/L = 0.75$ and $X_1/L = 0.91$. ALM —, ALM/IV —, ALM/IVT —

becomes more important and affects relevantly the distribution of the angle of attack. This causes a significant decrease in the aerodynamic forces in the outer part of the blades, which are the parts contributing the most to the the aerodynamic torque and thrust.

Finally, Figure 6.12 reports the phase-averaged angle of attack and aerodynamic flapwise force for some radial sections. Apart from the mean value, the figure reveals also that the more complete structural state of the ALM/IVT case introduces another small contribution to the general dynamics of the problem, as shown by the different recovery of the curves from the minimum in correspondence of the tower angle.

6.4 Reactions

To complete the structural analysis of the results, we analyse the behaviour of the root reactions. In particular, we name R_i the reaction force along the i-th axis of the structural FOR $\mathcal{R}_E$, and M_i^R the reaction moment around the same axis, with sign defined in accordance with the right-hand rule (see Figure 4.5).
Figure 6.13 reports the phase-averaged reactions and their correspondent time averages for all the 6 DOFs in correspondence of the root. The curves confirm the predominance of the gravitational force on the axial and edgewise DOFs (Figure 6.13a, Figure 6.13c and Figure 6.13e respectively), in spite of the torsional and flapwise ones (Figure 6.13d, Figure 6.13b and Figure 6.13f respectively) which are more affected by the

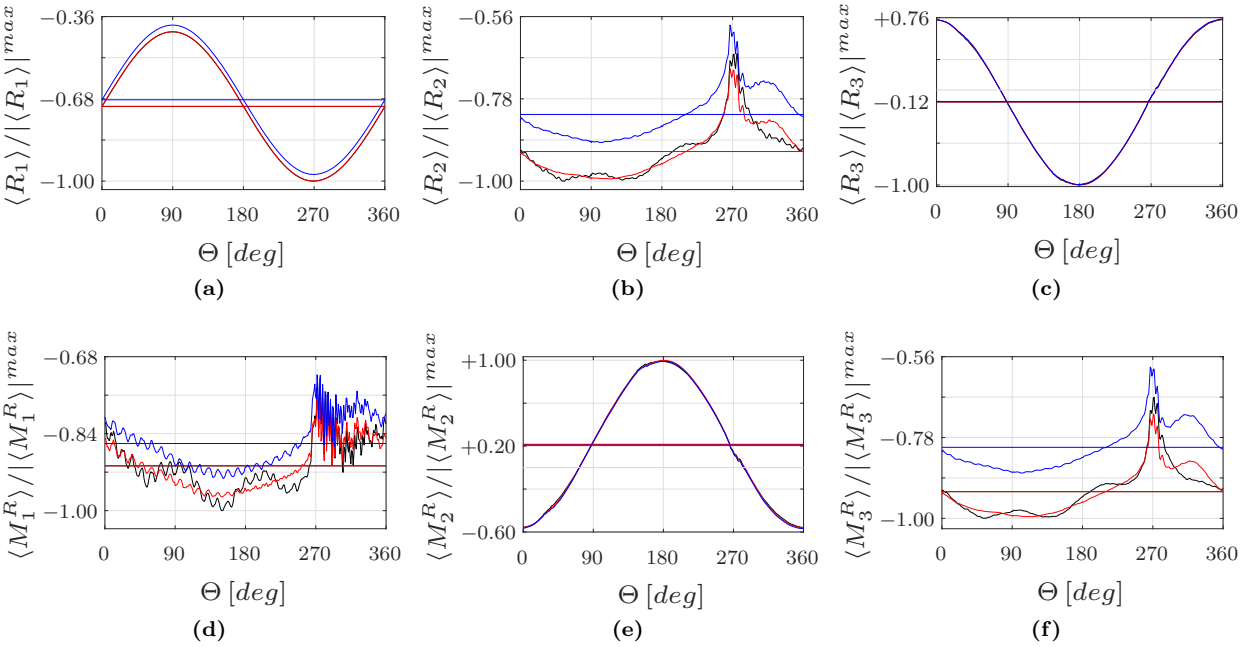

Figure 6.13: Phase-averaged root reaction components. Horizontal lines indicate the corresponding time-averaged values. ALM —, ALM/IV —, ALM/IVT —.
The maximum absolute values of the phase-averaged quantities used for the normalisations are: $|\langle R_1\rangle|^{max} = 5.95 \cdot 10^5\ N$, $|\langle R_2\rangle|^{max} = 2.18 \cdot 10^5\ N$, $|\langle R_3\rangle|^{max} = 2.00 \cdot 10^5\ N$, $|\langle M_1^R\rangle|^{max} = 9.77 \cdot 10^4\ N\,m$, $|\langle M_2^R\rangle|^{max} = 4.58 \cdot 10^6\ N\,m$, $|\langle M_3^R\rangle|^{max} = 8.69 \cdot 10^6\ N\,m$,

aerodynamic forces, and thus are more influenced by the FSI coupling. Furthermore, the high mean value of the axial reaction component reveals the almost constant centrifugal force acting radially.

In addition to generally reduced values because of the diminished aerodynamic loads, the ALM/IVT case presents also a small phase shift after the tower azimuthal position, where the torsional dynamics imposes a faster recovery of the aerodynamic loads than in the ALM/IV case (see also Figure 6.3). Finally, the time-averaged values differ only in the ALM/IVT case, and are in line with other studies with similar flow conditions [67], confirming the general validity of our model.

Given the highly unsteady loads imposed by the fluctuating wind conditions, it is critical to evaluate the fatigue properties of the structure and to assess the effect of the aeroelastic coupling procedures on them. Among the different possible characterisations, a widely used measure of the impact of the fatigue loads on the structure is the Damage Equivalent Load (DEL) [176], which represents the amplitude of the single constant-rate alternating load that produces the same total damage of the real load spectrum.
We evaluated the DELs for the reactions of each case by means of the post-processing tool MCrunch [177], adopting fatigue-life calculations that conforms to the IEC 61400-1 Ed.3 standard [172]. The tool counts the cycles by means of the popular *rainflow counting algorithm* [178], adopts the Palmgren-Miner linear rule *i.e.* the Miner's rule, for damage accumulation [179], and uses a standard S-N fitting curve to characterise the material behaviour, for which we chose a constant slope typical of composite materials.

[176]: Sutherland (1999), *On the fatigue analysis of wind turbines*

[177]: Buhl (2008), *MCrunch user's guide for version 1.00*

[178]: Downing et al. (1982), 'Simple rainflow counting algorithms'

[179]: Miner (1945), 'Cumulative fatigue damage'

According to the linear Palmgren-Miner rule for damage accumulation, the total cumulative damage D sustained by a structure is given by:

$$D = \sum_{i=1}^{M} \frac{n_i}{N_i}, \tag{6.3}$$

where n_i is the number of cycles at stress level σ_i estimated from the actual stress signal, N_i is the number of cycles to failure at stress level σ_i, and M is the number of stress levels observed. The number of cycles to failure N_i represents the endurance to stress cycles of the particular material considered. Usually, for composite materials the standard S-N fitting curve is used to represent the fatigue behaviour, stating that:

$$\sigma = \sigma_u \, N^{-1/m}, \tag{6.4}$$

where N is the number of cycles to failure at stress level σ, σ_u is the ultimate stress level, and m is the so-called fatigue exponent, which for composite materials is typically equal to 10.

The Miner's rule assumes that the cumulative damage brings to failure if the total damage D is equal to 1. To this end, two different loading histories are equivalent if the total damage produced is the same. From here follows the definition of the Damage Equivalent Load (DEL), according to which a single sinusoidal load, with given frequency f_0, produces the same damage of the real spectrum for the total time covered by the load spectrum T. Hence, one has that:

$$\frac{n_{DEL}}{N_{DEL}} = \sum_{i=1}^{M} \frac{n_i}{N_i}. \tag{6.5}$$

where n_{DEL} and N_{DEL} are the number of equivalent cycles and the DEL number of cycles to failure respectively. Given Equation 6.4 and that $n_{DEL} = f_0 \, T$, one obtains that:

$$DEL = \left[\frac{1}{f_0 T} \sum_{i=1}^{M} n_i \, (\sigma_i)^m \right]^{1/m}. \tag{6.6}$$

The stress level is characterised by a mean stress σ_m and a stress amplitude σ_a, and it is usually assumed that the mean stress is constant. Finally, by means of the simplified method of Freebury and Musial, 2000 [180], the actual procedure to determine the Damage Equivalent Load remains unaltered, but no conversion to stresses from the actual load signal, *i.e.* the root reaction signal, is needed, and an equivalent $M - N$ curve is used such that:

[180]: Freebury et al. (2000), 'Determining equivalent damage loading for full-scale wind turbine blade fatigue tests'

$$M_a = M_u \, N^{-1/m} \tag{6.7}$$

where M_a is the load (moment or force) amplitude in one load cycle, M_u is the ultimate load of the blade, which is assumed to be equal to $1.5 - 4.5$ times the maximum characteristic load recorded in the real load spectrum, while N and m have the same meaning as in Equation 6.4. The effect of the mean load on the DEL is usually not considered.

Table 6.2 reports the percentage differences ΔR_i % of the two-way

Table 6.2: Percentage difference of root reaction DELs for the ALM/IV and ALM/IVT cases with respect to the ALM case.

DEL	$\Delta R_1\,\%$	$\Delta R_2\,\%$	$\Delta R_3\,\%$	$\Delta M_1^R\,\%$	$\Delta M_2^R\,\%$	$\Delta M_3^R\,\%$
ALM/IV	0.00 %	−14.19 %	+0.31 %	−23.33 %	+0.74 %	−15.57 %
ALM/IVT	−0.17 %	− 8.68 %	+0.03 %	− 7.28 %	+0.41 %	−11.58 %

coupled cases with respect to the one-way coupled case, defined as:

$$\Delta R_i\% = 100 \cdot \frac{DEL_{R_i} - DEL_{R_i}^{ALM}}{DEL_{R_i}^{ALM}}, \tag{6.8}$$

where DEL_{R_i} is the Damage Equivalent Load of the two-way coupled case considered, and $DEL_{R_i}^{ALM}$ is that of the one-way coupled case. The results show that, in general, the one-way coupled simulation overestimates the fluctuations of the loads, and that the aerodynamic damping caused by the introduction of the deformation velocity limits the low-frequency fluctuations of the blade loading. Furthermore, the ALM/IVT case shows only a slightly larger DEL than the ALM/IV case, especially in the torsional root reaction component, *i.e.* $DEL(M_1^R)$. In fact, the direct influence of the high-frequency/small-amplitude torsional oscillation in the ALM/IVT case induces fluctuations that are slightly more relevant for this component, as shown in Figure 6.13d. However, the small amplitude of the torsional angle fluctuations is insufficient to affect the low frequency unsteadiness of the gravity and the aerodynamic loads in edgewise and flapwise directions respectively.

6.5 Fluid Flow

As a final step, we analyse the fluid variables. Figure 6.14 shows the time-averaged streamwise velocity component on a vertical slice through the turbine centre and on a horizontal slice at hub height for the three cases. In the vertical plane, it can be seen that the action of the blades decelerates the flow, while the tower induces a recirculation region behind the turbine, which thus breaks the symmetry of the flow between the bottom and the top part of the rotor. In particular, the region of reversed flow is divided into three parts: a lower part, behind the section of the tower uncovered by the blades, an intermediate part, behind the section of the tower covered by the external half of the rotor, and a higher part, behind the nacelle and the section of the tower covered by the internal half of the rotor. While the bottom part is only affected by the undisturbed flow, the intermediate part is influenced by the presence of the blades, and indeed its longitudinal extent is reduced by the upstream deceleration imposed by the rotor to the fluid. Finally, the higher part has again a larger extent, because of the larger longitudinal size of the nacelle compared to the tower, and because of the higher fluid velocity at hub height and above.

Furthermore, an asymmetric behaviour of the wake is shown also in the horizontal plane. In fact, the tower and the nacelle obstruct the flow and induce a Von Kármán vortex street, which is tilted by the

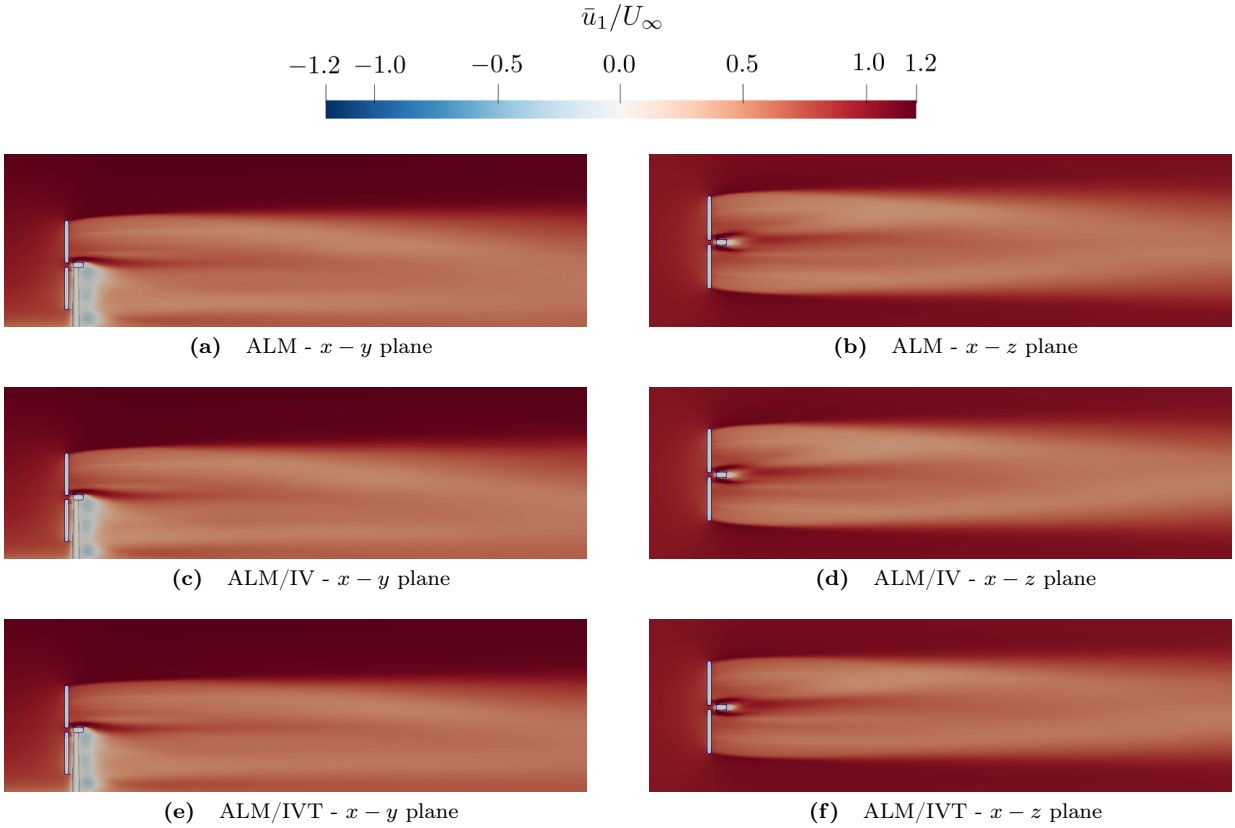

(a) ALM - $x-y$ plane

(b) ALM - $x-z$ plane

(c) ALM/IV - $x-y$ plane

(d) ALM/IV - $x-z$ plane

(e) ALM/IVT - $x-y$ plane

(f) ALM/IVT - $x-z$ plane

Figure 6.14: Time-averaged streamwise velocity on a vertical slice through the wind turbine centre (left) and on a horizontal slice at hub height (right).

helical motion given by the revolution of the blades, as already shown in Santoni et al., 2017 [106].

However, from the comparison of the three cases, no significant difference can be observed, except for some very small quantitative changes in the ALM/IVT case caused by the reduced aerodynamic forces.

Finally, we compare the instantaneous coherent structures of the flow for a generic instant with $\Theta = 90°$, represented by means of the Q-criterion [181] in Figure 6.15. The root vortices generated close to the hub are promptly disrupted by their interaction with the wake of the nacelle, whereas the tip vortices are dissipated after approximately one diameter from the tower. As expected, the mild wind shear imposed, and thus the different convection velocity of the vortices at different heights, causes only a modest change in slope of the helical structures in the wake that is slightly visible from the lateral views. On the horizontal slice at the tower base instead, it is possible to appreciate the trace of the induced Von Kármán vortex street generated by the tower obstruction. The comparison of the isosurfaces in Figure 6.15 shows that the three cases under study are essentially similar. However, as we already commented, the reduced forces along the blades in the ALM/IVT case cause thinner and less intense tip vortices. Moreover, the reduced angular velocity increased the pitch of the helical wake structure.

[181]: Dubief et al. (2000), 'On coherent-vortex identification in turbulence'

Ultimately, we can conclude that our simulations suggest that from

the point of view of the fluid dynamics, the aeroelastic coupling for the wind turbine under study has a small effect, limited to the very near wake only.

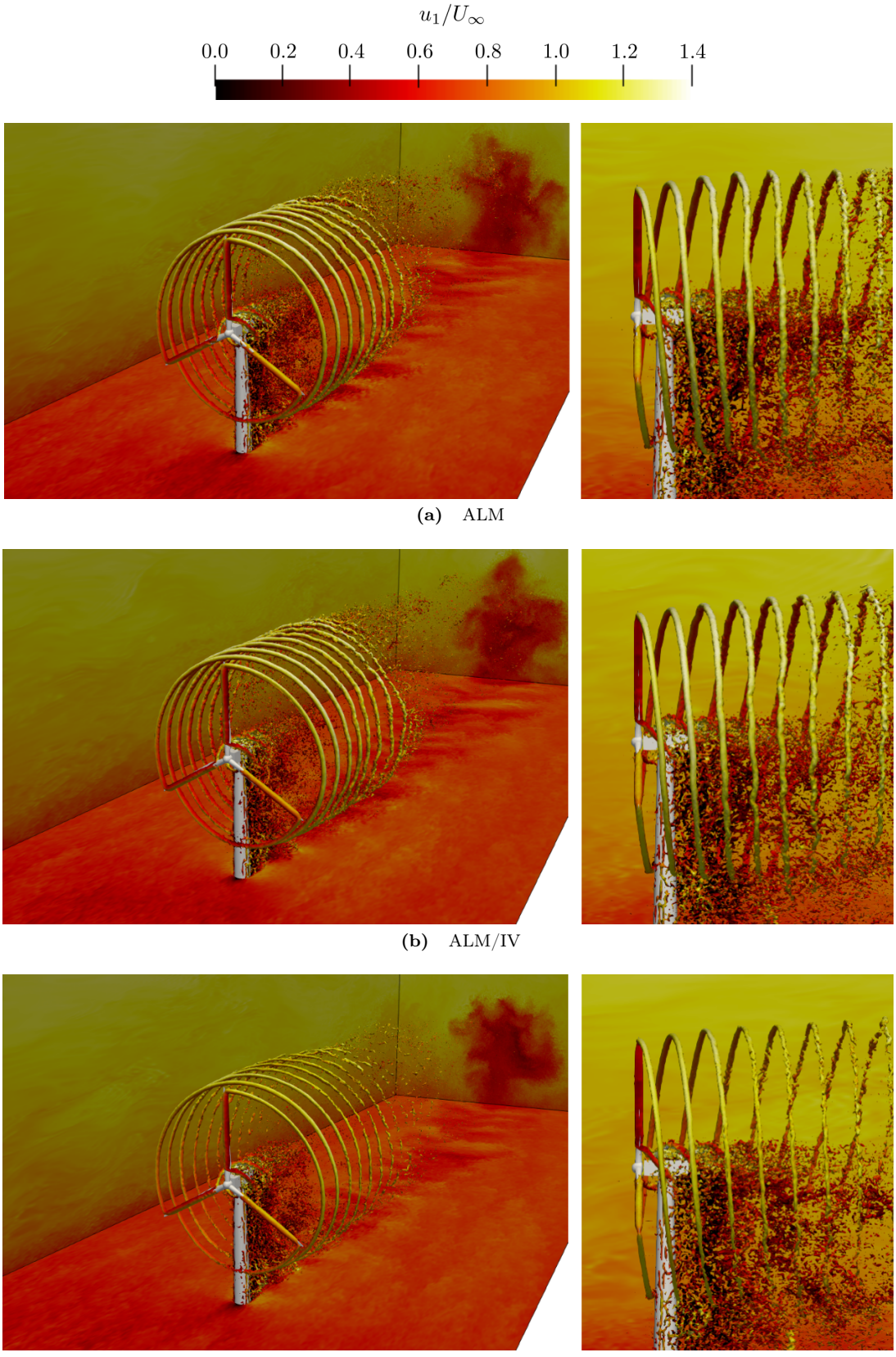

(a) ALM

(b) ALM/IV

(c) ALM/IVT

Figure 6.15: Instantaneous isosurface of the Q-criterion variable coloured by the streamwise velocity. Three-point perspective projection of the field on the left, and lateral view on the $x - y$ plane on the right.

7 Effects of the Unsteady Aerodynamics

This chapter presents the analysis of the results of the last eight sets of simulations. The aim of the comparison is to evaluate the effect of the unsteady aerodynamics on the response of the NREL 5 MW wind turbine.

In the following, we consider the behaviour of the power and the thurst, of the aerodynamics loads, of the structural response and of the reactions. Then, we examine some of the variables introduced by the UA model, and finally, we analyse the fluid flow behaviour.

As in the previous chapter, we indicate the time average with $\overline{\bullet}$, the phase average with $\langle\bullet\rangle$, and the average on the rotor area with $\langle\bullet\rangle_A$. Table 7.1 reports the simulations considered in this chapter.

#	Name	Inflow	FSI	UA
1	L-ALM	Uniform	No	No
2	L-ALM/IV	Uniform	Yes	No
3	L-ALM-UA	Uniform	No	Yes
4	L-ALM/IV-UA	Uniform	Yes	Yes
5	T-ALM	Turbulent	No	No
6	T-ALM/IV	Turbulent	Yes	No
7	T-ALM-UA	Turbulent	No	Yes
8	T-ALM/IV-UA	Turbulent	Yes	Yes

Table 7.1: Outline of the simulations taken into consideration in this chapter. Inflow can be uniform or sheared turbulent. Classic ALM with rigid blades is used when FSI is not considered, whereas tabulated airfoil data are used when UA is not considered. Different colours indicate the different cases.

The photograph from 1915 shows an airfoil with separated flow, and attests the long-standing interest of fluid dynamicists for unsteady aerodynamics.
The credits for the image above the chapter title go to DLR. http://www.dlr.de/100Jahre/DesktopDefault.aspx/tabid-3300/5149_read-7460/gallery-1/gallery_read-Image.37.2921/

7.1 Power and thrust

At first, we compare the fluctuations relative to the mean value of the phase-averaged normalised power and thrust. Since power and thrust are obviously affected by the velocity of the flow impacting the wind turbine, in the turbulent cases these quantities show large scale fluctuations, overlapped to local oscillations that are more associated with the tower shadowing, the aeroelastic interaction and the unsteady aerodynamics (see Figure 7.1). To verify if the period considered for the averaging is sufficient to filter out the large scale turbulent fluctuations, we high-pass filtered the power and thrust signals of the turbulent cases to remove the large scale fluctuations, and we then derived the corresponding phase averages.[11] Given the large computational cost of the simulations, the time period considered is limited, however the good agreement between the filtered and non-filtered phase averages for the turbulent cases (Figure 7.2) demonstrates that the period considered is sufficient to filter out the large scale fluctuations. Hence, we assume that it is reasonable to compare the phase-averaged results relative to the laminar and turbulent cases.

11: The generic filtered signal A^f is the subtraction from the original signal A of the low-pass filtered signal obtained by means of a 1-D digital FIR filter [182].

From Figure 7.2, reporting the above presented fluctuations, we can see that the unsteady aerodynamics has a limited effect on power and thrust, and thus that the local loads' fluctuations have a zero mean around the corresponding steady-state values, and also that their distribution does not affect the integration of the loads along the blades' span. On the other hand, the introduction of the aeroelastic feedback induces the peculiar patterns shown also in the previoius chapter. In general, the passage of the blades in front of the tower triggers their structural vibration. The structural feedback introduced with the deformation velocity (especially the flapwise component) induces load fluctuations, that account for the oscillations of the power and thrust after the drops due to tower shadowing.

The distribution of the phase-averaged coefficients differs from the laminar, uniform cases and the turbulent, sheared cases. Laminar cases have sharp transitions between the distinct states that characterise the signal, which are the tower shadowing dips, the undisturbed top value (clearly visible in the one-way coupled cases), and the vibration-induced peaks (for the two-way coupled cases only). On the other hand, the influence of mean wind shear and turbulence makes the transition between the different states smoother and the amplitude of the fluctuations weaker.

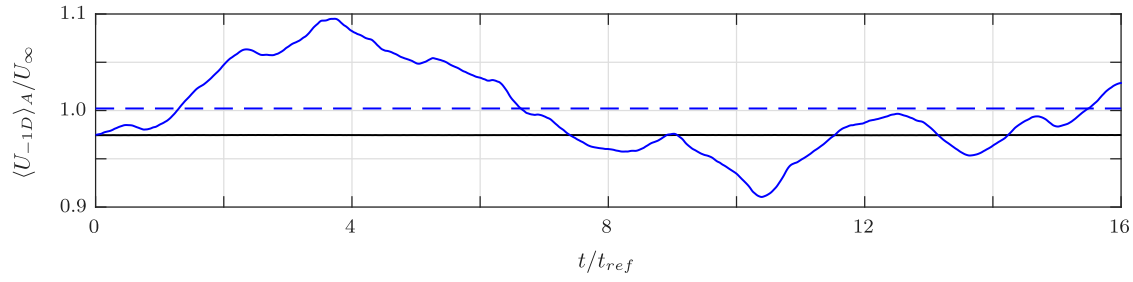

(a) $\langle U_{-1D}\rangle_A/U_\infty$

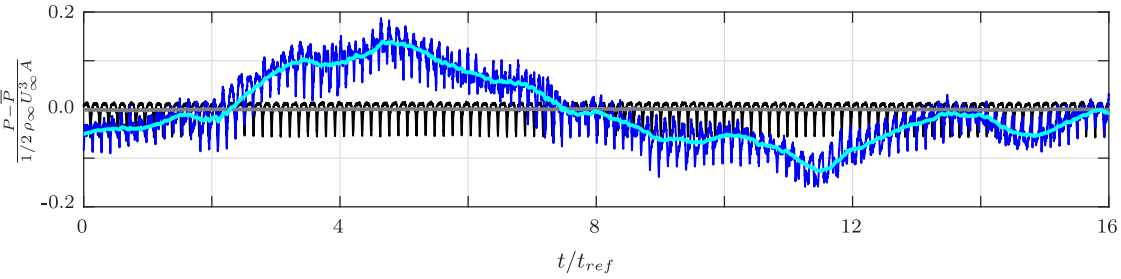

(b) $\frac{P-\overline{P}}{1/2\,\rho_\infty U_\infty^3 A}$

Figure 7.1: Time history of the rotor-averaged streamwise velocity at one diameter from the hub $\langle U_{-1D}\rangle_A/U_\infty$ and of the normalised power fluctuations for the L-ALM and the T-ALM cases. The corresponding low-pass filtered signals are indicated in grey and cyan respectively.

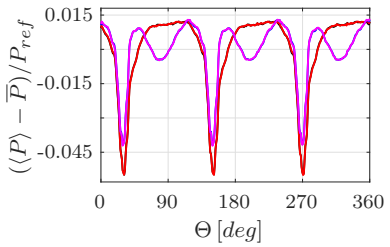

(a) Normalised Power - Laminar

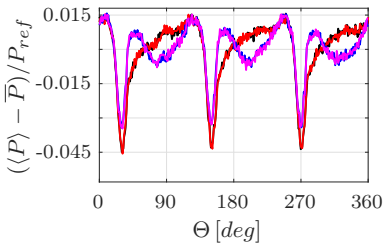

(b) Normalised Power - Turbulent

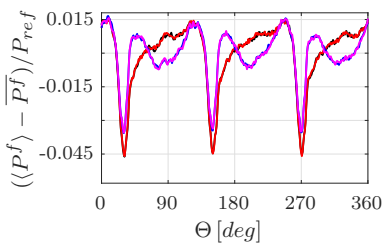

(c) Normalised Filtered Power - Turbulent

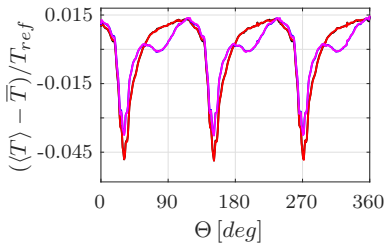

(d) Normalised Thrust - Laminar

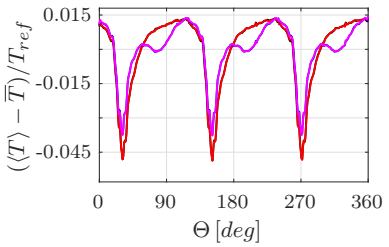

(e) Normalised Thrust - Turbulent

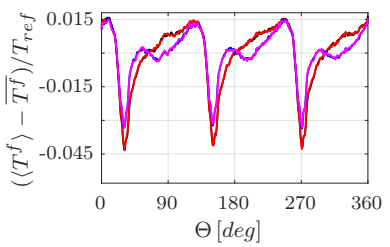

(f) Normalised Thrust - Turbulent

Figure 7.2: Phase-averaged fluctuations with respect to the mean value of the normalised power (top) and thrust (bottom) for the laminar case (left), the turbulent case (centre), the filtered turbulent case (right). Colours from Table 7.1. $P_{ref} = 1/2\,\rho_\infty U_\infty^3 A$ and $T_{ref} = 1/2\,\rho_\infty U_\infty^2 A$.

7.2 Aerodynamic forces

Figure 7.3 reports the time average of the aerodynamic forces in the flapwise and edgewise direction, $\overline{F_2}$ and $\overline{F_3}$ respectively, and of the pitching moment, $\overline{M}$, along the blades' span. The distributions, that match well the results of Heinz [46] for the same case, show that the time average of the aerodynamic forces is the same for the same inflow. FSI and UA preserve the mean loads, which thus can be estimated by one-way coupled simulations with classic sectional aerodynamics. A slight increase in the airloads can be noticed for the turbulent case, due – most likely – to a slightly higher mean velocity at the inlet. Moreover, the results confirm the capability of the UA model to recover the steady-state values of the averaged forces.

However, the standard deviation of the airloads along the blade in Figure 7.4 starts to unveil the differences in the data set. The cases using the UA model exhibit a relevant increase in the airloads variability in the first half of the blade, whereas the cases with two-way FSI coupling exhibit a slight reduction towards the tip, as shown in our previous works. These effects are dominant in the laminar cases, where the root values can reach five – or even more – times the values towards the tip, while their importance is reduced in the turbulent simulations. For the latter, even if the first half of the blade still presents larger standard deviations, these remains comparable with the tip values. Moreover, the structural feedback lowers the load variance towards the tip and slightly increases it towards the hub.

From here, we can start to observe the division of the blades in two regions: the tip portion, mostly affected by the aeroelastic interaction, since here the deformations and the vibrations are more important, and the root portion, mostly affected by the unsteady aerodynamics effects. In fact, in the inner region of the blade, the fluctuations of α are substantial and the velocity is small. This makes the local flow highly unsteady and hence the airloads of the hub sections highly sensitive to the noncirculatory mechanisms and to other hysteresis phenomena strongly depending on $\dot{\alpha}$ (Equation 2.71).

The pitching moment deserves careful scrutiny. The increase of the moment variability with the UA model is particularly high with both inflows. We will see that special attention must be devoted to the improvement of the description of the torsional moment. As a matter of fact, the modelling of the pitching moment dynamics is often disregarded in the literature, and also semi-empirical procedures used to determine it are not unambiguous compared to the descriptions of the normal force components, and thus their accuracy can be questioned.

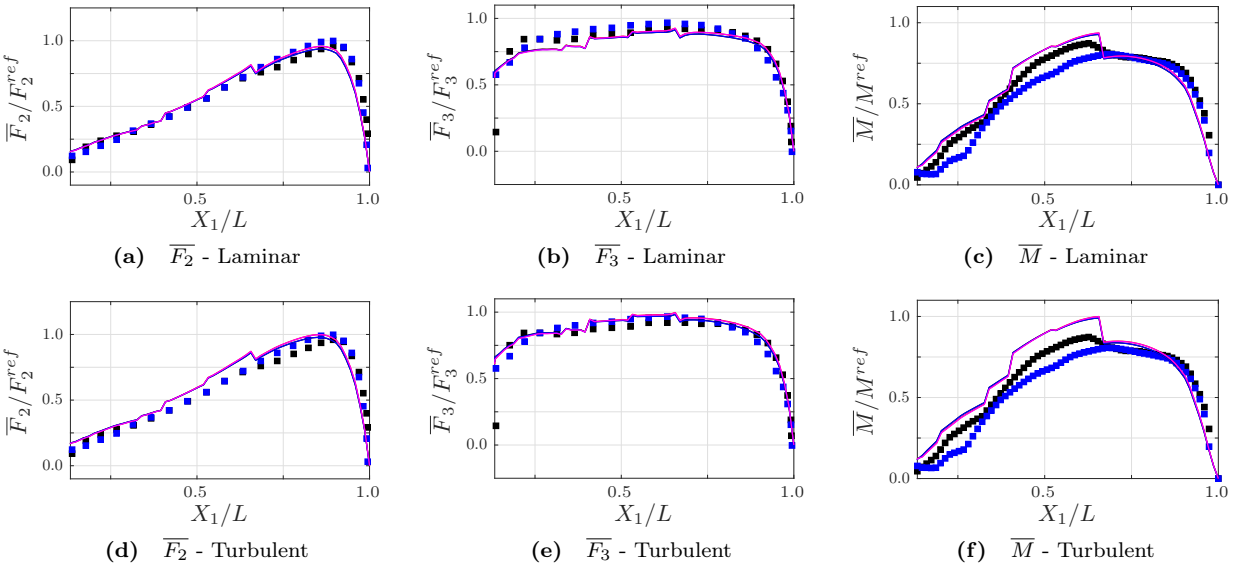

(a) $\overline{F_2}$ - Laminar **(b)** $\overline{F_3}$ - Laminar **(c)** $\overline{M}$ - Laminar

(d) $\overline{F_2}$ - Turbulent **(e)** $\overline{F_3}$ - Turbulent **(f)** $\overline{M}$ - Turbulent

Figure 7.3: Time-averaged airloads per unit length along the blade span. Scatter data from Heinz [46]: ■ HAWC2 (one-way coupled simulations) ■ HAWC2-FSI (two-way coupled simulations). Colours from Table 7.1. $F_2^{ref} = 6510\,\mathrm{N/m}$, $F_3^{ref} = 669\,\mathrm{N/m}$, $M^{ref} = 2760\,\mathrm{N}$.

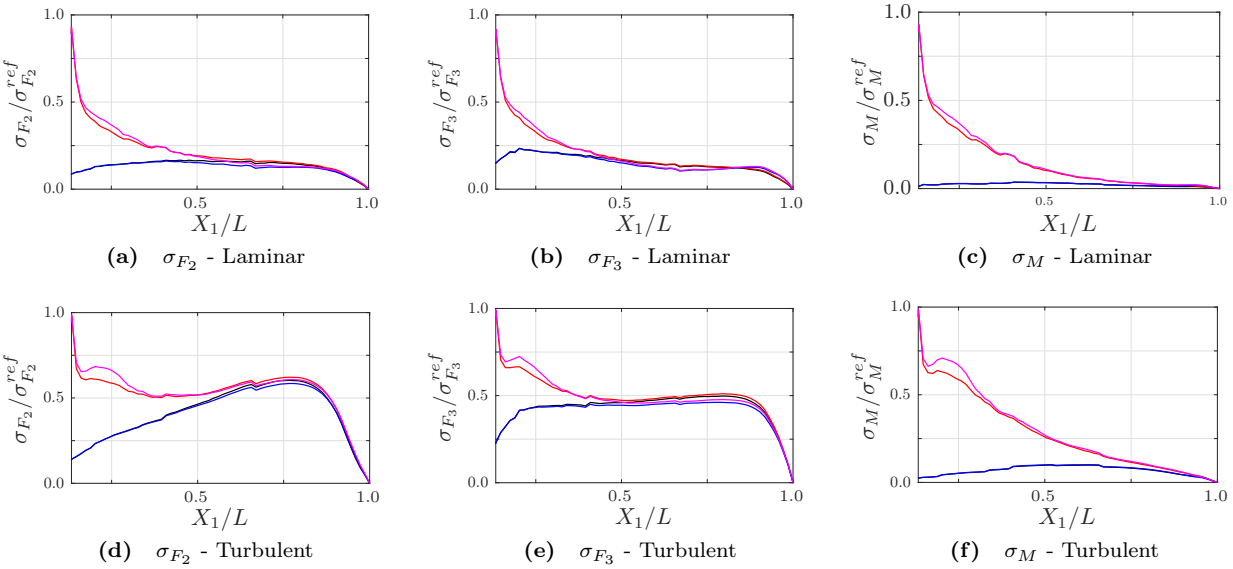

(a) σ_{F_2} - Laminar **(b)** σ_{F_3} - Laminar **(c)** σ_M - Laminar

(d) σ_{F_2} - Turbulent **(e)** σ_{F_3} - Turbulent **(f)** σ_M - Turbulent

Figure 7.4: Standard deviation of the airloads per unit length along the blade span. Colours from Table 7.1. $\sigma_{F_2}^{ref} = 1320\,\mathrm{N/m}$, $\sigma_{F_3}^{ref} = 315\,\mathrm{N/m}$, $\sigma_M^{ref} = 2430\,\mathrm{N}$.

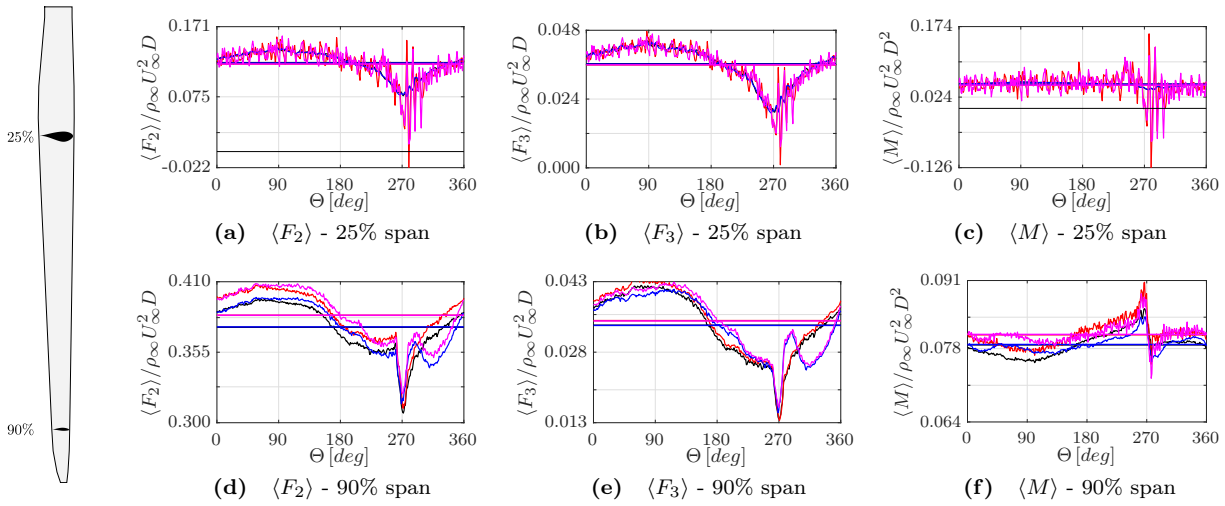

Figure 7.5: Phase-averaged airloads per unit length in the turbulent cases at 25% (DU35_A17 airfoil, top row) and 90% (NACA64_A17, bottom row) of the blade (left). Colours from Table 7.1.

To inspect the local airloads, Figure 7.5 reports the phase-averaged airloads in the turbulent cases for two sections of the blade, respectively at 25% (DU35_A17 airfoil) and 90% (NACA64_A17 airfoil). From the plots, the distinction of the two regions of influence is even clearer. For the root region, the faster and larger fluctuations of α with low incoming velocity induce sharp variations of the aerodynamic forces around the corresponding steady-state values obtained without UA. In particular, in correspondence of $\Theta = 270\,deg$, the passage of the blade in front of the tower produces the largest variations of the loads. On the other hand, the effect of the structural vibrations close to the clumped hub is practically null, and thus there is no relevant difference between the one-way and the two-way coupled cases. For the tip region, instead, the velocity is higher and the fluctuations of the incidence are smaller. The contributions from the UA model to the airloads is thus almost null, except a small increase in the mean values due also to small compressibility effects ($M^{max} \approx 0.2$ at 90% of the blade). Conversely, the structural vibrations are here mostly important, and affect the behaviour of the airloads, especially in the last quarter of revolution. In the IV cases, it has been demonstrated in the previous chapter that the incidence and absolute value of the velocity are primarily influenced by the flapwise deformation velocity component v_2 of the structure. In particular, a positive increase of v_2 induces a reduction of both the incidence and the velocity magnitude, which thus lowers the aerodynamic forces, and vice versa. Thus, when comparing the ALM and ALM/IV cases, the differences are determined by the behaviour of v_2: if v_2 increases, the aerodynamic loads in the ALM/IV case decrease compared to the ALM case; if v_2 decreases, the aerodynamic loads in the ALM/IV case increase compared to the ALM case. Moreover, the ALM/IV and ALM/IV-UA cases do not show relevant differences, confirming that the effects of UA and FSI remain separated.

The local distribution of the phase-averaged pitching moment (Figure 7.5c) explicitly shows the very large and abrupt fluctuations deducible from the standard deviation. In fact, if small – but noticeable – fluc-

tuations are present even at the tip, which do not affect the overall phase behaviour, high fluctuations, related to the noncirculatory normal force coefficient (see Section 7.5), alter completely the unsteady aerodynamic response, with severe overshoots compared to ALM and ALM/IV results with traditional tabulated airfoil data.

Finally, Figure 7.6 shows the instantaneous and phase-averaged airloads as a function of the instantaneous incidence at 25% and 90% of the blade for the T-ALM/IV and T-ALM/IV-UA cases. The phase-averaged values are coloured on the basis of the corresponding azimuthal position of the blade. In this way, we can observe the aggregated hysteresis of the loads, including not only the hysteresis of the aerodynamic coefficients (see Section 7.5), but also the effect of the velocity fluctuations. The coloured phase averages show that the majority of the incidence variation is related to the tower shadowing and confined in the last quarter of revolution. The strong and sudden variation in angle of attack and velocity generates an hysteresis in the loads of both the sections. However, the larger hysteresis of the aerodynamic coefficients makes the variation of the loads at the root larger compared to the ones at the tip. In the end, the increased airloads variability, of the pitching moment in particular, is visible from the increased area covered by the instantaneous airloads in gray.

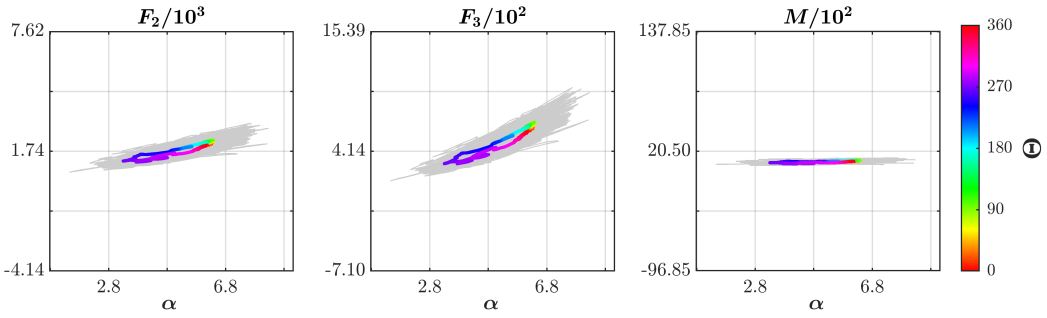

(a) Airloads at 25% span - T-ALM/IV case

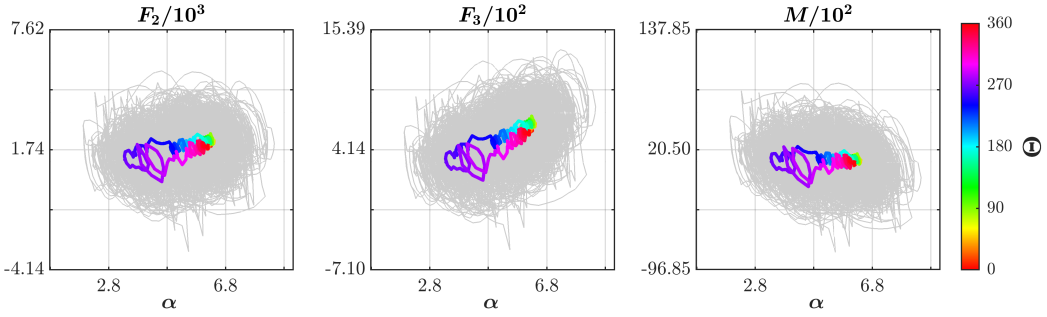

(b) Airloads at 25% span - T-ALM/IV-UA case

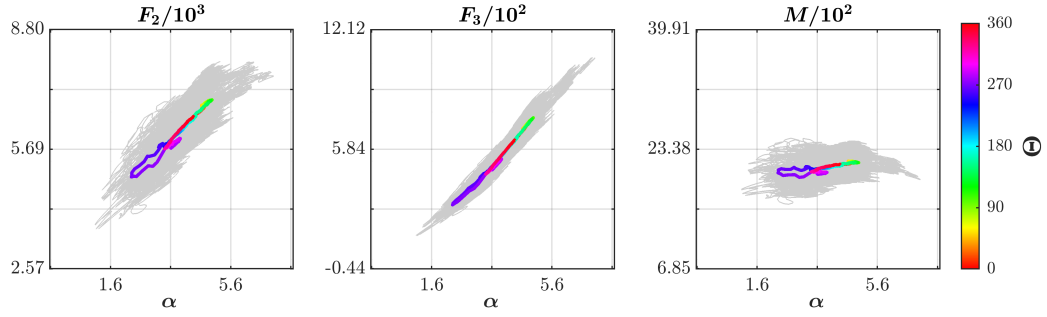

(c) Airloads at 90% span - T-ALM/IV case

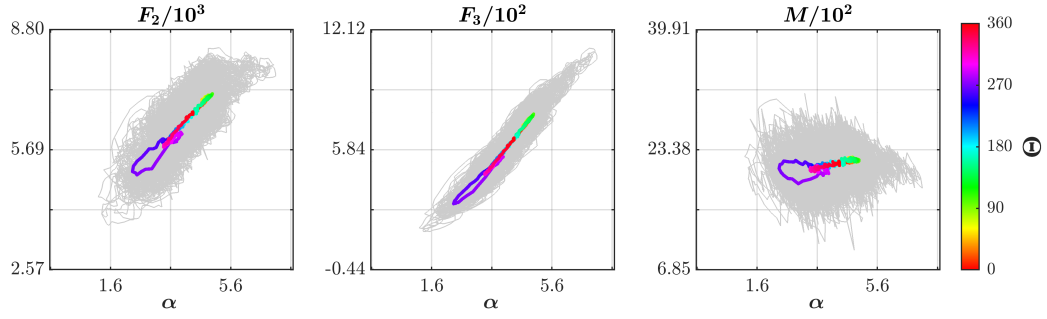

(d) Airloads at 90% span - T-ALM/IV-UA case

Figure 7.6: Instantaneous and phase-averaged airloads per unit length as a function of the incidence in the turbulent cases at 25% and 90% of the blade span. The colormap indicates the azimuthal angle in the phase average.

7.3 Structural dynamics

Figure 7.7 shows the phase average of the flapwise, edgewise and torsional components of the displacement and of the deformation velocity at the blade's tip, for the turbulent cases only. We can see that the FSI coupling has a major impact on the flapwise and torsional components, confirming the explained flapwise damping mechanisms, whereas it has a practically negligible effect on the edgewise component, dominated by the sinusoidal weight force on the blade. The premultiplied PSD of the tip flapwise deformation velocity in Figure 7.8 testifies how the aeroelastic coupling dampens the oscillations of the first flapwise mode. The $\langle v_2 \rangle$ fluctuations, mostly triggered by the passage of the blade in front of the tower, reach values that are comparable with the upstream fluid velocity in the last quadrant, and thus influence largely the definition of the local aerodynamic forces. On the other hand, the smaller variation of the incidence and the larger importance of the structural vibrations towards the free tip of the long blades make the effect of UA at the tip practically negligible.

A final comment on the dynamics of the torsional angle. Even if the variation of the pitching moment is large in the UA cases, the blade is particularly stiff torsionally, and thus the increased fluctuations at high frequencies, potentially close to the natural torsional frequencies (first torsional mode at $f \approx 5.58\,\mathrm{Hz}$), do not affect dramatically the overall dynamics of θ_1. As a consequence, also the indirect effect of the torsion on the flapwise motion, due to the eventual flexo-torsional coupling in the blade's structure, is rather small. This limits the possible indirect damage done by the uncertain accuracy of the pitching moment UA model to the FSI coupling procedure used in this work. However, we can see from Figure 7.8 that the increased fluctuations due to the UA model in the ALM/IV-UA cases, start to reinforce the high-frequency spectral components, activating also the torsional modes. As a result, if torsion had been included in the local definition of the incidence, this could have influenced directly and even more the aeroelastic response of the blades in general. In fact, with the addition of a model for the unsteady aerodynamics, the airloads are more sensitive to the instantaneous turbulent fluctuations of the velocity, which makes stronger the possible coupling between the high-frequency modes of the structure and the unsteady aerodynamics itself. Among the structural modes, torsional ones are particularly critical given their influence on the local incidence.

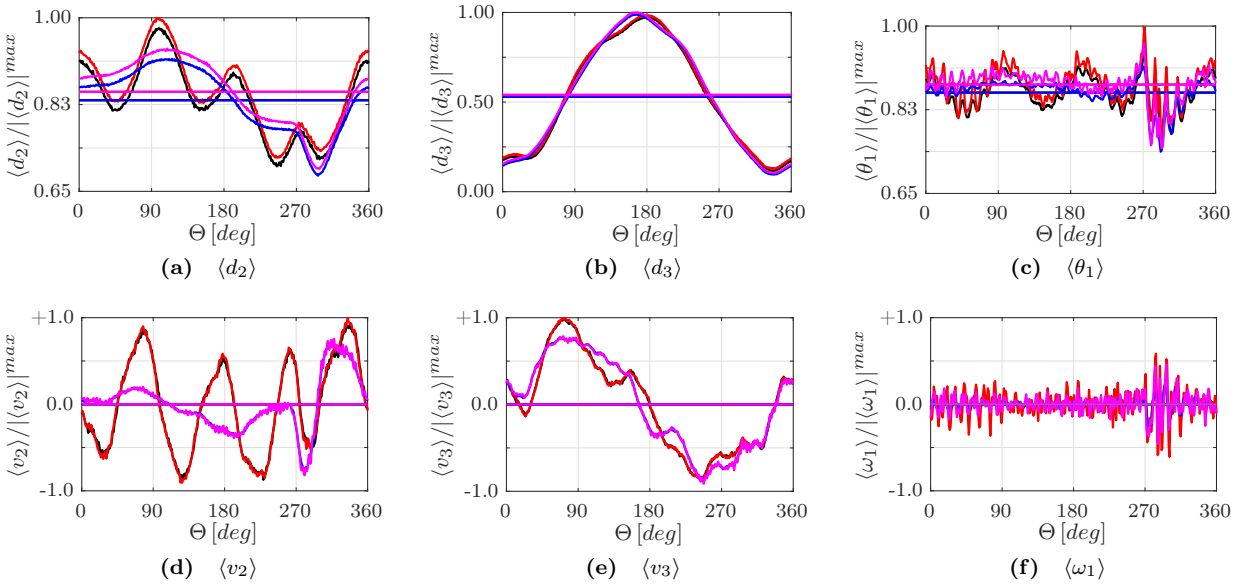

Figure 7.7: Flapwise (left), edgewise (centre) and torsional (right) components of the displacement (top) and corresponding components of the deformation velocity (bottom) at the blade tip for the turbulent cases only. Colours from Table 7.1. $|d_2|^{max} = 5.96\,\text{m}$, $|d_3|^{max} = 1.08\,\text{m}$, $|\theta_1|^{max} = 2.89\,\text{deg}$, $|v_2|^{max} = 2.45\,\text{m/s}$, $|v_3|^{max} = 0.789\,\text{m/s}$, $|\omega_1|^{max} = 18.6\,\text{deg/s}$.

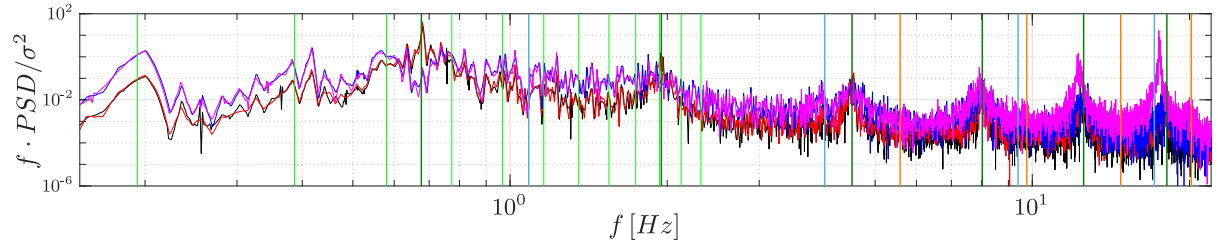

Figure 7.8: Pre-multiplied Power Spectral Density of the flapwise deformation velocity at the tip, normalised by the corresponding variance. Colours from Table 7.1. Vertical lines indicates the frequencies corresponding to: first 12 multiples of the rotational frequency, first 6 flapwise modes, first 4 edgewise modes, first 4 torsional modes. The last two modes reported are flexo-torsional modes with a dominant flapwise nature in the first case and a dominant torsional nature in the second case.

7.4 Reactions

Figure 7.9 shows the phase average of the six components of the reaction at the blade's root for the turbulent cases. We indicate with R_1, R_2 and R_3 the axial, flapwise and edgewise components of the reaction force respectively, and with M_1^R, M_2^R and M_3^R the torsional, edgewise, and flapwise reaction moment components respectively.

As expected, R_3 and M_2^R are mostly sinusoidal and determined by the gravitational force that is maximum at the multiples of $\Theta = 180\,\text{deg}$. The axial component R_1 instead is completely determined by the gravity and the centrifugal force. On the other hand, the flapwise and torsional components show the influence of the structural vibrations, which is dominant around the main source of structural unsteadiness, *i.e.* the tower. Moreover, UA introduces additional oscillations affecting the local behaviour. The amplitude of these contributions is larger for the torsional root moment, which experiences the large variability of the pitching moment.

As in the previous chapter, we compare the fatigue properties from the

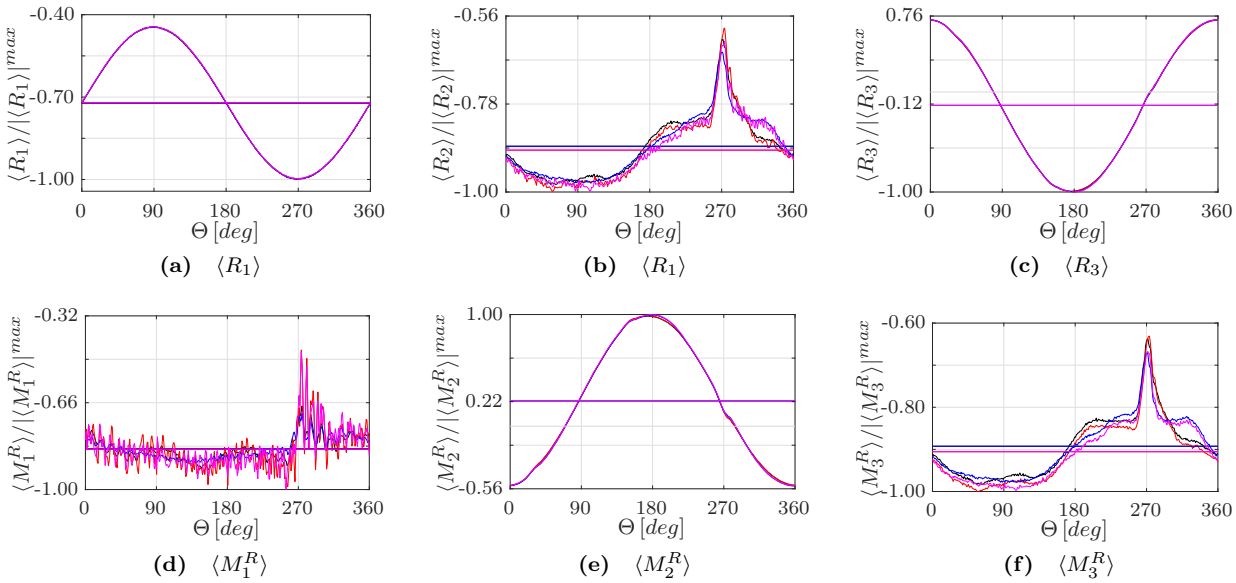

Figure 7.9: Phase-averaged force and moment components of the root reaction for the turbulent cases only. Colours from Table 7.1. $|R_1|^{max} = 6.24{\cdot}10^5$ N, $|R_2|^{max} = 2.41{\cdot}10^5$ N, $|R_3|^{max} = 2.00{\cdot}10^5$ N, $|M_1^R|^{max} = 1.13{\cdot}10^5$ N $\cdot$ m, $|M_2^R|^{max} = 4.60{\cdot}10^6$ N $\cdot$ m, $|M_3^R|^{max} = 9.54 \cdot 10^6$ N $\cdot$ m.

root reactions by means of the Damage Equivalent Load [176] from the post-processing tool MCrunch [177].

Table 7.2 and Table 7.3 report the DELs for the L-ALM and T-ALM reference cases and the percentage differences between each case and the relative reference one. The results confirm the findings of the previous chapter regarding the overprediction of the load fluctuations by using one-way coupled simulations. In particular, we demonstrated how the aerodynamic damping due to FSI coupling limits the flapwise and torsional vibrations of the blade and thus reduces by almost 10% - 20% the DELs of the corresponding components. By comparing the laminar and turbulent results, turbulence and mean shear increase by almost the double the equivalent airloads of the laminar cases. Meanwhile, the turbulent inflow limits the differences between the one- and two-way coupled cases, which confirms that turbulence mitigates the impact of the structural vibrations on the aerodynamics. However, torsional root reactions does not seem to be affected by the different coupling conditions, with only small differences between the laminar and the turbulent cases.

On the contrary, the introduction of the UA model has an opposite effect on the equivalent airloads: the additional fluctuations produced by the airloads hysteresis increase considerably all the DELs, especially the flapwise components affected by the hysteresis of C_n. We point out the large differences caused by the pitching moment dynamics on M_1^R, underlining that this issue will need special attention in future studies.

As a result of the two counteracting effects, the DELs of the IV-UA cases have an intermediate shift with respect to the ALM cases. In particular, they show that the increase due to the unsteady aerodynamics dominates over the decrease due to the aeroelastic coupling for

Table 7.2: Damage Equivalent Load of the reaction components: laminar inflow. The DELs of the baseline L-ALM case are reported together with the percentage differences for the other cases. The percentage difference for the generic root reaction component R_i is defined as $\Delta R_i\% = 100 \cdot (DEL_{R_i} - DEL_{R_i}^{ALM})/DEL_{R_i}^{ALM}$, where DEL_{R_i} is the DEL of the i-th root component of the case considered, and $DEL_{R_i}^{ALM}$ is that of the corresponding one-way coupled case without unsteady aerodynamics and with the same inflow (L-ALM).

DEL	$R_1\,[N]$	$R_2\,[N]$	$R_3\,[N]$	$M_1^R\,[N \cdot m]$	$M_2^R\,[N \cdot m]$	$M_3^R\,[N \cdot m]$
L-ALM	146.0	24.73	145.9	12.01	2988	942.0
$\Delta R_i\,\%$	$\Delta R_1\,\%$	$\Delta R_2\,\%$	$\Delta R_3\,\%$	$\Delta M_1^R\,\%$	$\Delta M_2^R\,\%$	$\Delta M_3^R\,\%$
L-ALM-UA	0.00 %	+24.73 %	+0.34 %	+268.71 %	+0.27 %	+ 8.28 %
L-ALM/IV	−0.03 %	−20.75 %	+0.10 %	− 21.81 %	+0.22 %	−24.58 %
L-ALM/IV-UA	0.00 %	+14.14 %	+0.58 %	+230.34 %	+0.49 %	−15.13 %

Table 7.3: Damage Equivalent Load of the reaction components: turbulent inflow. As in Table 7.2, but the baseline is the T-ALM case.

DEL	$R_1\,[N]$	$R_2\,[N]$	$R_3\,[N]$	$M_1^R\,[N \cdot m]$	$M_2^R\,[N \cdot m]$	$M_3^R\,[N \cdot m]$
T-ALM	152.0	47.95	146.0	23.98	2992	1840
$\Delta R_i\,\%$	$\Delta R_1\,\%$	$\Delta R_2\,\%$	$\Delta R_3\,\%$	$\Delta M_1^R\,\%$	$\Delta M_2^R\,\%$	$\Delta M_3^R\,\%$
T-ALM-UA	−0.07 %	+15.11 %	+0.48 %	+193.58 %	+0.25 %	+7.09 %
T-ALM/IV	0.00 %	−11.27 %	+0.41 %	− 25.35 %	+0.70 %	−13.56 %
T-ALM/IV-UA	−0.10 %	+ 7.81 %	+1.44 %	+196.50 %	+1.19 %	− 6.39 %

R_2, while the contrary happens for M_3^R. This disagreement is actually coherent with the distribution of the forces and with the different regions of influence along the blade. In fact, the force component is only given by a thorough integration of the force along the span, which makes no distinction concerning where the sectional force is applied. On the other hand, the moment depends on where the sectional force is applied and privileges the forces towards the tip. As a consequence, for M_3^R, the diminishing effect of the tip aeroelastic coupling prevails over the increasing effect of the root unsteady aerodynamics.

7.5 Unsteady aerodynamics variables

In this section, we examine the phase average of the various definitions of the incidence, the delayed separation point, and the contributions to the attached normal force component introduced by the UA model for two sections at 25% and 90% of the blade respectively.

Figure 7.10 reports the comparison between the T-ALM/UA and the T-ALM/IV-UA cases at 25% and 90% of the blade. The curves in Figure 7.10a confirm that the incidence is not affected by the structural vibrations close to the root of the blade, while the curves in Figure 7.10d show the sinusoidal variation due to the mean shear and confirm the effect of the aeroelastic interaction, especially in the last quadrant. Furthermore, it is visible that in the first half of the blade, the UA model introduces a noticeable delay between the geometric incidence $\langle\alpha\rangle$, the effective incidence $\langle\alpha_f\rangle$, and even more in the chordwise-effective incidence $\langle\alpha''\rangle$. It is also possible to see that, given the small time in which the blade covers the azimuthal region around the tower,

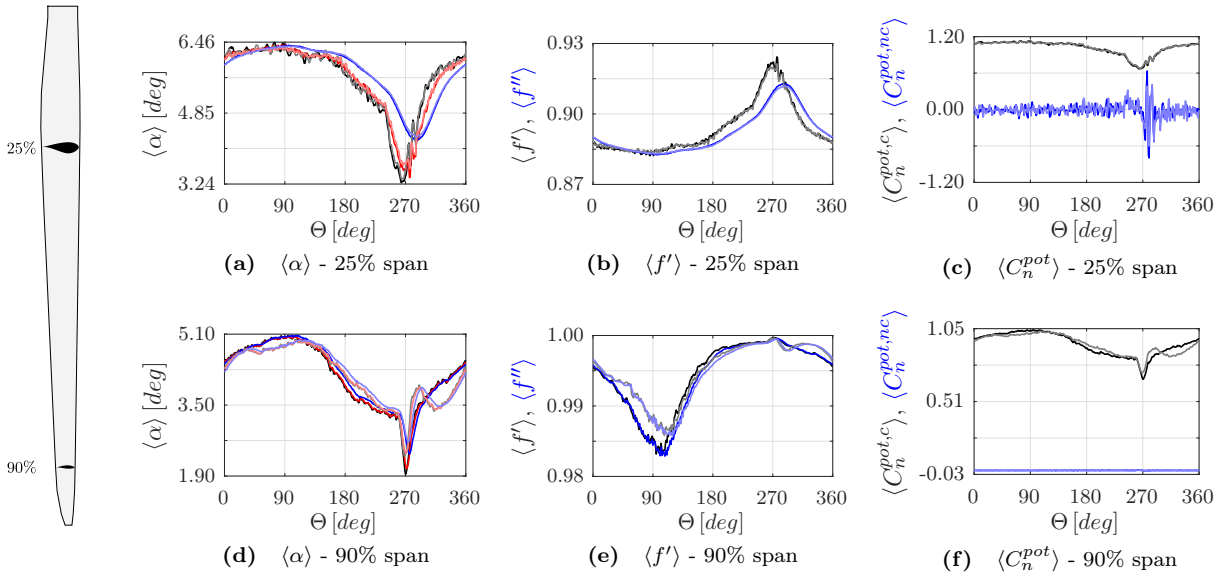

(a) $\langle\alpha\rangle$ - 25% span **(b)** $\langle f'\rangle$ - 25% span **(c)** $\langle C_n^{pot}\rangle$ - 25% span

(d) $\langle\alpha\rangle$ - 90% span **(e)** $\langle f'\rangle$ - 90% span **(f)** $\langle C_n^{pot}\rangle$ - 90% span

Figure 7.10: Phase average of some variables of the UA model for the T-ALM-UA case and the T-ALM/IV-UA at 25% (top) and 90% (bottom) of the blade span (shown on the left): various definitions of the angle of attack, delayed separation point, contributions to the attached normal force coefficient. Full lines are referred to the T-ALM-UA case, shaded lines to the T-ALM/IV-UA case. In the incidence plots, we report the instantaneous geometric incidence α, the effective incidence α_f, and the chordwise-effective incidence α''.

large derivatives of the incidence take place close to the root at low velocities, suggesting the relevant role of noncirculatory components here.

The decrease of the incidence shown in the tower region accounts for the gradual increase of the separation point function $\langle f\rangle$ and of its delayed estimation $\langle f''\rangle$, which is visible in Figure 7.10b. Close to the hub, the flow on the airfoil is always separated, with approximately 10% of the chord always covered by separated flow, and there is a relevant delay between $\langle f\rangle$ and $\langle f''\rangle$. On the other hand, towards the tip of the blade, the flow is almost fully attached, and the main source of motion to the separation point becomes the sinusoidal fluctuations imposed by the wind shear and the aeroelastic modifications. Moreover, the delay between $\langle f\rangle$ and $\langle f''\rangle$ is almost null.

The different response of the separation point to a qualitatively similar variation of the angle of attack throughout the rotor revolution depends mostly on the different $f-\alpha$ curves of the airfoils of the two regions. In particular, Figure 7.11 shows that the incidence fluctuations close to the tip take place near the sharp knee between the flat and steep regions of the separation point curve, while close to the hub they take place in a region with approximately uniform slope. Indeed, the airfoils closer to the tip are thinner and have a broader linear attached region in the aerodynamic polar, which makes the f curve flat on top for a broader region and then suddenly steep. Thick profiles in the first half of the blade, and especially really close to the root, have instead a more limited linear portion, since flow tends to separate soon and progressively, and thus their f curves have smoother knee on top. As a result, even assuming the same history of the incidence, the response $f(\alpha(t))$ is different.

Figures 7.10c - 7.10f report the comparison of the contributions to

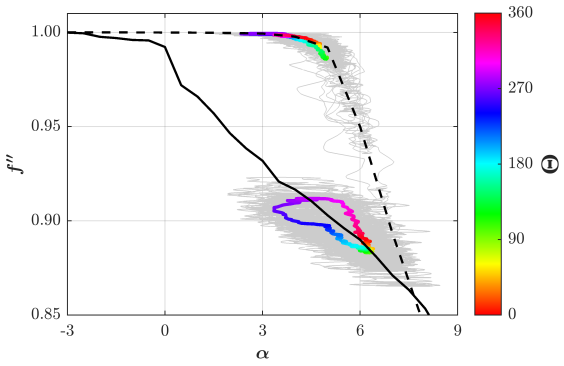

Figure 7.11: Hysteresis of the separation point at 25% (DU35_A17 $f - \alpha$ curve, –) and 90% (NACA64_A17 $f - \alpha$ curve, - -): instantaneous and phase-averaged f'' as a function of the incidence in the T-ALM/IV-UA case. The colormap indicates the azimuthal angle in the phase average.

the potential normal force coefficient. The differences in C_n^{pot} for the different cases are actually the origin of the differences in the complete airfoil coefficients, since the contribution from the LEV is almost null (not shown for brevity). We can immediately notice that the aeroelastic coupling has only an effect on the circulatory component of the tip profile, since it influences directly the modification of the geometric incidence. On the other hand, the noncirculatory component is insignificant at the tip, while being comparable to the circulatory component at the root. Here, where the variability of the incidence and the chord are larger, and the flow velocity is smaller (q at the root can be even 6 times higher than at the tip), the oscillations of $C_n^{pot,nc}$ can even overshadow the main $C_n^{pot,c}$ especially close the tower passage, which remains the main source of unsteadiness for both the structure and the aerodynamics.

In the end, similarly to the complete airloads in Figure 7.6, Figure 7.12 reports the phase-averaged and instantaneous hysteresis of the airload coefficients only for the T-ALM/IV-UA case at 25% and 90% of the blade. The coefficients oscillate around the steady-state values, confirming the ability of our UA model to recover in the average the usual tabulated values, and attest the main source of variation around $\Theta = 270\,\text{deg}$. Besides noting generally the different extent of the hystereses at the two sections, we highlight the narrower hysteresis of C_c related to the limited variability of the circulatory component of C_n, from which C_c mainly depends (Equation 2.97). Finally, we observe the very large hysteresis of C_m. For this component, the noncirculatory component remains significant also at the tip, and far larger than the small circulatory part typical for small angles of attack.

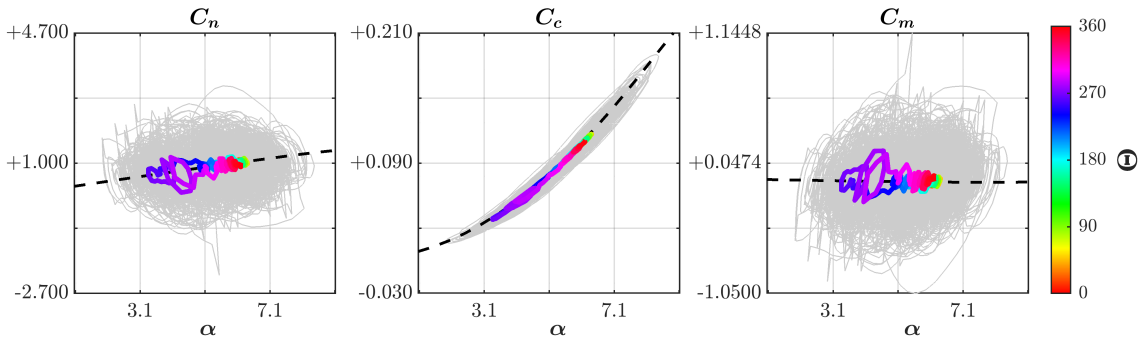

(a) Airloads at 25% span - T-ALM/IV-UA case

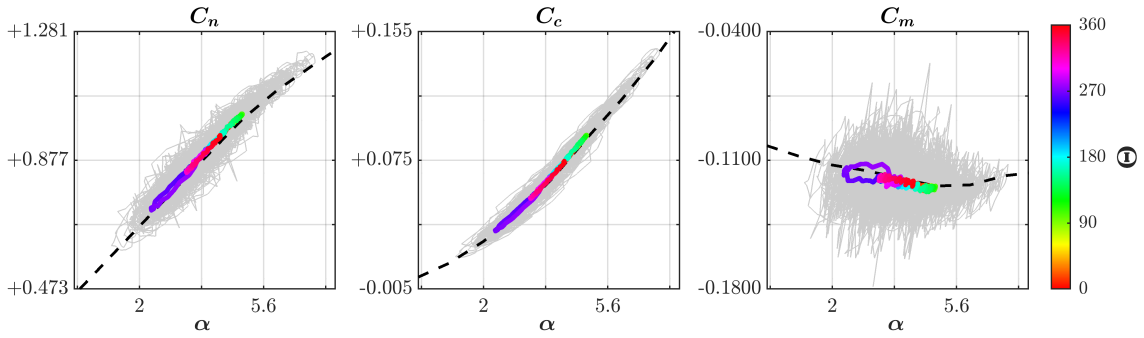

(b) Airloads at 90% span - T-ALM/IV-UA case

Figure 7.12: Instantaneous and phase-averaged airload coefficients as a function of the incidence in the turbulent cases at 25% (top) and 90% (bottom). The colormap indicates the azimuthal angle in the phase average.

7.6 Fluid flow

In general, we have noticed that the mean fluid flow is not affected significantly by the aeroelastic coupling and the unsteady aerodynamics. For this reason, we present in the following only a rapid comparison between L-ALM and T-ALM cases and an overview of the flow topology in the rotor region influencing the response of the blades.

Figure 7.13 compares the mean Turbulent Kinetic Energy (TKE) for the L-ALM and the T-ALM cases on vertical and horizontal slices through the hub. The contours show that the tower introduces an asymmetry in the wake, with a recirculation region just behind the tower and the nacelle. Moreover, the increased mixing induced by the turbulent inflow stimulates a more intense activity behind the wind turbine, promoting a faster wake recovery, as observable also from the rotor averaged velocity along the streamwise axis in Figure 7.14. Small differences in the organisation of the flow just behind the tower and the nacelle can also be noticed: the imposed mean shear reduces the extent of the recirculating region at the feet of the tower and enhances the one behind the nacelle.

Figure 7.15 reports instead the time-averaged velocity components for the L-ALM case on a vertical slice in correspondence of the rotor, with arrows indicating the velocity in the plane. The figures spotlight how the 3D and complex interaction between the disc blockage, the tower shadowing and the swirl induced by the blades break the axisymmetry of the flow in the proximity of the rotor, affecting the local fluid dynamics that determines the aerodynamic loads on the blades. In particular, the

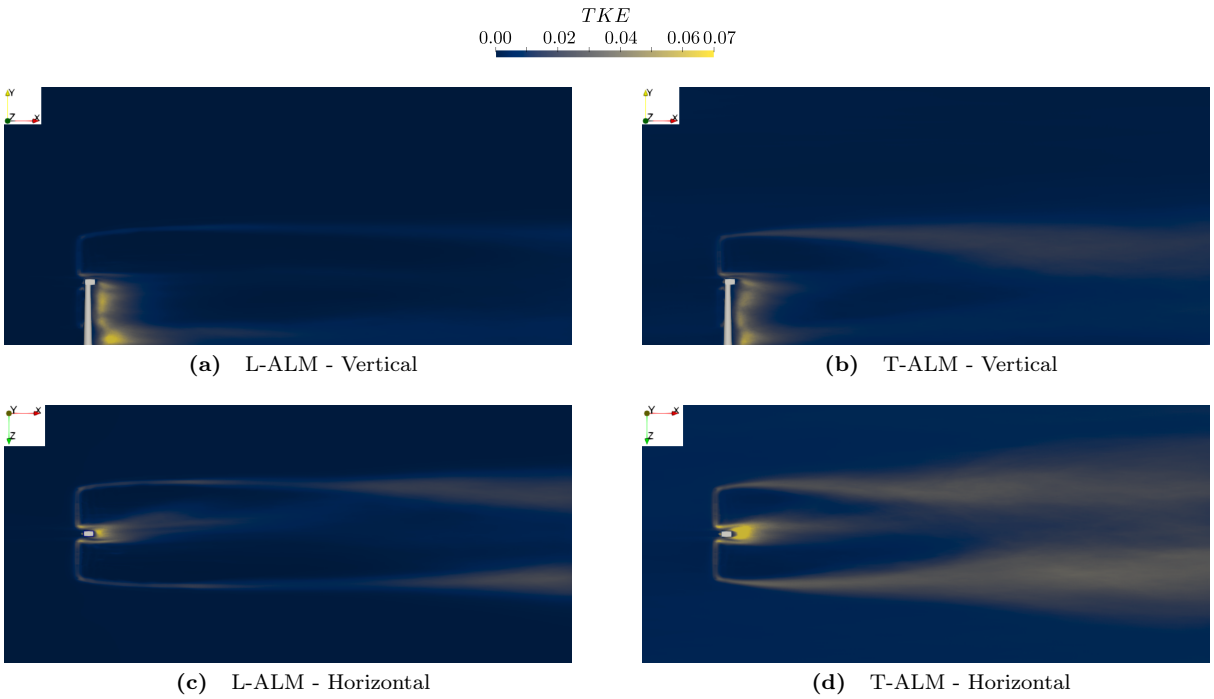

(a) L-ALM - Vertical

(b) T-ALM - Vertical

(c) L-ALM - Horizontal

(d) T-ALM - Horizontal

Figure 7.13: Time-averaged Turbulent Kinetic Energy on vertical (top) and horizontal (bottom) slices through the hub. L-ALM (left), T-ALM (right).

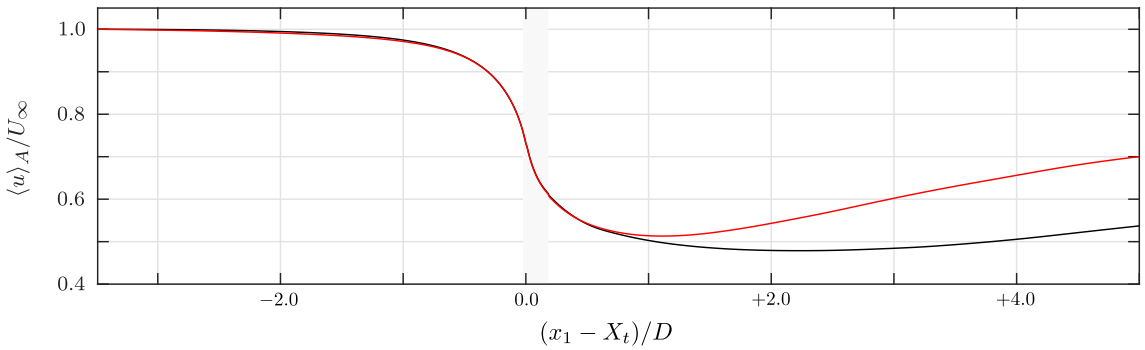

Figure 7.14: Rotor-averaged velocity along $(x_1 - X_t)/D$. T-ALM curve is scaled by the value of the rotor-averaged velocity at the inlet, which is slightly larger than U_∞. The region occupied by the wind turbine is indicated in gray. L-ALM –, T-ALM –.

interaction between the tower and the swirled flow induced by the rotor generates a mean flow slightly skewed towards the left ($z < z_t$) for a counterclockwise-rotating rotor. The obstruction due to the asymmetric recirculation region behind the tower induces the streamwise velocity to slightly increase on the left and and vice versa on the right. Moreover, the assumed conical shape of the tower generates a decrease of the flow velocity that is not homogeneous in the vertical direction. Thus, the lower part of the blades feels more the tower shadowing and the imposed flow deceleration.

As a result, we can divide the flow in the proximity of the rotor into five different regions:

- close to the terrain, the tower is not hidden by the rotor and the flow is deviated symmetrically in the lateral directions.
- In the bottom tip region, the enlargement of the stream tube impacting the rotor induces a radial flow component. The flow

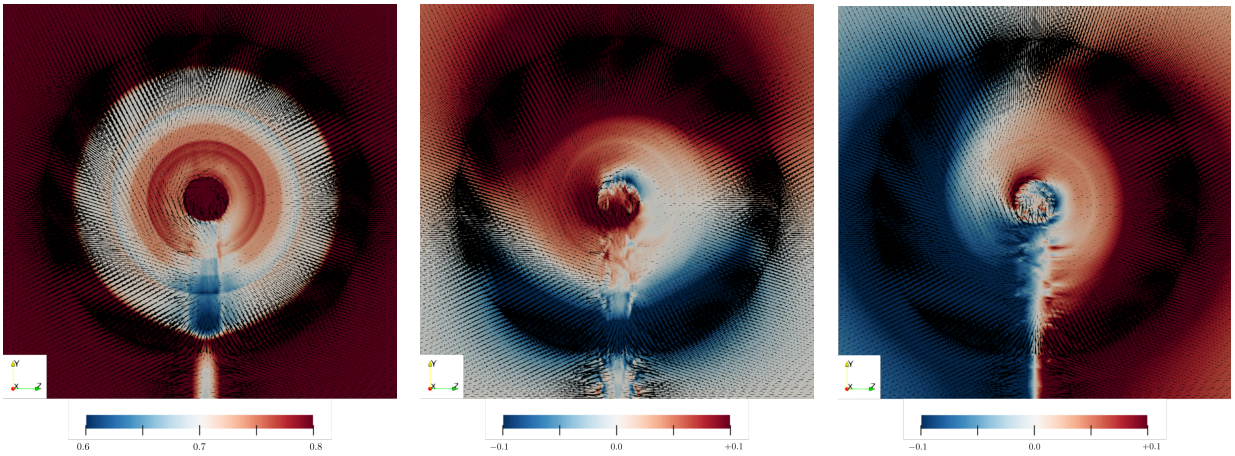

(a) $\overline{u}_1$ **(b)** $\overline{u}_2$ **(c)** $\overline{u}_3$

Figure 7.15: Time-averaged streamwise (left), vertical (centre), spanwise (right) velocity components on a vertical plane in correspondence of the rotor for the L-ALM case, with arrows indicating the velocity in the plane.

is determined by the combination of this component with the tower shadowing, whose effect is maximum here. From here, we can observe the asymmetry of the flow towards the left side of the turbine: while the fluid particles on the left do not find any obstacle in following the imposed clockwise swirl, the fluid particles on the right are blocked by the tower and thus forced to flow more radially, towards the terrain.

- After a region of transition, close to the root, the tower shadowing is less evident and the flow is dominated by the blades' swirl at the left of the tower. At the right, the decelerated flow remains mainly streamwise and progressively goes radially proceeding towards the tip of the blade, because of the increase in the stream tube area. Future works will consider also the presence of the hub in the geometry of the immersed body, whose lack in this case accounts for the overestimated velocities in the central region.
- On top of the nacelle, where there is no tower shadowing, the left and right flows merge together producing a flow that – in the plane – gradually tends to follow the opening of the stream tube towards the tip and the rotation imposed by the blades.

Discussion

8 Conclusions

Given the large increase in the electricity demand and the great expectations about the capabilities of green, renewable energy sources, the wind energy field is expected to grow and to play a central role in the future of the power generation.

8.1 With Great Power Come Great. . . Problems

To face these urgent requests and to reduce the Levelised Costs Of Energy (LCOE), wind turbines are getting bigger and bigger. The latest prototypes have rotor diameters around 220 metres and rated capacities of 15 MW. One single rotation could power one household for more than two days. However, with great power come great problems. Considering high towers with very large blades brings the need to better evaluate the interaction of the wind farms with the Atmospheric Boundary Layer (ABL), to better optimise the control systems of the large wind plants, and to better examine the complex physics of the response of these colossal rotating machines. In particular, huge, slender, and flexible blades ask for the assessment of coupling phenomena between unsteady, nonlinear fluid and structural dynamics. Obviously, the dimensions of the physical problem forbid almost completely controlled experimental measurements, but also theoretical modelling becomes difficult because of the inherent nonlinearities of the multi-physics problem.

8.2 Numerical Hopes

As a result, the scientific and industrial community has great expectations about the potential of proper multi-physics numerical modelling,

The credits for the image above the chapter title go to Offshore-Windindustry.com. https://www.offshore-windindustry.com/images/IWR/BilderKategorien/Fotolia_52430002_L_1280_512.jpg

able to simulate with adequate levels of fidelity the holistic response of the wind turbine. In this contest, numerical modelling of Fluid-Structure Interaction (FSI) has already demonstrated its capacity in the past, even with simplified, low-fidelity, engineering models. The coupling between simple structural models and the well-known Blade Element Momentum (BEM) theory provided a useful tool for the design of past wind turbines. However, with the advent of enhanced computational methods and resources, this method starts to be inadequate to describe the three-dimensional and unsteady interaction between the fluid and the solid parts. Given the evolution of Computational Fluid Dynamics (CFD) and Computational Structural Dynamics (CSD) methods, researchers envisage the development of high-fidelity CFD-CSD methods that provide sounder and more accurate representations of the wind turbine behaviour and that yield a deeper physical insight into realistic conditions.

However, high-fidelity, wall-resolved Direct Numerical Simulation (DNS) or Large Eddy Simulation (LES) of wind turbines are still out of question, given the large range of scales to be solved in the problem. For this reason, generalised actuator disc models are widely adopted to reduce the computational burden of the fluid dynamics simulations: additional body forces mimic the action of the blades' solid boundaries onto the fluid in the Navier-Stokes equations, avoiding the resolution of the exact surface geometry. A sectional blade-element approach defines the blades' airloads on the basis of tabulated airfoil data and of the local kinematics, while the Navier-Stokes equations describe the resulting 3D wake dynamics.

8.3 What We Aim For

The main idea of this work is to exploit the formulation of one of these models, the Actuator Line Model (ALM), to couple an high-fidelity fluid solver with an efficient simplified structural solver. Without practically affecting the heavy computational cost of an LES solver already validated for wind energy, our method allows estimating the aeroelastic response of the blades in a fluid solver that evaluates properly the unsteady and three-dimensional features of the flow impacting the rotor.

Furthermore, the sectional estimation of the airload coefficients of the actuator line model, offered us also the possibility to consider an additional element which is usually neglected in Horizontal Axis Wind Turbines (HAWTs), but that can be crucial for long blades and their aeroelastic response: the Unsteady Aerodynamics (UA). Despite the potential role of the UA phenomena for increasingly large wind turbines, their effects on the local aerodynamics have been scarcely considered and investigated to improve the modelling of state-of-the-art CFD simulations. The adoption of a UA model to estimate the airloads' coefficients has the potential to complete the description of the local aerodynamics in solvers that adopt steady-state tabulated airfoil data from wind tunnel measurements, and that do not use the

sufficient resolution to solve explicitly the unsteady behaviour of the blade boundary layer.

The aim of this work is therefore twofold.
In the first part, we presented our novel high-fidelity CFD-CSD model for the study of the aeroelastic response of HAWTs. The CFD solver adopts an LES approach modelling the rotor by means of the Actuator Line Model (ALM), and the tower and the nacelle by means of an Immersed Boundary Method (IBM). On the other hand, the CSD solver adopts a modal approach modelling the blades only as rotating cantilever beams, and includes the inertial effects in modal basis by means of the method followed by Saltari et al [155]. The coupling adopted is loose and staggered, to avoid undermining the computational efficiency of the complete coupled scheme, and takes advantage of the sectional evaluation of the aerodynamic forces of ALM, which thus provides a natural and efficient interface between the two physical subproblems.
In the second part, we examined the effects of an unsteady aerodynamics model for the evaluation of the sectional aerodynamic forces in the developed solver. A semi-empirical Beddoes-Leishman model has been implemented to evaluate dynamically the aerodynamic coefficients of the blade's airfoil in the ALM formulation of our LES solver, instead of using fixed tabulated airfoil data.

In all of our simulations, we considered the well-known baseline onshore HAWT defined in detail by the National Renewable Energy Laboratory (NREL), with a rated capacity of 5 MW, a diameter of 126 m and an hub height of 90 m [51].

For laminar, uniform and turbulent, sheared inflows, for one- and two-way coupled simulations – with different kinds of structural feedback – and for tabulated and dynamic aerodynamics, we examined the behaviour of such a utility-scale wind turbine by taking into consideration the time and phase average of the power and the thrust, the aerodynamic forces along the span, the structural displacements and their derivatives, the reactions and the related fatigue properties, but also the fluid field produced.

8.4 Effects of the Flexibility

In the first part, we compared the results of three sets of simulations that we named ALM, ALM/IV, and ALM/IVT. In the first case, we considered only a one-way coupling approach in which the LES solver provided the aerodynamic loading to the structural solver running in parallel; in the second case, we introduced in the definition of the local angle of attack a first structural feedback, made of the instantaneous bending deformation velocity in and out of the plane; in the third case, we added also the instantaneous torsional deformation caused by the unsteady loads to the structural feedback.
Our results showed that:

- The dynamics of the deformation velocity introduces an important variation in terms of power production, loads distribution,

structural dynamics and fatigue properties. In particular, the dynamics of the flapwise deformation velocity introduces a relevant aeroelastic damping that the one-way coupled simulations are not able to capture. The effect of the edgewise deformation velocity, instead, besides being ambiguous, is overshadowed by the larger rotational velocity.

- The effect of the torsional dynamics in the ALM/IVT case, often neglected in the literature, impacts significantly the estimated performances. In particular, the mean nose-down deformation of the blades reduces the aerodynamic loads, which thus suggests an overestimation of the generated power when adopting one-way coupled simulations. The dynamic effect of the torsional fluctuations instead is in general modest and, although some small effects on the other DOFs and on the root reactions start to be visible, the amplitude of the vibrations is still not sufficient to cause substantial differences for the turbine considered. However, different studies [61] have shown that the NREL 5 MW wind turbine has rather stiff blades. Thus, for longer and more flexible blades, it is not excluded that torsional dynamics could play a more influential role in FSI.
- The presence of the tower is key to predicting correctly the fluid and structural dynamics. On the one hand, it breaks the symmetry of the fluid field and the coherence of the wake structures; on the other hand, it is the main source of unsteadiness in the structural dynamics. Moreover, the reduced aerodynamic loads caused by the tower draw attention to the the effect of the aeroelastic coupling, which is amplified by the large vibrations of the structure in the quarter of revolution following the tower itself. However, given the strong influence of the various features of the atmospheric flow on the turbine performance [183, 184], further in-depth analysis must be carried out to better characterise the turbine aeroelastic response for different and more turbulent inflows. Indeed, turbulence intensity in these cases was rather low, and more intense turbulent structures could affect significantly the coupled dynamics and even dominate the tower-induced unsteadiness.
- The flapwise and the torsional vibrations are those more affected by the aerodynamic loads and thus by the FSI coupling mechanisms under study. On the contrary, the axial and edgewise DOFs are mainly affected by the gravitational force, given the large mass of each blade, as shown also in other works [53].
- While the structural dynamics, the aerodynamic loads, and the wind turbine coefficients show the effects of the different coupling procedures, the fluid field quantities are less or in no way sensitive to them.

[183]: Chamorro et al. (2015), 'Turbulence effects on a full-scale 2.5 MW horizontal-axis wind turbine under neutrally stratified conditions'
[184]: Howard et al. (2015), 'Characterizing the response of a wind turbine model under complex inflow conditions'

The time-averaged results were in general in good agreement with similar studies with different techniques, but the inherent features of our high-fidelity CFD-CSD approach accurately provided additional information also on the unsteady and distinct effects of the coupling procedures. These simulations thus explicitly assessed the unsteady impact of the aeroelastic mechanisms on a utility-scale wind turbine

under turbulent operative conditions, by means of a simplified but accurate numerical rotor modelling.

8.5 Effects of the Unsteady Aerodynamics

In the second part, we examined a set of eight simulations, in which we considered all the combinations between a uniform, laminar inflow and a sheared, turbulent inflow, one-way and two-way FSI coupling (with the deformation velocity feedback only) and with and without the UA model. This time, the turbulent intensity for the turbulent cases was higher and typical of a real conditions.

Our results showed that:

- The effects of both UA and FSI are not directly visible in the time-averaged behaviour, but rather more in the variability of all the aerodynamic and structural quantities. For fully-coupled simulations, we observed that the blade is divided into two regions of influence: the tip region, mainly influenced by important flapwise vibrations affecting the local incidence, and the root region, mainly influenced by important oscillations of the angle of attack at low fluid velocity that generate large noncirculatory contributions to the airfoil coefficients. Inflow turbulence mitigates the differences between the two regions, and increases the variability of the loads throughout the blade.
- Even for the more turbulent cases, the dominant source of aerodynamic and structural unsteadiness remains the presence of the tower, which is thus a critical element to be considered to properly estimate the overall wind turbine behaviour. As already shown in the first part, tower shadowing causes a sudden variation of the flow that curtails the airloads, promotes the flapwise and torsional structural vibration, causes a mean deflection in the wake flow, and additionally, triggers the surge of added mass effects that amplify the airload hysteresis.
- No particular interaction between UA and FSI takes place, although the spectral analysis of the deformation velocity reveals that the increased unsteadiness introduced by the UA fluctuations starts to trigger the high-frequency structural modes, which affect also the torsional dynamics with potential effects in the aeroelastic response of the blade.
- The analysis of the fatigue properties from the root reaction components indicated also that the two models have competing effects, whose net effect depends on the reaction component considered. While the FSI-induced aerodynamic damping reduces the load fluctuations almost exclusively at the tip, the hysteresis of the airloads from the UA module increases them more, but primarily at the root, as previously shown for tidal turbines [185].
- Finally, the flow dynamics primarily changes basically because of the different inflow, with increased wave recovery promoted by the more realistic turbulent inflow, but is again almost insensitive to the variations induced by the structural vibrations and the unsteady aerodynamics. Anyway, the analysis of the mean flow

[185]: Scarlett et al. (2019), 'Unsteady hydrodynamics of a full-scale tidal turbine operating in large wave conditions'

close to the rotor showed the complexity induced by the critical presence of the tower, which affects the definition of the incidence for the blades' airfoils and the airloads in turn.

We acknowledge that the pitching moment UA model needs further studies, given its intrinsic empiricism. But does its use invalidate all the results, especially about the aeroelastic interaction? Since some high-frequency contributions around the torsional natural frequencies are present in the spectra of the flapwise deformation velocity, some effects of the enhanced torsional dynamics start to be felt. However, the flexo-torsional coupling in the blade we considered has a limited importance for the low natural frequencies of the structure, which still remain the dominant ones. Hence, we believe that our conclusions about the FSI coupling are still valid.

In any case, despite the expected limits of the semi-empirical UA model, our study puts under the spotlight the potential impact of the unsteady aerodynamics on the general behaviour of large HAWTs and points out the need to cover a gap in the representation of the local aerodynamics for simplified CFD methods used in wind energy.

8.6 Very Final Conclusions

In the end, in this work we tried to cover some of the gaps in the numerical modelling of the complete physics of wind turbines. First of all, we tried to prove the validity of a simplified FSI coupling, and we demonstrated that in order to properly describe the aeroelastic response of the blades, especially the structural behaviour, one-way coupled simulations overpredict both vibrations and load fluctuations, with relevant consequences on the estimation of crucial fatigue properties. Moreover, the often neglected torsional degree of freedom starts to play a role in the estimation of the airloads, and neglecting it can induce further differences with one-way coupled results. On the other hand, if one is interested only in the behaviour of the fluid flow, two-way coupling has practically no effect on the wake. However, further studies need to assess how wind turbines can interact and how the aeroelasticity of the blades could modify the functioning of the standalone wind turbines.

Another critical aspect is the presence of the tower in the numerical modelling. Our results confirm that neglecting the fixed elements of the wind turbine in the fluid domain would mean completely ignoring the main source of unsteadiness of the structure and also of the unsteady aerodynamics. The tower induces a significant asymmetry in the wake and a relevant perturbation in the local flow close to the rotor, with obvious consequences for the local incidence determining the airloads along the blades. The slowdown of the flow generates a limited low-velocity region that induces a sharp variation in the incidence. The fluctuations of the airloads accounts for the increased vibrations of the structure – especially flapwise and at the blade tip –, which thus become relevant for the aeroelastic coupling. Moreover, the sudden variations of the incidence at low velocities accounts also for the generation of noncirculatory components in the aerodynamic coefficients that can

become dominant – especially in the normal component and at the blade root.

The introduction of the unsteady aerodynamics, instead, unveiled that for large blades, the extent of the region affected by relevant hysteresis phenomena increases and that the consequent additional contributions to the airfoil forces can even start to affect the structural dynamics, especially in the high-frequency domain.

Future studies could follow different paths to enhance the developed model.
First of all, recent works [160] stated that linear models start to describe defectively very long composite blades with pre-bending, coning, sweep and other geometrical complications. As a result, it would be interesting to upgrade the structural model with more complex beam theories [21] to assess the effects of the structural nonlinearities on the response of blades larger than the ones studied [186].

[186]: Bak et al. (2013), *Description of the DTU 10 MW reference wind turbine*

Moreover, severe fluctuations of the incidence cause high-frequency and high-amplitude fluctuations of the aerodynamic coefficients, triggering even more high-frequency structural modes. These includes torsional and more coupled structural modes, which thus paves the way for torsion to come into play in the definition of the incidence more and more. As a result, after having improved the UA model and fixed the critical issues mentioned above, it will be interesting to examine how the inclusion of the torsional degree of freedom in the structural feedback changes the aeroelastic response also with UA.

Finally, wind farms are the main ingredient of the future of wind energy. Several studies [14] [187] have demonstrated the capability of LES solvers to simulate numerically the effects of the fluid interaction between turbines in realistic layouts of wind farms, but under the assumption of rigid structures. The presented method will allow us in future works to assess also the aeroelastic unsteady effects on the loading of turbines in waked operational regimes.

[187]: Archer et al. (2013), 'Quantifying the sensitivity of wind farm performance to array layout options using large-eddy simulation'

Appendix

A

Unsteady Aerodynamics Details

A.1 Validation of the model: the S809 airfoil

Here in the following, for the S809 airfoil in different conditions, we report a comparison of the results of our BL model against the experimental measurements from the Ohio State University [188] and against the numerical results provided by another slightly different implementation of the Beddoes and Leishman model for the same profile and the same conditions [189].

[188]: Ramsay et al. (1995), *Effects of grit roughness and pitch oscillations on the S809 airfoil*

[189]: Gupta et al. (2006), 'Dynamic stall modelling of the S809 aerofoil and comparison with experiments'

The results show that the qualitative unsteady behaviour of the aerodynamic response is predicted adequately, even if in some conditions the model slightly underpredicts the quantitative amplitude of the oscillations. This certainly depends on the precise value of all the empirical constants in the model, as can be seen from the results of the same model with different airfoil parameters used in Damiani et al., 2016.[99] However, fine tuning of all these constants for our specific implementation is out of the scope of this work, since the S809 airfoil is not of our interest for the wind turbine considered and since no experimental data are available for the unsteady aerodynamics of the NREL 5 MW wind turbine's airfoils. Moreover, unlike the code, the coefficients below are evaluated by using the effective incidence for the circulatory potential part provided by the classic superposition of indicial responses. These tests demonstrate only the ability of our model to capture the unsteady features of the aerodynamics and to preserve the specific features of the original static aerodynamic polars.

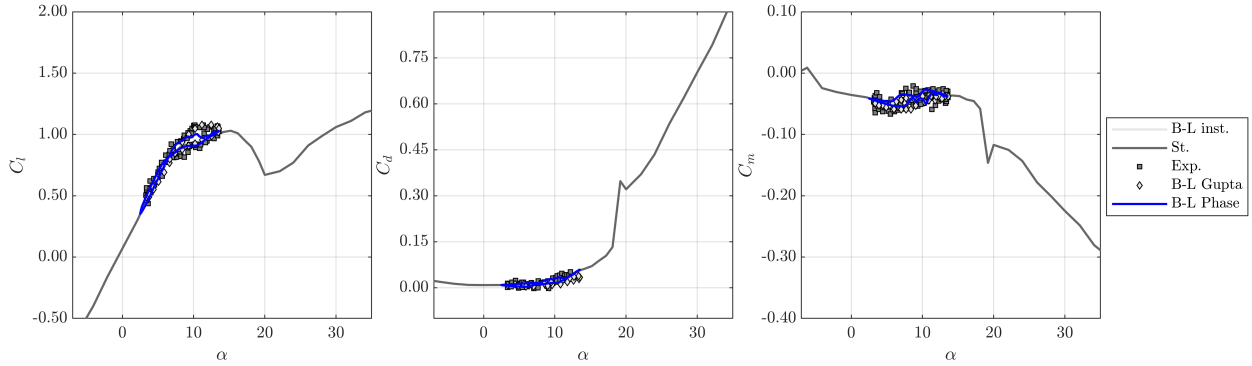

(a) $\Delta\alpha = 5.5°, k = 0.0026$

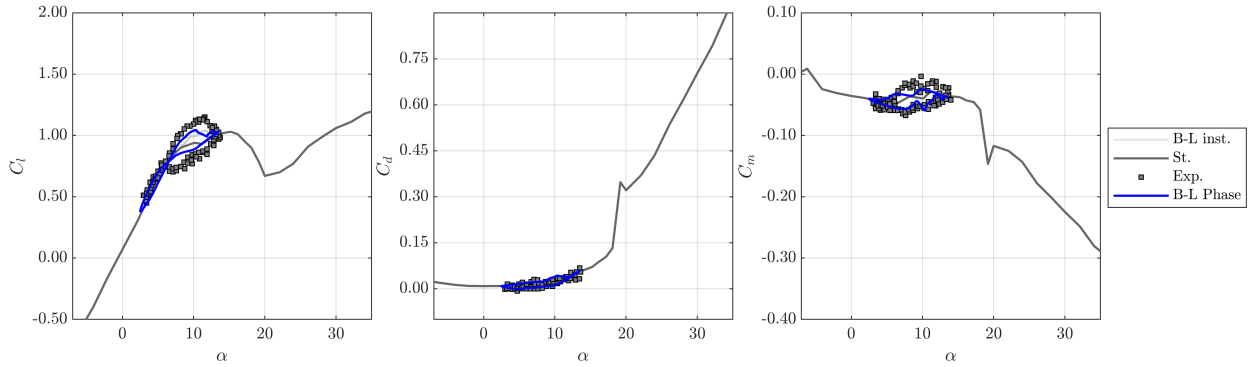

(b) $\Delta\alpha = 5.5°, k = 0.050$

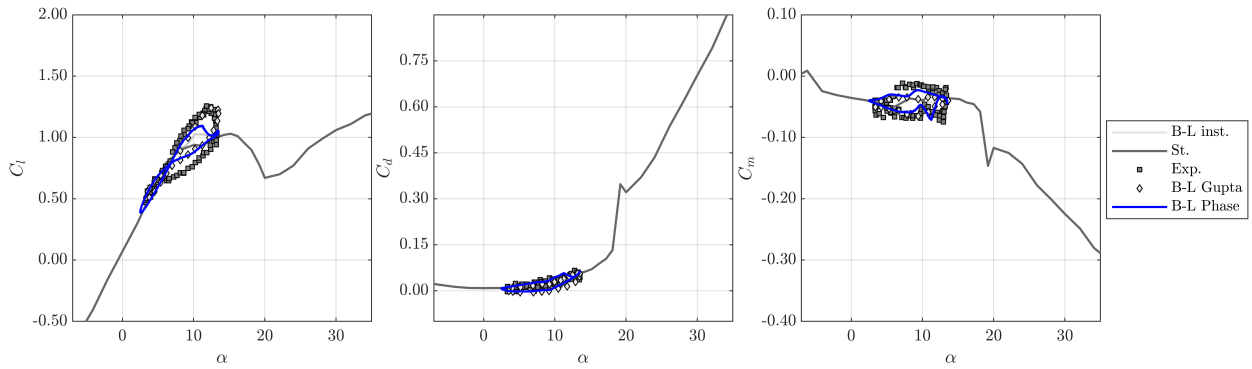

(c) $\Delta\alpha = 5.5°, k = 0.077$

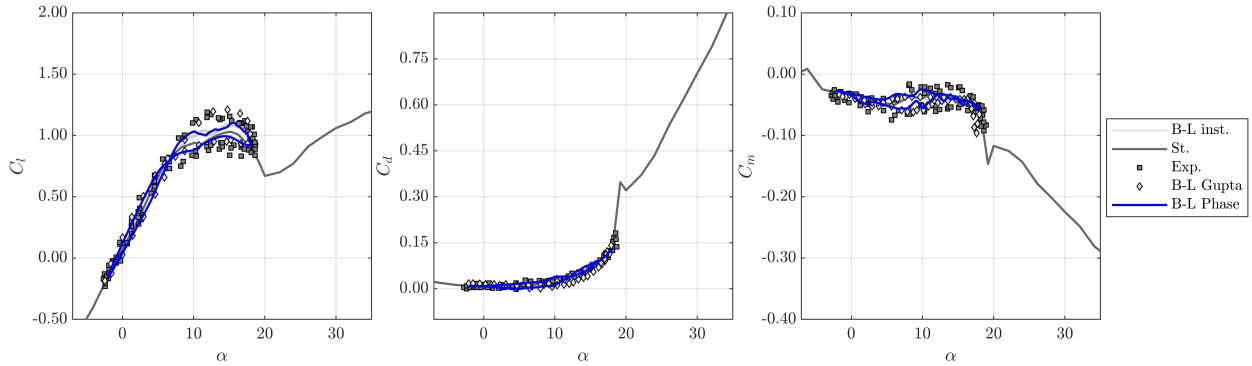

(d) $\Delta\alpha = 10°, k = 0.0026$

Figure A.1: Comparison of the S809 airfoil coefficients for $\bar{\alpha} = 8°$.

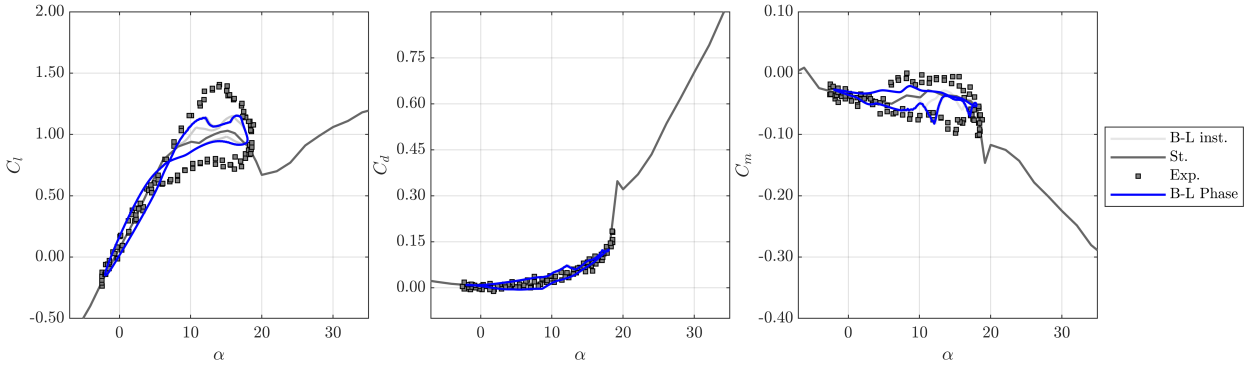

(e) $\Delta\alpha = 10°, k = 0.050$

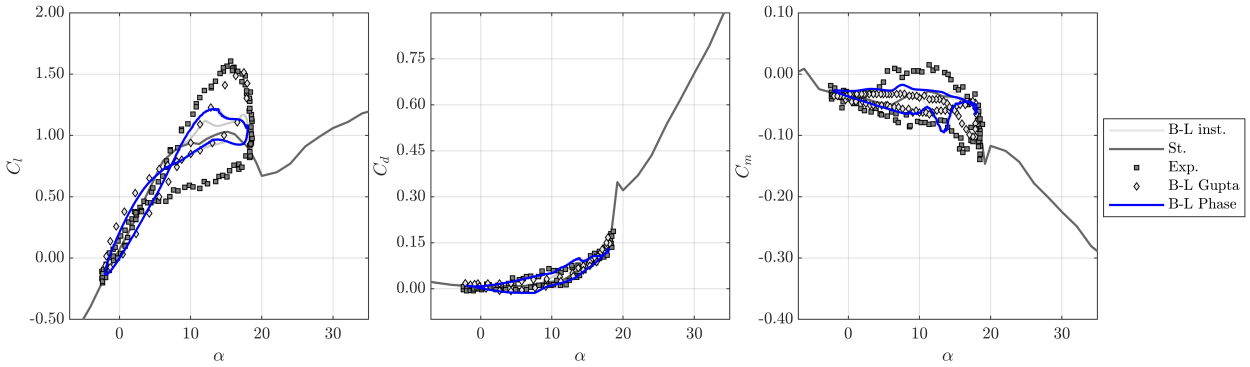

(f) $\Delta\alpha = 10°, k = 0.077$

Figure A.1a: Comparison of the S809 airfoil coefficients for $\bar{\alpha} = 8°$.

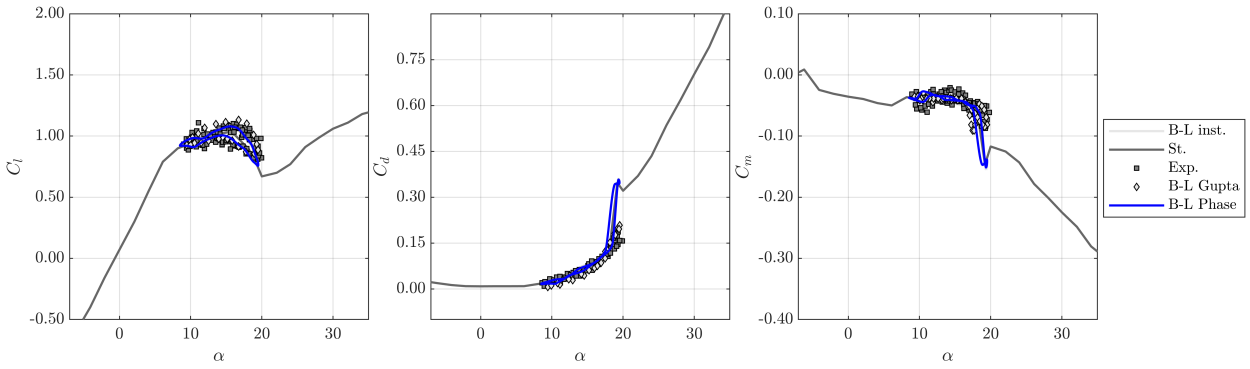

(a) $\Delta\alpha = 5.5°, k = 0.0026$

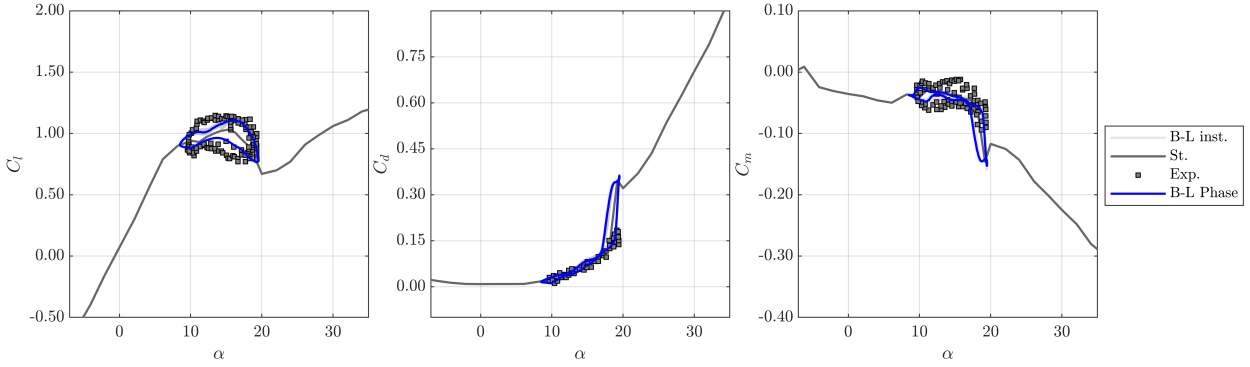

(b) $\Delta\alpha = 5.5°, k = 0.050$

Figure A.2: Comparison of the S809 airfoil coefficients for $\bar{\alpha} = 14°$.

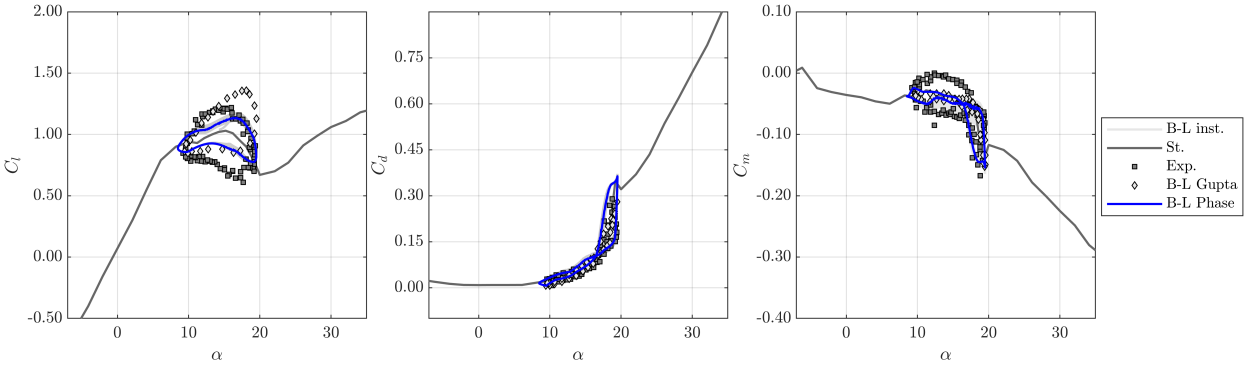

(c) $\Delta\alpha = 5.5°, k = 0.077$

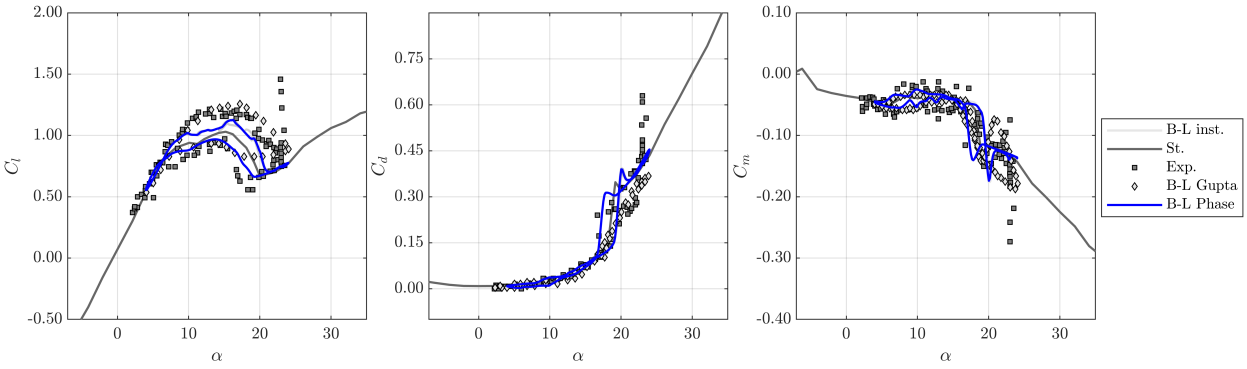

(d) $\Delta\alpha = 10°, k = 0.0026$

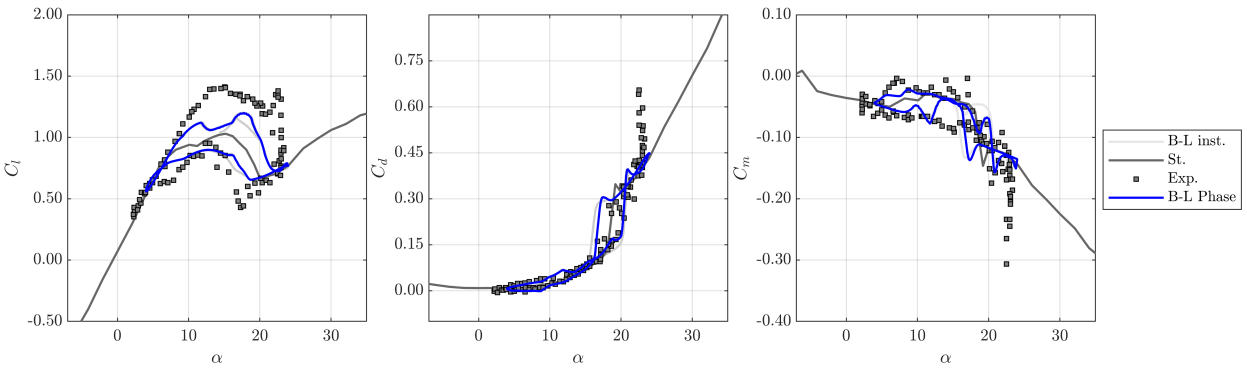

(e) $\Delta\alpha = 10°, k = 0.050$

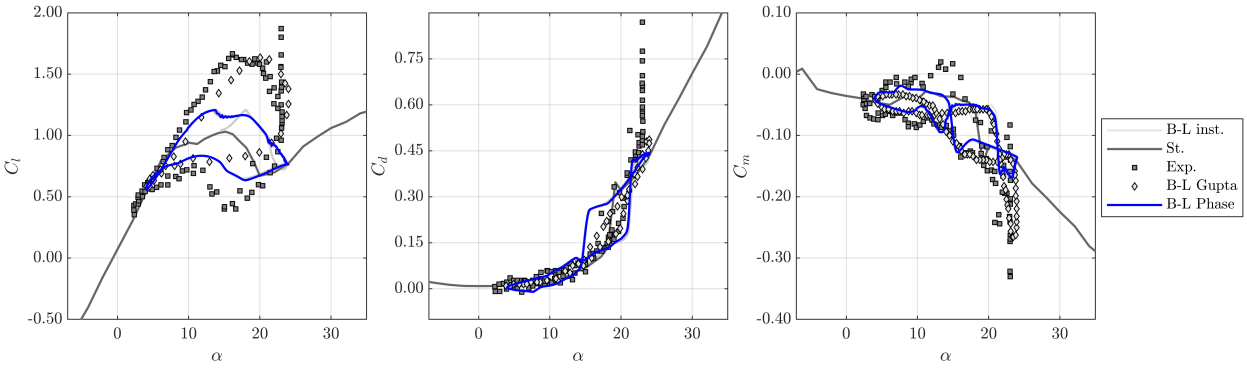

(f) $\Delta\alpha = 10°, k = 0.077$

Figure A.2a: Comparison of the S809 airfoil coefficients for $\bar{\alpha} = 14°$.

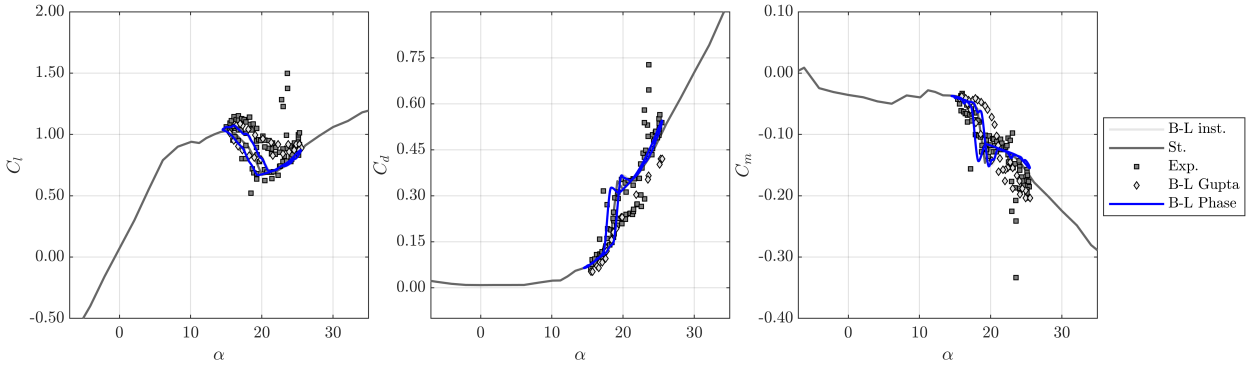

(a) $\Delta\alpha = 5.5°, k = 0.0026$

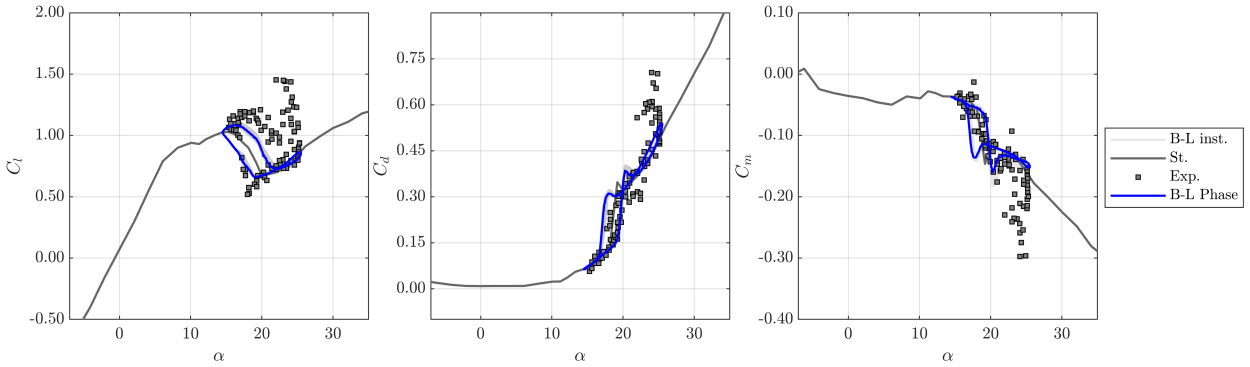

(b) $\Delta\alpha = 5.5°, k = 0.050$

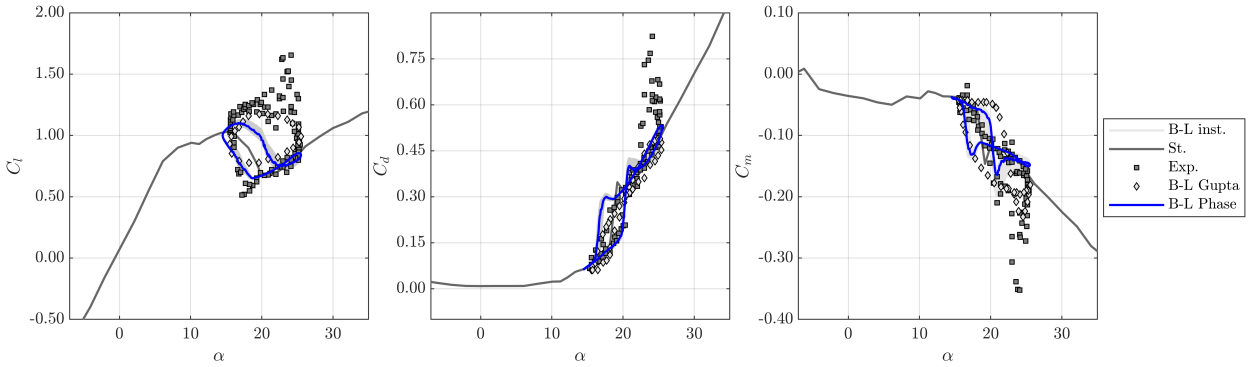

(c) $\Delta\alpha = 5.5°, k = 0.077$

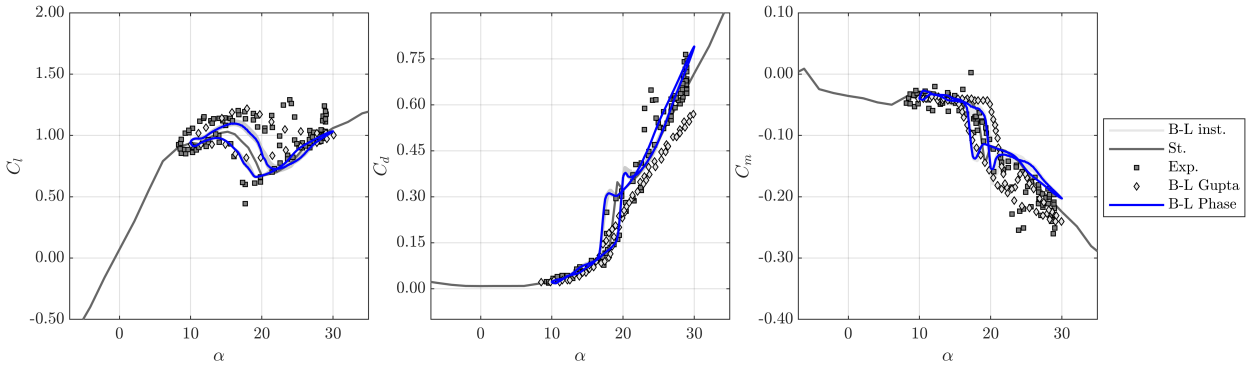

(d) $\Delta\alpha = 10°, k = 0.0026$

Figure A.3: Comparison of the S809 airfoil coefficients for $\bar{\alpha} = 20°$.

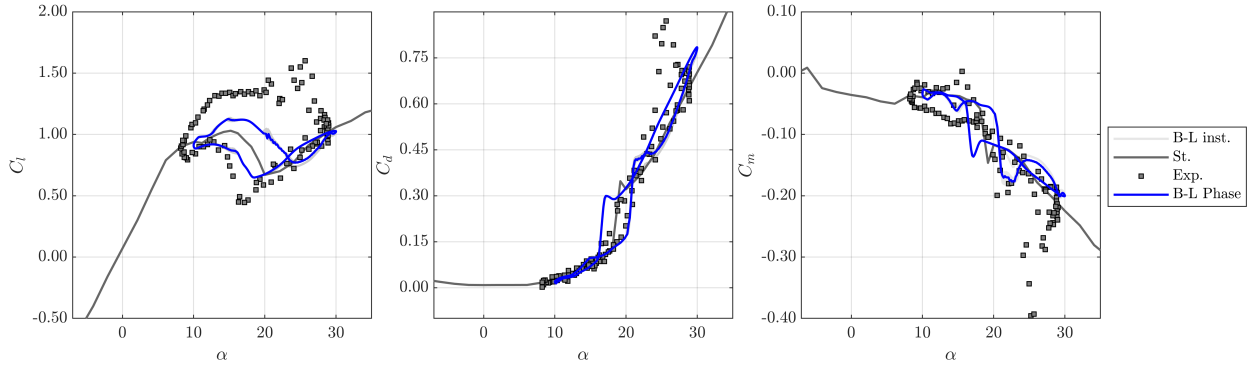

(e) $\Delta\alpha = 10°, k = 0.050$

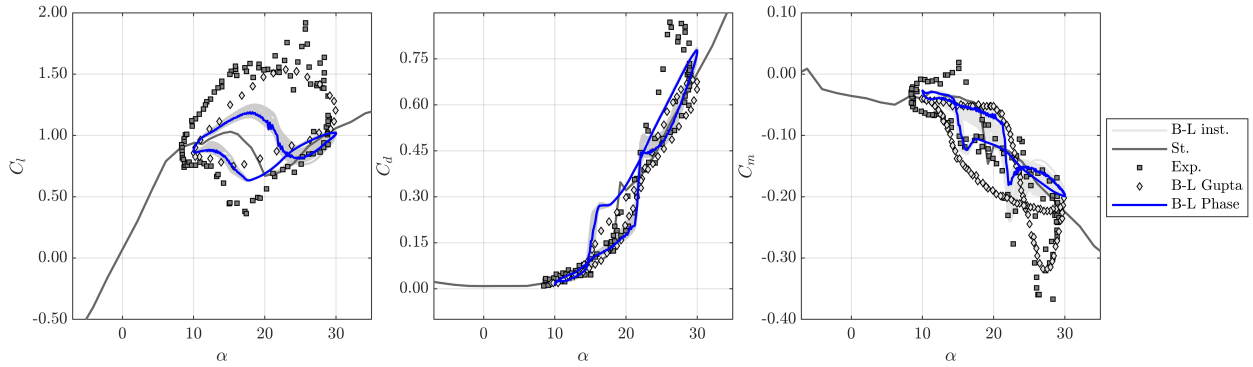

(f) $\Delta\alpha = 10°, k = 0.077$

Figure A.3a: Comparison of the S809 airfoil coefficients for $\bar{\alpha} = 20°$.

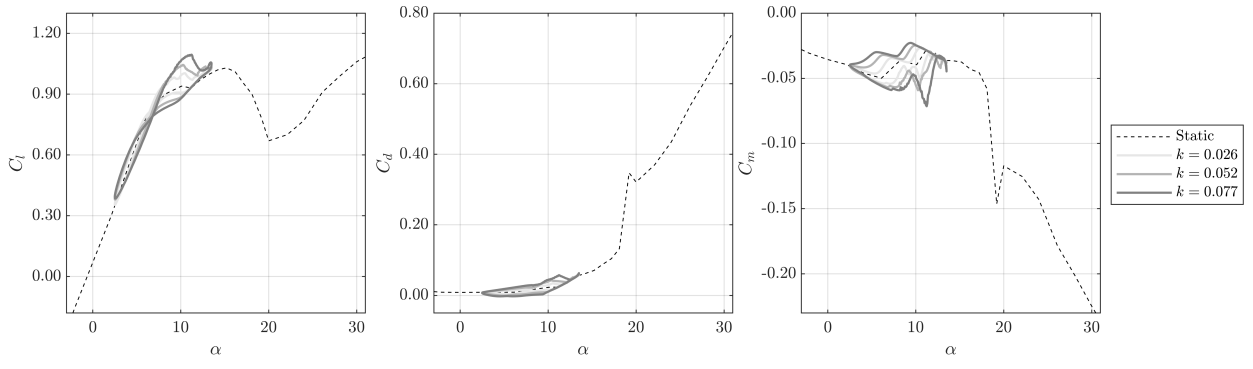

(a) $\bar{\alpha} = 8°, \Delta\alpha = 5.5°$

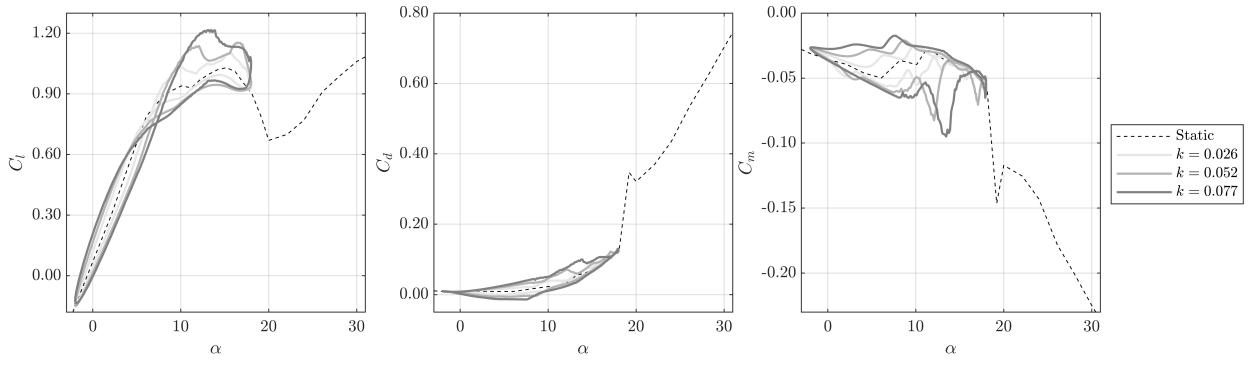

(b) $\bar{\alpha} = 8°, \Delta\alpha = 10°$

Figure A.4: Comparison for different k and same $\bar{\alpha}$ and $\Delta\alpha$.

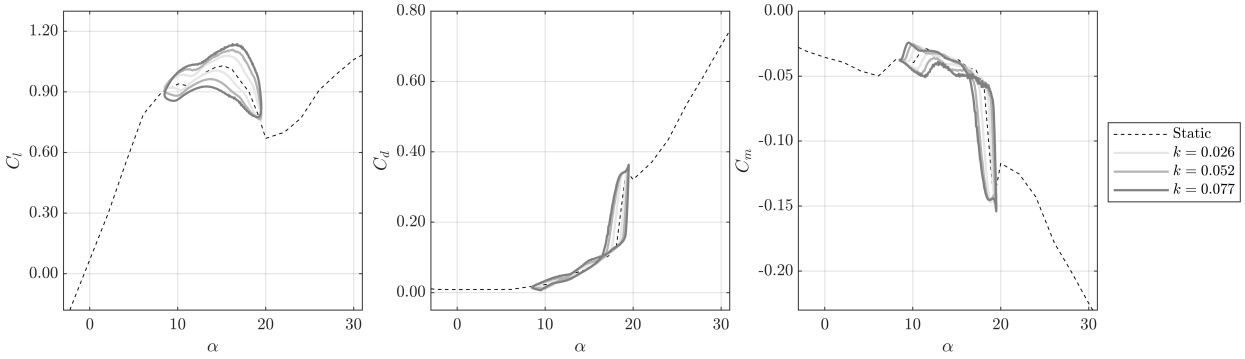

(c) $\bar{\alpha} = 14°, \Delta\alpha = 5.5°$

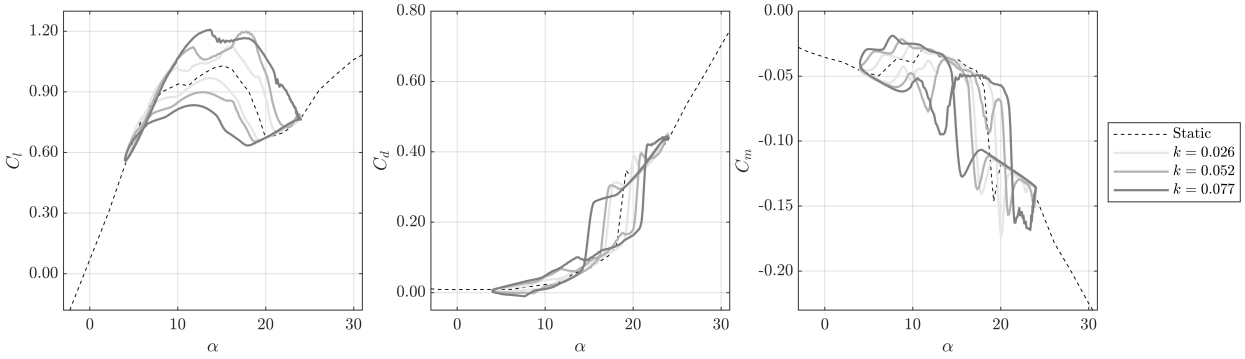

(d) $\bar{\alpha} = 14°, \Delta\alpha = 10°$

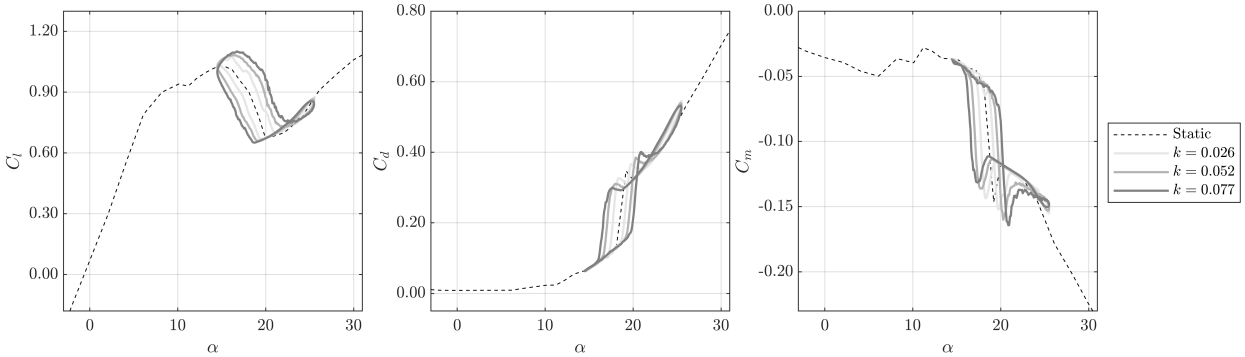

(e) $\bar{\alpha} = 20°, \Delta\alpha = 5.5°$

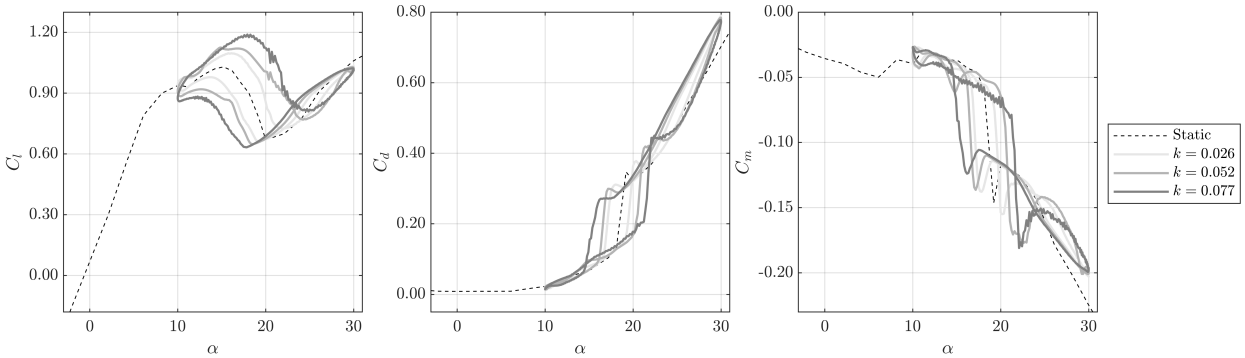

(f) $\bar{\alpha} = 20°, \Delta\alpha = 10°$

Figure A.4a: Comparison for different k and same $\bar{\alpha}$ and $\Delta\alpha$.

A.2 T_f modifications

In order to account for the different times of the different processes taking place during separation at the *trailing* edge, the variable σ_1 modifies the initial value T_{f0} of the time constant $T_f = T_{f0}/\sigma_1$. The initial value of the variable $\sigma_1 = 1$ is modified according to the conditions reported in the pseudocode below, from the reference paper for the unsteady aerodynamics [142]. The logical variables TESF, LESF, VRTX are true if trailing-edge separation, leading-edge separation and vortex advection are taking place respectively, according to the conditions explained in Section 2.5.

```
IF TESF = True THEN: (trailing-edge separation)
  IF K_α(α − α_0) < 0 THEN:
    σ_1 = 2 (accelerated f motion, moving towards α_0)
  ELSE IF LESF = True THEN:
    σ_1 = 1 (possible leading-edge separation, moving away from α_0)
  ELSEIF f''_{n−1} ≤ 0.7 THEN:
    σ_1 = 2 (accelerated f motion when separation is occurring)
  ELSE:
    σ_1 = 1.75 (accelerated f motion)
ELSE: (reattachment)
  IF LESF = False THEN:
    σ_1 = 0.5 (decelerated reattachment)
  IF VRTX = True AND τ_V ∈ [0, T_VL] THEN:
    σ_1 = 0.25 (no reattachment if vortex shedding in progress)
  IF K_α(α − α_0) > 0 THEN:
    σ_1 = 0.75 (default)
```

A.3 T_V modifications

Analogously to T_f, to consider the different times of the different processes taking place during separation at the *leading* edge, the variable σ_3 modifies the initial value T_{V0} of the time constant $T_V = T_{V0}/\sigma_3$. The initial value of the variable $\sigma_3 = 1$ is modified according to the conditions reported in the pseudocode below, from the reference paper for the unsteady aerodynamics [142], when $LESF = True$.

```
1) Is the vortex past the trailing edge, but less than 2 chords?
IF τ_V ∈ [T_VL, 2T_VL] THEN:
  σ_3 = 3 (accelerated vorticity decay in post-shedding)
  IF TESF = False THEN:
    σ_3 = 4 (accelerated vorticity decay if reattaching flow)
2) Is the vortex on the airfoil?
ELSEIF VRTX = True AND τ_V ∈ [0, T_VL] THEN:
    IF K_α(α − α_0) < 0 THEN:
      σ_3 = 2 (accelerated vorticity decay if moving towards α_0)
    ELSE
      σ_3 = 1 (default)
3) Is the vortex over the airfoil, but still close, and is it
    moving away from stall?
ELSEIF K_α(α − α_0) < 0 THEN:
  σ_3 = 4 (fast vorticity decay)
```

```
4) Vorticity enhancement if flow is reattaching and rate of change
     of the AoA is slowing down.
IF TESF = False AND K_q(α − α_0) < 0 THEN:
  σ_3 = 1 (default)
```

Bibliography

Here are the references in citation order.

[1] United Nations. *The 2019 Revision of World Population Prospects*. [Online; accessed 30. Dec. 2020]. Aug. 2019 (cited on page 3).

[2] Enerdata. *Electricity domestic consumption.* [Online; accessed 30. Dec. 2020]. Dec. 2019 (cited on page 3).

[3] Ipek Gencsu and Nathaniel Mason. *Unlocking the inclusive growth story of the 21st century: accelerating climate action in urgent times*. [Online; accessed 30. Dec. 2020]. Apr. 2019 (cited on page 3).

[4] International Energy Agency. *Global Energy Review 2020*. [Online; accessed 30. Dec. 2020]. Apr. 2020 (cited on page 4).

[5] Ivan Komusanac, Daniel Fraile, and Guy Brindley. *Wind Energy in Europe in 2018 – Trends and statistics*. Tech. rep. Bruxelles, Belgium: Wind Europe, 2018 (cited on page 4).

[6] Eric Lantz, Ryan Wiser, and Maureen Hand. *IEA Wind Task 26: past and future cost of wind energy*. Tech. rep. National Renewable Energy Lab. (NREL), Golden, CO (US), 2012 (cited on page 4).

[7] November Lazard. *Lazard's Levelized Cost of Energy Analysis–Version 9.0*. 2016 (cited on page 4).

[8] Paul Veers et al. 'Grand challenges in the science of wind energy'. In: *Science* 366.6464 (2019), eaau2027. DOI: 10.1126/science.aau2027 (cited on pages 5, 6).

[9] James F Manwell, Jon G McGowan, and Anthony L Rogers. *Wind energy explained: theory, design and application*. John Wiley & Sons, 2010 (cited on pages 5, 9, 106).

[10] Ivan Komusanac, Daniel Fraile, and Guy Brindley. *Wind Energy in Europe - 2020 Statistics and the outlook for 2021-2025*. Tech. rep. Bruxelles, Belgium: Wind Europe, 2020 (cited on page 5).

[11] Jeffrey Winters and Zina Saunders. 'The Largest Wind Turbine Ever'. In: *Mechanical Engineering* 140.12 (2018), pp. 31–31. DOI: 10.1115/1.2018-DEC-2 (cited on page 5).

[12] Steve Sawyer, Sven Teske, and Morten Dyrholm. *Global Wind Energy Outlook 2014*. Tech. rep. 2014 (cited on page 6).

[13] G. A. M. van Kuik et al. 'Long-term research challenges in wind energy – a research agenda by the European Academy of Wind Energy'. In: *Wind Energy Science* 1.1 (2016), pp. 1–39. DOI: 10.5194/wes-1-1-2016 (cited on pages 6, 9).

[14] Marc Calaf, Charles Meneveau, and Johan Meyers. 'Large eddy simulation study of fully developed wind-turbine array boundary layers'. In: *Physics of Fluids* 22.1 (2010), p. 015110. DOI: 10.1063/1.3291077 (cited on pages 6, 159).

[15] Francesco Grasso, Arne van Garrel, and Gerard Schepers. 'Development and validation of generalized lifting line based code for wind turbine aerodynamics'. In: *49th AIAA Aerospace Sciences Meeting including the New Horizons Forum and Aerospace Exposition*. 2011, p. 146. DOI: 10.2514/6.2011-146 (cited on page 7).

[16] Giacomo Valerio Iungo, Yu-Ting Wu, and Fernando Porté-Agel. 'Field measurements of wind turbine wakes with lidars'. In: *Journal of Atmospheric and Oceanic Technology* 30.2 (2013), pp. 274–287. DOI: 10.1175/JTECH-D-12-00051.1 (cited on page 7).

[17] Don W Lobitz. 'Flutter speed predictions for MW-sized wind turbine blades'. In: *Wind Energy* 7.3 (2004), pp. 211–224. DOI: 10.1002/we.120 (cited on page 8).

[18] Linyue Gao et al. 'Effects of inflow turbulence on structural response of wind turbine blades'. In: *Journal of Wind Engineering and Industrial Aerodynamics* 199 (2020), p. 104137. DOI: 10.1016/j.jweia.2020.104137 (cited on page 8).

[19] Jason Mark Jonkman and Marshall L Buhl Jr. *Fast user's guide-updated august 2005*. Tech. rep. Golden, CO (USA): NREL, 2005 (cited on page 8).

[20] NREL. *OpenFAST*. https://github.com/OpenFAST/openfast, (accessed: October 30, 2020). 2020 (cited on page 8).

[21] Dewey H Hodges. *Nonlinear composite beam theory*. AIAA, 2006 (cited on pages 9, 82, 159).

[22] Torben Juul Larsen and Anders Melchior Hansen. *How 2 HAWC2, the user's manual*. Tech. rep. Risø-R-1597. https://www.hawc2.dk. Roskilde and Kgs. Lyngby, Denmark: Risø National Laboratory, Technical University of Denmark, 2007 (cited on pages 9, 12).

[23] David Simms et al. *NREL unsteady aerodynamics experiment in the NASA-Ames wind tunnel: a comparison of predictions to measurements*. Tech. rep. NREL/TP-500-29494. Golden, CO (USA): NREL, 2001. DOI: 10.2172/783409 (cited on page 9).

[24] Sandeep Gupta. 'Development of a time-accurate viscous Lagrangian vortex wake model for wind turbine applications'. PhD thesis. College Park, Maryland: University of Maryland, 2006 (cited on page 9).

[25] Krista M Kecskemety and Jack J McNamara. 'Influence of wake dynamics on the performance and aeroelasticity of wind turbines'. In: *Renewable Energy* 88 (2016), pp. 333–345. DOI: 10.1016/j.renene.2015.11.031 (cited on page 9).

[26] Louis Melville Milne-Thomson. *Theoretical aerodynamics*. Courier Corporation, 1973 (cited on page 9).

[27] John L. Hess. 'Review of integral-equation techniques for solving potential-flow problems with emphasis on the surface-source method'. In: *Computer Methods in Applied Mechanics and Engineering* 5.2 (1975), pp. 145–196. DOI: 10.1016/0045-7825(75)90051-1 (cited on page 9).

[28] Oskar Karl Gustav Tietjens and Ludwig Prandtl. *Applied hydro-and aeromechanics: based on lectures of L. Prandtl*. Vol. 2. Courier Corporation, 1957 (cited on page 9).

[29] Sergei Vladimirovich Alekseenko, Pavel Anatolevich Kuibin, and Valerii Leonidovich Okulov. *Theory of concentrated vortices: an introduction*. Springer Science & Business Media, 2007 (cited on page 9).

[30] Jens Nørkær Sørensen et al. 'Three-Level, Viscous-Inviscid Interaction Technique for the Prediction of Separated Flow Past Rotating Wing'. PhD thesis. Technical University of Denmark, 1986 (cited on page 9).

[31] Martin Otto Laver Hansen et al. 'State of the art in wind turbine aerodynamics and aeroelasticity'. In: *Progress in Aerosp. Sciences* 42.4 (2006), pp. 285–330. DOI: 10.1016/j.paerosci.2006.10.002 (cited on page 9).

[32] Pinting Zhang and Shuhong Huang. 'Review of aeroelasticity for wind turbine: Current status, research focus and future perspectives'. In: *Frontiers in Energy* 5.4 (2011), pp. 419–434. DOI: 10.1007/s11708-011-0166-6 (cited on page 9).

[33] Gerard Cortina, Marc Calaf, and Raúl Bayoán Cal. 'Distribution of mean kinetic energy around an isolated wind turbine and a characteristic wind turbine of a very large wind farm'. In: *Physical Review Fluids* 1.7 (2016), p. 074402. DOI: 10.1103/PhysRevFluids.1.074402 (cited on page 9).

[34] Charles Meneveau. 'Big wind power: Seven questions for turbulence research'. In: *Journal of Turbulence* 20.1 (2019), pp. 2–20. DOI: 10.1080/14685248.2019.1584664 (cited on page 9).

[35] Philippe R Spalart. 'Detached-eddy simulation'. In: *Annual Review of Fluid Mechanics* 41 (2009), pp. 181–202. DOI: 10.1146/annurev.fluid.010908.165130 (cited on pages 10, 27).

[36] Haecheon Choi and Parviz Moin. 'Grid-point requirements for large eddy simulation: Chapman's estimates revisited'. In: *Physics of fluids* 24.1 (2012), p. 011702. DOI: 10.1063/1.3676783 (cited on page 10).

[37] Robert Mikkelsen et al. 'Actuator disc methods applied to wind turbines'. PhD thesis. Kgs. Lyngby, Denmark: Technical University of Denmark, 2003 (cited on page 10).

[38] Jens Nørkær Sørensen and Wen Zhong Shen. 'Numerical modeling of wind turbine wakes'. In: *Journal of Fluids Engineering* 124.2 (2002), pp. 393–399. DOI: 10.1115/1.1471361 (cited on pages 10, 38).

[39] Wen Zhong Shen, Wei Jun Zhu, and Jens Nørkær Sørensen. 'Actuator line/ Navier–Stokes computations for the MEXICO rotor: comparison with detailed measurements'. In: *Wind Energy* 15.5 (2012), pp. 811–825. DOI: 10.1002/we.510 (cited on page 10).

[40] Jens N Sørensen et al. 'Simulation of wind turbine wakes using the actuator line technique'. In: *Philosophical Transactions of the Royal Society A* 373.2035 (2015), p. 20140071. DOI: 10.1098/rsta.2014.0071 (cited on page 10).

[41] Shengbai Xie and Cristina L Archer. 'Self-similarity and turbulence characteristics of wind turbine wakes via large-eddy simulation'. In: *Wind Energy* 18.10 (2015), pp. 1815–1838. DOI: 10.1002/we.1792 (cited on page 10).

[42] Yuri Bazilevs et al. 'Isogeometric fluid–structure interaction analysis with applications to arterial blood flow'. In: *Computational Mechanics* 38.4 (2006), pp. 310–322. DOI: 10.1007/s00466-006-0084-3 (cited on page 11).

[43] Keith Stein et al. 'Parachute fluid–structure interactions: 3-D computation'. In: *Computer Methods in Applied Mechanics and Engineering* 190.3 (2000), pp. 373–386. DOI: 10.1016/S0045-7825(00)00208-5 (cited on page 11).

[44] C Farhat and M Lesoinne. 'On the accuracy, stability, and performance of the solution of three-dimensional nonlinear transient aeroelastic problems by partitioned procedures'. In: *37th Structure, Structural Dynamics and Materials Conf.* 1996. DOI: 10.2514/6.1996-1388 (cited on pages 11, 13, 93).

[45] Ming-Chen Hsu and Yuri Bazilevs. 'Fluid–structure interaction modeling of wind turbines: simulating the full machine'. In: *Computational Mechanics* 50.6 (2012), pp. 821–833. DOI: 10.1007/s00466-012-0772-0 (cited on pages 11, 12).

[46] Joachim Christian Heinz. 'Partitioned fluid-structure interaction for full rotor computations using CFD'. PhD thesis. Kgs. Lyngby, Denmark: Technical University of Denmark, 2013 (cited on pages 11, 12, 92, 106, 123, 125, 136, 137).

[47] Carlos A. Felippa, K.C. Park, and Charbel Farhat. 'Partitioned analysis of coupled mechanical systems'. In: *Computer Methods in Applied Mechanics and Engineering* 190.24 (2001). Advances in Computational Methods for Fluid-Structure Interaction, pp. 3247–3270. DOI: 10.1016/S0045-7825(00)00391-1 (cited on pages 11, 95).

[48] Keith Stein, Tayfun E Tezduyar, and Richard Benney. 'Automatic mesh update with the solid-extension mesh moving technique'. In: *Computer Methods in Applied Mechanics and Engineering* 193.21-22 (2004), pp. 2019–2032. DOI: 10.1016/j.cma.2003.12.046 (cited on page 12).

[49] Yuri Bazilevs, Kenji Takizawa, and Tayfun E Tezduyar. *Computational fluid-structure interaction: methods and applications*. John Wiley & Sons, 2013 (cited on page 12).

[50] Tayfun E Tezduyar. 'Finite element methods for flow problems with moving boundaries and interfaces'. In: *Archives of Computational Methods in Engineering* 8.2 (2001), pp. 83–130. DOI: 10.1007/BF02897870 (cited on page 12).

[51] Jason Jonkman et al. *Definition of a 5-MW reference wind turbine for offshore system development*. Tech. rep. NREL/TP-500-38060. Golden, CO (USA): NREL, 2009. DOI: 10.2172/947422 (cited on pages 12, 99, 101, 118, 155).

[52] Jess A Michelsen. *Block structured Multigrid solution of 2D and 3D elliptic PDE's*. Technical University of Denmark, 1994 (cited on page 12).

[53] Dong Ok Yu and Oh Joon Kwon. 'Predicting wind turbine blade loads and aeroelastic response using a coupled CFD–CSD method'. In: *Renewable Energy* 70 (2014), pp. 184–196. DOI: 10.1016/j.renene.2014.03.033 (cited on pages 12, 156).

[54] Min-Soo Jeong et al. 'Effects of torsional degree of freedom, geometric nonlinearity, and gravity on aeroelastic behavior of large-scale horizontal axis wind turbine blades under varying wind speed conditions'. In: *Journal of Renewable and Sustainable Energy* 6.2 (2014), p. 023126. DOI: 10.1063/1.4873130 (cited on pages 12, 120).

[55] Zhanwei Li et al. 'Aerodynamic and aeroelastic characteristics of flexible wind turbine blades under periodic unsteady inflows'. In: *Journal of Wind Engineering & Industrial Aerodynamics* 197 (2020), p. 104057. DOI: 10.1016/j.jweia.2019.104057 (cited on page 12).

[56] Y Li et al. 'Coupled multi-body dynamics and CFD for wind turbine simulation including explicit wind turbulence'. In: *Renewable Energy* 76 (2015), pp. 338–361. DOI: 10.1016/j.renene.2014.11.014 (cited on pages 13, 118).

[57] Jakob Mann. 'Wind field simulation'. In: *Probabilistic Engineering Mechanics* 13.4 (1998), pp. 269–282. DOI: 10.1016/S0266-8920(97)00036-2 (cited on pages 13, 106).

[58] B Dose et al. 'Fluid-structure coupled computations of the NREL 5 MW wind turbine by means of CFD'. In: *Renewable Energy* 129 (2018), pp. 591–605. DOI: 10.1016/j.renene.2018.05.064 (cited on page 13).

[59] Hrvoje Jasak, Aleksandar Jemcov, Zeljko Tukovic, et al. 'OpenFOAM: A C++ library for complex physics simulations'. In: *International workshop on coupled methods in numerical dynamics*. IUC Dubrovnik Croatia. 2007 (cited on page 13).

[60] Eric Reissner. 'On one-dimensional finite-strain beam theory: the plane problem'. In: *Zeitschrift für angewandte Mathematik und Physik ZAMP* 23.5 (1972), pp. 795–804. DOI: 10.1007/BF01602645 (cited on page 13).

[61] MA Sprague et al. 'ExaWind: A multi-fidelity modeling and simulation environment for wind energy'. In: *Journal of Physics: Conference Series*. 2020 (cited on pages 13, 83, 156).

[62] S Domino. *Sierra low mach module: Nalu theory manual 1.0*. Tech. rep. SAND2015-3107W. Sandia National Laboratories, 2015 (cited on page 13).

[63] RC Storey et al. 'Large eddy simulation of dynamically controlled wind turbines in an offshore environment'. In: *Wind Energy* 16.6 (2013), pp. 845–864. DOI: 10.1002/we.1525 (cited on page 13).

[64] RC Storey, SE Norris, and JE Cater. 'An actuator sector method for efficient transient wind turbine simulation'. In: *Wind Energy* 18.4 (2015), pp. 699–711. DOI: 10.1002/we.1722 (cited on page 13).

[65] Matthew J Churchfield et al. 'A numerical study of the effects of atmospheric and wake turbulence on wind turbine dynamics'. In: *Journal of Turbulence* 13 (2012), N14. DOI: 10.1080/14685248.2012.668191 (cited on page 14).

[66] S Lee et al. 'A numerical study of atmospheric and wake turbulence impacts on wind turbine fatigue loadings'. In: *Journal of Solar Energy Engineering* 135.3 (2013). DOI: 10.1115/1.4023319 (cited on page 14).

[67] Hang Meng, Fue-Sang Lien, and Li Li. 'Elastic actuator line modelling for wake-induced fatigue analysis of horizontal axis wind turbine blade'. In: *Renewable Energy* 116 (2018), pp. 423–437. DOI: 10.1016/j.renene.2017.08.074 (cited on pages 14, 127).

[68] Hang Meng et al. 'Study on wake-induced fatigue on wind turbine blade based on elastic actuator line model and two-dimensional finite element model'. In: *Wind Engineering* 43.1 (2019), pp. 64–82. DOI: 10.1177/0309524X18819898 (cited on page 14).

[69] J Gordon Leishman. 'Challenges in modelling the unsteady aerodynamics of wind turbines'. In: *Wind Energy* 5.2-3 (2002), pp. 85–132. DOI: 10.1002/we.62 (cited on pages 14, 15, 19, 42).

[70] Victor Mendoza et al. 'Validation of an Actuator Line Model Coupled to a Dynamic Stall Model for Pitching Motions Characteristic to Vertical Axis Turbines'. In: *Journal of Physics: Conference Series* 753 (Sept. 2016), p. 022043. DOI: 10.1088/1742-6596/753/2/022043 (cited on page 14).

[71] Victor Mendoza et al. 'Near-wake flow simulation of a vertical axis turbine using an actuator line model'. In: *Wind Energy* 22.2 (2019), pp. 171–188. DOI: 10.1002/we.2277 (cited on page 14).

[72] DC Quarton. 'The evolution of wind turbine design analysis—a twenty year progress review'. In: *Wind Energy* 1.S1 (1998), pp. 5–24. DOI: 10.1002/(SICI)1099-1824(199804)1:1+<5::AID-WE1>3.0.CO;2-I (cited on page 14).

[73] Wouter Haans and Robert Mikkelsen. 'Airfoil models in the actuator line code assessed with near-wake measurements on a yawed rotor'. In: *45th AIAA Aerospace Sciences Meeting and Exhibit*. 2012. DOI: 10.2514/6.2007-424 (cited on page 14).

[74] Flemming Rasmussen et al. 'Present status of aeroelasticity of wind turbines'. In: *Wind Energy* 6.3 (2003), pp. 213–228. DOI: 10.1002/we.98 (cited on pages 14, 55).

[75] Stig Øye. 'Dynamic stall simulated as time lag of separation'. In: *Proceedings of the 4th IEA Symposium on the aerodynamics of wind turbines*. 1991 (cited on pages 14, 20).

[76] F Rasmussen et al. *Response of stall regulated wind turbines. Stall induced vibrations*. Tech. rep. RISO-R-691(EN). Roskilde (Denmark), 1993 (cited on page 15).

[77] Gordon J Leishman. *Principles of helicopter aerodynamics*. Cambridge University Press, 2006 (cited on pages 15, 17, 44, 46, 48).

[78] Ganesh Vijayakumar et al. 'Enhancement of Unsteady and 3D Aerodynamics Models using Machine Learning'. In: *Journal of Physics: Conference Series*. Vol. 1452. 1. IOP Publishing. 2020, p. 012065 (cited on page 15).

[79] Touraj Farsadi and Altan Kayran. 'Classical flutter analysis of composite wind turbine blades including compressibility'. In: *Wind Energy* (2020). DOI: 10.1002/we.2559 (cited on pages 15, 25).

[80] Peter Bachant, Anders Goude, and Martin Wosnik. 'Actuator line modeling of vertical-axis turbines'. In: *arXiv preprint arXiv:1605.01449* (2016) (cited on page 16).

[81] Ricardo Pereira, Gerard Schepers, and Marilena D. Pavel. 'Validation of the Beddoes–Leishman dynamic stall model for horizontal axis wind turbines using MEXICO data'. In: *Wind Energy* 16.2 (2013), pp. 207–219. DOI: 10.1002/we.541 (cited on page 16).

[82] Theodore Theodorsen and WH Mutchler. 'General theory of aerodynamic instability and the mechanism of flutter'. In: (1935) (cited on page 16).

[83] Herbert Wagner. 'Über die Entstehung des dynamischen Auftriebes von Tragflügeln'. In: (1924) (cited on page 16).

[84] Hans Georg Küssner. *The Present Stage of Development of the Problem of Wing Flutter*. Aeronautical Research Council, 1935 (cited on page 16).

[85] Th H von Karman and William R Sears. 'Airfoil theory for non-uniform motion'. In: *Journal of the Aeronautical Sciences* 5.10 (1938), pp. 379–390. DOI: 10.2514/8.674 (cited on page 16).

[86] Harvard Lomax et al. *Two-and three-dimensional unsteady lift problems in high-speed flight*. Tech. rep. 19930092122. 1952 (cited on pages 16, 44).

[87] Robert G Loewy. 'A two-dimensional approximation to the unsteady aerodynamics of rotary wings'. In: *Journal of the Aeronautical Sciences* 24.2 (1957), pp. 81–92. DOI: 10.2514/8.3777 (cited on page 16).

[88] Robert T Jones. *The unsteady lift of a wing of finite aspect ratio*. Tech. rep. 681. 1940 (cited on page 17).

[89] JG Leishman. 'Validation of approximate indicial aerodynamic functions for two-dimensional subsonic flow'. In: *Journal of Aircraft* 25.10 (1988), pp. 914–922. DOI: 10.2514/3.45680 (cited on page 17).

[90] Steven L Brunton, Clarence W Rowley, and David R Williams. 'Reduced-order unsteady aerodynamic models at low Reynolds numbers'. In: *Journal of Fluid Mechanics* 724 (2013), pp. 203–233. DOI: 10.1017/jfm.2013.163 (cited on pages 17, 20).

[91] William J McCroskey. 'Unsteady airfoils'. In: *Annual Review of Fluid Mechanics* 14.1 (1982), pp. 285–311. DOI: 10.1146/annurev.fl.14.010182.001441 (cited on page 17).

[92] Bryan Thwaites. *Incompressible aerodynamics*. Oxford University Press, 1960 (cited on page 18).

[93] Maksim Isidorovich Gurevich. *The theory of jets in an ideal fluid*. Pergamon Press, 1966 (cited on page 18).

[94] Jesper Winther Larsen, Søren RK Nielsen, and Steen Krenk. 'Dynamic stall model for wind turbine airfoils'. In: *Journal of Fluids and Structures* 23.7 (2007), pp. 959–982. DOI: 10.1016/j.jfluidstructs.2007.02.005 (cited on pages 19, 20, 42, 52).

[95] CT Tran and D Petot. 'Semi-empirical model for the dynamic stall of airfoils in view of the application to the calculation of responses of a helicopter blade in forward flight'. In: *Vertica* 5 (1980), pp. 35–53 (cited on page 20).

[96] Morten Hartvig Hansen, Mac Gaunaa, and Helge Aagaard Madsen. *A Beddoes-Leishman type dynamic stall model in state-space and indicial formulations*. Tech. rep. Risø-R-1354(EN). 2004 (cited on pages 20, 42).

[97] FJ Tarzanin. 'Prediction of control loads due to blade stall'. In: *Journal of the American Helicopter Society* 17.2 (1972), pp. 33–46. DOI: 10.4050/JAHS.17.33 (cited on page 20).

[98] J Gordon Leishman and TS Beddoes. 'A Semi-Empirical model for dynamic stall'. In: *Journal of the American Helicopter Society* 34.3 (1989), pp. 3–17. DOI: 10.4050/JAHS.34.3.3 (cited on pages 20, 41, 44, 45).

[99] Rick Damiani et al. 'Development and Validation of a New Unsteady Airfoil Aerodynamics Model Within AeroDyn'. In: *34th Wind Energy Symposium*. 2016, p. 1007. DOI: 10.2514/6.2016-1007 (cited on pages 20, 42, 163).

[100] Peter Lorber, Alfred Covino JR, and Franklin Carta. 'Dynamic stall experiments on a swept 3D wing in compressible flow'. In: *22nd Fluid Dynamics, Plasma Dynamics and Lasers Conference*. 91-1795. AIAA, 1991. DOI: 10.2514/6.1991-1795 (cited on page 20).

[101] H Snel. 'Scaling laws for the boundary layer flow on rotating wind turbine blades'. In: *4th IEA symposium on aerodynamics for wind turbines, Rome*. 1991 (cited on page 20).

[102] Zhaohui Du and Michael Selig. 'A 3-D stall-delay model for horizontal axis wind turbine performance prediction'. In: *1998 ASME Wind Energy Symposium*. 1998, p. 21. DOI: 10.2514/6.1998-21 (cited on page 20).

[103] A Eggers Jr et al. 'Modeling of yawing and furling behavior of small wind turbines'. In: *2000 ASME Wind Energy Symposium*. 2000, p. 20. DOI: 10.2514/6.2000-20 (cited on page 20).

[104] AO St Hilaire and FO Carta. *Analysis of Unswept and Swept Wing Chordwise Pressure Data from an Oscillating NACA 0012 Airfoil Experiment*. Tech. rep. ADA126797. 1983 (cited on page 20).

[105] Christian Santoni et al. 'One-way mesoscale-microscale coupling for simulating a wind farm in North Texas: Assessment against SCADA and LiDAR data'. In: *Wind Energy* 23.3 (2020), pp. 691–710. DOI: 10.1002/we.2452 (cited on pages 21, 32).

[106] Christian Santoni et al. 'Effect of tower and nacelle on the flow past a wind turbine'. In: *Wind Energy* 20.12 (2017), pp. 1927–1939. DOI: 10.1002/we.2130 (cited on pages 21, 31, 37, 38, 130).

[107] Giovanni De Cillis et al. 'POD-based analysis of a wind turbine wake under the influence of tower and nacelle'. In: *Wind Energy* 24.6 (2021), pp. 609–633. DOI: 10.1002/we.2592 (cited on page 21).

[108] Paolo Orlandi and Stefano Leonardi. 'DNS of turbulent channel flows with two-and three-dimensional roughness'. In: *Journal of Turbulence* 7 (2006), N73. DOI: 10.1080/14685240600827526 (cited on page 21).

[109] J. G. Schepers and S. J. Schreck. 'Aerodynamic measurements on wind turbines'. In: *WIREs Energy and Environment* 8.1 (2019), e320. DOI: https://doi.org/10.1002/wene.320 (cited on page 25).

[110] PK Chaviaropoulos et al. 'Viscous and aeroelastic effects on wind turbine blades. The VISCEL project. Part I: 3D Navier–Stokes rotor simulations'. In: *Wind Energy* 6.4 (2003), pp. 365–385. DOI: 10.1002/we.100 (cited on page 25).

[111] John David Anderson Jr. *Fundamentals of aerodynamics*. Tata McGraw-Hill Education, 2010 (cited on page 26).

[112] Uriel Frisch. *Turbulence: the legacy of AN Kolmogorov*. Cambridge university press, 1995 (cited on page 26).

[113] Niels N Sørensen. 'The EllipSys 2D/3D code and its application within wind turbine aerodynamics'. In: *Workshop on future aero-elastic tools for wind turbines*. 2008 (cited on page 27).

[114] David C Wilcox et al. *Turbulence modeling for CFD*. Vol. 2. DCW industries La Canada, CA, 1998 (cited on page 27).

[115] Charles Mockett. *A Comprehensive Study of Detached Eddy Simulation*. Univerlagtuberlin, 2009 (cited on page 28).

[116] S-P Breton et al. 'A survey of modelling methods for high-fidelity wind farm simulations using large eddy simulation'. In: *Philosophical Transactions of the Royal Society A: Mathematical, Physical and Engineering Sciences* 375.2091 (2017), p. 20160097. DOI: 10.1098/rsta.2016.0097 (cited on page 28).

[117] Pierre Sagaut. *Large eddy simulation for incompressible flows: an introduction*. Springer Science & Business Media, 2006 (cited on page 29).

[118] A. Leonard. 'Energy Cascade in Large-Eddy Simulations of Turbulent Fluid Flows'. In: *Turbulent Diffusion in Environmental Pollution*. Ed. by F.N. Frenkiel and R.E. Munn. Vol. 18. Advances in Geophysics. Elsevier, 1975, pp. 237–248. DOI: 10.1016/S0065-2687(08)60464-1 (cited on page 30).

[119] Stephen B Pope. *Turbulent flows*. IOP Publishing, 2001 (cited on pages 30, 31).

[120] Charles G Speziale. 'Galilean invariance of subgrid-scale stress models in the large-eddy simulation of turbulence'. In: *Journal of Fluid Mechanics* 156 (1985), pp. 55–62. DOI: 10.1017/S0022112085001987 (cited on page 30).

[121] Massimo Germano. 'A proposal for a redefinition of the turbulent stresses in the filtered Navier–Stokes equations'. In: *The Physics of fluids* 29.7 (1986), pp. 2323–2324. DOI: 10.1063/1.865568 (cited on page 30).

[122] Marcel Lesieur. *Turbulence in fluids*. Vol. 40. Springer Science & Business Media, 2012 (cited on page 31).

[123] Joseph Smagorinsky. 'General circulation experiments with the primitive equations: I. The basic experiment'. In: *Monthly weather review* 91.3 (1963), pp. 99–164. DOI: 10.1175/1520-0493(1963)091<0099:GCEWTP>2.3.CO;2 (cited on page 31).

[124] Christian Santoni et al. 'Development of a high fidelity CFD code for wind farm control'. In: *2015 American Control Conference (ACC)*. IEEE. 2015, pp. 1715–1720. DOI: 10.1109/ACC.2015.7170980 (cited on page 31).

[125] Parviz Moin and John Kim. 'Numerical investigation of turbulent channel flow'. In: *Journal of Fluid Mechanics* 118 (1982), pp. 341–377. DOI: 10.1017/S0022112082001116 (cited on pages 31, 35, 105).

[126] Paolo Orlandi. *Fluid flow phenomena: a numerical toolkit*. Vol. 55. Springer Science & Business Media, 2012 (cited on pages 32, 34).

[127] Clive AJ Fletcher. *Computational techniques for fluid dynamics 2: Specific techniques for different flow categories*. Springer Science & Business Media, 2012 (cited on page 32).

[128] Joel H Ferziger, Milovan Perić, and Robert L Street. *Computational methods for fluid dynamics*. Vol. 3. Springer, 2002 (cited on page 32).

[129] Alan A Wray. 'Very low storage time-advancement schemes'. In: *Internal Report, Moffett Field, CA, NASA-Ames Research Center* (1986) (cited on page 33).

[130] R. Courant, K. Friedrichs, and H. Lewy. 'On the Partial Difference Equations of Mathematical Physics'. In: *IBM Journal of Research and Development* 11.2 (1967), pp. 215–234. DOI: 10.1147/rd.112.0215 (cited on page 36).

[131] Luis A Martínez-Tossas, Matthew J Churchfield, and Stefano Leonardi. 'Large eddy simulations of the flow past wind turbines: actuator line and disk modeling'. In: *Wind Energy* 18.6 (2015), pp. 1047–1060. DOI: 10.1002/we.1747 (cited on page 37).

[132] Niels Troldborg, Jens Nørkær Sørensen, and Robert Flemming Mikkelsen. 'Actuator line modeling of wind turbine wakes'. PhD thesis. Technical University of Denmark, 2009 (cited on pages 37, 39, 104, 114).

[133] Roger Peyret and Thomas D Taylor. *Computational methods for fluid flow*. Springer Science & Business Media, 2012 (cited on page 37).

[134] Charles S. Peskin. 'The immersed boundary method'. In: *Acta Numerica* 11 (2002), pp. 479–517. DOI: 10.1017/S0962492902000077 (cited on page 37).

[135] Dokyun Kim and Haecheon Choi. 'Immersed boundary method for flow around an arbitrarily moving body'. In: *Journal of Computational Physics* 212.2 (2006), pp. 662–680. DOI: 10.1016/j.jcp.2005.07.010 (cited on page 38).

[136] WZ Shen et al. 'Tip loss corrections for wind turbine computations'. In: *Wind Energy* 8.4 (2005), pp. 457–475. DOI: 10.1002/we.153 (cited on page 39).

[137] Pankaj K Jha et al. 'Guidelines for volume force distributions within actuator line modeling of wind turbines on large-eddy simulation-type grids'. In: *Journal of Solar Energy Engineering* 136.3 (2014). DOI: 10.1115/1.4026252 (cited on pages 39, 114).

[138] Matthew J Churchfield et al. 'An advanced actuator line method for wind energy applications and beyond'. In: *35th Wind Energy Symposium*. 2017, p. 1998. DOI: 10.2514/6.2017-1998 (cited on page 39).

[139] Luis A Martínez-Tossas, Matthew J Churchfield, and Charles Meneveau. 'Optimal smoothing length scale for actuator line models of wind turbine blades based on Gaussian body force distribution'. In: *Wind Energy* 20.6 (2017), pp. 1083–1096. DOI: 10.1002/we.2081 (cited on page 39).

[140] Kathryn E Johnson et al. 'Control of variable-speed wind turbines: standard and adaptive techniques for maximizing energy capture'. In: *IEEE Control Systems Magazine* 26.3 (2006), pp. 70–81. DOI: 10.1109/MCS.2006.1636311 (cited on page 41).

[141] Wanan Sheng, RA Galbraith, and FN Coton. 'A modified dynamic stall model for low Mach numbers'. In: *Journal of Solar Energy Engineering* 130.3 (2008). DOI: 10.1115/1.2931509 (cited on pages 42, 50, 52).

[142] Rick R. Damiani and Gregory Hayman. *The Unsteady Aerodynamics Module For FAST8*. Tech. rep. Nov. 2019. DOI: 10.2172/1576488 (cited on pages 42, 43, 50, 53, 54, 170).

[143] Jeppe Johansen. *Unsteady airfoil flows with application to aeroelastic stability*. Tech. rep. Risø-R-1116(EN). 1999 (cited on pages 44, 48).

[144] Raymond L Bisplinghoff and Holt Ashley. *Principles of aeroelasticity*. Courier Corporation, 2013 (cited on page 46).

[145] Berend G van der Wall and J Gordon Leishman. 'On the influence of time-varying flow velocity on unsteady aerodynamics'. In: *Journal of the American Helicopter Society* 39.4 (1994), pp. 25–36. DOI: 10.4050/JAHS.39.25 (cited on page 46).

[146] J.G. Leishman and T.S. Beoddoes. 'A general model for airload unsteady behavior and dynamic stall using the indicial method'. In: *Proceedings of the 42nd Annual Forum of the American Helicopter Society*. American Helicopter Society, 1986, pp. 243–266 (cited on pages 47, 52).

[147] Patrick J Moriarty and A Craig Hansen. *AeroDyn theory manual*. Tech. rep. 2005. DOI: 10.2172/15014831 (cited on page 49).

[148] Xiong Liu et al. 'An improved dynamic stall model and its effect on wind turbine fatigue load prediction'. In: *Renewable Energy* 156 (2020), pp. 117–130. DOI: 10.1016/j.renene.2020.04.040 (cited on page 49).

[149] J.G. Leishman. *Final report: assessment of 'Aerodyn' theory basis including unsteady aerodynamics modules*. Tech. rep. DE-AC36-08GO28308. 2011 (cited on pages 51, 54).

[150] Benedetto Rocchio et al. 'A simple model for deep dynamic stall conditions'. In: *Wind Energy* 23.4 (2020), pp. 915–938. DOI: 10.1002/we.2463 (cited on page 52).

[151] Kirk Gee Pierce. 'Wind turbine load prediction using the Beddoes-Leishman model for unsteady aerodynamics and dynamic stall'. MA thesis. Department of Mechanical Engineering, University of Utah, 1996 (cited on page 54).

[152] Morten Hartvig Hansen. 'Aeroelastic instability problems for wind turbines'. In: *Wind Energy* 10.6 (2007), pp. 551–577. DOI: 10.1002/we.242 (cited on pages 55, 122).

[153] Luigi Morino and Richard B Noll. 'FCAP—A new tool for the performance and structural analysis for complex flexible aircraft with active control'. In: *Computers & Structures* 7.2 (1977), pp. 275–282. DOI: 10.1016/0045-7949(77)90046-3 (cited on page 56).

[154] Janusz S Przemieniecki and Przemieniecki. *Theory of matrix structural analysis*. Vol. 1. McGraw-Hill New York, 1968 (cited on pages 56, 67).

[155] Francesco Saltari et al. 'Finite-Element-Based Modeling for Flight Dynamics and Aeroelasticity of Flexible Aircraft'. In: *Journal of Aircraft* 54.6 (2017), pp. 2350–2366. DOI: 10.2514/1.C034159 (cited on pages 60, 63, 78, 155).

[156] Christian Reschke. 'Flight loads analysis with inertially coupled equations of motion'. In: *AIAA Atmospheric Flight Mechanics Conference and Exhibit*. 2005, p. 6026. DOI: 10.2514/6.2005-6026 (cited on pages 60, 80).

[157] V Ph Zhuravlev. 'Spectral properties of linear gyroscopic systems'. In: *Mechanics of solids* 44.2 (2009), pp. 165–168. DOI: 10.3103/S0025654409020010 (cited on page 64).

[158] Roy R Craig and Andrew J Kurdila. *Fundamentals of structural dynamics*. John Wiley & Sons, 2006 (cited on page 78).

[159] Gerhard Alfred Holzapfel. *Nonlinear Solid Mechanics: A Continuum Approach for Engineering*. Wiley, 2000 (cited on page 82).

[160] G. Migliaccio et al. 'Beamlike models for the analyses of curved, twisted and tapered horizontal-axis wind turbine (HAWT) blades undergoing large displacements'. In: *Wind Energy Science* 5.2 (2020), pp. 685–698. DOI: 10.5194/wes-5-685-2020 (cited on pages 82, 159).

[161] G Migliaccio and G Ruta. 'The influence of an initial twisting on tapered beams undergoing large displacements'. In: *Meccanica* (2021), pp. 1–15. DOI: 10.1007/s11012-021-01334-2 (cited on page 82).

[162] VA Riziotis et al. 'Identification of structural non-linearities due to large deflections on a 5MW wind turbine blade'. In: *Proceedings of the 2008 European Wind Energy Conference and Exhibition*. EWEA: Brussels. 2008, pp. 9–14 (cited on page 83).

[163] Thomas JR Hughes. *The finite element method: linear static and dynamic finite element analysis*. Courier Corporation, 2012 (cited on page 83).

[164] Nathan M. Newmark. 'A Method of Computation for Structural Dynamics'. In: *Journal of the Engineering Mechanics Division* 85.3 (1959), pp. 67–94. DOI: 10.1061/JMCEA3.0000098 (cited on page 84).

[165] Hans M Hilber, Thomas JR Hughes, and Robert L Taylor. 'Improved numerical dissipation for time integration algorithms in structural dynamics'. In: *Earthquake Engineering & Structural Dynamics* 5.3 (1977), pp. 283–292. DOI: 10.1002/eqe.4290050306 (cited on page 85).

[166] J. Chung and G. M. Hulbert. 'A Time Integration Algorithm for Structural Dynamics With Improved Numerical Dissipation: The Generalized-α Method'. In: *Journal of Applied Mechanics* 60.2 (June 1993), pp. 371–375. DOI: 10.1115/1.2900803 (cited on page 85).

[167] WL Wood, M Bossak, and OC Zienkiewicz. 'An alpha modification of Newmark's method'. In: *International Journal for Numerical Methods in Engineering* 15.10 (1980), pp. 1562–1566. DOI: 10.1002/nme.1620151011 (cited on page 85).

[168] C Lindenburg et al. *Aeroelastic modelling of the LMH64-5 blade*. Tech. rep. DOWEC-02-KL-083/0. Energy Research Center of the Netherlands, 2002 (cited on pages 100, 101).

[169] H. Sarlak et al. 'Assessment of blockage effects on the wake characteristics and power of wind turbines'. In: *Renewable Energy* 93 (2016), pp. 340–352. DOI: 10.1016/j.renene.2016.01.101 (cited on page 103).

[170] Jakob Mann. 'The spatial structure of neutral atmospheric surface-layer turbulence'. In: *Journal of Fluid Mechanics* 273 (1994), pp. 141–168. DOI: 10.1017/S0022112094001886 (cited on page 106).

[171] WAsP Engineering. *Wind conditions for fatigue loads, extreme loads and siting*. https://www.wasp.dk/weng#details__iec-turbulence-simulator, (accessed: September 09, 2021). 2020 (cited on page 106).

[172] IEC. *IEC 61400-1 ed. 3. Wind turbines - part 1: Design requirements*. Tech. rep. Geneva, Switzerland, 2005 (cited on pages 106, 127).

[173] Theodore Von Karman. 'Progress in the statistical theory of turbulence'. In: *Proceedings of the National Academy of Sciences of the United States of America* 34.11 (1948), p. 530. DOI: 10.1073/pnas.34.11.530 (cited on page 107).

[174] Jae Sang Moon et al. 'Toward Development of a Stochastic Wake Model: Validation Using LES and Turbine Loads'. In: *Energies* 11.1 (2018). DOI: 10.3390/en11010053 (cited on page 115).

[175] J Feliciano et al. 'Generalized analytical displacement model for wind turbine towers under aerodynamic loading'. In: *J. Wind. Eng. Ind. Aerodyn.* 176 (2018), pp. 120–130. DOI: 10.1016/j.jweia.2018.03.018 (cited on page 118).

[176] Herbert J Sutherland. *On the fatigue analysis of wind turbines*. Tech. rep. Albuquerque, NM (US): Sandia National Labs, 1999. DOI: 10.2172/9460 (cited on pages 127, 143).

[177] Marshall L Buhl. *MCrunch user's guide for version 1.00*. Tech. rep. TP-500-43139. 2008 (cited on pages 127, 143).

[178] Stephen D Downing and DF Socie. 'Simple rainflow counting algorithms'. In: *International Journal of Fatigue* 4.1 (1982), pp. 31–40. DOI: 10.1016/0142-1123(82)90018-4 (cited on page 127).

[179] MA Miner. 'Cumulative fatigue damage'. In: *Journal of Applied Mechanics* 12.3 (1945), pp. 159–164. DOI: 10.1115/1.4009458 (cited on page 127).

[180] Gregg Freebury and Walter Musial. 'Determining equivalent damage loading for full-scale wind turbine blade fatigue tests'. In: *2000 ASME Wind Energy Symposium*. 2000, p. 50. DOI: 10.2514/6.2000-50 (cited on page 128).

[181] Yves Dubief and Franck Delcayre. 'On coherent-vortex identification in turbulence'. In: *Journal of Turbulence* 1.1 (2000), pp. 011–011. DOI: 10.1088/1468-5248/1/1/011 (cited on page 130).

[182] Charles L Phillips, John M Parr, and Eve Ann Riskin. *Signals, systems, and transforms*. Prentice Hall Upper Saddle River, 2003 (cited on page 134).

[183] Leonardo P Chamorro et al. 'Turbulence effects on a full-scale 2.5 MW horizontal-axis wind turbine under neutrally stratified conditions'. In: *Wind Energy* 18.2 (2015), pp. 339–349. DOI: 10.1002/we.1700 (cited on page 156).

[184] KB Howard et al. 'Characterizing the response of a wind turbine model under complex inflow conditions'. In: *Wind Energy* 18.4 (2015), pp. 729–743. DOI: 10.1002/we.1724 (cited on page 156).

[185] Gabriel Thomas Scarlett et al. 'Unsteady hydrodynamics of a full-scale tidal turbine operating in large wave conditions'. In: *Renewable Energy* 143 (2019), pp. 199–213. DOI: 10.1016/j.renene.2019.04.123 (cited on page 157).

[186] Christian Bak et al. *Description of the DTU 10 MW reference wind turbine*. Tech. rep. DTU Wind Energy Report-I-0092. Kgs. Lyngby, Denmark: DTU, 2013 (cited on page 159).

[187] Cristina L Archer, Sina Mirzaeisefat, and Sang Lee. 'Quantifying the sensitivity of wind farm performance to array layout options using large-eddy simulation'. In: *Geophysical Research Letters* 40.18 (2013), pp. 4963–4970. DOI: 10.1002/grl.50911 (cited on page 159).

[188] R F Ramsay, M J Hoffman, and G M Gregorek. *Effects of grit roughness and pitch oscillations on the S809 airfoil*. Tech. rep. Dec. 1995. DOI: 10.2172/205563 (cited on page 163).

[189] Sandeep Gupta and J Gordon Leishman. 'Dynamic stall modelling of the S809 aerofoil and comparison with experiments'. In: *Wind Energy* 9.6 (2006), pp. 521–547. DOI: 10.1002/we.200 (cited on page 163).

Special Terms

A
ABL Atmospheric Boundary Layer. 6, 7, 153
ALE Arbitrary Lagrangian-Eulerian. 12
ALM Actuator Line Model. 10, 16, 21, 92, 93, 133, 154, 155

B
BEM Blade Element Momentum. 8, 9, 100, 154
BL Beddoes and Leishman. 21, 42, 43, 45, 48, 49, 52, 163

C
CFD Computational Fluid Dynamics. 7, 9–11, 16, 21, 49, 154, 158
CFL Courant-Friedrichs-Lewy. 36
CSD Computational Structural Dynamics. 9, 12, 154

D
DEL Damage Equivalent Load. 127–129, 143
DES Detached Eddy Simulation. 13
DNS Direct Numerical Simulation. 9, 10, 26–28, 154
DOF Degree of Freedom. 21, 41, 59, 65–70, 72, 74–78, 109, 111, 112, 120, 126, 156

F
FEM Finite-Element Method. 10, 12, 13, 55, 66, 73
FOR Frame of Reference. 60, 61, 65, 66, 72, 73, 75, 78, 87–94, 126
FSI Fluid-Structure Interaction. 8, 10–13, 15, 21, 25, 55, 82, 86, 91–93, 95, 106, 115, 116, 124, 127, 133, 136, 138, 141, 143, 154, 156–158

G
GEBT Geometrically-Exact Beam Theory. 9, 13, 82

H
HAWT Horizontal Axis Wind Turbine. 14, 16, 21, 154, 155, 158

I
IBM Immersed Boundary Method. 21, 37, 38, 155

L
LCOE Levelised Costs Of Energy. 4, 5, 153
LES Large Eddy Simulation. 10, 13, 14, 21, 25, 27, 28, 31, 45, 93, 99, 106, 107, 154, 155
LEV Leading-Edge Vortex. 19, 42, 146

M
MPI Message Passing Interface. 33

N
NREL National Renewable Energy Laboratory. 9, 12–14, 42, 99, 155

P
pdf probability density function. 119, 120
PSD Power Spectral Density. 118, 119, 122, 141

R

RANS Reynolds-Averaged Navier-Stokes Equations Simulation. 9, 10, 12–14, 27, 28
RK Runge-Kutta. 92, 93, 95

S
SEMMT Solid-Extension Mesh Moving Technique. 12
SGS Subgrid-Scale. 29

T
TKE Turbulent Kinetic Energy. 147

U
UA Unsteady Aerodynamics. 14–16, 20, 21, 45, 101, 116, 133, 136, 138, 141–146, 154, 157–159

V
VAWT Vertical Axis Wind Turbine. 14, 16